TU Delft

Delft University of Technology

Document Version
Final published version

Citation (APA)
Sheikhi, M. A. (2027). *Data-Driven Fault Diagnosis in High-Tech Manufacturing Systems*. [Dissertation (TU Delft), Delft University of Technology]. https://doi.org/10.4233/uuid:fb3ce3f4-b07e-41f2-b6ab-c8c7cd4bbf91

Important note
To cite this publication, please use the final published version (if applicable).
Please check the document version above.

Copyright
In case the licence states “Dutch Copyright Act (Article 25fa)”, this publication was made available Green Open Access via the TU Delft Institutional Repository pursuant to Dutch Copyright Act (Article 25fa, the Taverne amendment). This provision does not affect copyright ownership.
Unless copyright is transferred by contract or statute, it remains with the copyright holder.

Sharing and reuse
Other than for strictly personal use, it is not permitted to download, forward or distribute the text or part of it, without the consent of the author(s) and/or copyright holder(s), unless the work is under an open content license such as Creative Commons.

Takedown policy
Please contact us and provide details if you believe this document breaches copyrights.
We will remove access to the work immediately and investigate your claim.

This work is downloaded from Delft University of Technology.

DATA-DRIVEN FAULT DIAGNOSIS IN HIGH-TECH MANUFACTURING SYSTEMS



MOHAMMAD AMIN SHEIKHI

Data-Driven Fault Diagnosis in High-Tech Manufacturing Systems

Data-Driven Fault Diagnosis in High-Tech Manufacturing Systems

Dissertation

for the purpose of obtaining the degree of doctor
at Delft University of Technology
by the authority of the Rector Magnificus,
Prof. dr. ir. H. Bijl,
Chair of the Board for Doctorates
to be defended publicly on
Monday 11 January 2027 at 12:30

by

Mohammad Amin SHEIKHI

This dissertation has been approved by the (co) promoters.

Composition of the doctoral committee:

Rector Magnificus,	chairperson
Prof. dr. T. Keviczky,	Delft University of Technology, promotor
Dr. P. Mohajerin Esfahani,	University of Toronto, Canada, promotor
Dr. G. de Albuquerque Gleizer,	Delft University of Technology, copromotor
Independent Members:	
Prof. dr. D.M. Raimondo,	University of Trieste, Italy
Prof. dr. C. Rojas,	KTH Royal Institue of Technology, Sweden
Prof. dr. ir. A.J. van der Veen,	Delft University of Technology
Prof. dr. N. van de Wouw,	Eindhoven University of Technology, The Netherlands
Prof. dr. ir. J.W. van Wingerden,	Delft University of Technology, reserve member

This work was supported by the Digital Twin project with project number P18-03 of the research programme TTW-Perspective which is (partly) financed by the Dutch Research Council (NWO).







Keywords: Data-driven control, fault diagnosis, fault detection and isolation, system identification, optimization, estimation, input reconstruction, input design, geometric control, linear systems

Printed by: Ridderprint, https://www.ridderprint.nl

Cover by: M.A. Sheikhi

Style: TU Delft House Style with modifications
https://github.com/Inventitech/phd-thesis-template

Copyright © 2026 by M.A. Sheikhi
ISBN 978-94-6518-556-9

An electronic version of this dissertation is available at:
https://doi.org/10.4233/uuid:fb3ce3f4-b07e-41f2-b6ab-c8c7cd4bbf91

درخت تو گر بار دانش بگیرد به زیر آوری چرخ نیلوفری را

If your tree bears the fruit of knowledge, you can govern the stars yourself.

ناصر خسرو Nasir-i Khusraw

Contents

Acknowledgments **xi**

Summary **xv**

Samenvatting **xvii**

1 Introduction **1**
1.1 Background and Context . . . 2
1.1.1 Real-World Case Studies . . . 2
1.1.2 Fault Diagnosis Problem Statement . . . 4
1.1.3 Geometric Interpretation . . . 5
1.2 Motivation and Research Gaps . . . 7
1.3 Research Objectives . . . 9
1.4 Thesis Outline and Original Contributions . . . 11
1.5 Notation . . . 12

2 Fault Diagnosis: Geometric Interpretation and Tractable Algorithms **17**
2.1 Fundamentals of Fault Diagnosis . . . 18
2.1.1 Settings . . . 18
2.1.2 Solution Approaches . . . 19
2.1.3 System Representations . . . 19
2.1.4 Residual Generation . . . 20
2.2 Detection . . . 23
2.2.1 Nonlinear and Robustification Approaches . . . 25
2.2.2 Model-Free Approaches . . . 28
2.3 Isolation . . . 31
2.3.1 Nonlinear Systems . . . 32
2.3.2 Multimodel Hypothesis: Passive and Active Methods . . . 33
2.3.3 Model-Free Approaches . . . 34
2.4 Estimation . . . 35
2.4.1 Linear Systems . . . 36
2.4.2 Nonlinear Systems . . . 38
2.4.3 Multiplicative Faults . . . 39
2.4.4 Active Methods and Input Design . . . 40
2.4.5 Model-Free Approaches . . . 40
2.5 Summary and Future Issues . . . 41

3 Data-Driven Fault Detection and Isolation 43
3.1 Introduction . . . 44
3.2 Null-Space-Based Residual Generation . . . 45
3.2.1 System . . . 45
3.2.2 Residual . . . 46
3.2.3 Subspace Perspective . . . 47
3.3 Fault Isolation Scheme . . . 48
3.3.1 Fault Dictionaries . . . 49
3.3.2 Geometric Classifier . . . 50
3.4 Fault Discernibility . . . 51
3.4.1 Intersection of Two Dictionaries . . . 52
3.5 Computing the Diagnosis Filter with Noisy Data . . . 53
3.6 Numerical Results . . . 55
3.7 Conclusions . . . 57

4 Data-Driven Characterization of Multivariable LTI Systems Zeros 59
4.1 Introduction . . . 60
4.2 Preliminaries . . . 62
4.2.1 System Properties from a Geometrical Perspective . . . 63
4.2.2 System Zeros . . . 65
4.3 Output-Zeroing Problem . . . 67
4.3.1 Characterization of Data Equation Null Space . . . 68
4.4 Data-Driven Computation of Zeros . . . 72
4.5 Numerical Examples and Applications . . . 75
4.5.1 Fault Discernibility . . . 75
4.5.2 Input Reconstruction . . . 76
4.5.3 Data-driven Invariant Zero Computation . . . 77
4.5.4 Data-Driven Input Redundancy Detection . . . 80
4.6 Conclusion . . . 80

5 Data-Driven Fault Estimation 83
5.1 Introduction . . . 84
5.2 Problem Statement . . . 85
5.2.1 Model . . . 86
5.3 Main Result . . . 87
5.3.1 Inverse-System-Based Filter . . . 88
5.3.2 Kernel-Based Regularization . . . 90
5.4 Simulation Results . . . 94
5.4.1 Comparison Study . . . 95
5.5 Conclusions . . . 98

6 Active Learning 99
6.1 Introduction . . . 100
6.2 Problem Statement . . . 101
6.2.1 Order Determination in Subspace Identification . . . 101

6.3 Proposed Method . . . 104
6.3.1 Optimal Input Design . . . 104
6.3.2 Experiment Application Loop . . . 107
6.4 Numerical Simulation . . . 110
6.5 Conclusions . . . 111

7 Conclusion **113**
7.1 Future Research Recommendations. . . . 116
7.2 Societal Impact . . . 118

A Technical Proofs of Chapter 3 **119**

B Appendices to Chapter 4 **123**
B.1 Duality Between Subspaces . . . 123
B.2 Auxiliary Results . . . 123
B.3 Technical Proofs . . . 124

C Rational Orthonormal Basis Functions Implementation **135**
C.1 Balanced State-Space Realization . . . 135
C.2 Rational Orthonormal Basis Functions . . . 136
C.2.1 All-Pass Transfer Function . . . 137
C.2.2 Basis Construction . . . 137
C.3 Implementation . . . 140
C.4 Kernel Regularization . . . 146

Bibliography **149**

List of Publications **167**

Acknowledgments

Despite the linearity assumption underlying my PhD research, the journey itself has been anything but linear; in fact, it has been highly nonlinear and stochastic, much like life itself. Expecting the unexpected brings both the greatest satisfaction and the most painful experiences. In the end, perhaps this is the paradox of pursuing a PhD: the person who begins it and the one who defends it are, in many ways, no longer the same. I could never name everyone who played a part, but I am grateful to all of you for helping me reach this milestone. Here, I would like to thank some of you by name.

First and foremost, I wish to acknowledge my promotors for offering me the position and granting me the freedom to grow into an independent researcher. Their invaluable guidance and unwavering support have been instrumental. **Tamás**, your discipline and professionalism set an excellent example for anyone who seeks to lead and manage a team. I still vividly remember our first meeting, when you presented a detailed agenda for the first academic year, along with practical advice that I later realized was a luxury not every PhD candidate benefited from. Our technical discussions always returned to the practical value of addressing research problems, thanks to your engineering perspective. I also learned a great deal about problem formulation, identifying core challenges, supervising master's students, and the ethics of research and collaboration. I am truly grateful for all of this. **Peyman**, it is no mystery to those who know you that your enthusiasm and passion for science make you different and inspire the researchers around you. I still remember our first meeting at the Digital Twin Programme's annual event, when we ended up discussing fault diagnosis problems on the train ride back. If I learned one thing from you, it is that a thorough understanding of a research question and its clear mathematical formulation go hand in hand. Thank you for your dedication and for bringing greater rigor to my research. My special thanks would definitely go to **Gabriel**. The evolution of our relationship throughout my PhD says it all, from being collaborators to becoming an amazing friend, later an officemate, and finally having you as my supervisor. I was the luckiest to share similar research interests with you, making our technical and non-technical discussions among the most enjoyable parts of my PhD. I learned a lot from you about writing rigorous mathematical statements and dealing with your killer counterexamples. Obrigado! You have been a big part of this thesis. And, of course, your daughter, **Liana**, for her contribution to Chapter 4.

My sincere thanks go to the members of my doctoral committee, **Davide M. Raimondo**, **Cristian R. Rojas**, **Alle-Jan van der Veen**, **Jan-Willem van Wingerden**, and **Nathan van de Wouw**, for reading my dissertation and providing valuable feedback. **Cristian**, thank you also for hosting my research visit to KTH, which led to a fruitful collaboration. **Nathan**, I greatly appreciate your leadership of Project 4 in the Digital Twin Programme and your continued support for its researchers.

This thesis was financially supported by NWO through the Digital Twin Programme, for which I thank all parties involved, especially the project leaders, **Paul** and **Bayu**. The

programme also offered valuable experience working with industrial partners on practical fault diagnosis problems, and I particularly thank **Jeroen** from ASML, and **Youri** and **Pim** from Canon, for their insights. I am also grateful to the master's students who contributed to my research, **Roos**, **Wouter**, and **Segher**. Finally, I enjoyed collaborating with **Farhad** and **Zhong** through Project 4.

I was fortunate to share my PhD journey with colleagues from diverse backgrounds who made life at DCSC enjoyable through sports, social events, and countless conversations. A big shoutout to **Sander** for organizing many of these activities and reviewing the Dutch summary! I also thank the DCSC staff for fostering a welcoming environment for research and social interaction. Over four years, I shared offices with 13 different people, a record unlikely to be broken anytime soon! Special thanks to my longtime officemates in C-3-330, Salim, Tolga, Giray, and Anil, for making our office a gem in DCSC where everyone was welcome, whether they were bored, looking for skilled foosball players, or simply after some of our diverse snacks. **Salim**, your attention to detail was unmatched, and you never approved of the way I used technology, even for a simple Google search, which you labelled an "inefficient" approach. Thanks for the cooking tips, the best brisket in town, introducing me to Cineville, and much more. **Tolga**, the kindest of all time, thanks for keeping me up to date with technology and for our grape-sharing tradition, later adjusted for inflation with mandarins. **Giray**, you kept the art of handwritten notes alive, while **Anil** made sure our office plants stayed alive. Thank you all for the memories! Of all the conference trips, IFAC 2026 in Busan was by far the most memorable, thanks to **Sam**, **Afra**, **Yichen**, **Fritz**, **Ioannis**, **Eva**, **Gianpietro**, **Zoe**, **Mahshad**, and **Reza (Rahimi)**. Many thanks also to **Maria** for her amazing parties, **David** for capturing memories through his camera, **Sreeshma** for being a great neighbour and sharing Indian desserts, **Roger** for making the ice cream business idea seem feasible, **Paul** for flexing his card tricks, **Guido** and **Matteo** for football conversations and Monday league games, **Edu** for showcasing Brazilian Joga Bonito, and **Léo** for always being willing to help. And to the many others with whom I shared memorable moments at DCSC: **Aasim**, **Alessandro**, **Alex de Ruijter**, **Alex Gallo**, **Amin**, **Arman**, **Arghya**, **Ashkan**, **Athina**, **Ciao**, **Darya**, **Daniel**, **Dimitris**, **Edoardo**, **Emilio**, **Eva**, **Faegheh**, **Francesco**, **Fredrik**, **Frida**, **Georgios**, **Gyula Max**, **Hossein**, **Ilias**, **Ivo**, **Jesse**, **Lotfi**, **Marcus**, **Max Sibeijn**, **Mohammad (Khosravi)**, **Pedro**, **Rayyan**, **Reza Riahi**, **Shabnam**, **Silvia**, **Suad**, **Tim**, **Ying**, and **Yun**.

Visiting KTH was a highlight of my academic journey, despite my initial reluctance to relocate in the final year. Thanks to everyone at DCS for the welcoming atmosphere and countless fikas! I first met **Andrea**, **Tommy**, and **Nicola** at CDC 2025 in Rio, never imagining we would later share an office. What a small world! Thanks also to **Daniel** and **Greg** for the conversations, gym sessions, and fun times, **Yibo** and **Mags** for exchanging research ideas, and **Giacomo** and **Fumiya** for joining me at all sorts of random events. **Amir** and **Sajjad**, it did not take long to realize how well we got along, but I never expected to make so many memories in such a short time, including playing FIFA at 5 a.m. Finally, thanks to **Lisa**, **Martina**, and **Joowon** for the coffee breaks and time spent together.

During my time in the Netherlands, I was lucky enough to cross paths with people who became friends and, hopefully, our friendships will last a lifetime. Sharing life experiences, supporting one another, and offering comfort when needed made your presence an important part of this journey. **Haiwei**, thanks for your excellent taste in upscale restau-

rants and our memorable trips. **Mohammad**, our spontaneous bike trips often took us to remote places, with what was supposed to be a short ride around the neighbourhood ending in another city! Your unusual desire for fruit, including eating five mangoes in one sitting by a lake, is certainly something else. I hope you never lose that wonderful spontaneity that makes you one of a kind. **Sasan**, your resilience throughout your PhD has been inspiring, and I cherish our friendship, trips, and shared rooms during courses. **Leila**, your positivity and ability to spread peace and love are remarkable. Thanks for all the movie nights, or simply for using movies as an excuse to hang out. And **Mohammad (Erisi)**, your take on movie scenes is always worth listening to. Thank you for all those moments. **Niloufar**, thanks for the events and parties we attended together and for being supportive. **Farnaz**, you were the first person I met in the Netherlands. Sharing our experiences and supporting each other through the challenges of living away from our home countries for the first time meant a lot to me.

Beyond the Netherlands, I am grateful to have longtime friends in different parts of the world whom I first met in Iran. Our conversations and video calls were vital in getting through some of the crises during my PhD. A million thanks for being there in those moments, especially **Abolfazl**, **Ali**, **Ayub**, **Danial**, **Hamed**, **Hamid**, **Iman**, **Masoud (Payandeh)**, **Mohammad (Raisi)**, **Mohammad Reza**, **Nazanin**, **Omid (Ranjbar)**, **Omid (Sobhani)**, **Roya**, **Yasin**, **Yousef**.

This dissertation is dedicated to my parents, **Masoumeh** and **Hassan**, who sacrificed so much to give me the opportunity to pursue my education. I will forever be in their debt, knowing that I can never repay their unconditional love and care. I extend my deepest gratitude to my older brother, **Sajjad**, for always being there for me and our parents, my sister-in-law, **Manosureh**, for checking on me and offering wholehearted support, and my beautiful niece and nephew, **Helma** and **Hami**, whose presence has brought immense joy to our family. I cannot wait to see them again in person. The following paragraph is in Persian:

تقدیم به
پدرم و مادرم
هرچه آموختم در مکتب عشق شما آموختم و هرچه بکوشم قطره‌ای از دریای بی‌کران مهربانیتان را سپاس نتوان بگویم، از صمیم قلب دوستتان دارم.

Amin
Delft, November 2026

Summary

Safety and predictability have become vital requirements for modern technological systems in an era increasingly dominated by automation. To meet these demands, control and performance monitoring units are placed at the core of supervisory architectures. As an integral part of such monitoring systems, fault diagnosis solutions are developed to detect abnormal behavior at an early stage, identify the underlying causes of degradation, and enable timely intervention before faults or adversarial events lead to downtime, unsafe operation, or costly system-wide failures. Fault diagnosis in general relies on hardware redundancy, physical systems, and/or predictive models derived from governing physical laws or digital representation of the underlying plant. However, developing accurate first-principles models for high-tech manufacturing systems is often cumbersome and, in many cases, impractical. Meanwhile, recent technological advances have substantially increased data accessibility and availability, contributing to the growing prominence of data-driven solutions.

This thesis studies fault diagnosis in data-driven settings. In particular, it develops novel diagnosis methods for linear time-invariant systems subject to additive faults. Although the problem has been extensively studied in the literature, this thesis offers a fresh system-theoretic perspective on different classes of fault diagnosis problems. Each problem class is formally characterized, and questions concerning fundamental performance limits are addressed. Moreover, whenever possible, geometric interpretations of the underlying diagnosis problems are also provided. The main findings benefit health monitoring in various application domains, including robotic manipulators, semiconductor manufacturing, power systems, and chemical processes, provided that the required assumptions are satisfied. Throughout the thesis, a central assumption is that only fault-free input–output data are available for designing the diagnosis filters.

Diagnosis problems can be studied from several perspectives. In the first part of this thesis, the fault diagnosis literature is systematically reviewed and classified with respect to diagnosis tasks, information settings, and solution approaches. A tractable optimization framework based on differential-algebraic equations is then introduced, which accommodates different classes of fault diagnosis problems and, more importantly, establishes connections with well-known existing results. Subsequently, the problem of fault isolation in data-driven settings is studied using null-space-based methods. For this diagnosis class, a new subspace-classification-based approach is proposed, showing that the achievable performance is determined by the zero structure of the underlying fault subsystem.

Inspired by the findings in the first part, the second part of the thesis begins by revisiting the characterization of multivariable system zeros in linear dynamical systems from a data-driven perspective. Although this topic is of independent interest, its treatment in this thesis is primarily motivated by its critical role in fault diagnosis. Next, the thesis addresses other classical problems related to fault diagnosis in a data-driven setting: fault estimation and input design for active learning and diagnosis. For fault estimation, a di-

rect system-inversion-based diagnosis filter is developed, allowing prior information of the inverse system to be incorporated through kernel regularization. Its performance is compared against state-of-the-art indirect approaches that first identify a forward model and subsequently perform model-based inversion. The results indicate that, although the indirect approach is often more intuitive, it is not necessarily optimal for fault estimation. Finally, a novel optimal input design scheme is proposed to reveal the true system order and enhance diagnosis performance.

In summary, this thesis advances the understanding and design of fault diagnosis systems in data-driven settings. Its contributions are twofold: first, it provides new system-theoretic insights into the fundamental limitations of diagnosis problems; second, it proposes novel methods that tackle these problems from alternative perspectives with the aim of achieving improved performance. Subspace identification and behavioral system theory serve as the main theoretical foundations throughout the thesis and underpin the development of the proposed diagnosis filters. The effectiveness of the proposed methods is evaluated through a series of numerical simulations. Collectively, these contributions support the development of reliable monitoring frameworks for safe, efficient, and autonomous operation in modern engineering systems.

Samenvatting

Veiligheid en voorspelbaarheid zijn essentiële vereisten geworden voor moderne technologische systemen in een tijdperk waarin automatisering een steeds grotere rol speelt. Om aan deze vereisten te voldoen, vormen regel- en prestatiebewakingseenheden de kern van overkoepelende bewakingsarchitecturen. Als integraal onderdeel van dergelijke bewakingssystemen worden foutdiagnosemethoden ontwikkeld om afwijkend gedrag vroegtijdig te detecteren, de onderliggende oorzaken van degradatie te identificeren en tijdig ingrijpen mogelijk te maken, voordat fouten of kwaadwillige verstoringen leiden tot stilstand, onveilige bedrijfsvoering of kostbare uitval van het gehele systeem. Foutdiagnose berust doorgaans op hardwareredundantie, fysieke systemen en/of voorspellende modellen die zijn afgeleid van de bepalende natuurkundige wetten of van een digitale representatie van het te bewaken systeem. Het ontwikkelen van nauwkeurige modellen op basis van fundamentele natuurkundige principes is voor geavanceerde productiesystemen echter vaak arbeidsintensief en in veel gevallen praktisch niet haalbaar. Tegelijkertijd hebben recente technologische ontwikkelingen de toegankelijkheid en beschikbaarheid van data aanzienlijk vergroot, waardoor datagedreven oplossingen steeds meer aan belang winnen.

Dit proefschrift onderzoekt foutdiagnose in een datagedreven context. In het bijzonder worden nieuwe diagnosemethoden ontwikkeld voor lineaire tijdinvariante systemen die onderhevig zijn aan additieve fouten. Hoewel dit onderwerp in de literatuur uitvoerig is bestudeerd, biedt dit proefschrift een nieuw systeemtheoretisch perspectief op verschillende klassen van foutdiagnoseproblemen. Elke probleemklasse wordt formeel gekarakteriseerd en vraagstukken over fundamentele prestatiegrenzen worden onderzocht. Waar mogelijk worden daarnaast geometrische interpretaties van de onderliggende diagnoseproblemen gegeven. De belangrijkste resultaten zijn relevant voor toestandsbewaking in uiteenlopende toepassingsgebieden, waaronder robotmanipulatoren, halfgeleiderproductie, elektrische energiesystemen en chemische processen, mits aan de vereiste aannames wordt voldaan. Een centrale aanname in het gehele proefschrift is dat voor het ontwerpen van de diagnosefilters uitsluitend ingangs-uitgangsdata beschikbaar zijn die onder foutvrije omstandigheden zijn verzameld.

Diagnoseproblemen kunnen vanuit verschillende perspectieven worden bestudeerd. In het eerste deel van dit proefschrift wordt de literatuur over foutdiagnose systematisch geanalyseerd en geclassificeerd naar diagnosetaak, beschikbare informatie en oplossingsbenadering. Vervolgens wordt een computationeel hanteerbaar optimalisatiekader op basis van differentiaal-algebraïsche vergelijkingen geïntroduceerd. Dit kader omvat verschillende klassen van foutdiagnoseproblemen en legt bovendien verbanden met bekende resultaten uit de literatuur. Daarna wordt het probleem van foutisolatie in een datagedreven context onderzocht met behulp van nulruimtegebaseerde methoden. Voor deze klasse van diagnoseproblemen wordt een nieuwe benadering op basis van deelruimteclassificatie voorgesteld. Daarbij wordt aangetoond dat de haalbare prestaties worden bepaald door de nulpuntenstructuur van het onderliggende foutsubsysteem.

Voortbouwend op de bevindingen uit het eerste deel begint het tweede deel van dit proefschrift met een hernieuwde beschouwing van de karakterisering van multivariabele systeemnulpunten in lineaire dynamische systemen vanuit een datagedreven perspectief. Hoewel dit onderwerp op zichzelf van belang is, wordt de behandeling ervan in dit proefschrift voornamelijk gemotiveerd door de cruciale rol van deze nulpunten bij foutdiagnose. Vervolgens worden andere klassieke problemen op het gebied van foutdiagnose in een datagedreven context behandeld: foutschatting en het ontwerpen van ingangssignalen voor actief leren en diagnose. Voor foutschatting wordt een direct diagnosefilter op basis van systeeminversie ontwikkeld, waarin voorkennis over het inverse systeem kan worden verwerkt via kernelregularisatie. De prestaties van dit filter worden vergeleken met die van geavanceerde indirecte benaderingen, waarbij eerst een voorwaarts model wordt geïdentificeerd en vervolgens modelgebaseerde inversie wordt uitgevoerd. De resultaten laten zien dat de indirecte benadering weliswaar vaak intuïtiever is, maar niet noodzakelijk optimaal voor foutschatting. Tot slot wordt een nieuwe methode voor het optimaal ontwerpen van ingangssignalen voorgesteld, waarmee de werkelijke systeemorde kan worden achterhaald en de diagnoseprestaties kunnen worden verbeterd.

Dit proefschrift draagt bij aan zowel het begrip als het ontwerp van foutdiagnosesystemen in een datagedreven context. De bijdragen zijn tweeledig: enerzijds biedt het nieuwe systeemtheoretische inzichten in de fundamentele beperkingen van diagnoseproblemen; anderzijds introduceert het nieuwe methoden die deze problemen vanuit alternatieve perspectieven benaderen om betere prestaties te realiseren. Deelruimte-identificatie en de gedragsbenadering binnen de systeemtheorie vormen de belangrijkste theoretische grondslagen van het proefschrift en liggen ten grondslag aan de ontwikkeling van de voorgestelde diagnosefilters. De effectiviteit van de voorgestelde methoden wordt geëvalueerd aan de hand van een reeks numerieke simulaties. Gezamenlijk ondersteunen deze bijdragen de ontwikkeling van betrouwbare bewakingskaders voor een veilige, efficiënte en autonome werking van moderne technische systemen.

1

Introduction

Reliable health monitoring and control of modern engineering systems are essential for ensuring safe, resilient, and uninterrupted operation. This necessity is particularly evident in safety-critical applications—such as automotive systems, semiconductor manufacturing, aerospace, and industrial processes—where malfunctions or failures can disrupt production lines and incur significant financial losses. In extreme cases, such failures may even endanger the workforce and the surrounding environment. Furthermore, the complex interplay among components and subsystems within a production process (e.g., physical plants, control systems, instrumentation, communication networks, and human interactions) calls for a systematic approach to addressing the underlying health-monitoring problem.

To meet these requirements, the broad research area of *fault diagnosis* addresses a wide range of related problems and challenges. Effective diagnostic techniques provide two primary benefits: first, mitigating the risk of unexpected failures; and second, enabling a preemptive maintenance approach by predicting and preventing faults before they have a significant impact. These capabilities reduce downtime and maintenance costs while enhancing overall system safety and sustainability. In practice, diagnostic solutions are commonly implemented as supervisory units operating in parallel with the physical system to continuously monitor its operational state.

At the same time, achieving these diagnostic goals is challenged by ever-increasing demands for high performance and quality, driving the development of more advanced systems. As a result of this growing complexity, physics-based models, such as those derived from first principles, are becoming less readily available, more costly, and more difficult to obtain. This limitation encourages the development of diagnostic approaches that extract information directly from recorded data rather than relying on explicit knowledge of the underlying data-generating process. Consequently, the shift from classical model-based techniques to data-driven methods ensures that diagnostic solutions remain both accessible and scalable as system complexity increases.

Accordingly, this thesis is concerned with fault diagnosis in a data-driven setting, assuming the underlying data are generated by a linear dynamical system while the parameters are not known *a priori*. However, the study is not restricted to this setting or class

1

of systems; we also review and examine the related literature covering broader settings and system classes. In this chapter, we formally state the fault diagnosis problem and its necessary components in a general sense. Building on this foundation, we identify and motivate the existing knowledge gaps. It is then that the key research questions are formulated to support the main thesis objective, which will be made precise later. Finally, the overall structure of the thesis is outlined.

1.1 Background and Context

It is important to clearly define the notion of a fault throughout this thesis. Here, the term "fault" is understood as any undesirable deviation from the nominal condition of the system, caused by sources such as internal malfunctions, hardware degradation, parameter variations, external disturbances, or stealthy (adversarial) manipulations. A similar definition appears in [1]. Fault diagnosis typically comprises four interrelated problems: *fault detection*, *fault isolation*, *fault estimation*, and *fault mitigation* or *fault-tolerant control*. Fault detection refers to the ability to determine whether an unexpected event or anomaly has occurred in a system [2, 3]. Once a fault is detected, fault isolation aims to identify the specific source or location of the fault within the system [4, 5]; it extends fault detection by distinguishing among multiple potential fault sources to determine which has occurred. Fault estimation is the next level of fault isolation and aims to quantify the magnitude, dynamics, or temporal evolution of the fault [6, 7]. Finally, fault mitigation involves designing corrective actions or control strategies to minimize the impact of the fault or restore system functionality [8, 9]. While the diagnosis problems exhibit increasing conceptual and technical complexity from detection to mitigation, each poses distinct theoretical and practical challenges depending on the system setting and available information. In this thesis, we focus on fault detection, isolation, and estimation, with particular emphasis on the geometric interpretation of diagnosis filters and the intuition behind how they partition the measurement space.

1.1.1 Real-World Case Studies

Before introducing the theoretical and mathematical foundations of each fault diagnosis class, several examples are presented below to highlight distinct diagnostic challenges encountered in modern industrial applications[1].

Power Systems Case Study: High-Dimensional Nonlinear Dynamics

Fault detection in large-scale power systems is a critical task, particularly in the face of cyber-physical threats and significant natural disturbances. These systems are characterized by nonlinear dynamics and high levels of ambient noise due to demand fluctuations, renewable integration, and load uncertainties. A representative scenario is the detection of cyberattacks on automatic generation control loops in multiarea power networks [16]. In such settings, faults or malicious disturbances are designed to mimic nominal behavior under natural fluctuations, making detection challenging.

[1]The provided use cases are (partially) part of the Digital Twin project with project number P18-03 of the research programme TTW-Perspective which is (partly) financed by the Dutch Research Council (NWO).

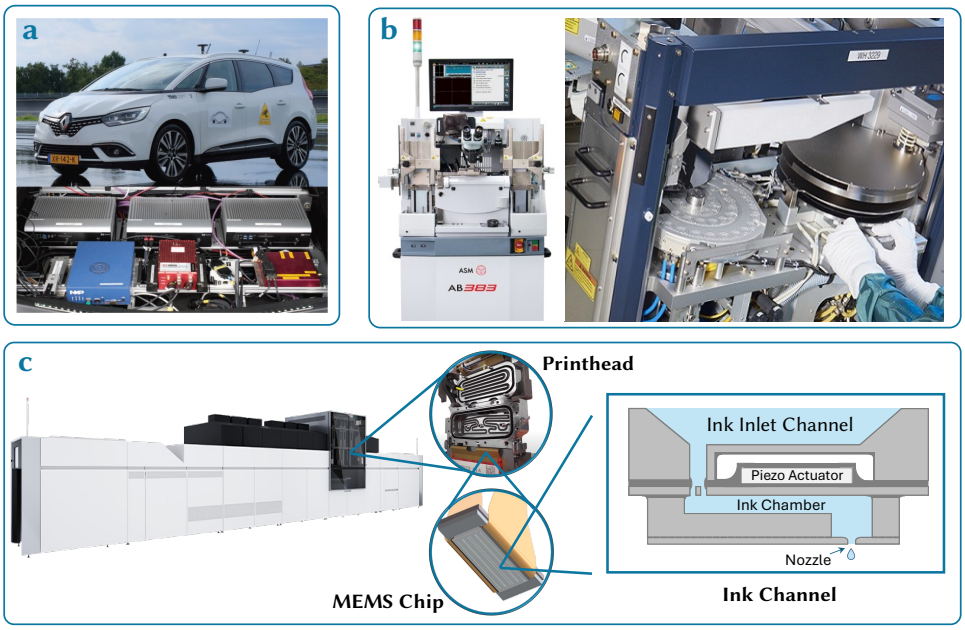

Figure 1.1: Fault diagnosis in real-world applications: (a) TNO Renault Grand Scénic autonomous driving test platform [10]. (b) ASMPT AB383 wire bonder [11] together with ASML and VDL-ETG wafer handling robot [12, 13]. (c) Canon Production Printing varioPRESS iV7 industrial printer, with schematic representation of the ink channel use case [14, 15].

Autonomous Vehicle Case Study: Inseparable Faults

Autonomous driving platforms require accurate real-time fault estimation to ensure safe operation under dynamic and uncertain conditions. This problem is typically addressed in systems modeled as linear but subject to structured uncertainties, actuator delays, and multiplicative noise whose dynamic effects are inseparable from some additive faults. Of particular interest are faults affecting steering performance, such as actuator degradation (multiplicative faults) or command biases (additive faults), which can degrade tracking performance or lead to unsafe maneuvers. Figure 1.1a shows an experimental setup of Renault Grand Scénic autonomous driving platform at TNO [10].

Mechatronics Case Study: Low Signal-to-Noise Ratio

Mechatronics in high-tech manufacturing, such as the ones in the electronics and semiconductor industries, pose unique challenges in fault diagnosis due to these systems' ultrahigh precision requirements. Faults in such systems are often extremely small, sometimes below 0.1%, and evolve slowly over time (e.g., the case of aging or wear and tear). In the fault diagnosis literature, such slow-developing faults are referred to as incipient faults. This calls for fault estimation techniques capable of handling low signal-to-noise ratio conditions, often using active detection strategies to enhance sensitivity. Figure 1.1b

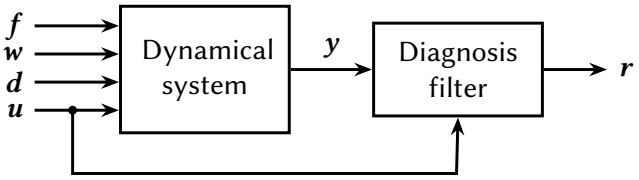

Figure 1.2: General configuration of systems and diagnosis filters. The filter processes the available control inputs $\boldsymbol{u}$ and output measurement $\boldsymbol{y}$ and generates the residual $\boldsymbol{r}$ that offers information on the fault signal $\boldsymbol{f}$, regardless of natural disturbance $\boldsymbol{d}$ and exogenous noise $\boldsymbol{w}$.

left illustrates the AB383 wire bonder, designed and fabricated by ASMPT Ltd, which creates connections between integrated circuits and their packaging. After prolonged operation, the positioning system is subject to multiplicative faults corresponding to parametric degradation (e.g., changes in stiffness, damping or available motor force), while additive faults represent factory floor vibrations. Figure 1.1b right depicts a selective compliance assembly robot arm (SCARA) manipulator developed by ASML for chip handling. Wafer-handling robots play a pivotal role in lithography machines, as they are responsible for loading and unloading wafers using robotic manipulators. The height of the end-effector tip as it enters the wafer stage is a crucial parameter. Various factors may cause this height to deviate from specification at the intended positions, potentially leading to collisions. In particular, possible faults include tilts of the gripper tip and/or those of the lower and upper arms. In this use case, multiplicative tilt faults of small angular magnitude typically develop gradually as incipient faults, making them particularly difficult to detect. Conversely, a broken belt represents another type of multiplicative fault in wafer-handling robots, characterized by an abrupt and significant impact on the system dynamics.

High-End Industrial Printers Case Study: Limited Sensors
High-end industrial inkjet printers operate under extreme precision requirements, yet a wide range of faults can degrade performance. Figure 1.1c shows the relevant components of the Canon Production Printing varioPRESS iV7 industrial printer, alongside a schematic representation of the ink channels. The ink flow is controlled by a piezoelectric actuator through deformation of the inlet membrane. Fault isolation in this context is challenging for several reasons. First, sensing at the nozzle level is very limited, with only a single sensor available for both actuation and measurement via self-sensing piezoelectric actuators. Second, most faults are multiplicative in nature, such as nozzle blockage, drying ink, or air bubbles.

1.1.2 Fault Diagnosis Problem Statement

Given a dynamical system of interest, a *diagnosis filter* is an engineered system that processes available measurements and provides the required information for detection, isolation, and/or estimation of faults present in the system. The standard setup is illustrated in Figure 1.2. Each block is subject to different multivariate signals. The signals $\boldsymbol{u}$[2] and $\boldsymbol{y}$ denote the control input and the dynamical system output, respectively, both of which are

[2]Signals in this section are defined as $\boldsymbol{x} : \mathcal{T} \to \mathbb{R}^{n_x}$, where the time set $\mathcal{T}$ can be either continuous or discrete time.

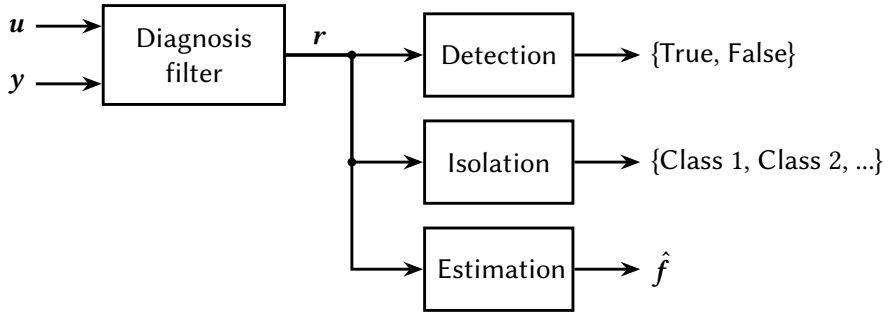

Figure 1.3: Classes of fault diagnosis systems: the diagnosis filter generates the residual signal $\boldsymbol{r}$ by processing the measured signals $\boldsymbol{u}$ and $\boldsymbol{y}$. The downstream diagnosis task is then formulated as binary classification, multiclass classification, or fault signal reconstruction $\hat{\boldsymbol{f}}$ (corresponding to detection, isolation, and estimation, respectively).

known and measurable. The unmeasured signals $\boldsymbol{f}$, $\boldsymbol{w}$, and $\boldsymbol{d}$ represent fault, noise, and natural disturbance, respectively. While the fault is the signal of interest, the remaining unknown signals are expected to be *filtered out* by the diagnosis filter. The distinction between *noise* and *disturbance* is common in the literature, but subtle, as it depends more on the problem than on the nature of the signals $\boldsymbol{d}$ and $\boldsymbol{w}$. The disturbance signal $\boldsymbol{d}$ is generally low-dimensional but has a large influence on the output, and as such it is expected to be *decoupled* at the diagnosis filter. In contrast, the signal $\boldsymbol{w}$ includes process and measurement noise that can have a larger dimension but limited impact, typically being characterized by a random process or a bounded signal. The diagnosis filter processes the available measurements $\boldsymbol{u}$ and $\boldsymbol{y}$ to generate the *residual* $\boldsymbol{r}$, which is the signal that enables the diagnosis task of interest. In general, the residual must be (approximately) zero irrespective of the natural disturbance $\boldsymbol{d}$, as long as the fault is zero (i.e., $\boldsymbol{f} = 0$). At this level of generality, we can formally introduce the residual as a function of the four exogenous signals (i.e., $\boldsymbol{r}(\boldsymbol{f}, \boldsymbol{w}, \boldsymbol{d}, \boldsymbol{u})$), and translate the fault detection problem using the following mappings:

$$\boldsymbol{d} \mapsto \boldsymbol{r}(\boldsymbol{0}, \boldsymbol{0}, \boldsymbol{d}, \boldsymbol{u}) \equiv \boldsymbol{0}, \quad \boldsymbol{d}, \forall \boldsymbol{u} \qquad \text{(disturbance decoupling)} \tag{1.1a}$$

$$\boldsymbol{f} \mapsto \boldsymbol{r}(\boldsymbol{f}, \boldsymbol{0}, \boldsymbol{d}, \boldsymbol{u}) \not\equiv \boldsymbol{0}, \quad \forall \boldsymbol{d}, \forall \boldsymbol{u} \qquad \text{(fault sensitivity)} \tag{1.1b}$$

Equation (1.1a) ensures perfect decoupling of $\boldsymbol{d}$ in the noise- and fault-free condition regardless of $\boldsymbol{u}$, whereas Equation (1.1b) guarantees sensitivity to the fault, even when $\boldsymbol{d}$ is present. With regard to the diagnostic objective, the fault diagnosis scheme reduces to processing the residual signal for binary classification (detection), multiclass classification (isolation), or signal reconstruction (estimation); see Figure 1.3. Each class of diagnosis problem is studied separately in Chapter 2, together with the related literature. Next, we examine the fault detection problem from a geometric perspective.

1.1.3 Geometric Interpretation

Consider the configuration illustrated in Figure 1.2 and the detection problem characterized through the mappings in Equation (1.1). The disturbance decoupling in Equation (1.1a)

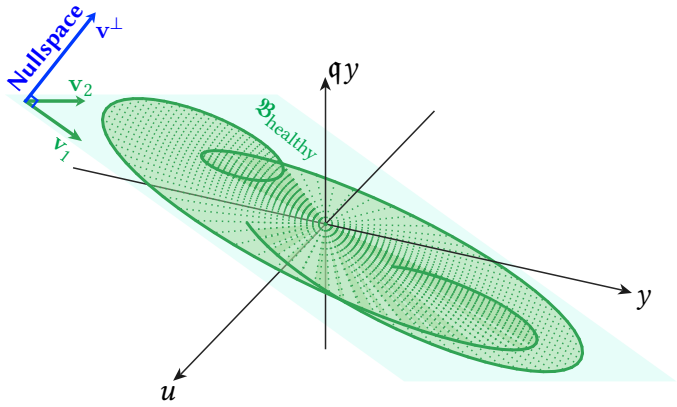

Figure 1.4: Two characterizations of a hyperplane (mint green) containing the healthy input–output trajectories $\mathfrak{B}_{\text{healthy}}$, when the diagnosis filter is a linear dynamical system: the span of the hyperplane using the basis $[\boldsymbol{v}_1, \boldsymbol{v}_2]$ (green) and the span of the null space (i.e., the orthogonal complement) using the basis $\boldsymbol{v}^\perp$ (blue).

essentially characterizes a set containing all the *healthy* trajectories of the pairs $(\boldsymbol{u}, \boldsymbol{y})$ for the underlying dynamical system in the absence of faults $\boldsymbol{f}$. The minimal among such sets is often referred to as the behavioral set [17] and is denoted hereafter by $\mathfrak{B}_{\text{healthy}}$.

The geometry of the set characterized by Equation (1.1a) is determined by the diagnosis filter, i.e., the mapping from $(\boldsymbol{u}, \boldsymbol{y})$ to the residual $\boldsymbol{r}$. When this diagnosis filter is itself a linear dynamical system, the set $\mathfrak{B}_{\text{healthy}}$ takes the form of a hyperplane, as depicted in Figure 1.4. There are two ways to characterize $\mathfrak{B}_{\text{healthy}}$: (a) describing the hyperplane using its basis and (b) describing its null space. The former is primarily a subject of the system identification (SysID) literature. Let us elaborate on this further through a simple example.

Example 1.1 (Characterization of healthy behavior)**.** Consider a first-order stable continuous-time system described with $\mathfrak{q}y + y = u$, where $\mathfrak{q}$ represents the differentiation operator. Equation (1.1a) indicates that $\boldsymbol{r} \equiv \boldsymbol{0}$ if $\mathfrak{q}y + y = u$. As such, it defines a hyperplane in the space with coordinates $(u, y, \mathfrak{q}y)$, where one such trajectory results from a sinusoidal input (see Figure 1.4). More specifically, any system trajectory $(u, y, \mathfrak{q}y)$ is healthy if any of the following hold:

$$\begin{bmatrix} u \\ y \\ \mathfrak{q}y \end{bmatrix} = \underbrace{\begin{bmatrix} 1 & 0 \\ 0 & 1 \\ 1 & -1 \end{bmatrix}}_{[\boldsymbol{v}_1, \boldsymbol{v}_2]} \begin{bmatrix} \alpha_1 \\ \alpha_2 \end{bmatrix} \text{ for some signals } \alpha_1, \alpha_2 \iff \underbrace{\begin{bmatrix} -1 & 1 & 1 \end{bmatrix}}_{\boldsymbol{v}^\perp} \begin{bmatrix} u \\ y \\ \mathfrak{q}y \end{bmatrix} = 0$$

The pair $[\boldsymbol{v}_1, \boldsymbol{v}_2]$ serves as a basis for the healthy hyperplane, while the vector $\boldsymbol{v}^\perp$ is a basis for the null space. An advantage of the null space representation is that it readily yields a potential filter $r = \mathfrak{q}y + y - u$.

While these characterizations perfectly fit healthy data points in linear systems, this may not hold for nonlinear dynamics, a topic further discussed in Sections 2.1.4 and 2.2.1.

1.2 Motivation and Research Gaps

A diagnostic filter can be designed using either model-based or data-driven approaches. A natural question, therefore, is when one should be preferred over the other. The answer is not straightforward, and each approach can be advantageous depending on the available information and the specific setting. When an accurate model of the system is available, model-based approaches are typically favored, and most of the existing theory has been developed for them. They provide a reliable framework for addressing diagnostic tasks and offer valuable benefits, particularly regarding physical interpretability and formal stability guarantees. However, model-based approaches become less tractable as system complexity and uncertainty increase. Data-driven approaches, in turn, are particularly suitable when the underlying system is complex or when obtaining an accurate model is cumbersome. These approaches not only maintain tractability as system dimensionality increases but also provide a viable alternative when only system trajectories are accessible for analysis. In this spirit, we highlight the key scientific gaps relevant to the diagnosis problem under consideration.

In the era of large language models and their widespread adoption across many disciplines, the data-driven paradigm has evolved from a recent shift to an established research direction over several decades. Within systems and control theory, data-driven control represents a major research stream that can be broadly divided into two bodies of literature. One line of work relies on conventional system identification methods to develop a model from data, followed by the application of model-based techniques (e.g., [18, 19]). The other bypasses the identification step, deriving the downstream design task directly from data (e.g., [20–22]). In the recent literature, the former is often referred to as a two-step or *indirect* approach, whereas the latter is termed a one-step or *direct* approach. Nevertheless, the distinction between direct and indirect methods remains subject to debate and is not yet clearly established [23]. In the context of data-driven fault diagnosis, similar indirect [24, 25] or direct [26, 27] design schemes can be employed for the synthesis of diagnosis filters.

Linear dynamical systems are by far the most studied class of systems in the literature. State-of-the-art results and formal guarantees in data-driven control primarily address problems for linear time-invariant systems [20, 22, 25], although recent efforts have sought to extend these results to more general classes of systems [28, 29]. Despite extensive study, not all questions have been answered. In fact, some fundamental questions remain open in data-driven settings with direct implications for fault diagnosis. Among these, the notion of dynamical system zeros is still insufficiently understood in the data-driven case, even though it is well established in the model-based literature [30–32]. System zeros characterize nontrivial state-input trajectories that make output zero, giving rise to a fundamental zero-output ambiguity set that plays a key role in formalizing fault detectability [6, 33, 34]. It is therefore important to investigate and quantify these concepts within a data-driven framework. Moreover, a systematic statistical treatment of noise in the data-driven design of controllers or diagnosis filters is still lacking, especially for direct data-driven methods. Instead, noise is typically modeled as a bounded disturbance in the

existing literature [22, 35].

From a system-theoretic viewpoint, the diagnosis filter in Figure 1.2 also describes the input–output relationship between the fault and residual signals. In this sense, fault detectability requires that any deviation from healthy behavior induced by the fault signal be reflected in the residual signal. The presence of zeros in the underlying fault-to-residual system implies the existence of a nontrivial zero-output ambiguity set. Fault detection becomes problematic when this set contains trajectories with nonzero fault components. In this case, there exists a nonzero fault signal $\boldsymbol{f}$ that results in $\boldsymbol{r}(\boldsymbol{f}, \mathbf{0}, \mathbf{0}, \mathbf{0}) = \mathbf{0}$ under a suitable initial condition, rendering the faulty trajectory indistinguishable from a healthy trajectory. In particular, undetectable faults may give rise to serious cybersecurity risks in safety-critical applications, as they can be exploited for stealthy adversarial manipulations [36]. For this reason, much of the data-driven fault diagnosis literature relies on the assumption that the underlying system has either no zeros or only stable zeros [6, 25, 37–39]. It is also crucial to investigate scenarios in which this assumption does not hold.

These challenges naturally extend to fault isolation, which generalizes the detection problem. Successful fault isolation requires diagnostic filters that can separate the effect of each fault from other system excitations. Null-space-based diagnosis filters are widely used for this purpose, as they enable the construction of residuals that are sensitive to a specific fault while rejecting the influence of others [5, 40]. In current practice, this often leads to the design of a bank of filters, each dedicated to a particular fault [41], where individual filters generate scalar residual signals to indicate fault occurrence. Despite their practical appeal, such approaches may impose intrinsic limitations on achievable isolation performance. In some cases, it may be infeasible to design dedicated filters for each fault in certain systems—for example, in single-input single-output systems with both actuator and sensor faults. This observation motivates the study of fundamental limits on isolability and the extent to which different faults can be distinguished. Compared with the model-based literature, theoretical developments in data-driven settings remain relatively limited. In this regard, moving from scalar to multidimensional residual signals, which are more natural in data-driven frameworks, may better capture structural limitations and deserves further investigation.

A review of the data-driven fault diagnosis literature discloses that fault estimation has received relatively less attention compared with detection and isolation [42]. This disparity stems from the inherent difficulty of estimation, which requires reconstructing the fault signal rather than merely classifying its presence or location. Once the fault signal is accurately estimated, the questions of detection and isolation are naturally addressed. In system-theoretic terms, fault estimation is closely linked to inverting the fault subsystem, that is, the mapping from the fault to the residual signal, and is essentially an inverse problem [43]. Existing data-driven fault estimation approaches typically rely on system inversion [25, 44]: the fault subsystem is first identified from fault-free input–output measurements, after which the fault signal is reconstructed by inverting the identified model. Such identification is meaningful under two assumptions. First, the fault signal is additive and affects the output either directly, as in sensor faults, or through the control input, as in actuator faults. Second, the fault channels are already known or have been identified using fault isolation. Access to fault-free measurements is generally not restrictive, as such data are often available in practice, unlike faulty datasets. However, since the identi-

fied model is ultimately inverted, inaccuracies in identification can propagate nonlinearly and significantly degrade estimation performance [25, 45]. Moreover, the identified model may not be optimal for inversion purposes. These limitations motivate the investigation of whether the inverse system can be identified directly from data, a promising yet largely unexplored research direction. Apart from modelling issues, the inversion step itself introduces additional challenges regarding stability and estimation delay. For instance, the inverse of a system with input–output delays is generally non-causal and thus not realizable. Furthermore, achieving unbiased fault estimation requires the inverse system to be stable, which implies that the underlying system must be minimum phase; otherwise, the reconstruction error grows unbounded [25, 37, 44]. Such a requirement once again underscores the importance of system zeros. This restrictive assumption is common to most existing data-driven fault estimation methods and motivates the need to develop approaches capable of handling non-minimum phase systems. Initial results in this direction include the work of [45], which addresses data-driven fault estimation for non-minimum phase systems using a mixed causal–noncausal filter.

Thus far, all aforementioned classes of diagnosis problems assume that the collected input–output data are fixed and that the user cannot interrupt normal operation, corresponding to a *passive* design regime. While this reflects the most common practical scenario, deliberately exciting the system in a controlled manner falls within the scope of *active* and online experimental design [46] and can enhance diagnostic reliability. In data-driven approaches, knowledge of the system order is an integral part of filter design, regardless of whether direct or indirect methods are employed. Subspace identification methods provide frameworks for system order estimation that employ thresholding techniques to distinguish signal from noise and have remained the most common tool [47, 48]. Nevertheless, the separation is not always straightforward, particularly under low signal-to-noise ratio conditions. In such cases, input design can be leveraged to improve data quality under the same operating conditions. A key aspect of data quality is the so-called quantitative persistency of excitation of the input signal [49]. At the same time, input design for system identification typically yields nonconvex optimization problems that are computationally intractable [50], posing a significant challenge. Although extensive literature exists on optimal threshold selection across systems and control, signal processing, information theory, and statistics, the use of active input design to enhance data quality and denoising remains relatively underexplored.

1.3 Research Objectives

This thesis aims to develop data-driven fault diagnosis frameworks that enable accurate and reliable predictive maintenance to support flexible manufacturing systems. The proposed developments can be integrated into online optimization-based, reconfigurable control architectures for composite manufacturing processes, robotic manipulators, and other high-tech systems and manufacturing applications. The main findings are expected to benefit both direct and indirect design schemes in the data-driven fault diagnosis literature. To pursue the thesis objective, the main research question is formulated as follows:

1

Main Research Question

How to develop data-driven fault diagnosis filters for linear systems with performance guarantees that are verifiable directly from data?

The objective is recast as a set of key research questions, each tackled in a dedicated chapter. These questions are grounded in the knowledge gaps identified in Section 1.2 and collectively contribute to the main objective. The scope of the diagnosis filters considered in this thesis encompasses both fault isolation and fault estimation. Existing data-driven methods generally provide limited insight into the achievable performance of null-space-based diagnosis filters in relation to the structural properties of the underlying system. To bridge this gap, we explore the geometry of the underlying classification problem by using a multidimensional residual signal. This motivates the first research question:

> RQ1—*What are the fundamental performance limits of null-space-based diagnosis filters in data-driven fault isolation for linear systems?*

As highlighted in Section 1.2, system zeros are fundamental structural properties that arise in many systems and control problems, including fault diagnosis. However, their characterization and computation are primarily based on model-based descriptions. This raises the question whether the system zero structure can be characterized and computed directly from input–output measurements within a data-driven framework, leading to the second research question:

> RQ2—*How to characterize system zeros in a data-driven framework and compute them from input–output measurements?*

The subsequent step is fault estimation. Current approaches typically rely on two-step procedures and impose restrictive assumptions such as the minimum phase assumption. Moreover, the connection to inverse problems suggests exploring whether the inverse system can be identified directly from data. Hence, the following research question is formulated as

> RQ3—*How to design a data-driven fault estimation filter for non-minimum phase systems using inverse system identification?*

Finally, improving diagnosis performance through input design introduces an additional degree of freedom, transferring the problem from passive to active design regime. Since the accuracy of system identification directly dictates the performance of the diagnosis filter—and is itself influenced by the input signal—designing informative inputs is crucial. Specifically, optimally designed excitation can significantly enhance performance, for instance, in estimating the system order within subspace identification methods. Despite its potential benefits, a systematic framework for input design in this context is largely lacking in the literature, and the resulting optimization problems are typically nonconvex and computationally intractable. Therefore, we propose the following research question:

> RQ4—*How to develop a tractable input design algorithm to improve the accuracy of system identification in the presence of noise?*

1.4 Thesis Outline and Original Contributions

The thesis is organized into seven chapters, with their interconnections illustrated in Figure 1.6. The following provides an overview of the contributions presented in each chapter:

Chapter 2—Fault Diagnosis: Geometric Interpretation and Tractable Algorithms
This chapter provides a system-theoretic review of the fault diagnosis literature, categorizing existing approaches according to system dynamics, information availability, filter parametrization, and solution methods, with particular emphasis on their geometric interpretations. It further investigates the classical problems of fault detection, isolation, and estimation through a differential-algebraic-equation-based framework and establishes their connections to alternative system representations. In addition, recent advances in model-free and active fault diagnosis are discussed, while noting that these directions are still underexplored.

Chapter 3—Data-Driven Fault Detection and Isolation
This chapter addresses fault detection and isolation in linear dynamical systems using a null-space-based diagnosis filter. The proposed data-driven framework tackles both additive sensor and actuator faults. The fault isolation problem is formulated as a subspace classification problem in which the residual space is partitioned according to individual fault classes. Within this framework, the notion of fault discernibility is introduced to characterize the fundamental performance limitations of this class of diagnosis filters. As demonstrated in this chapter, fault discernibility is intrinsically linked to the output-zeroing problem studied in Chapter 4.

Chapter 4—Data-Driven Characterization and Computation of Multivariable LTI Systems Zeros
Following the results presented in Chapter 3, this chapter investigates the relationship between the output-zeroing problem, the system zero structure, and its structural properties in a data-driven setting. To this end, the output-zeroing problem is formulated in terms of the null space of the output data equation, yielding a complete characterization of the null space through the system zeros and structural properties. In addition, a direct data-driven method is developed to identify the system zeros and their corresponding zero directions using only input–output data.

Chapter 5—Data-Driven Fault Estimation
This chapter considers fault estimation in linear time-invariant systems subject to unknown additive actuator faults, without imposing assumptions on their temporal evolution. An inverse-system-based filter is developed for both minimum and non-minimum phase systems. Unlike conventional two-step approaches, it directly estimates the filter parameters from input–output data, avoiding the propagation of forward-model identification errors through inversion. For non-minimum phase systems, stable inversion is achieved using a bilateral impulse-response model. The resulting infinite-dimensional optimization problem is rendered finite-dimensional through reproducing kernel Hilbert space regularization, which controls model complexity and allows prior knowledge of the system behavior to be incorporated.

1

Chapter 6—Active Learning
Different from the preceding chapters, this chapter adopts an active design approach in which a bounded input signal is designed over a finite number of experiments. It develops an optimal input design framework for determining the system order and improving identification accuracy, ultimately enhancing fault detectability and isolability. The framework comprises two nested loops: an inner loop that optimizes the input and an outer loop that uses hypothesis testing to confirm or falsify candidate system orders.

Chapter 7—Conclusion
This chapter concludes the thesis and outlines potential avenues for future research.

1.5 Notation

This section establishes the general notation fundamental to the developments presented throughout this thesis.

Sets and spaces

Calligraphic uppercase letters denote sets, while blackboard bold letters represent standard well-known sets. Following these conventions, the sets $\mathbb{Z}$ ($\mathbb{Z}_{\geq 0}$), $\mathbb{R}$ ($\mathbb{R}_{\geq 0}$), and $\mathbb{C}$ denote the integers (non-negative integers), the real numbers (non-negative real numbers), and complex numbers, respectively. For strict positivity, we use $\mathbb{Z}_{>0}$ and $\mathbb{R}_{>0}$. In the complex plane, $\mathbb{D}$ denotes the interior of the unit circle, and $\mathbb{T}$ represents the unit circle itself. The n-dimensional real Euclidean vector space is denoted by $\mathbb{R}^n$, whereas $\mathbb{C}^n$ denotes the space of n-dimensional complex vectors. Similarly, $\mathbb{R}^{m\times n}$ and $\mathbb{C}^{m\times n}$ represent, respectively, the spaces of real and complex matrices of size $m \times n$. For a complex number $z \in \mathbb{C}$, $\operatorname{Re} z$ and $\operatorname{Im} z$ refer to its real and imaginary parts, while $\overline{z}$ and $|z|$ denote its complex conjugate and absolute value, respectively. Let $\mathcal{V}$ be a subspace of a linear vector space. Its dimension is denoted by $\dim \mathcal{V}$, representing the number of linearly independent vectors required to span the subspace. For a linear mapping $\boldsymbol{A} : \mathcal{X} \to \mathcal{Y}$, not necessarily invertible, and a subspace $\mathcal{V} \subseteq \mathcal{Y}$, the preimage of $\mathcal{V}$ under $\boldsymbol{A}$ is defined by $\boldsymbol{A}^{-1}\mathcal{V} := \{\boldsymbol{x} \in \mathcal{X} \mid \boldsymbol{A}\boldsymbol{x} \in \mathcal{V}\}$, whereas $\boldsymbol{A}^{-1}$ denotes the ordinary matrix inverse whenever it exists, unless followed by a set; when $\boldsymbol{A}$ is invertible, both operations coincide. If $\boldsymbol{A} : \mathcal{X} \to \mathcal{X}$ and the subspace $\mathcal{V} \subseteq \mathcal{X}$ is $\boldsymbol{A}$-invariant, then $\boldsymbol{A}|_{\mathcal{V}}$ denotes the restriction of $\boldsymbol{A}$ to $\mathcal{V}$, that is, $\boldsymbol{A}|_{\mathcal{V}} : \mathcal{V} \to \mathcal{V}$. The orthogonal complement of $\mathcal{V} \subseteq \mathbb{R}^n$ is denoted by $\mathcal{V}^{\perp}$. For subspaces $\mathcal{W} \subseteq \mathcal{V}$, we abuse the notation of quotient by writing $\mathcal{V}/\mathcal{W}$ to refer to the orthocomplementation $\mathcal{V} \cap \mathcal{W}^{\perp}$. Lastly, the lattice diagram of subspaces $\mathcal{V}_1, \mathcal{V}_2 \subseteq \mathbb{R}^n$ reads as in Figure 1.5.

Matrices and vectors

Italic lowercase letters denote scalars, italic bold lowercase letters denote vectors, and upright bold lowercase letters indicate structured vectors. Similarly, italic bold uppercase letters denote matrices, whereas upright bold uppercase letters are reserved for structured matrices. The identity matrix is denoted by $\mathbf{I}$, with $\mathbf{I}_n$ specifying its dimension when it is not clear from the context. Likewise, $\mathbf{0}$ represents the zero matrix, with the dimensions $\mathbf{0}_{m\times n}$ or $\mathbf{0}_n$ (for square matrices) provided where necessary. In the following, we define several fundamental mathematical operations on vectors and matrices. For a vector $\boldsymbol{v}$

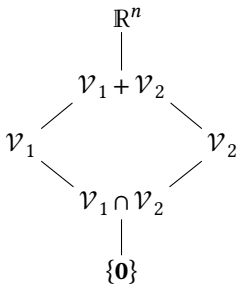

Figure 1.5: Lattice diagram.

and a matrix $\boldsymbol{M}$ over an arbitrary field, the transpose operation is denoted by $\boldsymbol{v}^\top$ and $\boldsymbol{M}^\top$, respectively. The notation $\operatorname{diag}(\boldsymbol{v})$ presents the diagonal matrix formed from $\boldsymbol{v}$. For a general matrix $\boldsymbol{M} \in \mathbb{R}^{m\times n}$, its column space is defined as $\operatorname{im}\boldsymbol{M} \coloneqq \{\boldsymbol{M}\boldsymbol{x} : \boldsymbol{x} \in \mathbb{R}^n\}$, its null space as $\ker \boldsymbol{M} \coloneqq \{\boldsymbol{x} \in \mathbb{R}^n : \boldsymbol{M}\boldsymbol{x} = \boldsymbol{0}\}$, and its rank as $\operatorname{rank}\boldsymbol{M} \coloneqq \dim(\operatorname{im}\boldsymbol{M})$. Furthermore, $\boldsymbol{M}^{-1}$ denotes the matrix inverse, if it exists, while $\boldsymbol{M}^\dagger$ represents the Moore-Penrose pseudoinverse. Let $\boldsymbol{M}^{\ker}$ represent any matrix whose columns form a basis for the null space of $\boldsymbol{M}$, i.e., $\operatorname{im}\boldsymbol{M}^{\ker} = \ker \boldsymbol{M}$. The operator $\operatorname{vec}(\boldsymbol{M})$ vectorizes the matrix $\boldsymbol{M}$ by stacking its columns into a single vector. The singular value decomposition of $\boldsymbol{M}$ is denoted by $\operatorname{SVD}(\boldsymbol{M})$, and its kth largest singular value by $\sigma_k(\boldsymbol{M})$. The spectrum of square $\boldsymbol{M}$, denoted by $\lambda(\boldsymbol{M})$, is the multiset of its eigenvalues. In addition, the maximum absolute value of the eigenvalues of $\boldsymbol{M}$, known as the spectral radius, is defined as $\rho(\boldsymbol{M}) \coloneqq \max\{|\lambda_i| : \lambda_i \in \lambda(\boldsymbol{M})\}$. For a given parameter q and parameter set $\mathcal{Q}$, the normal (maximal) rank of a parameterized matrix $\boldsymbol{M}(q)$ is defined as $\operatorname{normalrank}\boldsymbol{M}(q) \coloneqq \max_{q\in\mathcal{Q}} \operatorname{rank}\boldsymbol{M}(q)$. The notations $\|\cdot\|_2$ and $\|\cdot\|_\infty$ correspond to 2-norm (the Euclidean norm) and infinity norm of a vector, respectively. To denote the Kronecker product, we use the symbol $\otimes$.

Signals

Signals in this thesis are (generalized) functions of either discrete or continuous time, depending on the context, and sometimes omit the argument when clear from the context. For example, a multivariate signal $\boldsymbol{x} : \mathcal{T} \to \mathbb{R}^{n_x}$, where the time set $\mathcal{T}$ is either $\mathbb{R}_{\geq 0}$ for continuous-time systems or $\mathbb{Z}_{\geq 0}$ for discrete-time systems, is represented simply by $\boldsymbol{x}$ in system equations. We use the operator $\mathfrak{q}$ for the differentiation or the forward time shift, i.e., $\mathfrak{q}\boldsymbol{x}(t) = \boldsymbol{x}(t+1)$ for a discrete-time signal $\boldsymbol{x}$, and $\mathfrak{q}\boldsymbol{x}(t) = \mathrm{d}\boldsymbol{x}(t)/\mathrm{d}t$ for a continuous-time signal. Since $\mathfrak{q}$ is a linear and commutative operator, we treat polynomials of $\mathfrak{q}$ as typical linear time-invariant systems, and occasionally evaluate these polynomials at some value of $\mathfrak{q}$ in $\mathbb{C}$ to reveal system properties such as poles, zeros, and matrix rank. Furthermore, $\|\cdot\|_{\mathcal{L}_2}$ denotes the $\mathcal{L}_2$-norm of a signal. We define a few structured matrices and vectors constructed from signals that are used frequently throughout this thesis. For a discrete-time signal $\boldsymbol{x} : \mathbb{Z}_{\geq 0} \to \mathbb{R}^{n_x}$ over the time interval $[t, t+T-1]$ of length T, the corresponding vertically stacked vector is denoted by $\mathbf{x}_{[t,t+T-1]} \coloneqq \begin{bmatrix}\boldsymbol{x}^\top(t) & \cdots & \boldsymbol{x}^\top(t+T-1)\end{bmatrix}^\top$. Further,

1

the associated Hankel matrix of depth L is defined as

$$\overset{\#}{\mathbf{X}}_{t,L,T} \coloneqq \begin{bmatrix} \boldsymbol{x}(t) & \boldsymbol{x}(t+1) & \cdots & \boldsymbol{x}(t+T-L) \\ \boldsymbol{x}(t+1) & \boldsymbol{x}(t+2) & \cdots & \boldsymbol{x}(t+T-L+1) \\ \vdots & \vdots & \ddots & \vdots \\ \boldsymbol{x}(t+L-1) & \boldsymbol{x}(t+L) & \cdots & \boldsymbol{x}(t+T-1) \end{bmatrix}$$

where the accent symbol reflects the underlying structure. Similar notation conventions are adopted to designate different data structures in subsequent chapters.

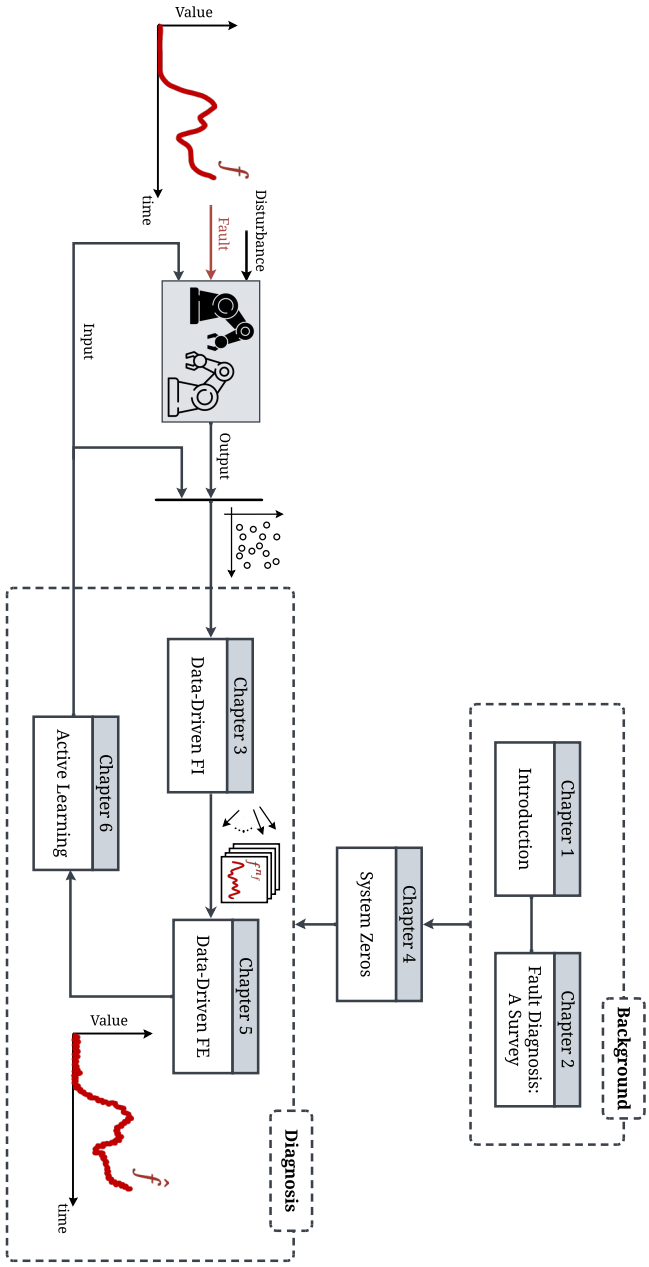

Figure 1.6: Overview of the thesis structure and the relationships among the chapters.

2

Fault Diagnosis: Geometric Interpretation and Tractable Algorithms

This survey reviews recent developments in fault diagnosis for both linear and nonlinear dynamical systems, covering model-based and data-driven approaches as well as passive and active detection and estimation methods. A central focus is placed on the geometric interpretation of diagnosis filters and their connection to the concept of behavioral sets, providing an intuitive view of their performance. We also review optimization-based techniques that enhance the robustness of linear filters when applied to nonlinear or uncertain systems. Furthermore, we point out recent progress in active fault diagnosis, where input design plays a key role in improving detectability and estimation accuracy.

This chapter is partly based on *Fault Diagnosis in Dynamical Systems: Geometric Interpretation and Tractable Algorithms* [42].

A structured overview of the fault diagnosis literature is presented, organized around key problem formulations, system dynamics and information settings, along with various solution approaches developed to address them. In this regard, the related works are categorized according to the corresponding diagnosis problem class.

2

2.1 Fundamentals of Fault Diagnosis

This section establishes a unified perspective for formulating and categorizing fault diagnosis problems. It also introduces the key dimensions along which diagnosis problems are commonly characterized, providing a conceptual foundation for structuring the literature review and subsequent analysis.

2.1.1 Settings

The analysis and design of fault diagnosis filters depend on several key components, including (a) the underlying system dynamics (linear versus nonlinear dynamics), (b) the available information (exact versus uncertain models), and (c) the degree of freedom (passive versus active diagnosis). With regard to the dynamics, the majority of fault diagnosis techniques have traditionally been developed for linear time-invariant (LTI) systems [51, 52], where the system's behavior can be fully captured by a fixed set of matrices. However, real-world systems often exhibit nonlinear behaviors, possibly influenced by multiplicative noise [53], time-varying parameters [54], or other general nonlinearities (e.g., 55–57). In such cases, fault diagnosis becomes significantly more complex. Another important consideration is the extent of model information available to the diagnosis algorithm. In some cases, the model is only partially known or contains structured uncertainties, requiring robust or adaptive approaches [58, 59]. In the extreme case, no model information is available, and data-driven methods are required [44, 60]. Furthermore, prior knowledge about the class of possible fault signals, such as their temporal profiles [61], magnitudes, or sparsity [39, 54], can significantly influence the design of detection and estimation schemes. Depending on the assumptions about fault signal behavior and uncertainty, fault diagnosis can be approached from a robust/adversarial perspective or a probabilistic/statistical framework [58], each of which offers different guarantees and trade-offs.

An alternative lens through which one can strike a balance between these knowns and unknowns at the modeling level is game theory, where the interaction between the diagnosis system and the fault signal can be modeled as a game between two players: a defender (the diagnosis filter) and an attacker (the fault signal). In this formulation, the diagnosis algorithm must be robust against worst-case scenarios, where the adversarial signal may actively seek to evade detection. It is worth noting that this game-theoretic viewpoint is typically less conservative than the classical robust approach, as it explicitly accounts for the strategic interaction between attacker and defender. The game-theoretic perspective is particularly suited for security-critical applications, such as cyber-physical systems [62] and autonomous vehicles [10], where faults may be deliberately introduced by intelligent attackers. However, game-theoretic formulations are beyond the scope of this survey and are not be covered.

While most existing work has focused on passive fault diagnosis, where the system is monitored without intervention, a promising yet underexplored direction is active fault di-

agnosis. This approach involves designing excitation inputs to improve fault detectability or enhance diagnostic performance. Active strategies are particularly valuable in low-signal-to-noise ratio settings [63] or when fault effects on measurements closely resemble those caused by normal disturbances [64]. Despite improving diagnosis performance, the design of optimal probing inputs poses its own set of additional challenges, as it often results in intractable, nonconvex optimization problems.

2.1.2 Solution Approaches

A core aspect of fault diagnosis is the design of filters or classifiers that process input–output measurements and generate residuals or decision signals indicative of faults. These filters are typically modeled as either LTI or nonlinear systems and are often parameterized to optimize performance criteria such as sensitivity, robustness, or detection delay. While linear residual generators are well-established for LTI systems [40, 65], nonlinear observers [55, 66] and data-driven classifiers—particularly those based on machine learning [67]—are gaining attention in handling nonlinear dynamics. The filter design inherently involves trade-offs between fault sensitivity and robustness to modeling uncertainties and disturbances. A unifying and intuitive way to interpret diagnosis filters is through their geometric effect on the measurement space [33]. Specifically, the filter induces a partition of the input–output measurement space, where each region corresponds to a particular fault mode [34]. In the case of linear filters, this often results in subspace partitioning, where the residual space is structured to separate nominal and faulty behaviors [68].

The survey discussion is organized based on system dynamics, available information, filter parameterization, and solution methods, with particular attention to their geometric insights. We also review emerging frameworks in game-theoretic and active detection, offering a comprehensive overview of current methodologies and outlining key directions for future research. Furthermore, we illustrate the relevance of these methods through several modern applications, including cyber-security in power systems, anomaly detection in autonomous vehicles, and health monitoring of high-end industrial printers, supported by real-world case studies and, where applicable, experimental implementations. Table 2.1 summarizes the reviewed literature.

2.1.3 System Representations

To provide a systematic way to characterize the healthy behavior in Figure 1.4, we consider a class of system dynamics as the mapping from $(\boldsymbol{f}, \boldsymbol{w}, \boldsymbol{d}, \boldsymbol{u})$ to $\boldsymbol{y}$ (see Figure 1.2) described via differential–algebraic equations (DAEs) as

$$\boldsymbol{H}(\mathfrak{q})\xi + \boldsymbol{L}(\mathfrak{q})z + \boldsymbol{F}(\mathfrak{q})f + \boldsymbol{W}(\mathfrak{q})w + \boldsymbol{\eta}(\xi, z) = \boldsymbol{0}, \tag{2.1}$$

where $\xi : \mathcal{T} \to \mathbb{R}^{n_\xi}$ is the unknown latent signal (e.g., internal states or natural exogenous disturbances), $z : \mathcal{T} \to \mathbb{R}^{n_z}$ is the known measurement signal (e.g., input–output trajectories), $f : \mathcal{T} \to \mathbb{R}^{n_f}$ is the fault signal (diagnosis target), and $w : \mathcal{T} \to \mathbb{R}^{n_w}$ represents the unknown stochastic or bounded signal (e.g., process and output noise). The matrices $\boldsymbol{H}(\mathfrak{q})$, $\boldsymbol{L}(\mathfrak{q})$, $\boldsymbol{F}(\mathfrak{q})$, and $\boldsymbol{W}(\mathfrak{q})$ are polynomial matrices in $\mathfrak{q}$. The nonlinearity is characterized by $\boldsymbol{\eta}(\xi, z)$, and without loss of generality, we assume that the nonlinear function $\boldsymbol{\eta}(\cdot)$ has no affine terms around the origin. The DAE is a rich modeling framework in the sense that it can encompass LTI systems and a class of nonlinear systems. For instance, consider the

Table 2.1: Summary of the literature reviewed in the survey.

		Fault Diagnosis problem		
Setting	**Dynamics**	**Detection**	**Isolation**	**Estimation**
Perfect model	Linear	40, 41, 52, 62, 65, 69–71	4, 5, 8, 33, 34, 39, 51, 72–76, 64, 77–80	6, 7, 53, 81–85, 63
	Nonlinear	55	55, 86–96	54, 97–100
Imperfect model	Linear	59, 101	102	37, 103, 104, 105
	Nonlinear	56, 58, 61, 106, 107	56, 57, 66, 106	10
Data-driven	Linear	60, 67, 108–112	24, 68, 113	25–27, 44, 45, 114–123
	Nonlinear	28, 124	125–128	129, 130

Non-underlined reference numbers are for work on passive diagnosis; underlined numbers are for active diagnosis.

state-space representation

$$\begin{aligned} \mathfrak{q}\boldsymbol{x} &= \boldsymbol{A}\boldsymbol{x} + \boldsymbol{B}_u\boldsymbol{u} + \boldsymbol{B}_f\boldsymbol{f} + \boldsymbol{B}_d\boldsymbol{d} + \boldsymbol{B}_w\boldsymbol{w}, \\ \boldsymbol{y} &= \boldsymbol{C}\boldsymbol{x} + \boldsymbol{D}_u\boldsymbol{u} + \boldsymbol{D}_f\boldsymbol{f} + \boldsymbol{D}_d\boldsymbol{d} + \boldsymbol{D}_w\boldsymbol{w}, \end{aligned} \tag{2.2}$$

in which the system state is represented by $\boldsymbol{x} : \mathcal{T} \to \mathbb{R}^{n_x}$. The system matrices $(\boldsymbol{A}, [\boldsymbol{B}_u, \boldsymbol{B}_f, \boldsymbol{B}_d, \boldsymbol{B}_w], \boldsymbol{C}, [\boldsymbol{D}_u, \boldsymbol{D}_f, \boldsymbol{D}_d, \boldsymbol{D}_w])$ form a state-space realization, which can be readily converted to transfer functions as well [131, 132], yielding

$$\boldsymbol{y} = \boldsymbol{G}_u(\mathfrak{q})\boldsymbol{u} + \boldsymbol{G}_f(\mathfrak{q})\boldsymbol{f} + \boldsymbol{G}_d(\mathfrak{q})\boldsymbol{d} + \boldsymbol{G}_w(\mathfrak{q})\boldsymbol{w}, \quad \boldsymbol{x}(0) = 0, \tag{2.3}$$

where $\boldsymbol{G}_u(\mathfrak{q}) \in \mathbb{R}^{n_y \times n_u}$, $\boldsymbol{G}_f(\mathfrak{q}) \in \mathbb{R}^{n_y \times n_f}$, $\boldsymbol{G}_d(\mathfrak{q}) \in \mathbb{R}^{n_y \times n_d}$, and $\boldsymbol{G}_w(\mathfrak{q}) \in \mathbb{R}^{n_y \times n_w}$ are transfer function (i.e., rational) matrices in $\mathfrak{q}$. The conversion from state space in Equation (2.2) to DAE in Equation (2.1) is obtained by defining the matrices

$$\boldsymbol{H}(\mathfrak{q}) \coloneqq \begin{bmatrix} \boldsymbol{A} - \mathfrak{q}\mathbf{I} & \boldsymbol{B}_d \\ \boldsymbol{C} & \boldsymbol{D}_d \end{bmatrix}, \quad \boldsymbol{\xi} \coloneqq \begin{bmatrix} \boldsymbol{x} \\ \boldsymbol{d} \end{bmatrix}, \quad \boldsymbol{L}(\mathfrak{q}) \coloneqq \begin{bmatrix} \boldsymbol{B}_u & \mathbf{0} \\ \boldsymbol{D}_u & -\mathbf{I} \end{bmatrix}, \quad \boldsymbol{z} \coloneqq \begin{bmatrix} \boldsymbol{u} \\ \boldsymbol{y} \end{bmatrix},$$
$$\boldsymbol{F}(\mathfrak{q}) \coloneqq \begin{bmatrix} \boldsymbol{B}_f \\ \boldsymbol{D}_f \end{bmatrix}, \qquad \boldsymbol{W}(\mathfrak{q}) \coloneqq \begin{bmatrix} \boldsymbol{B}_w \\ \boldsymbol{D}_w \end{bmatrix}.$$

The nonlinear extension is straightforward, for which we direct readers to Reference [16].

2.1.4 Residual Generation

Residual signals are typically generated using either hardware redundancy or analytical redundancy. While hardware redundancy is commonly recommended in safety-critical applications [133], this thesis focuses on the use of analytical redundancy to generate

residuals. An example of analytical redundancy is a mathematical model describing the system under consideration. Taking the difference between the actual system output and the model output readily yields a residual signal for diagnosis. However, in many cases, such as in the presence of the external disturbance signal $\boldsymbol{d}$, satisfying the conditions in Equation (1.1a) and Equation (1.1b) requires a more involved residual generation process.

Consider the noise-free linear system following the DAE model in Equation (2.1) by setting $\boldsymbol{\eta}(\xi, z) = \mathbf{0}$ and $\boldsymbol{w} = \mathbf{0}$. In this formulation, the aim is to exclude the contribution of the signal ξ from the residual. We begin by formally defining the healthy behavioral sets $\mathfrak{B}_{\text{healthy}}$ visualized in Figure 1.4, as the sets of available measurement signal z consistent with specific properties dictated by the model. The healthy and faulty behaviors of a linear deterministic system ($\boldsymbol{\eta}(\xi, z) = \mathbf{0}, \boldsymbol{w} = \mathbf{0}$) are described as

$$\begin{aligned}\mathfrak{B}_{\text{healthy}} &:= \{z \mid \exists \xi \ : \ \boldsymbol{H}(\mathfrak{q})\xi + \boldsymbol{L}(\mathfrak{q})z = \mathbf{0}\},\\ \mathfrak{B}_{\text{faulty}} &:= \{z \mid \exists \boldsymbol{f} \not\equiv \mathbf{0}, \xi \ : \ \boldsymbol{H}(\mathfrak{q})\xi + \boldsymbol{L}(\mathfrak{q})z + \boldsymbol{F}(\mathfrak{q})\boldsymbol{f} = \mathbf{0}\},\end{aligned}$$

which reflects a similar notion introduced in the behavioral approach theory [134].

We are now ready to parameterize the residual generator (diagnosis filter block in Figure 1.2) for a given model in Equation (2.1). Let $\boldsymbol{N}_H(\mathfrak{q})$ be the polynomial matrix whose rows span the left null space of $\boldsymbol{H}(q)$, forming a minimal polynomial basis [52]. The healthy behavior set $\mathfrak{B}_{\text{healthy}}$ can then be equivalently characterized by

$$\mathfrak{B}_{\text{healthy}} := \{z \mid \boldsymbol{N}_H(\mathfrak{q})\boldsymbol{L}(\mathfrak{q})z = \mathbf{0}\},$$

allows us to generate the residual signal using polynomial matrix equations. Left-multiplying Equation (2.1) by $\boldsymbol{N}_H(\mathfrak{q})$ yields the residual signal

$$\boldsymbol{r} = \boldsymbol{N}_H(\mathfrak{q})\boldsymbol{L}(\mathfrak{q})z = -\boldsymbol{N}_H(\mathfrak{q})\boldsymbol{F}(\mathfrak{q})\boldsymbol{f},$$

provided that $\boldsymbol{N}_H(\mathfrak{q})\boldsymbol{F}(\mathfrak{q}) \not\equiv \mathbf{0}$. This parameterization effectively enforces the decoupling and sensitivity conditions described in Equations (1.1a) and (1.1b), respectively. To ensure the filter is realizable, an arbitrary stable polynomial $a(\mathfrak{q})$ of sufficient order is introduced[1], leading to the residual generator

$$\boldsymbol{r} = \boldsymbol{R}(\mathfrak{q})z = a^{-1}(\mathfrak{q})\boldsymbol{N}_H(\mathfrak{q})\boldsymbol{L}(\mathfrak{q})z, \tag{2.4}$$

which serves as a baseline for dealing with different classes of fault diagnosis. This practical introduction of poles creates transient behavior in the residual, even in the absence of faults. Therefore, the decoupling criterion of Equation (1.1a) holds only asymptotically. That is, the residual satisfies the following properties:

(i) $\lim_{t\to\infty} \boldsymbol{r}(t) = \mathbf{0}$ for all $z \in \mathfrak{B}_{\text{healthy}}$.

(ii) $\boldsymbol{r}(t) \not\equiv \mathbf{0}$ for all $z \in \mathfrak{B}_{\text{faulty}}$.

[1]Once $\boldsymbol{N}_H(\mathfrak{q})$ has been designed and its degree is known, $a(\mathfrak{q})$ can be selected as a stable monic polynomial of equal or higher degree, with poles chosen depending on, e.g., the dominant frequency characteristics of the signals involved.

Such a linear filter falls into the category of null-space-based residual generators that decouple the contributions of internal states and possibly natural disturbances [132]. For the more restricted class of state-space systems, the filter in Equation (2.4) is a kernel representation of the system [69, 135]. In this representation, the governing equations are expressed in a form where both independent (inputs) and dependent (outputs) signals appear as arguments of a zero equation. The kernel-representation literature typically parameterizes the filter via state-space or transfer-function approaches. For detailed presentations, we direct readers to References [41, 131, 132].

Another method to generate residuals is through observers. Unknown input observers (UIOs) were initially proposed for unbiased state estimation in the presence of inputs that are not directly measurable [136]. The design principle enforces that the estimation error be independent of a subset of inputs, typically unmeasurable ones such as disturbances and input noise. This methodology has been extended to residual generation in fault diagnosis schemes [34]. For brevity, we keep the noise-free assumption. Then, an observer-based residual generator for the system in Equation (2.2) takes the form

$$\begin{aligned} \mathfrak{q}\hat{\boldsymbol{x}} &= \boldsymbol{A}_{\mathrm{UIO}}\hat{\boldsymbol{x}} + (\boldsymbol{T}\boldsymbol{B}_u - \boldsymbol{K}\boldsymbol{D}_u)\boldsymbol{u} + \boldsymbol{K}\boldsymbol{y}, \\ \boldsymbol{r} &= \boldsymbol{C}_{\mathrm{UIO}}\hat{\boldsymbol{x}} + \boldsymbol{D}_{\mathrm{UIO}}(\boldsymbol{y} - \boldsymbol{D}_u\boldsymbol{u}), \end{aligned} \implies \begin{aligned} \mathfrak{q}\boldsymbol{e} &= \boldsymbol{A}_{\mathrm{UIO}}\boldsymbol{e} + (\boldsymbol{K}\boldsymbol{D}_f - \boldsymbol{T}\boldsymbol{B}_f)\boldsymbol{f}, \\ \boldsymbol{r} &= \boldsymbol{C}_{\mathrm{UIO}}\boldsymbol{e} + \boldsymbol{D}_{\mathrm{UIO}}\boldsymbol{D}_f\boldsymbol{f}, \end{aligned} \tag{2.5}$$

where $\boldsymbol{e} \coloneqq \hat{\boldsymbol{x}} - \boldsymbol{T}\boldsymbol{x}$ denotes the estimation error, and the design parameters $\boldsymbol{T}$, $\boldsymbol{K}$, $\boldsymbol{A}_{\mathrm{UIO}}$, $\boldsymbol{C}_{\mathrm{UIO}}$, and $\boldsymbol{D}_{\mathrm{UIO}}$ are subject to the following matrix equality constraint:

$$\begin{bmatrix} \boldsymbol{T} & -\boldsymbol{K} \\ \boldsymbol{0} & \boldsymbol{D}_{\mathrm{UIO}} \end{bmatrix} \begin{bmatrix} \boldsymbol{A} & \boldsymbol{B}_d \\ \boldsymbol{C} & \boldsymbol{D}_d \end{bmatrix} = \begin{bmatrix} \boldsymbol{A}_{\mathrm{UIO}}\boldsymbol{T} & \boldsymbol{0} \\ -\boldsymbol{C}_{\mathrm{UIO}}\boldsymbol{T} & \boldsymbol{0} \end{bmatrix}, \text{ and } \boldsymbol{A}_{\mathrm{UIO}} \text{ is Schur/Hurwitz stable}. \tag{2.6}$$

A system is said to be Schur (Hurwitz) stable if all eigenvalues of the state matrix, equivalently the roots of the characteristic polynomial, lie in the open unit circle (open left half-plane) of the complex plane. The necessary and sufficient conditions for the existence of a solution to Equation (2.6), assuming $\boldsymbol{B}_d$ is full column rank without loss of generality, are given by the following [34]

(i) $\operatorname{rank} \boldsymbol{D}_{\mathrm{UIO}}\boldsymbol{C} = \operatorname{rank} \boldsymbol{B}_d$,

(ii) $(\bar{\boldsymbol{A}}, \boldsymbol{D}_{\mathrm{UIO}}\boldsymbol{C})$ is a detectable pair, where $\bar{\boldsymbol{A}} \coloneqq \boldsymbol{A} - \boldsymbol{B}_d(\boldsymbol{D}_{\mathrm{UIO}}\boldsymbol{C}\boldsymbol{B}_d)^{\dagger}\boldsymbol{D}_{\mathrm{UIO}}\boldsymbol{C}\boldsymbol{A}$.

A residual generator satisfying Equation (2.6) simultaneously decouples both $\boldsymbol{d}$ and $\boldsymbol{x}$ in the same way that the null-space-based filter in Equation (2.4) does. Ding, Guo, and Frank [65] demonstrated the equivalence between the observer and transfer-function parameterizations.

Finally, residual generators can also be built by exploiting the left null-space of the extended observability matrix, which can be fully parameterized by the pair $(\boldsymbol{A}, \boldsymbol{C})$. This approach is the so-called parity relation [51, 70]. This method exploits temporal redundancy between inputs and outputs to check the consistency of the system's mathematical equations with the measurements over a time-window. A classical result from Patton and Chen [137] shows that the parity relation design is equivalent to the use of a deadbeat observer. The simplicity of the design renders parity-based filters attractive for fault diagnosis applications, as further detailed in the next section.

2.2 Detection

In this section, we present the problem of fault detection and review existing formulations. We also compare different detection schemes from a design perspective.

Fault detection problems are binary classification problems in which the decision-making system determines whether the operational state is faulty or healthy. According to the residual properties, a nonzero value of $\boldsymbol{r}$ is sufficient to indicate a fault. Therefore, the diagnostic residual signal does not necessarily need to be multivariate for the purpose of detection. In fact, any linear combination of rows in $\boldsymbol{N}_H(\mathfrak{q})$, leading to a scalar residual, can serve as a basis for designing the detection filter. To take this into consideration, the filter transfer function $\boldsymbol{R}(\mathfrak{q})$ in Equation (2.4) is modified to

$$\boldsymbol{R}(\mathfrak{q}) = a^{-1}(\mathfrak{q})\boldsymbol{\gamma}(\mathfrak{q})\boldsymbol{N}_H(\mathfrak{q})\boldsymbol{L}(\mathfrak{q}) = a^{-1}(\mathfrak{q})\boldsymbol{N}(\mathfrak{q})\boldsymbol{L}(\mathfrak{q}), \tag{2.7}$$

where $\boldsymbol{\gamma}(\mathfrak{q})$ is a polynomial row vector representing a linear combination of the rows of $\boldsymbol{N}_H(\mathfrak{q})$. Defining $\boldsymbol{N}(\mathfrak{q}) := \boldsymbol{\gamma}(\mathfrak{q})\boldsymbol{N}_H(\mathfrak{q})$ implicitly incorporates the role of $\boldsymbol{\gamma}(\mathfrak{q})$ into the design while simultaneously resulting in a scalar residual signal. Hence, filter design amounts to designing the row polynomial vector $\boldsymbol{N}(\mathfrak{q})$ and the realization poles $a(\mathfrak{q})$. However, in this review, we keep $a(\mathfrak{q})$ fixed and focus on determining an optimal $\boldsymbol{N}(\mathfrak{q})$ based on the given filter performance criterion. The filter design, in its simplest form, can be expressed as a polynomial matrix inequality:

$$\begin{aligned} \boldsymbol{N}(\mathfrak{q})\boldsymbol{H}(\mathfrak{q}) &= \boldsymbol{0}, \\ \boldsymbol{N}(\mathfrak{q})\boldsymbol{F}(\mathfrak{q}) &\neq \boldsymbol{0}. \end{aligned} \tag{2.8}$$

Whether this problem can be solved or not is assessed via the property of fault detectability for linear DAE systems, formally defined as follows.

Definition 2.1 (Fault detectability)**.** A nonzero fault signal $\boldsymbol{f}$ is detectable if for any $\boldsymbol{z}$ and $\boldsymbol{\xi}$ satisfying $\boldsymbol{H}(\mathfrak{q})\boldsymbol{\xi} + \boldsymbol{L}(\mathfrak{q})\boldsymbol{z} + \boldsymbol{F}(\mathfrak{q})\boldsymbol{f} = \boldsymbol{0}$, $\boldsymbol{z}$ lies outside the healthy behavior set—i.e., $\boldsymbol{z} \notin \mathfrak{B}_{\text{healthy}}$. Moreover, a system described by Equation (2.1) is fault detectable if any fault $\boldsymbol{f}$ satisfying $\boldsymbol{F}(\mathfrak{q})\boldsymbol{f} \not\equiv \boldsymbol{0}$ is detectable.

A necessary and sufficient condition guaranteeing both the fault detectability and the feasibility problem in Equation (2.8) is provided by [72]:

$$\operatorname{normalrank}\begin{bmatrix}\boldsymbol{H}(\mathfrak{q}) & \boldsymbol{F}(q)\end{bmatrix} > \operatorname{normalrank}\boldsymbol{H}(\mathfrak{q}).$$

If we use the methods presented in the box titled From Polynomial Matrix Algebra to Linear Algebra, then the problem in Equation (2.8) is equivalent, up to a scalar factor, to the following:

$$\begin{aligned} \bar{\overline{\mathbf{N}}}\bar{\overline{\mathbf{H}}}_p &= \mathbf{0}, && \text{(disturbance decoupling)} \\ \left\|\bar{\overline{\mathbf{N}}}\bar{\overline{\mathbf{F}}}_p\right\|_\infty &\geq 1, && \text{(fault sensitivity)} \end{aligned} \tag{2.9}$$

where p must be chosen sufficiently large, so that $p+1$ is the degree of $\boldsymbol{N}(\mathfrak{q})$. Mohajerin Esfahani and Lygeros [58] reformulated this nonconvex problem as a series of linear programs.

From Polynomial Matrix Algebra to Linear Algebra

Representing polynomial matrices as certain types of real-(complex-)valued matrices is particularly useful for fault diagnosis filter design. First, it enables efficient methods for performing operations with them [138], such as products, inverses, and null spaces. Second, it further allows one to place polynomial matrix constraints and objectives in standard convex optimization methods.

Let $X(\mathfrak{q})$ and $Y(\mathfrak{q})$ be polynomial matrices in operator $\mathfrak{q}$ of sizes $n_\mathrm{r} \times n_\mathrm{c}$ and $n_\mathrm{rr} \times n_\mathrm{r}$, respectively. Then, we have

$$X(\mathfrak{q}) := \sum_{i=0}^{p_X} X_i \mathfrak{q}^i, Y(\mathfrak{q}) := \sum_{i=0}^{p_Y} Y_i \mathfrak{q}^i,$$

where $Y_i \in \mathbb{R}^{n_\mathrm{rr} \times n_\mathrm{r}}$ and $X_i \in \mathbb{R}^{n_\mathrm{r} \times n_\mathrm{c}}$ are constant matrices. We define the following representations, which are a block row form and a block Toeplitz form, respectively:

$$\bar{\mathrm{Y}} := \begin{bmatrix} Y_0 & Y_1 & \cdots & Y_{p_Y} \end{bmatrix} \in \mathbb{R}^{n_\mathrm{rr} \times (p_Y+1) n_\mathrm{r}}$$

$$\overset{\approx}{\mathrm{X}}_p := \begin{bmatrix} X_0 & X_1 & \cdots & X_{p_X} & \mathbf{0} & \cdots & \mathbf{0} \\ \mathbf{0} & X_0 & X_1 & \cdots & X_{p_X} & \mathbf{0} & \vdots \\ \vdots & & \ddots & \ddots & & \ddots & \mathbf{0} \\ \mathbf{0} & \cdots & \mathbf{0} & X_0 & X_1 & \cdots & X_{p_X} \end{bmatrix} \in \mathbb{R}^{p n_\mathrm{r} \times (p+p_X) n_\mathrm{c}},$$

where p determines the number of block rows of $\overset{\approx}{\mathrm{X}}_p$. The product of two polynomial matrices satisfies

$$Y(\mathfrak{q})X(\mathfrak{q}) = \bar{\mathrm{Y}} \overset{\approx}{\mathrm{X}}_{p_Y+1} \begin{bmatrix} \mathbf{I} & \mathfrak{q}\mathbf{I} & \mathfrak{q}^2\mathbf{I} & \cdots & \mathfrak{q}^{p_Y+p_X}\mathbf{I} \end{bmatrix}^\top.$$

For example, the polynomial matrix $X(\mathfrak{q}) = \begin{bmatrix} 1-\mathfrak{q} \\ 2 \end{bmatrix}$ can be decomposed as

$$X(\mathfrak{q}) = \underbrace{\begin{bmatrix} -1 \\ 0 \end{bmatrix}}_{X_1} \mathfrak{q} + \underbrace{\begin{bmatrix} 1 \\ 2 \end{bmatrix}}_{X_0} = \sum_{i=0}^{p_X=1} X_i \mathfrak{q}^i.$$

Letting $p = 2$, the Toeplitz format of $X(\mathfrak{q})$ is given by

$$\overset{\approx}{\mathrm{X}}_2 = \begin{bmatrix} 1 & -1 & 0 \\ 2 & 0 & 0 \\ 0 & 1 & -1 \\ 0 & 2 & 0 \end{bmatrix}.$$

Its left null space is spanned by the vector $\begin{bmatrix} 2 & -1 & 0 & 1 \end{bmatrix}$, which gives that $N(\mathfrak{q}) = \begin{bmatrix} 2 & -1+\mathfrak{q} \end{bmatrix}$ satisfies $N(\mathfrak{q})X(\mathfrak{q}) \equiv \mathbf{0}$. Additionally, computing a left inverse, i.e., solving $Y(\mathfrak{q})X(\mathfrak{q}) = 1$, is the same as finding $\bar{\mathrm{Y}}$ such that $\bar{\mathrm{Y}} \overset{\approx}{\mathrm{X}}_2 = \begin{bmatrix} 1 & 0 & 0 \end{bmatrix}$, which gives the obvious solution $\bar{\mathrm{Y}} = \begin{bmatrix} 0 & 0.5 & 0 & 0 \end{bmatrix}$, i.e., $Y(\mathfrak{q}) = \begin{bmatrix} 0 & 0.5 \end{bmatrix}$.

Here, we provide a simpler solution to the feasibility problem in Equation (2.9) via the linear algebraic approach outlined in the box titled From Polynomial Matrix Algebra to Linear Algebra. First, find $\bar{\mathbf{N}}_H$ as the left null space of $\bar{\bar{\bar{\mathbf{H}}}}_p$. Next, take $\boldsymbol{\mu}$ as the leading left singular vector of $\bar{\mathbf{N}}_H \bar{\bar{\bar{\mathbf{F}}}}_p$, which ensures that $\boldsymbol{\mu}^\top \bar{\mathbf{N}}_H \bar{\bar{\bar{\mathbf{F}}}}_p \neq \mathbf{0}$, provided that the system is fault detectable and p is sufficiently large. Finally, rescale $\boldsymbol{\mu}$ so that $\|\boldsymbol{\mu}^\top \bar{\mathbf{N}}_H \bar{\bar{\bar{\mathbf{F}}}}_p\|_\infty \leq 1$. By construction, $\bar{\boldsymbol{\gamma}} \coloneqq \boldsymbol{\mu}^\top \bar{\mathbf{N}}_H$ satisfies the conditions in Equation (2.8).

Once the residual generator is designed, detection logic is applied in the diagnosis filter:

$$\begin{cases} J(r) \leq J_{\text{th}} & \Longrightarrow \text{ no fault}, \\ J(r) > J_{\text{th}} & \Longrightarrow \text{ fault occurrence}. \end{cases} \tag{2.10}$$

where $J(r)$ denotes an evaluation function applied to the residual signal, and J_{th} is the detection threshold that must be determined during the training phase [1, 59, 96]. In the ideal scenario (i.e., a noise-free linear system), J_{th} is set to zero, and any nonzero residual is interpreted as an indication of a fault.

2.2.1 Nonlinear and Robustification Approaches

The set of feasible residual generators, as solutions to Equation (2.9), results in detection filters that are effective under the noise-free linear assumption (i.e., $\boldsymbol{w} = \mathbf{0}$ and $\boldsymbol{\eta}(\xi, z) = \mathbf{0}$). However, this assumption rarely holds in practical scenarios due to inevitable model imperfections. To address this, one may consider enhancing the robustness of the filter. We begin by identifying the sources of such imperfections, followed by proposing a mechanism to mitigate their impacts.

On the one hand, model imperfections may arise from various sources, including unmodeled dynamics, inherent model uncertainties [10], and natural noise components that cannot be entirely decoupled; in addition, nonlinearities can be treated as a form of imperfection within the class of linear diagnosis filters. On the other hand, the mechanism for filter robustification remains consistent, regardless of the specific cause of these imperfections. In the general DAE formulation given by Equation (2.1), these effects are accounted for by the terms $\boldsymbol{W}(\mathfrak{q})\boldsymbol{w} + \boldsymbol{\eta}(\xi, z)$, which we refer to here as *model mismatch*. If we left multiply Equation (2.1) by $a^{-1}(\mathfrak{q})\boldsymbol{N}(\mathfrak{q})$, the scalar residual r becomes

$$r = \frac{\boldsymbol{N}(\mathfrak{q})}{a(\mathfrak{q})} \boldsymbol{L}(\mathfrak{q}) z = \underbrace{-\frac{\boldsymbol{N}(\mathfrak{q})}{a(\mathfrak{q})} \boldsymbol{H}(\mathfrak{q}) \xi}_{=0} \underbrace{- \frac{\boldsymbol{N}(\mathfrak{q})}{a(\mathfrak{q})} \boldsymbol{F}(\mathfrak{q}) \boldsymbol{f}}_{r_f} \underbrace{- \frac{\boldsymbol{N}(\mathfrak{q})}{a(\mathfrak{q})} \boldsymbol{W}(\mathfrak{q}) \boldsymbol{w} - \frac{\boldsymbol{N}(\mathfrak{q})}{a(\mathfrak{q})} \boldsymbol{\eta}(\xi, z)}_{r_{\text{MM}}}. \tag{2.11}$$

Ideally, in null-space-based filters, only the fault contribution r_f should be present in the residual signal; however, simultaneous contribution from model mismatch r_{MM} degrades the filter performance. We hereafter refer to r_{MM} as the "mismatch signature." Therefore, the objective of residual generation is twofold: (a) to maximize fault sensitivity and (b) to minimize the impact of model mismatch. These objectives are inherently conflicting—i.e., minimizing the influence of model mismatch often leads to reduced fault sensitivity and vice versa. This interplay is commonly referred to as the FAR/MAR (false-alarm rate/missed-alarm rate) trade-off, which can be adjusted by appropriately setting the detection threshold in Equation (2.10) [58, 101].

To robustify the residual generator against model mismatch, it is necessary to quantify the contribution of model mismatch to the residual signal. To achieve this, Mohajerin Esfahani and Lygeros [58] proposed a semi-supervised approach that integrates available model information with fault-free data obtained from the real system [10], a high-fidelity simulator [61], or a digital twin [139]. The underlying intuition is straightforward: The data may compensate for the missing knowledge of the system. As a result, the extent to which the acquired data are representative of the model mismatch can directly affect the filter performance.

The terms $\boldsymbol{W}(\mathfrak{q})$ and $\boldsymbol{\eta}(\xi, z)$ may or may not be explicitly known. In either case, the primary assumption is that r_{MM} can be computed over a finite time window under the fault-free condition. Depending on the model information available in the training phase, there are two ways to calculate the mismatch signature:

$$r_{\mathrm{MM}} = \begin{cases} -a^{-1}(\mathfrak{q})\boldsymbol{N}(\mathfrak{q})\big(\boldsymbol{W}(\mathfrak{q})\boldsymbol{w} + \boldsymbol{\eta}(\xi, z^{\mathrm{real}})\big) & \xi, \boldsymbol{w}, \boldsymbol{W}(\mathfrak{q}), \boldsymbol{\eta}(\cdot), \\ a^{-1}(\mathfrak{q})\boldsymbol{N}(\mathfrak{q})\boldsymbol{L}(\mathfrak{q})\big(z^{\mathrm{real}} - z^{\mathrm{lin}}\big) & \underbrace{z^{\mathrm{lin}}, \boldsymbol{L}(\mathfrak{q}),}_{\text{information}} \end{cases} \tag{2.12}$$

where z^{lin} corresponds to the linear model. In the first case, full knowledge of the real system is assumed to be available during training [58], which is rarely practical in real-world applications. In contrast, the second case relies only on measurable signals, namely z^{real} and z^{lin}, thus enabling broader applicability. For instance, z typically denotes an augmented vector of input–output signals, which, in a special case, reduces to the output difference—i.e., $z^{\mathrm{real}} - z^{\mathrm{lin}} \equiv y^{\mathrm{real}} - y^{\mathrm{lin}}$, since both systems are driven by the same input signal $\boldsymbol{u}$ [61]. The goal is to suppress the contribution of r_{MM} to the residual signal, which can be achieved by minimizing the $\mathcal{L}_2$-norm of r_{MM} recorded over a finite time interval $[0, T] \in \mathcal{T}$. Accordingly, the filter robustification is translated into an optimization framework

$$\begin{aligned} \underset{\bar{\mathbf{N}}}{\text{minimize}} \quad & \|r_{\mathrm{MM}}\|_{\mathcal{L}_2}^2 \\ \text{subject to} \quad & \bar{\mathbf{N}}\overline{\overline{\mathbf{H}}}_p = \mathbf{0}, \\ & \left\|\bar{\mathbf{N}}\overline{\overline{\mathbf{F}}}_p\right\|_\infty \geq 1, \end{aligned} \tag{2.13}$$

where the optimization problem can be presented and solved as a sequence of quadratic programs with linear constraints [10, 58, 61]. The key point in deriving the quadratic program reformulation is to express the cost function as a quadratic form in terms of the filter parameter $\bar{\mathbf{N}}$—i.e., $\|r_{\mathrm{MM}}\|_{\mathcal{L}_2}^2 = \bar{\mathbf{N}}\boldsymbol{Q}_{\mathrm{MM}}\bar{\mathbf{N}}^\top$ in which the positive semi-definite $\boldsymbol{Q}_{\mathrm{MM}}$ is referred to as the mismatch signature matrix [58]. In continuous time, a set of basis functions is proposed to approximate $\boldsymbol{Q}_{\mathrm{MM}}$, whereas in discrete time the computation is less involved as the basis functions reduce to simple time-shift bases [61].

The optimization can be extended to accommodate multiple sets of signature signals resulting from separate experiments. Let N_{exp} stand for the number of experiments. Then,

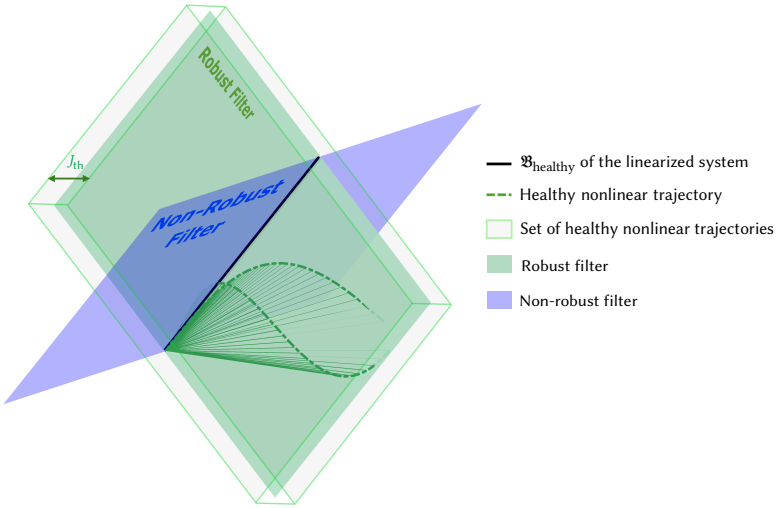

Figure 2.1: Geometry of robust linear filters. The black solid line is the healthy behavior $\mathfrak{B}_{\text{healthy}}$ of the linearized dynamic system, the dashed green lines are two sample trajectories of the healthy nonlinear system, and the green and blue hyperplanes represent two linear filters. Both hyperplanes contain $\mathfrak{B}_{\text{healthy}}$; the green is the robust one containing the healthy nonlinear system trajectories with a smaller threshold J_{th}.

the optimization problem in Equation (2.13) can be modified to

$$\begin{aligned} &\underset{\bar{\mathbf{N}}}{\text{minimize}} && \ell(\bar{\mathbf{N}}) \\ &\text{subject to} && \bar{\mathbf{N}}\bar{\mathbf{H}}_p = \mathbf{0}, \\ &&& \left\|\bar{\mathbf{N}}\bar{\mathbf{F}}_p\right\|_\infty \geq 1, \end{aligned} \qquad \text{with } \ell := \begin{cases} \bar{\mathbf{N}}\left(\dfrac{1}{N_{\text{exp}}}\displaystyle\sum_{i=1}^{N_{\text{exp}}} Q_{\text{MM}}^{(i)}\right)\bar{\mathbf{N}}^\top & : \text{Average cost} \\ \displaystyle\max_{i\leq N_{\text{exp}}} \bar{\mathbf{N}} Q_{\text{MM}}^{(i)} \bar{\mathbf{N}}^\top & : \text{Worst-case cost} \end{cases}$$

Although the constraint $\|\bar{\mathbf{N}}\bar{\mathbf{F}}_p\|_\infty \geq 1$ is nonconvex, it can be reformulated as a finite set of linear constraints, whose number of constraints scales linearly with the filter degree [58]. Building on this, the proposed optimization framework offers three key advantages: (a) Convexity ensures computational tractability and the ability to use commercial solvers (e.g., MOSEK, Gurobi, CPLEX); (b) the formulation scales efficiently, making it suitable for high-dimensional complex systems; and (c) the underlying convex structure (i.e., having feasible sets as a union of convex sets) allows the use of tools from the scenario approach literature (e.g., [140]) in order to provide statistical guarantees for unseen mismatch signature matrices, which represent plausible future experimental settings [58, 141]. Figure 2.1 illustrates the robustified linear filters obtained through this technique, together with a threshold defined by Equation (2.10). In [10], a more specific formulation tailored to structural model uncertainties is presented, demonstrating that the framework in Equation (2.13) can be adapted to various scenarios given the available model information. It is important to emphasize that the filter design assumes no prior knowledge of the fault signal. However, in certain applications, such as power grids [61] and wind turbines [142, 143], partial information about fault characteristics may be available. In such cases, the filter performance can be enhanced by incorporating this fault information into the

filter synthesis process, specifically within the optimization framework of Equation (2.13). In [104], the frequency content of faults is exploited by optimizing a mixed $\mathcal{H}_-/\mathcal{H}_2$ performance index over certain frequency ranges. The results given by [62] assume that the fault signals can be represented as a linear combination of predefined basis functions. Regarding these parameterizations, the fault feasible set $\mathcal{F}$ is summarized as

$$\mathcal{F} := \begin{cases} \{f \in \mathbb{R}^{n_f} \mid f = \int_\Theta \mathrm{FT}\{f\} e^{j\theta}\, d\theta,\ \Theta \subset [\pi, -\pi]\} & \text{frequency-content} \\ \{f \in \mathbb{R}^{n_f} \mid f = \sum_{i=1}^{n_b} \alpha_i \phi_b^{(i)},\ \alpha \in \mathbb{R}, \text{basis } \phi_b^{(i)}\} & \text{basis functions} \end{cases}$$

Hence, addressing the underlying diagnosis problem in an optimization framework provides the flexibility to incorporate additional prior information through new constraints or an alternative parameterization or by modifying the objective function.

For the specific case of linear time-varying systems, the detection threshold is robustified using a projection-based filter [107]. More recently, distributionally robust techniques have been proposed to enhance filter performance, particularly when the noise is assumed to be drawn from an uncertain but structured family of distributions [59, 101]. At the same time, set-based methods have received more attention, owing to recent advances in reachability analysis tools such as zonotopic methods and the suitability of such methods for bounded cyber-attack estimation [71]. [144] [144] recently performed a comparison of several methods. Similar to the case of fault isolation, set-based methods have the advantage of being applicable to a broad class of nonlinear systems but suffer from higher online computational cost and difficulty with scalability.

2.2.2 Model-Free Approaches

Model-free approaches utilize historical data instead of models to solve diagnosis problems. These methods can generally be categorized into unsupervised and supervised approaches. In the unsupervised category, training data are used primarily either to learn statistical models [67, 124] or to extract latent statistical structures for performing classical variational analysis and hypothesis testing. Techniques such as principal component analysis [109], partial least squares [110], canonical variate analysis [111], and their variants are widely employed for anomaly detection (for a survey, see [145]). In the supervised category, data-driven solutions are predominantly based on system identification methods, which assume that the observed data belong to a known system class. Conventional two-stage, or *indirect*, designs typically involve first identifying the system model parameters, followed by the application of model-based diagnostic methods. Subspace identification methods are well-established techniques for linear system modeling, with notable variants including N4SID (numerical algorithms for subspace state-space system identification) [47], MOESP (multivariable output-error state space) [146], and PBSID (predictor-based subspace identification) [147]. Compared with the standard prediction-error method [50] and maximum likelihood estimation [148], subspace identification methods offer advantages such as avoiding nonconvex optimization and providing better numerical stability. *Direct* designs, on the other hand, leverage subspace identification methods to construct observers or diagnosis filters directly from input–output data, bypassing explicit system modeling. These approaches have been successfully applied in several fault detection studies [24, 149].

When dealing only with sampled data, it is more natural to frame the problem in discrete time. For brevity, we adopt the following *innovation form* as the data-generating system, representing a minimal state-space realization of a finite-dimensional LTI system [50]:

$$\begin{aligned} \boldsymbol{x}(t+1) &= \boldsymbol{A}\boldsymbol{x}(t) + \boldsymbol{B}_u\boldsymbol{u}(t) + \boldsymbol{B}_f\boldsymbol{f}(t) + \boldsymbol{K}\boldsymbol{e}(t), \\ \boldsymbol{y}(t) &= \boldsymbol{C}\boldsymbol{x}(t) + \boldsymbol{D}_u\boldsymbol{u}(t) + \boldsymbol{D}_f\boldsymbol{f}(t) + \boldsymbol{e}(t), \end{aligned} \tag{2.14}$$

Process and measurement noises are modeled through the zero-mean innovation signal $\boldsymbol{e}(t) \in \mathbb{R}^{n_y}$ with a steady-state Kalman gain $\boldsymbol{K} \in \mathbb{R}^{n_x \times n_y}$ [150]. In data-driven settings, the Toeplitz and Hankel data structures are instrumental in problem formulation and are introduced below. Let N represent the number of collected samples in the training dataset. Define L as the depth of the Hankel matrix constructed from N data points of an arbitrary signal $\boldsymbol{s}(t)$, as follows:

$$\overset{///}{\mathrm{S}}_{t,L,N} := \begin{bmatrix} \boldsymbol{s}(t) & \boldsymbol{s}(t+1) & \cdots & \boldsymbol{s}(t+N-L) \\ \boldsymbol{s}(t+1) & \boldsymbol{s}(t+2) & \cdots & \boldsymbol{s}(t+N-L+1) \\ \vdots & \vdots & \ddots & \vdots \\ \boldsymbol{s}(t+L-1) & \boldsymbol{s}(t+L) & \cdots & \boldsymbol{s}(t+N-1) \end{bmatrix},$$

The data collected over the time interval $[t_1, t_2]$ are stacked into a column vector $\mathbf{s}_{[t_1,t_2]} := [\boldsymbol{s}^\top(t_1) \quad \boldsymbol{s}^\top(t_1+1) \quad \cdots \quad \boldsymbol{s}^\top(t_2)]^\top$. Similarly, the state trajectory over this interval is gathered in the matrix $\mathrm{X}_{[t_1,t_2]} := [\boldsymbol{x}(t_1) \quad \boldsymbol{x}(t_1+1) \quad \cdots \quad \boldsymbol{x}(t_2)]$. The data equation corresponding to the system in Equation (2.14) for a dataset of size N over a sliding time window of length L follows:

$$\begin{bmatrix} \overset{///}{\mathrm{U}}_{t,L,N} \\ \overset{///}{\mathrm{Y}}_{t,L,N} \end{bmatrix} = \underbrace{\begin{bmatrix} \mathbf{I} & \mathbf{0} \\ \mathrm{T}_L^u & \mathrm{O}_L \end{bmatrix}}_{\mathrm{G}_L} \begin{bmatrix} \overset{///}{\mathrm{U}}_{t,L,N} \\ \mathrm{X}_{[t,t+N-L]} \end{bmatrix} + \begin{bmatrix} \mathbf{0} \\ \mathrm{T}_L^f \overset{///}{\mathrm{F}}_{t,L,N} + \mathrm{T}_L^e \overset{///}{\mathrm{E}}_{t,L,N} \end{bmatrix}, \tag{2.15}$$

in which O_L represents the extended observability and $\mathrm{T}_L^\star$ is the lower triangular block-Toeplitz matrix of Markov parameters (impulse responses) structured as

$$\mathrm{O}_L = \begin{bmatrix} \boldsymbol{C} \\ \boldsymbol{C}\boldsymbol{A} \\ \vdots \\ \boldsymbol{C}\boldsymbol{A}^{L-1} \end{bmatrix}, \quad \mathrm{T}_L^\star = \begin{bmatrix} \boldsymbol{M}_0^\star & \mathbf{0} & \cdots & \mathbf{0} \\ \boldsymbol{M}_1^\star & \boldsymbol{M}_0^\star & \ddots & \vdots \\ \vdots & \vdots & \ddots & \mathbf{0} \\ \boldsymbol{M}_{L-1}^\star & \boldsymbol{M}_{L-2}^\star & \cdots & \boldsymbol{M}_0^\star \end{bmatrix}$$

with $\star$ representing u, f, or e. The corresponding Markov parameters are given by

$$\boldsymbol{M}_i^u = \begin{cases} \boldsymbol{D}_u & i = 0 \\ \boldsymbol{C}\boldsymbol{A}^{i-1}\boldsymbol{B}_u & i > 0 \end{cases}, \; \boldsymbol{M}_i^f = \begin{cases} \boldsymbol{D}_f & i = 0 \\ \boldsymbol{C}\boldsymbol{A}^{i-1}\boldsymbol{B}_f & i > 0 \end{cases}, \; \boldsymbol{M}_i^e = \begin{cases} \mathbf{I}_{n_y} & i = 0 \\ \boldsymbol{C}\boldsymbol{A}^{i-1}\boldsymbol{K} & i > 0 \end{cases}.$$

Define $\mathbf{K}_L$ such that its rows span the left null space of G_L, implying $\mathbf{K}_L\mathrm{G}_L = \mathbf{0}$. For a sufficiently large value of L, the existence of a solution for $\mathbf{K}_L$ is guaranteed by the Cayley–Hamilton theorem, exploiting the inherent temporal redundancy of LTI systems [51]. One should note that G_L and $\mathbf{K}_L$ respectively parameterize the hyperplane (green) and the

normal subspace (blue) illustrated in Figure 2.1 given a fault- and noise-free condition. In this context, data-driven null-space-based filters aim to estimate $\mathbf{K}_L$ directly from the recorded data [60, 108], whereas conventional subspace identification methods focus on identifying $\mathbf{G}_L$ [18, 48].

Regardless of the objective, two fundamental assumptions are typically required in data-driven designs:

(a) The training dataset $\mathcal{D}_{\text{healthy}} := \{\boldsymbol{u}(t), \boldsymbol{y}(t)\}_{t=0}^{N-1}$ is fault-free, and

(b) the data are recorded such that $\operatorname{rank}\begin{bmatrix}\mathbf{X}_{[0,N-L]} \\ \hat{\mathbf{U}}_{0,L,N}\end{bmatrix} = n_x + Ln_u$ (a condition that can be ensured by designing an input signal with a persistency of excitation of sufficient order; see [17]).

Definition 2.2 (Persistency of excitation)**.** A discrete-time input signal $\boldsymbol{u}(t)$ for $t \in [0, N-1]$ is persistently exciting of order L if the Hankel matrix $\hat{\mathbf{U}}_{0,L,N}$ has full row rank.

According to *Willems' fundamental lemma* [17], any healthy noise-free trajectory of the system with length L satisfies

$$\forall \mathbf{u}_{[t,t+L-1]}, \boldsymbol{x}_t, \quad \mathbf{K}_L \begin{bmatrix}\mathbf{u}_{[t,t+L-1]} \\ \mathbf{y}_{[t,t+L-1]}\end{bmatrix} = \mathbf{0}, \text{ and } \mathbf{K}_L \begin{bmatrix}\hat{\mathbf{U}}_{t,L,N} \\ \hat{\mathbf{Y}}_{t,L,N}\end{bmatrix} = \mathbf{0}, \tag{2.16}$$

which can be seen as the data-based kernel representation [135]. The corresponding residual generator is designed as

$$\boldsymbol{r} := \underbrace{\begin{bmatrix}\mathbf{K}_L^u & \mathbf{K}_L^y\end{bmatrix}}_{\mathbf{K}_L} \begin{bmatrix}\mathbf{u}_{[t,t+L-1]} \\ \mathbf{y}_{[t,t+L-1]}\end{bmatrix} = \mathbf{K}_L^y(\mathbf{T}_L^f \mathbf{f}_{[t,t+L-1]} + \mathbf{T}_L^e \mathbf{e}_{[t,t+L-1]}), \tag{2.17}$$

where $\mathbf{K}_L^y \mathbf{O}_L = \mathbf{0}$ and $\mathbf{K}_L^u = -\mathbf{K}_L^y \mathbf{T}_L^u$.

The proposed residual generator is a finite impulse response filter with horizon L as a design parameter. In the diagnosis literature, $\mathbf{K}_L^y$ characterizes the so-called *parity space* [1, 70]. As proved by Chen and Patton [136],Patton and Chen [137], and Ding [131], for any parity-relation-based residual generator, one can derive an observer-based diagnosis filter with identical dynamics. Thus, we suggest using the parity space at the design stage for its simplicity and then realize the solution in the observer form for its recursive implementation, which is online friendly. From Equation (2.17), it follows that this approach provides decoupling only regarding the system states, and not the innovation (noise) signal. As a result, ensuring satisfactory fault detection performance requires the detection threshold to be robust against the noise level [58, 59, 104].

Chen et al. [28] extend the kernel-representation-based design to a class of Lipschitz nonlinear systems, where $\mathbf{K}_L$ is a nonlinear operator. Krishnan and Pasqualetti [112] characterized the fault detectability in a data-driven sense based on the observed data informativity. Another class of data-driven diagnosis schemes extends the UIO design

(Equation (2.5)) to data-driven settings by additionally assuming access to the state trajectory $\mathbf{X}_{[0,N-L]}$ [117, 151], unlike the data-based kernel-representation solutions (Equation (2.16)). This assumption is justified in applications where the state information can be obtained or estimated reliably [152].

2.3 Isolation

This section discusses the isolation task as a natural extension to a *multi-classification* problem. Assuming $n_f > 1$, the objective is to identify the specific source responsible for triggering the fault alarm.

Whereas a scalar residual signal is sufficient for the detection, isolating the fault generally necessitates multiple residuals or a residual vector. Designing a set of dedicated filters, each tailored to be sensitive to a subset of faults while remaining insensitive to others, leads to what is known as the bank-of-filters approach [2, 24]. This can be implemented in the DAE framework by augmenting ξ with fault signals intended to be decoupled from the residual signal [72]. In other words, to isolate the ith additive fault f_i from the remaining faults $\tilde{f} := [f_1 \quad f_2 \quad \cdots \quad f_{i-1} \quad f_{i+1} \quad \cdots]$, the system can be represented as

$$\begin{bmatrix} \boldsymbol{H}(\mathfrak{q}) & \widetilde{\boldsymbol{F}}(\mathfrak{q}) \end{bmatrix} \begin{bmatrix} \xi \\ \tilde{f} \end{bmatrix} + \boldsymbol{L}(\mathfrak{q})z + \boldsymbol{F}_i(\mathfrak{q})f_i + \boldsymbol{W}(\mathfrak{q})w + \boldsymbol{\eta}(\xi, z) = \mathbf{0},$$

where $\boldsymbol{F}_i(\mathfrak{q})$ is the ith column of $\boldsymbol{F}(\mathfrak{q})$, and the remaining columns are kept in $\widetilde{\boldsymbol{F}}(\mathfrak{q})$ with respect to $\tilde{f}$. The rest of the design follows similar steps outlined in Section 2.2. The necessary and sufficient condition for the *fault isolability* of f_i is given by [72]

$$\operatorname{normalrank}\begin{bmatrix} \boldsymbol{H}(\mathfrak{q}) & \widetilde{\boldsymbol{F}}(q) & \boldsymbol{F}_i(\mathfrak{q}) \end{bmatrix} > \operatorname{normalrank}\begin{bmatrix} \boldsymbol{H}(\mathfrak{q}) & \widetilde{\boldsymbol{F}}(q) \end{bmatrix}.$$

In this scheme, each filter generates a scalar residual signal that indicates the presence of the corresponding fault. A key idea in deriving the isolation scheme from existing approaches is to treat the fault signals that the filter should ignore as additional disturbances to be completely rejected (not to be confused with noise to be mitigated). In the null-space-based filters, the transfer function $\boldsymbol{G}_d(\mathfrak{q})$ is built on the augmented polynomial matrix $\begin{bmatrix} \boldsymbol{H}(\mathfrak{q}) & \widetilde{\boldsymbol{F}}(\mathfrak{q}) \end{bmatrix}$ [41]. Accordingly, the solvability constraint in Equation (2.6) must be adapted so that $(\boldsymbol{B}_d, \boldsymbol{D}_d)$ includes the corresponding columns of $(\boldsymbol{B}_f, \boldsymbol{D}_f)$ in observer-based approaches [34].

In a similar fashion, parity-relation-based designs leverage the multidimensionality of the generated residual to meet additional requirements posed by the isolation problem [24]—for instance, in the case of f_i

$$1)\, \alpha_i \mathbf{K}_L^y \mathbf{T}_L^{\tilde{f}} = 0, \qquad 2)\, \alpha_i \mathbf{K}_L^y \mathbf{T}_L^{f_i} \neq 0,$$

Here, α_i is a newly introduced design parameter taking a linear combination of rows in $\mathcal{K}_L^y$. The block Toeplitz matrices $\mathbf{T}_L^{\tilde{f}}$ and $\mathbf{T}_L^{f_i}$ are constructed based on the associated columns in $(\boldsymbol{B}_f, \boldsymbol{D}_f)$. The existence of a solution to the bank of filters is linked to the left invertibility of the fault subsystem, i.e., the system from $\boldsymbol{f}$ to $\boldsymbol{y}$ [6, 84]. In the DAE framework, this is expressed as

$$\operatorname{normalrank}\begin{bmatrix} \boldsymbol{H}(\mathfrak{q}) & \boldsymbol{F}(\mathfrak{q}) \end{bmatrix} = n_f + \operatorname{normalrank}\begin{bmatrix} \boldsymbol{H}(\mathfrak{q}) \end{bmatrix},$$

which carries equivalent implications in both the state-space and the transfer-function model descriptions [153, 154]. An immediate consequence of the left invertibility is that $n_y \geq n_f$.

In cases where designing dedicated filters for individual faults is not feasible, a possible relaxation is to group a subset of fault signals and reconsider the isolation problem. This leads to the concept of a structured residual set [4]. A different perspective to achieve fault isolability involves assigning a unique directional residual induced by a particular fault in the residual space, referred to as the signature direction [8, 34]. The isolation task, therefore, amounts to determining which signature direction the generated residual signal most closely aligns with. The relative signature directions can be optimized to maximize their separability. Although handling simultaneous faults is straightforward with a bank of filters, it is generally more challenging in the directional residual method. On the other hand, a bank of filters imposes stricter requirements on the system structure. Further, Beard [8] and Massoumnia [33] investigated the underlying problem from a geometrical standpoint and derived the necessary conditions for fault isolability in terms of output separability.

2.3.1 Nonlinear Systems

Fault isolation for nonlinear systems was first addressed using linearization at local operating points, followed by decoupling the disturbances together with the higher-order terms from the residuals (see, e.g., [106]; for a survey, see [155]). Zhang et al. [66] used a nonlinear DAE approach, relying on differential-polynomial representations. With that, Ritt–Wu's algorithm is used to decouple the effect of particular faults. A seminal work by De Persis and Isidori [55] used a geometric approach to formulate the theory of diagnosability in nonlinear systems, considering continuous-time input- and fault-affine systems of the form

$$\begin{aligned} \mathfrak{q}\boldsymbol{x} &= \boldsymbol{g}(\boldsymbol{x}) + \boldsymbol{g}_u(\boldsymbol{x})\boldsymbol{u} + \boldsymbol{g}_f(\boldsymbol{x})\boldsymbol{f}, \\ \boldsymbol{y} &= \boldsymbol{h}(\boldsymbol{x}). \end{aligned}$$

In this setup, the authors found geometric conditions for the problem of designing an observer-based residual generator that is sensitive to only one of the faults $\boldsymbol{f}$, proceeding to show how to design such observers using a high-gain approach.

Both the algebraic method of Zhang et al. [66] and the geometric approach of De Persis and Isidori [55] suffer from sheer design complexity, sometimes requiring pencil-and-paper calculations or computations with non-trivial complexity such as Ritt–Wu's method. Therefore, linear approximations may be necessary for larger-scale problems. LTI approximations can be (implicitly) used via the robustification approaches presented in Section 2.2 (see [58, 61]). Alternatively, linear time-varying approximations or the particular case of linear parameter-varying approximations can be used. Bokor and Balas [56] and van der Ploeg et al. [86] developed the robustification approach for linear parameter-varying systems in [56, 86]. In the specific case of actuator faults, Zhang [87] provided an adaptive Kalman filter for linear time-varying systems with stability and minimum variance guarantees. Venkateswaran et al. [88] recently showed that, depending on some differential conditions on $\boldsymbol{g}(\cdot)$ and $\boldsymbol{h}(\cdot)$, linear residual generators exist that provide perfect decoupling

of nonlinear systems; in this case, a systematic approach for designing diagnosis filters is available.

Several works have used nonlinear state estimators to approximate the nonlinear terms [57, 89, 90]. Boem et al. [91] addressed large-scale nonlinear systems subject to stochastic noise, which give probabilistic false-alarm guarantees.

2.3.2 Multimodel Hypothesis: Passive and Active Methods

Instead of trying to understand which channel from a specified fault matrix is active, certain classes of fault detection and isolation problems are better modeled by a multimodel hypothesis. That is, in the DAE framework, a model of the type

$$\boldsymbol{H}(\mathfrak{q})\boldsymbol{x} + \boldsymbol{L}(\mathfrak{q})\boldsymbol{z} + \boldsymbol{W}(\mathfrak{q})\boldsymbol{w} + \boldsymbol{\eta}(\boldsymbol{x}, \boldsymbol{z}) = \boldsymbol{0}$$

is considered healthy, while m models of the type

$$\boldsymbol{H}_i(\mathfrak{q})\boldsymbol{x} + \boldsymbol{L}_i(\mathfrak{q})\boldsymbol{z} + \boldsymbol{W}_i(\mathfrak{q})\boldsymbol{w} + \boldsymbol{\eta}_i(\boldsymbol{x}, \boldsymbol{z}) = \boldsymbol{0} \quad \text{with} \quad i \in \{1, \dots, m\}$$

are considered to be the potential m faulty modes. The objective of the fault isolation filter in this multimodel classification scenario is to identify which of the $m+1$ modes is active. Halimi et al. [92] and Küsters and Trenn [93] established the necessary rank conditions to guarantee that any two subsystems can be distinguished from each other.

Passive isolation

To address the isolation problem, the bank-of-filters approach has been developed using methods such as parity space [73], UIOs [74], and sliding mode observers [94, 95]. However, a drawback of this approach is that the computational complexity of the filters, in both design and implementation, increases significantly as the system dimension and the number of modes increase. Dong et al. [96] designed the filters via DAE methods, enabling reduced-order designs that are tractable via convex optimization formulations. For linear systems under sub-Gaussian stochastic noise, they provided false-alarm rate bounds that admit a logarithmic dependency with respect to the desired reliability level, improving on the polynomial rate in the work by Boem et al. [91].

Another approach for mode detection uses set-membership methods, which rely on reachability analysis. These methods are better suited under bounded noise assumptions instead of probabilistic ones. In set-based methods, the current output is compared with the reachable sets of each mode, which enables the exclusion of modes whenever the output is out of the corresponding mode's reachable set. Harirchi and Ozay [102] reduced the set-membership check to the feasibility of a mixed-integer linear programming problem.

Active methods

Multimodel classification performance is highly dependent on the input. Therefore, designing optimal inputs can help better distinguish between the possible modes. Heirung and Mesbah [46] published a survey on input design for the multimodel classification problem that extensively reviews methods for both stochastic and set-based settings. For a few cases—e.g., single input–single output LTI systems with a two-model hypothesis and simple input constraints—analytical solutions have been derived. The focus in the past two

decades has been on more complex cases that require computational methods, and dealing with the tractability of the nonconvex optimization problems they form.

Scott et al. [77] and Marseglia and Raimondo [64] used an active set-based diagnosis approach, where an optimally separating input sequence is designed to maximize the chances of pinpointing a single mode. Set-based methods are known to be computationally demanding, and input design problems are particularly expensive. Blanchini et al. [78] partially addressed this issue by placing the uncertainty propagation burden offline. More recent research has focused on the tractability and generality of the set computations involved, and for that sets such as constrained zonotopes [75] for discrete-time ordinary differential equations and line zonotopes [76] for discrete-time DAEs have been developed.

Despite having better computation tractability, the stochastic case also involves nonconvex optimization problems. Noom et al. [113] have recently made advances in this area; they used disciplined concave minimization by operating on a subdomain of the input space and showed that a concave function serves as a good envelope approximation of the Bhattacharyya separation criterion. A recent alternative is to use chance-constrained optimization. Guo et al. [79] proposed a new separation criterion based on the Cauchy–Schwarz divergence, requiring a three-stage optimization to obtain the optimal input. Qiu et al. [80] combined bounded and Gaussian uncertainties using set-based confidence levels; the resulting input design problem is a mathematical program with complementarity constraints.

2.3.3 Model-Free Approaches

Providing data-driven solutions to the fault isolation problem depends on the type of fault information available prior to design. In general, it is assumed that only fault-free system trajectories are collected and that $F(\mathfrak{q})$ is not known explicitly. Based on healthy data, it is reasonable to assume that any present fault enters the system through actuators and/or sensors. The literature on data-driven fault isolation design was developed predominantly for a class of additive actuator/sensor faults (e.g., [24, 68, 119]). Accordingly, in the state-space representation, the pair (B_f, D_f) takes values from the columns of (B_u, D_u) for actuator faults and from $(\mathbf{0}, \mathbf{I}_{n_y})$ for sensor faults. For the DAE formulation, we have

$$F(\mathfrak{q}) = \begin{bmatrix} L_{11} & \mathbf{0} \\ L_{21} & \mathbf{I} \end{bmatrix}.$$

Once fault matrices are considered this way, one approach is to identify (B_u, D_u) using subspace identification techniques in order to apply model-based methods for isolation. Instead of the mentioned indirect approach, a direct estimation of $\mathbf{K}_L^y \mathbf{T}_L^u$ from the data is sufficient to implement a parity-relation-based bank of filters, as proposed by Ding et al. [24].

Regarding directional residual signals, Sheikhi et al. [68] showed that the signature matrix $\mathbf{K}_L^y \mathbf{T}_L^{f_i}$ corresponding to an actuator or sensor fault can be estimated directly from the given data, up to a similarity transformation. In fact, signature matrices characterize the subspaces spanned by the columns of $\mathbf{K}_L^y \mathbf{T}_L^{f_i}$, and can be directly retrieved using subspace identification techniques. Thanks to the multidimensionality of the residual signal for a

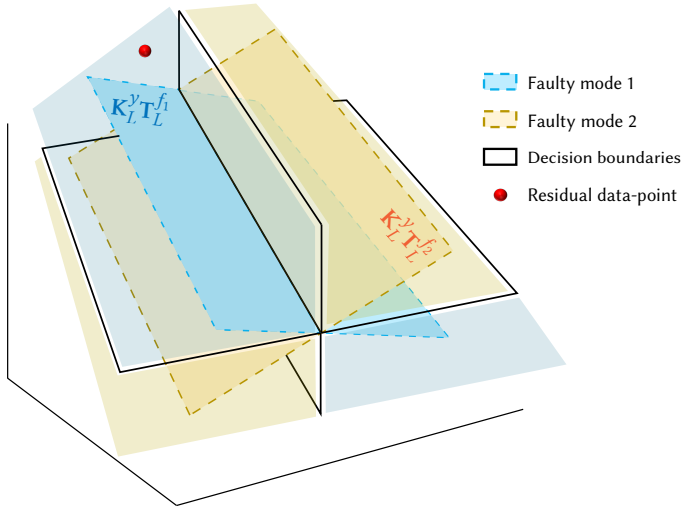

Figure 2.2: Conic partitioning of the residual space, a lower-dimensional projection of the input–output measurement space, for the isolation problem using a linear filter. The dashed blue and orange hyperplanes depict the column spaces of the signature matrices corresponding to faulty modes 1 and 2, respectively ($\mathbf{K}_L^y \mathbf{T}_L^{f_i}, i \in \{1,2\}$). The solid lines denote the decision boundaries set by the isolation logic. Based on these boundaries, the blue and orange cones indicate the partitions associated with fault modes 1 and 2, respectively. The red circle is a sample residual signal, identified as fault mode 1 since it lies within the corresponding conic region, i.e., closer to the blue hyperplane.

sufficiently large filter horizon L, the directional residual approach partitions the residual space according to each fault-induced direction, as illustrated in Figure 2.2. In this space, each hyperplane corresponds to a specific fault-induced signature matrix. The intersection of these hyperplanes is related to the underlying system zeros and is fundamental for characterizing *mutual fault isolability* [5], which can be verified using only data [68]. Although Gleizer [123] recently showed that the span of fault matrices can be identified, data-driven fault isolation for general fault matrices remains a relatively under-researched area. For nonlinear systems, data-driven fault isolation solutions have been proposed for class of nonlinear systems described by Takagi–Sugeno fuzzy models [125], basis functions [126], deep neural networks [127], and Koopman operators with guaranteed input-to-state stability [128].

2.4 Estimation

In estimation problems, the objective of the diagnosis filter (Figure 1.2) is that the residual $\boldsymbol{r}$ tracks or reconstructs the fault signal $\boldsymbol{f}$. Referring to Equation (2.1), we can see that in the absence of noise (i.e., $\boldsymbol{w} = \mathbf{0}$), this leads to the following objectives

- Tracking: For any $\boldsymbol{x}$, $\lim_{t\to\infty} |\boldsymbol{f}(t) - \boldsymbol{r}(t)| = \mathbf{0}$.
- Reconstruction: For any $\boldsymbol{x}$, $\boldsymbol{r} = \mathfrak{q}^{-\tau} \boldsymbol{f}$ for some prescribed delay τ.

Note that delayed reconstruction problems are only well-defined in discrete time, and can be understood as deadbeat implementations of tracking filters.

The filter design can make use of additional information about the fault signal. For example, the fault may be assumed to piecewise constant or polynomial[53, 63, 97], band limited [104], slow [116], periodic [118, 129], generated by a known autonomous system [156, section. 8.5], or sparse [39, 54, 119]. Fault estimation problems can be further characterized by the nature of the fault's effect on the system. The standard DAE description in Equation (2.1) presents what is called an additive fault signal. In some cases, the faulty behavior is better described by multiplicative faults, i.e., when the fault signal $\boldsymbol{f}$ multiplies other system variables such as $\boldsymbol{x}$ and $\boldsymbol{z}$. Estimation of multiplicative faults has its particular challenges and is therefore addressed separately in Section 2.4.3 for passive methods and Section 2.4.4 for active methods. The remaining subsections are devoted to additive fault estimation: Sections 2.4.1 and 2.4.2 are devoted to model-based estimation methods for linear and nonlinear systems, respectively, and Section 2.4.5 is devoted to model-free methods.

2.4.1 Linear Systems

Using Equation (2.1) with $\boldsymbol{\eta}(\cdot,\cdot) \equiv \mathbf{0}$, the fault estimation filter $-a(\mathfrak{q})^{-1}\boldsymbol{N}(\mathfrak{q})\boldsymbol{L}(\mathfrak{q})$ must satisfy one of the criteria established above for fault tracking or reconstruction. First, note that for any $\boldsymbol{N}(\mathfrak{q})$ subject to $\boldsymbol{N}(\mathfrak{q})\boldsymbol{H}(\mathfrak{q}) = \mathbf{0}$, we have that $a(\mathfrak{q})\boldsymbol{r} = \boldsymbol{N}(\mathfrak{q})\boldsymbol{F}(\mathfrak{q})\boldsymbol{f}$. If no more information on the fault signal is known, this gives the following estimation condition:

$$\boldsymbol{N}(\mathfrak{q})\boldsymbol{F}(\mathfrak{q}) \equiv a(\mathfrak{q})\mathbf{I}. \tag{2.18}$$

Equation (2.18) may be difficult to solve in practice. The first observation is that one must find a pair $\boldsymbol{N}(\mathfrak{q}), a(\mathfrak{q})$ such that the degree of $\boldsymbol{N}(\mathfrak{q})\boldsymbol{L}(\mathfrak{q})$ is no greater than that of $a(\mathfrak{q})$. For state-space systems with $\boldsymbol{B}_f \neq \mathbf{0}$ and $\boldsymbol{D}_f = \mathbf{0}$, this is not possible, and the estimator needs differentiators in the continuous-time case [7, 157]. In discrete time, differentiation is replaced by a time shift, and as such, it is possible to relax the criterion in Equation (2.18) to a τ-delay fault estimation [84] criterion,

$$\boldsymbol{N}(\mathfrak{q})\boldsymbol{F}(\mathfrak{q}) \equiv \mathbf{I}, \tag{2.19}$$

which results in the residual satisfying $\boldsymbol{r} = a(\mathfrak{q})^{-1}\boldsymbol{f}$. Thus, by picking $a(\mathfrak{q}) = \mathfrak{q}^{\tau}$, where τ is at least the degree of $\boldsymbol{N}(\mathfrak{q})\boldsymbol{L}(\mathfrak{q})$, we achieve a maximal-bandwidth delayed input reconstruction, also referred to as deadbeat estimation [85]. Gillijns and De Moor Gillijns and De Moor, Kirtikar et al. [84], and Yong et al. [37] showed for minimal state-space realizations that simultaneous τ-delay *initial state* and input reconstruction requires that the fault-output subsystem be (τ-delay) left invertible and have no invariant zeros, a condition that translates, in the DAE framework, to the existence of a matrix $\boldsymbol{M}(\mathfrak{q})$ such that $\boldsymbol{M}(\mathfrak{q})[\boldsymbol{H}(\mathfrak{q}) \;\; \boldsymbol{F}(\mathfrak{q})] = \mathbf{I}$ for all $\mathfrak{q} \in \mathbb{C}$ [63]. We can see that the combined conditions $\boldsymbol{N}(\mathfrak{q})\boldsymbol{H}(\mathfrak{q}) = \mathbf{0}$ and $\boldsymbol{N}(\mathfrak{q})\boldsymbol{F}(\mathfrak{q}) = \mathbf{I}$ are a strict subset of the latter via the following trivial example:

$$\begin{aligned} \mathfrak{q}\boldsymbol{x} + \boldsymbol{x} + \boldsymbol{u} + \boldsymbol{d} + \boldsymbol{f} &= 0, \\ \boldsymbol{y} + \boldsymbol{f} &= 0, \end{aligned}$$

where obviously the filter $\boldsymbol{r} \equiv -\boldsymbol{y}$ provides delay-free fault estimation even though the state is not observable. On the other hand, for systems with at least one invariant zero, *asymptotic estimation* can be considered [37, 81–83, 103].

Given how difficult it is to find residual generators satisfying Equations 2.18 or 2.19, several recent works have focused on estimation when some information about the fault is known. For example, Van der Ploeg et al. [53] considered the case of piecewise-constant faults, which reduces the estimation criterion to the DC-gain version $\boldsymbol{N}(1)\boldsymbol{F}(1) = a(1)\mathbf{I}$ in discrete time. The fault can also be assumed to have a more generic frequency content. This was considered by Dong et al. [104] in the discrete-time case, where it is assumed that the fault spectrum lies in a subset $\Omega \subset \mathbb{R}_+$. Then, the corresponding stringent condition

$$\boldsymbol{N}(\mathrm{e}^{\mathrm{j}\omega})\boldsymbol{F}(\mathrm{e}^{\mathrm{j}\omega}) = a(\mathrm{e}^{\mathrm{j}\omega})\mathbf{I}, \quad \forall \omega \in \Omega,$$

which may be as difficult to solve as Equation (2.18), is replaced by

$$\|\boldsymbol{N}(\mathrm{e}^{\mathrm{j}\omega})\boldsymbol{F}(\mathrm{e}^{\mathrm{j}\omega}) - d(\mathrm{e}^{\mathrm{j}\omega})\mathbf{I}\|_2^2 \leq \eta_1, \quad \text{for a finite collection of } \omega \in \Omega, \tag{2.20}$$

making it amenable to use in optimization problems. In particular, Dong et al. [104] considered a combination of the approximate tracking condition in Equation (2.20) with the $\mathcal{H}_2$-norm of the transfer function from noise $\boldsymbol{w}$ to residual, which can be formulated as a simple quadratic constraint. The result is a quadratic program problem, which makes it suitable for large-scale problems.

When the fault is assumed to be a function of time with unknown parameters, fault estimation can often be recast as a state observer problem using a generator subsystem approach. For example, a fault that is a polynomial function of time can be modeled as a chain of integrators whose initial states must be reconstructed in what is called an ultra-local approach [97]. This approach has been well-developed for nonlinear systems (see Section 2.4.2). Many other functions of time can be modeled; e.g., a sinusoid $f(t) = f_0 \sin(t) + f_1 \cos(t)$ can be modeled as the outcome of the autonomous system $\ddot{f} + f = 0$.

Most fault reconstruction works rely on a state–fault parameterization of the behavioral set, by first removing the contribution of the input $\boldsymbol{u}$. Referring to Equation (2.2) in the absence of noise gives the condition

$$\boldsymbol{r} \coloneqq \mathbf{y}_{[t,t+L-1]} - \mathbf{T}_L^u \mathbf{u}_{[t,t+L-1]} = \mathbf{O}_L \boldsymbol{x}_0 + \mathbf{T}_L^f \mathbf{f}_{[t,t+L-1]}. \tag{2.21}$$

Therefore, simply using a left inverse of $\begin{bmatrix}\mathbf{O}_L & \mathbf{T}_L^f\end{bmatrix}$ provides a perfect L-delay fault reconstruction, provided such a left inverse exists. This coincides with the τ-delay initial state and input reconstructability conditions of Kirtikar et al. [84]. Dong and Verhaegen [44, 114] noted that the inversion of $\begin{bmatrix}\mathbf{O}_L & \mathbf{T}_L^f\end{bmatrix}$ can be avoided if one refrains from estimating or annihilating the initial state; instead, by using a stable Kalman predictor representation, the filter is built by inverting only $\mathbf{T}_L^f$, ignoring the presence of $\boldsymbol{x}_0$ in Equation (2.21). The critical observation is that the estimation bias depends on the transmission zeros from fault to output: When there are minimum-phase zeros, the bias decreases exponentially with L, and when there are non-minimum-phase zeros [25], a mixed causal–anticausal representation (as proposed in [45]) enables minimal bias somewhere in the

middle of the reconstruction window; thus, tuning the delay becomes a fundamental step, and faults in non-minimum-phase systems can only be estimated accurately with very long delays. For zeros located on the unit circle, the bias cannot be controlled with the delay; e.g., for a zero at 1, the fault reconstruction has a constant bias. Finally, the Markov-parameter approach facilitates the consideration of time-domain properties of the fault signal. For example, Zhang [54] and Noom et al. [119] considered the scenario where the fault is assumed to be the combination of a few signals from a dictionary of possible fault signals. The sparsity in terms of the number of active dictionary entries is achieved by adding a 1-norm regularizer on the fault signal. In large-scale systems, not all components of the fault signal are necessarily nonzero at the same time; rather, only a subset may be active during the filter horizon. This induces sparsity at the signal level, which Anguluri et al. [39] exploited to recover the nonzero components.

2.4.2 Nonlinear Systems

When the nominal system has nonlinear dynamics, there are two dominant approaches in the literature. One is to design a nonlinear fault estimator that effectively captures the effect of the nonlinearities in the behavior; the other is to design a linear fault estimation filter that is robust against the nonlinearities. The latter may use techniques similar to those discussed in Section 2.2. For certain classes of nonlinearities, linear filters suffice. For instance, if the nonlinear term in Equation (2.1) is just a function of z, then a new known signal $z' = E(z)$ can be generated online, effectively turning the nonlinear DAE into a linear DAE for estimation purposes. In the cases where $E(z)$ multiplies the fault signal, this becomes a multiplicative fault problem, which is reviewed in Section 2.4.3.

Ghanipoor et al. [97] extended the ultralocal approach in Section 2.4.1 to nonlinear systems, approximating the fault signal as the outcome of a chain of integrators:

$$\begin{cases} \dot{\bar{\zeta}}_j = \bar{\zeta}_{j+1}, & 0 < j < r, \\ \dot{\bar{\zeta}}_r = \mathbf{0}, \\ \bar{f} = \bar{\zeta}_1, \end{cases} \tag{2.22}$$

where $\bar{\zeta}_j \in \mathbb{R}^{n_f}$. This technique requires that the fault be r times differentiable, and can provide the rth order Taylor expansion of the fault signal at a given point. The fault estimation filter then becomes a nonlinear observer, in which the original system state is augmented with the states of the actual fault internal state. The solution to the design problem is obtained by solving linear matrix inequalities, providing an input-to-state stable nonlinear filter. These inequalities can include objective functions, yielding semidefinite programs that minimize either the $\mathcal{L}_2$ gain or the $\mathcal{L}_2$-$\mathcal{L}_\infty$ induced norm from uncertainties to residual. Increasing r leads to high-dimensional observers and scalability issues, yet also provides more degrees of freedom for optimal synthesis.

Witczak et al. [98] also used linear matrix inequalities for observer design; the noise $\boldsymbol{w}$ and the time difference of the fault $\boldsymbol{f}_{k+1} - \boldsymbol{f}_k$ are assumed to be in ℓ_2, and the nonlinearities satisfy certain Lipschitz assumptions. In addition, the so-called observer matching condition $\operatorname{rank} \boldsymbol{B}_f = \operatorname{rank} \boldsymbol{C}\boldsymbol{B}_f = n_f$ is imposed. Zhu et al. [99] circumvented this condition; their approach also relies on linear matrix inequalities to build an intermediate estimator, instead of imposing that there are no invariant zeros between the fault and output of

the linear part of the system. More classical results rely on adaptive high-gain observers [100], where the additive fault is assumed to be the sum of known function templates whose weights are to be estimated.

2.4.3 Multiplicative Faults

Faults are often better represented by changes in system parameters or unexpected dynamics that enter the system. It is more appropriate to model such faults as signals that multiply the system's signals, such as inputs, outputs, and internal states. van der Ploeg et al. [86] and de Albuquerque Gleizer et al. [63] addressed the estimation of multiplicative faults under the DAE framework. The combined approaches enable the estimation of faults represented as

$$\Big(\boldsymbol{H}(\mathfrak{q})+\sum_{i=1}^{m} f_i^{\mathrm{m}}\boldsymbol{H}_i'(\mathfrak{q})\Big)\xi+\Big(\boldsymbol{L}(\mathfrak{q})+\sum_{i=1}^{m} f_i^{\mathrm{m}}\boldsymbol{L}_i'(\mathfrak{q})\Big)\boldsymbol{z}+\boldsymbol{F}(\mathfrak{q})(\boldsymbol{f}^{\mathrm{a}}+E(\boldsymbol{z})\boldsymbol{f}^{\mathrm{m}})+\boldsymbol{W}(\mathfrak{q})\boldsymbol{w}=\boldsymbol{0}, \quad (2.23)$$

where $\boldsymbol{f}^{\mathrm{m}}$ and $\boldsymbol{f}^{\mathrm{a}}$ represent multiplicative and additive faults, respectively. In much of the literature, multiplicative faults are recast as intermediate additive faults. For example, instead of trying to separately estimate $\boldsymbol{f}^{\mathrm{a}}$ and $\boldsymbol{f}^{\mathrm{m}}$, one may choose to estimate the combined signal $\boldsymbol{f}' \coloneqq \boldsymbol{f}^{\mathrm{a}} + E(\boldsymbol{z})\boldsymbol{f}^{\mathrm{m}}$, and at a later stage distinguish the individual components. This approach, however, can make the estimation problem infeasible. Suppose, for example, that only one scalar multiplicative fault is modeled, with $\boldsymbol{H}'(\mathfrak{q}) = \boldsymbol{0}$ and $f^{\mathrm{m}}\boldsymbol{L}'(\mathfrak{q})\boldsymbol{z} = \begin{bmatrix} f^{\mathrm{m}}u & f^{\mathrm{m}}y_1 & f^{\mathrm{m}}y_2 \end{bmatrix}\top$. By simply recasting $f_1^{\mathrm{a}} \coloneqq f^{\mathrm{m}}u$, $f_2^{\mathrm{a}} \coloneqq f^{\mathrm{m}}y_1$, and $f_3^{\mathrm{a}} \coloneqq f^{\mathrm{m}}y_2$, one must estimate three fault signals instead of one, which, in fact, is structurally infeasible if the system has only two outputs. In addition to these technical challenges, estimating the multiplicative component is generally more informative than estimating the combined fault signal.

Multiplicative fault estimation poses distinct challenges. Even with knowledge of $E(\boldsymbol{z})$, it is not possible to separate the individual contributions from additive and multiplicative components of $\boldsymbol{f}^{\mathrm{a}} + E(\boldsymbol{z})\boldsymbol{f}^{\mathrm{m}}$ without extra assumptions about the fault signals, such as frequency content. Furthermore, the multiplicative nature of the fault signal makes the map from $\boldsymbol{f}^{\mathrm{m}}$ to the residual a nonlinear map, thus requiring nonlinear components in the estimation design. Van der Ploeg et al. [53] assumed that the faults are piecewise constant; and [63] [63], extended this work to the case where the faults are a combination of known time signals—i.e., $f_i^{\mathrm{m,a}}(t) = \sum_j p_{ij}\phi_{ij}(t)$, where p_{ij} are parameters to be identified. This includes polynomial functions, which represent an ultralocal approach. The fault estimation method proposed by Van der Ploeg et al. [53] and de Albuquerque Gleizer et al. [63] involves three main components as depicted in Figure 2.3: a residual generator, a so-called *regressor generator*, and a regression block. To explain the concept, consider the case of (piecewise) constant faults and one additive fault, where all faults only multiply known signals, i.e., $\boldsymbol{H}_i'(\mathfrak{q}) = \boldsymbol{0}$ for all i. Let $\boldsymbol{z}' \coloneqq E(\boldsymbol{z})$ be the result of the nonlinearity applied to the known signals $\boldsymbol{z}$. Then, referring back to Equation (2.23), we can see that if $\boldsymbol{N}(\mathfrak{q})\boldsymbol{H}(\mathfrak{q}) = \boldsymbol{0}$, then the residual described by $a(\mathfrak{q})r = -\boldsymbol{N}(\mathfrak{q})\boldsymbol{L}(\mathfrak{q})\boldsymbol{z}$ satisfies

$$r = a(\mathfrak{q})^{-1}\boldsymbol{N}(\mathfrak{q})\Big(\sum_i (\boldsymbol{G}_i'(\mathfrak{q})\boldsymbol{z}+\boldsymbol{F}(\mathfrak{q})\boldsymbol{z}')f_i^{\mathrm{m}}+\boldsymbol{F}(\mathfrak{q})f^{\mathrm{a}}\Big) =: \sum_{i=1}^{m} f_i^{\mathrm{m}}\boldsymbol{M}_i^{\mathrm{m}}(\mathfrak{q})\begin{bmatrix}\boldsymbol{z}\\ \boldsymbol{z}'\end{bmatrix} + f^{\mathrm{a}}\boldsymbol{M}^{\mathrm{a}}(\mathfrak{q})\boldsymbol{1}, \quad (2.24)$$

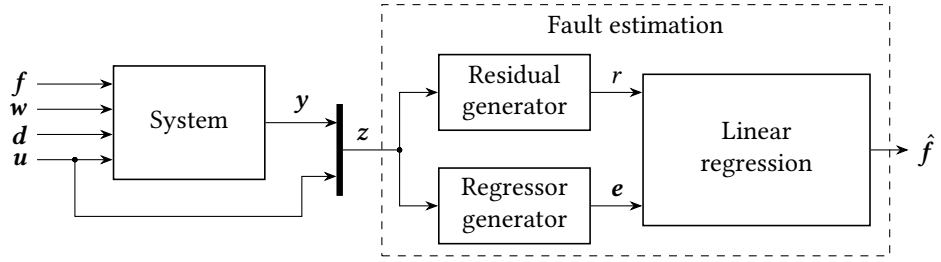

Figure 2.3: Fault estimation diagram for multiplicative faults. The regressor generator produces signals e_i representing the contribution of a unit fault. A moving-horizon linear regression computes the fault estimates $\hat{\boldsymbol{f}}$.

where $\boldsymbol{G}_i(\mathfrak{q}) = \boldsymbol{L}_i'(\mathfrak{q})$ for all $i = 1, \dots, m$, and $\mathbf{1}(t) \equiv 1$ is the constant signal equal to 1. That is, the residual is a linear combination, weighted by the faults, of the output of multiple linear filters of the signals $\boldsymbol{z}$, $\boldsymbol{z}' = E(\boldsymbol{z})$, and $\mathbf{1}$. The outputs are collected in the signal $\boldsymbol{e}$ in Figure 2.3. With this, a linear regression can be performed from $\boldsymbol{e}$ to r over a user-specified time horizon to retrieve the fault estimates $\hat{\boldsymbol{f}}$. When $\boldsymbol{H}_i'(\mathfrak{q}) \not\equiv \mathbf{0}$ (i.e., the faults also multiply functions of the latent variables $\boldsymbol{x}$), Equation (2.24) holds approximately provided that the matrix $\boldsymbol{H}(\mathfrak{q})$ admits a polynomial left inverse and includes extra terms in $\boldsymbol{G}_i'(\mathfrak{q})$ (see [63]).

2.4.4 Active Methods and Input Design

For linear systems with perfect model information, the performance of additive fault estimation does not depend on the input. This is not the case in the presence of model uncertainties or multiplicative faults. Similar to the multimodel isolation case (Section 2.3.2), active methods can dramatically improve diagnosis performance.

Tan et al. [105] used a set-based approach to address the input design of additive faults in linear parameter-varying systems with inexact scheduling variables. In such a case, the optimal input tries to concentrate the system behavior where the scheduling variable uncertainty is the least. The one-step-ahead problem is non-convex, but the global optimal input can be computed by solving 2^{n_u} quadratic programs. The authors also investigated how to combine fault estimation and mitigation within the same framework.

Considering the estimation framework in Section 2.4.3, de Albuquerque Gleizer et al. [63] proposed an input design method for multiplicative fault estimation and found that it requires that the regressors be persistently exciting of sufficiently high order. Moreover, when the noise $\boldsymbol{w}$ is nonzero, the bias and variance of the estimation decrease as the richness of the regressor signal increases. The authors proposed designing $\boldsymbol{u}$ to maximally excite the regressor $\boldsymbol{e}$, which is a non-convex problem; therefore, local optimization methods are exploited, together with a convex relaxation to provide sub-optimality bounds.

2.4.5 Model-Free Approaches

Most of the literature on model-free (or data-driven) fault estimation considers LTI systems and assumes that a fault-free dataset is initially available. This essentially allows a model to be identified either directly or indirectly. Referring to the state-space description in Equation (2.2), one can adopt a similar fault modeling approach to that in Section 2.3.3—i.e., if the class of faults is restricted to sensors ($\boldsymbol{B}_f = \mathbf{0}, \boldsymbol{D}_f = \mathbf{I}$), actuators

($B_f = B_u, D_f = D_u$) [121, 122], or load disturbances ($B_f = \mathbf{I}, D_f = \mathbf{0}$) [118], then the full faulty system can be identified from healthy data. Existing literature has addressed this identification problem through system matrices and/or Markov parameters [25, 44, 45], basis functions [122], or behavioral subspaces [26]; Ding [149] provided an overview of the more established methods.

Once a model is (implicitly) identified, model-based methods can be used. A challenge that appears in the data-driven settings, though, is that identification errors can render the left inverse unstable, even when the real system admits stable left inverses. Wan et al. [120] explicitly addressed this challenge and showed how to design stable approximate left inverses for fault estimation by using high-order vector autoregressive with exogenous inputs (VARX) approximations of the Kalman predictor representation of the system. Their method requires the fault–output system to have no non-minimum-phase zeros, an assumption later dropped in a work by Yu and Verhaegen [45]. Challenges related to forward and inverse stability are overcome by designing bilateral finite impulse response approaches (e.g., [122]).

The problem of simultaneously identifying a system and its external input (or fault) has received less attention. Several works have addressed the cases where several assumptions can be imposed on the fault signal, such as being constant, slow-varying, or periodic [116, 118, 129]. The more fundamental problem where no assumptions are made about the fault signal first appeared in a work by Palanthandalam-Madapusi and Bernstein [115]. They used subspace methods to fully estimate ($A, [B_u, B_f], C, [D_u, D_f]$) directly from faulty data, assuming only that the unknown input space dimension is known and the fault–output system is input and state observable. Gleizer [123] recently extended this work and showed that the input–output system can be identified irrespective of the presence of faults and without requiring unknown input observability, provided that the faults are open-loop and the input is random and zero-mean. This work then provides methods that enable finding the smallest unknown input space dimension and the corresponding span of fault matrices (B_f, D_f) that explain the data. These methods are exact in the absence of noise and rely on simple linear algebra, but can suffer from severe noise sensitivity. When considering the fault signals to be a sparse linear combination of known signals, Noom et al. [119] also provided a model-free version, where the identification of system parameters is done simultaneously with the fault identification. This involves a combination of convex relaxations: nuclear norms as a relaxation of the rank for the identification part and the 1-norm as a relaxation of the 0-norm (sparsity) for the fault part. Liu et al. [130] suggested using a fuzzy model to design an adaptive filter for a class of Lipschitz nonlinear systems.

2.5 Summary and Future Issues

The main insights from this survey can be summarized along three dimensions:

1. **Problems and scalable solutions.** Classical fault detection, isolation, and estimation problems can be studied within a unified framework based on differential-algebraic system descriptions. This perspective reveals connections among alternative system representations and enables scalable diagnosis filter design through convex optimization, including for nonlinear systems.

2. **Geometric interpretation.** Geometric interpretations connect the underlying diagnosis problems to general classification problems, providing a deeper understanding of their structure and suggesting alternative solution approaches.

3. **Active and model-free design.** Recent developments in active and model-free fault diagnosis offer promising directions for advancing the field, although both are still underexplored.

According to this survey, several open issues and promising research directions merit further investigation:

- **Computational scalability in active design.** A formidable challenge in active design is the inherent nonconvexity of the resulting optimization problems. Recent developments in nonconvex optimization algorithms (e.g., distributed optimization) can be helpful in this direction.

- **New robust design paradigms.** Robust fault diagnosis often leads to conservative designs. Promising directions to alleviate this conservatism include game-theoretic and distributionally robust optimization approaches.

- **Direct model-free design.** Most data-driven methods in fault diagnosis still rely on a two-step approach, although direct data-driven design has only recently begun to emerge in the diagnosis. However, performance characterization of direct approaches under noisy conditions is still missing. Furthermore, access to fault-free data is often a prerequisite in these approaches, which may not be available in certain applications.

3

Data-Driven Fault Detection and Isolation

This chapter studies the problem of fault isolation in linear systems with actuator and sensor faults within a data-driven framework, where fault detection is treated as a special case. We propose a null-space-based diagnosis filter that uses solely fault-free input–output data collected under process and measurement noises. By reparameterizing the problem within a behavioral framework, we achieve a direct fault isolation filter design that is independent of any explicit system model. The underlying classification problem is approached from a geometric perspective, enabling a characterization of mutual fault discernibility in terms of fundamental system properties given a noise-free setting. In addition, the provided conditions can be evaluated using only the available data. Finally, a simulation study is conducted to demonstrate the effectiveness of the proposed method.

This chapter is partly based on *Data-Driven Fault Isolation in Linear Time-Invariant Systems: A Subspace Classification Approach* [68].

3.1 Introduction

Fault detection and isolation are essential components of modern health monitoring systems. Identifying the root cause of faulty behavior, as the primary task in fault isolation, enables corrective actions and mitigation strategies tailored to the specific fault type.

To assess the operational state of a system, diagnosis filters should block the influence of all external inputs on the system output except for the fault signal. The resulting residual signal can be generated using either model-based or data-driven approaches (see Section 2.3). In the data-driven setting—the focus of this chapter—behavioral methods based on Willems' *fundamental lemma* [135] enable direct parameterization of the diagnosis filter from fault-free training data without requiring explicit system identification[27]. Classical data-driven methods, on the other hand, rely on system identification followed by model-based diagnosis filter design [24, 40, 58, 132]. Two commonly used system representations in this context are differential-algebraic equations [40, 58] and kernel representations [24, 60, 108].

Unknown input observers are a class of observer-based diagnosis filters that solve an input-decoupling problem to generate the residual signal [34, 74]. The behavioral approach has recently been employed in [151] to develop a data-driven unknown input observer. Another important family of diagnosis filters is based on null space [40, 51], [112], which we build upon in this work. These methods exploit the left null space of the extended observability matrix to filter out the contribution of the system internal states to the output. Parity-space-based approaches also belong to this category [24, 73]. In linear systems, it can be shown that the null-space-based filters and unknown input observers are equivalent under certain conditions [137]. Following these methods, a bank of filters can be designed for fault isolation by ensuring that each filter is sensitive to only one specific fault rather than all faults (see, e.g., [58, 60]). Subsequent works primarily focus on optimizing the threshold setting in diagnosis filters, such as the work of [101], which considers a distributionally robust approach to improve the robustness.

While the theoretical foundations of null-space-based fault isolation filters have been extensively studied (e.g., [5, 40, 132]), their performance limits in a data-driven setting remain largely unexplored; more importantly, fault discernibility is not fully understood. Additionally, state-of-the-art bank-of-filters approaches, which rely on scalar residual signals, may impose limitations on filter performance [60], including the infeasibility of designing dedicated filters in certain cases. This chapter bridges these gaps within a data-driven framework.

Contributions. A geometric approach based on behavioral null spaces is proposed to design a fault isolation scheme for both sensor and actuator faults. Instead of scalar residuals, a multidimensional residual signal is constructed, which fully exploits the available analytical redundancy. The resulting classification problem is formulated in a high-dimensional measurement space, where each hyperplane corresponds to a specific fault. In this setting, fault discernibility can be characterized through the intersection properties of these hyperplanes under a noise-free condition. Furthermore, it is shown that fault signals associated with transmission zeros of certain subsystems are inherently indiscernible, causing isolation ambiguities. Notably, the indiscernible fault subspaces can be identified directly from data.

3.2 Null-Space-Based Residual Generation

In this section, we develop a null-space-based residual generation method for linear systems subject to additive faults, without having access to the underlying system matrices. The proposed method is based on the behavioral approach, which allows for direct derivation of the filter parameters. We assume healthy input–output data are available in the presence of process and measurement noises. The following subsections provide the necessary background and details of the proposed method.

3.2.1 System

A general discrete-time finite-dimensional linear time-invariant (LTI) system, in the presence of additive faults, can be represented in the following innovation form [146]

$$\begin{aligned} \boldsymbol{x}(t+1) &= \boldsymbol{A}\boldsymbol{x}(t) + \boldsymbol{B}_u\boldsymbol{u}(t) + \boldsymbol{B}_f\boldsymbol{f}(t) + \boldsymbol{K}\boldsymbol{e}(t), \quad \boldsymbol{x}(0) = \boldsymbol{x}_0, \\ \boldsymbol{y}(t) &= \boldsymbol{C}\boldsymbol{x}(t) + \boldsymbol{D}_u\boldsymbol{u}(t) + \boldsymbol{D}_f\boldsymbol{f}(t) + \boldsymbol{e}(t), \end{aligned} \tag{3.1}$$

where the tuple $(\boldsymbol{A}, [\boldsymbol{B}_u, \boldsymbol{B}_f], \boldsymbol{C}, [\boldsymbol{D}_u, \boldsymbol{D}_f])$ represents a minimal state-space realization of the system matrices with appropriate dimensions. The state vector $\boldsymbol{x}(t)$ is n-dimensional, corresponding to the order of the system and $t \in \mathbb{Z}_{\geq 0}$. The input, output, and fault signals are denoted by $\boldsymbol{u}(t) \in \mathbb{R}^{n_u}$, $\boldsymbol{y}(t) \in \mathbb{R}^{n_y}$, and $\boldsymbol{f}(t) \in \mathbb{R}^{n_f}$, respectively. $\boldsymbol{K} \in \mathbb{R}^{n \times n_y}$ is a steady-state Kalman gain, and $\boldsymbol{e}(t) \in \mathbb{R}^{n_y}$ is the stochastic innovation process. The ith fault component can be modeled as either a sensor or an actuator fault as follows:

$$\begin{aligned} &j\text{th actuator fault: } \boldsymbol{B}_f^{[i]} = \boldsymbol{B}_u^{[j]}, \quad \boldsymbol{D}_f^{[i]} = \boldsymbol{D}_u^{[j]}, \\ &j\text{th sensor fault: } \boldsymbol{B}_f^{[i]} = \boldsymbol{0}, \quad \boldsymbol{D}_f^{[i]} = \mathbf{I}_{n_y}^{[j]}, \end{aligned} \tag{3.2}$$

where superscripts $[i]$ and $[j]$ refer to the ith and jth columns of the associated matrices. Next, we define the required definitions and assumptions for our method.

Definition 3.1 (Left-invertibility, [84])**.** A system defined by an $n_y \times n_u$ proper transfer function $G(\mathfrak{q}) := \boldsymbol{C}(\mathfrak{q}\mathbf{I} - \boldsymbol{A})^{-1}\boldsymbol{B}_u + \boldsymbol{D}_u$ is τ-delay left invertible if there exists an $n_u \times n_y$ proper transfer function $G_\tau^+(\mathfrak{q})$ such that $G_\tau^+(\mathfrak{q})G(\mathfrak{q}) = \mathfrak{q}^{-\tau}\mathbf{I}_{n_u}$ for almost all $\mathfrak{q} \in \mathbb{C}$ and nonnegative integer τ. If one such τ exists, the system is simply called left invertible. Lastly, the smallest nonnegative integer τ for which the system is left invertible is called the relative degree of the system.

Proposition 3.1 ([84, Theorem 1])**.** *The following statements are equivalent:*

(i) The system $(\boldsymbol{A}, \boldsymbol{B}_u, \boldsymbol{C}, \boldsymbol{D}_u)$ is left invertible.

(ii) $\operatorname{rank}\begin{bmatrix} \boldsymbol{A} - \mathfrak{q}\mathbf{I} & \boldsymbol{B}_u \\ \boldsymbol{C} & \boldsymbol{D}_u \end{bmatrix} = n + n_u$ *for almost all* $\mathfrak{q} \in \mathbb{C}$.

Assumption 3.1. The fault subsystem $(\boldsymbol{A}, \boldsymbol{B}_f, \boldsymbol{C}, \boldsymbol{D}_f)$ is τ-delay left invertible.

A necessary condition for left invertibility is the number of outputs being greater than or equal to the number of inputs. Therefore, Assumption 3.1 implies that $n_y \geq n_f \geq 2$, as

the problem concerns fault isolation. Using Theorem 3.1, we can verify the left invertibility of the fault subsystem by checking the rank condition on the system matrices; in other words, we have

$$\operatorname{rank}\begin{bmatrix} A-\mathfrak{q}\mathbf{I} & B_f \\ C & D_f \end{bmatrix} = n + n_f \quad \text{for almost all } \mathfrak{q} \in \mathbb{C}.$$

Let the notation $\mathbf{w}_{[t_1,t_2]} \coloneqq [\boldsymbol{w}^\top(t_1) \quad \boldsymbol{w}^\top(t_1+1) \quad \cdots \quad \boldsymbol{w}^\top(t_2)]^\top$ describe a time window of data points associated with an arbitrary signal $\boldsymbol{w}(t)$. The measurements over a sliding window of length L are given by the following data equation

$$\mathbf{y}_{[t,t+L-1]} = \mathbf{O}_L \boldsymbol{x}(t) + \mathbf{T}_L^u \mathbf{u}_{[t,t+L-1]} + \mathbf{T}_L^f \mathbf{f}_{[t,t+L-1]} + \mathbf{T}_L^e \mathbf{e}_{[t,t+L-1]} \tag{3.3}$$

in which $\mathbf{O}_L$ represents the extended observability and $\boldsymbol{T}_L^\star$ is the lower triangular block-Toeplitz matrix structured as

$$\mathbf{O}_L = \begin{bmatrix} C \\ CA \\ \vdots \\ CA^{L-1} \end{bmatrix}, \quad \mathbf{T}_L^\star = \begin{bmatrix} \boldsymbol{M}_0^\star & \mathbf{0} & \cdots & \mathbf{0} \\ \boldsymbol{M}_1^\star & \boldsymbol{M}_0^\star & \ddots & \vdots \\ \vdots & \vdots & \ddots & \mathbf{0} \\ \boldsymbol{M}_{L-1}^\star & \boldsymbol{M}_{L-2}^\star & \cdots & \boldsymbol{M}_0^\star \end{bmatrix}$$

with $\star$ representing u, f, or e. The corresponding Markov parameters are given by

$$\boldsymbol{M}_i^u = \begin{cases} D_u & i=0 \\ CA^{i-1}B_u & i>0 \end{cases}, \boldsymbol{M}_i^f = \begin{cases} D_f & i=0 \\ CA^{i-1}B_f & i>0 \end{cases}, \boldsymbol{M}_i^e = \begin{cases} \mathbf{I}_{n_y} & i=0 \\ CA^{i-1}K & i>0 \end{cases}.$$

Let N represent the total number of samples in the dataset. Denote by $\overiii{\mathbf{W}}_{t,L,N}$ the corresponding Hankel matrix of an arbitrary signal $\boldsymbol{w}(t)$, and by $\mathbf{X}_{[t_1,t_2]}$ the sequence of system states over time interval $[t_1,t_2]$. The Hankel format of the data equation (3.3) is obtained by

$$\overiii{\mathbf{Y}}_{t,L,N} = \mathbf{O}_L \mathbf{X}_{[t,t+N-L]} + \mathbf{T}_L^u \overiii{\mathbf{U}}_{t,L,N} + \mathbf{T}_L^f \overiii{\mathbf{F}}_{t,L,N} + \mathbf{T}_L^e \overiii{\mathbf{E}}_{t,L,N}, \tag{3.4}$$

leading to

$$\begin{bmatrix} \overiii{\mathbf{U}}_{t,L,N} \\ \overiii{\mathbf{Y}}_{t,L,N} \end{bmatrix} = \mathbf{G}_L \begin{bmatrix} \overiii{\mathbf{U}}_{t,L,N} \\ \mathbf{X}_{[t,t+N-L]} \end{bmatrix} + \begin{bmatrix} \mathbf{0} \\ \mathbf{T}_L^f \overiii{\mathbf{F}}_{t,L,N} + \mathbf{T}_L^e \overiii{\mathbf{E}}_{t,L,N} \end{bmatrix}, \tag{3.5}$$

with $\mathbf{G}_L \coloneqq \begin{bmatrix} \mathbf{I} & \mathbf{0} \\ \mathbf{T}_L^u & \mathbf{O}_L \end{bmatrix}$, providing a compact representation of the underlying fault/noise-free system.

3.2.2 Residual

Null-space-based diagnosis filter design requires identifying the left null space of $\mathbf{G}_L$ from the given fault-free input–output data $\{\boldsymbol{u}(t), \boldsymbol{y}(t)\}_{t=0}^{N-1}$. This subspace is described by $\mathbf{K}_L$,

i.e., $\operatorname{im}\mathbf{K}_L^\top = \ker \mathbf{G}_L^\top$. Behavioral system theory gives that, for any healthy noise-free trajectory of the system, the *kernel representation* is given by [134]

$$\forall \mathbf{u}_{[t,t+L-1]}, \boldsymbol{x}(t), \quad \mathbf{K}_L \begin{bmatrix} \mathbf{u}_{[t,t+L-1]} \\ \mathbf{y}_{[t,t+L-1]} \end{bmatrix} = \mathbf{0}, \text{ and } \mathbf{K}_L \begin{bmatrix} \hat{\mathbf{U}}_{t,L,N} \\ \hat{\mathbf{Y}}_{t,L,N} \end{bmatrix} = \mathbf{0}. \tag{3.6}$$

By partitioning $\mathbf{K}_L$ into $[\mathbf{K}_L^u \quad \mathbf{K}_L^y]$ and using (3.5), the following relationships hold:

$$\mathbf{K}_L^y \mathbf{O}_L = \mathbf{0} \Longleftrightarrow \operatorname{im}(\mathbf{K}_L^y)^\top = \ker \mathbf{O}_L^\top; \quad \mathbf{K}_L^u = -\mathbf{K}_L^y \mathbf{T}_L^u,$$

using the fact that $\mathbf{K}_L \mathbf{G}_L = 0$. $\mathbf{K}_L^y$ is referred to as the parity space in the literature [51]. Rewriting (3.3) into form of (3.5) for $[\mathbf{u}_{[t,t+L-1]}^\top, \mathbf{y}_{[t,t+L-1]}^\top]^\top$, and pre-multiplying by $\mathbf{K}_L$ results in the residual signal

$$\boldsymbol{r}(t) = \mathbf{K}_L \begin{bmatrix} \mathbf{u}_{[t,t+L-1]} \\ \mathbf{y}_{[t,t+L-1]} \end{bmatrix} = \mathbf{K}_L^y (\mathbf{T}_L^f \mathbf{f}_{[t,t+L-1]} + \mathbf{T}_L^e \mathbf{e}_{[t,t+L-1]}).$$

The detection filter, therefore, is entirely designed by obtaining a proper $\mathbf{K}_L$ satisfying (3.6). The subspace represented by $\mathbf{K}_L$ can be consistently estimated when the input–output data are corrupted by noise. For details on designing and optimizing such a detection filter, we refer readers to [60, 101]. However, in this work we focus on the fault isolation task, which follows immediately after the detection.

3.2.3 Subspace Perspective

For any choice of L such that $Ln_y > n$, the extended observability matrix $\mathbf{O}_L$ is row rank-deficient, since the underlying system is of order n. This implies that there exists not only a low-rank subspace in the measurement space $\mathbb{R}^{Ln_y}$, but also a nontrivial null space of dimension of $Ln_y - n$, which plays a central role in the proposed diagnosis filter design. The following example illustrates this low-rank structure.

Example 3.1 (Low-rank structure in the measurement space)**.** Consider an autonomous second-order system with a single output, described by the following state-space representation:

$$\boldsymbol{x}(t+1) = \boldsymbol{A}\boldsymbol{x}(t),\ \boldsymbol{y}(t) = \boldsymbol{C}\boldsymbol{x}(t);\ \text{with}\ \boldsymbol{A} = \begin{bmatrix} 1.81 & -0.9048 \\ 1 & 0 \end{bmatrix},\ \boldsymbol{C} = \begin{bmatrix} 0.048 \\ 0.0464 \end{bmatrix}.$$

Let the horizon length be $L = 3$. Putting the generated system trajectories in the Hankel format gives

$$\hat{\mathbf{Y}}_{0,3,N} = \begin{bmatrix} \boldsymbol{y}(0) & \boldsymbol{y}(1) & & \boldsymbol{y}(N-3) \\ \boldsymbol{y}(1) & \boldsymbol{y}(2) & \cdots & \boldsymbol{y}(N-2) \\ \boldsymbol{y}(2) & \boldsymbol{y}(3) & & \boldsymbol{y}(N-1) \end{bmatrix}.$$

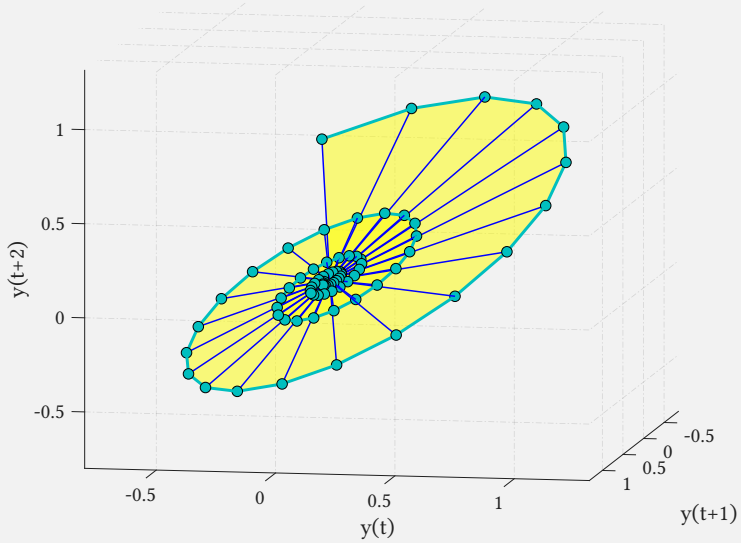

Figure 3.1: The data points (green) generated by the second-order system in Example 3.1 in a three-dimensional measurement space. The points lie in a two-dimensional subspace represented by the yellow plane.

We plot the result in three-dimensional space $\mathbb{R}^3$ where each data point represents $(\boldsymbol{y}(t), \boldsymbol{y}(t+1), \boldsymbol{y}(t+2))$. From Figure 3.1, it can be seen that all data points are residing in a plane. In general, $(\boldsymbol{A}, \boldsymbol{C})$ determines the corresponding hyperplane.

3.3 Fault Isolation Scheme

Given $\mathbf{K}_L$ satisfying (2.16), the resulting residual signal $\boldsymbol{r}(t)$ carries all the system's fault information. One key observation is that $\boldsymbol{r}(t)$ is possibly multidimensional, depending on the nullity of $\mathbf{G}_L^\top$, i.e., $\dim(\ker \mathbf{G}_L^\top)$. In this sense, each row of $\mathbf{K}_L$ acts as a single-output finite-impulse-response detection filter. This fact has been utilized in designing bank of filters in [24, 58], which can discard information. To avoid that, we propose working with the full multidimensional residual signal. With this, we fully exploit the available analytical redundancy, and the number of rows in $\mathbf{K}_L$ determines the degree of freedom in the design.

By the block triangular structure of $\mathbf{G}_L$, it is easy to show $\dim(\ker \mathbf{G}_L^\top) = \dim(\ker \mathbf{O}_L^\top)$. Moreover, by examining the observability index, we can choose a sufficiently large horizon L to ensure a nontrivial $\ker \mathbf{O}_L^\top$ exists. This is given in the following proposition:

Proposition 3.2. *Let n_o be the observability index of $(\boldsymbol{A}, \boldsymbol{C})$. For $L > n_\mathrm{o}$, there exists a matrix $\mathbf{K}_L^y \in \mathbb{R}^{(Ln_y - n) \times Ln_y}$ with full row rank such that $\mathbf{K}_L^y \mathbf{O}_L = \mathbf{0}$.*

For the sake of brevity, we develop the foundations in this section without considering

noise, i.e., $\boldsymbol{e}(t) = \mathbf{0}$. The effect of noise is empirically investigated in Section 3.6.

By choosing L according to Proposition 3.2, the multidimensional residual signal at time instant t satisfies

$$\boldsymbol{r}(t) = \mathbf{K}_L^y \mathbf{T}_L^f \mathbf{f}_{[t,t+L-1]}. \tag{3.7}$$

This implies that the residual signal belongs to the column space of $\mathbf{K}_L^y \mathbf{T}_L^f$ through the linear map $\Phi : \mathbb{R}^{Ln_f} \to \mathbb{R}^{Ln_y - n}$, where $\Phi(x) \coloneqq \mathbf{K}_L^y \mathbf{T}_L^f x$. Thus, the residual signal is a linear combination of fault signals present in the system, i.e.,

$$\boldsymbol{r}(t) = \sum_{i=1}^{n_f} \mathbf{K}_L^y \mathbf{T}_L^{f_i} \mathbf{f}_{[t,t+L-1]}^{(i)},$$

where the column vector $\mathbf{f}_{[t,t+L-1]}^{(i)}$ contains only the values of the ith fault signal over the filter horizon, and $\mathbf{T}_L^{f_i}$ denotes the corresponding block-Toeplitz matrix.

3.3.1 Fault Dictionaries

In this section, we show how to construct $\pi_L^{(i)}$ from of input–output data in a data-driven FI framework. First, the fault block-Toeplitz matrix $\mathbf{T}_L^f$ is expressed based on (3.2). Then, we show how these bases are transformed by pre-multiplying them with $\mathbf{K}_L^y$. To do so, the range of $\mathbf{T}_L^u$ is needed to be recovered from the fault-free input–output data.

Assumption 3.2 (Data rank condition)**.** The healthy data $\{\boldsymbol{u}(t), \boldsymbol{y}(t)\}_{t=0}^{N-1}$ is recorded such that

$$\operatorname{rank}\begin{bmatrix} \mathbf{X}_{[0,N-L]} \\ /\!/ \\ \mathbf{U}_{0,L,N} \end{bmatrix} = n + Ln_u.$$

Remark 3.1. In practice, Assumption 3.2 can be ensured when the data is collected in open-loop using an input signal $\boldsymbol{u}(t)$ that is persistently exciting (PE) of sufficient order [146].

Proposition 3.3. *Suppose the input signal satisfies Assumption 3.2. Given fault- and noise-free data* $\{\boldsymbol{u}(t), \boldsymbol{y}(t)\}_{t=0}^{N-1}$*, we have* $\operatorname{im}(\mathbf{K}_L^y)^\top = \ker \boldsymbol{L}_{22}^\top$ *and* $\mathbf{K}_L^y \mathbf{T}_L^u = \mathbf{K}_L^y \boldsymbol{L}_{21} \boldsymbol{L}_{11}^{-1}$ *where* $\boldsymbol{L}_{11}$*,* $\boldsymbol{L}_{21}$ *and* $\boldsymbol{L}_{22}$ *are derived from the following LQ decomposition*

$$\begin{bmatrix} /\!/ \\ \mathbf{U}_{0,L,N} \\ /\!/ \\ \mathbf{Y}_{0,L,N} \end{bmatrix} = \begin{bmatrix} \boldsymbol{L}_{11} & \mathbf{0} \\ \boldsymbol{L}_{21} & \boldsymbol{L}_{22} \end{bmatrix} \begin{bmatrix} \boldsymbol{Q}_1^\top \\ \boldsymbol{Q}_2^\top \end{bmatrix}.$$

Proof. See Appendix A. ∎

Looking at the definition of fault matrices (3.2), we observe that the columns of $\mathbf{T}_L^u$ and $\mathbf{I}_{n_y}$ serve as the building blocks of $\mathbf{T}_L^f$. That is, $\operatorname{im} \mathbf{T}_L^f \subseteq \operatorname{im} \mathbf{T}_L^u$ in case of faulty actuators, as well as $\operatorname{im} \mathbf{T}_L^f \subseteq \operatorname{im}(\mathbf{I}_L \otimes \mathbf{I}_{n_y})$ for faulty sensors.

Let $\mathbf{T}_L^{\mathrm{a}_i}$ and $\mathbf{T}_L^{\mathrm{s}_i}$ represent the *signatures* of the ith actuator fault and sensor fault, respectively, and define them as

$$\mathbf{T}_L^{\mathrm{a}_i} = \left(\boldsymbol{L}_{21}\boldsymbol{L}_{11}^{-1}\right)_{\Omega_{\mathrm{a},i}}; \mathbf{T}_L^{\mathrm{s}_i} = \left(\mathbf{I}_L \otimes \mathbf{I}_{n_y}\right)_{\Omega_{\mathrm{s},i}},$$
$$\Omega_{\mathrm{a},i} = \{k \in \mathbb{Z}_{>0} \,:\, k = i + t\,n_u,\, t \in \mathbb{N}_0,\, k \le (L-1)n_u + i\},$$
$$\Omega_{\mathrm{s},i} = \{k \in \mathbb{Z}_{>0} \,:\, k = i + t\,n_y,\, t \in \mathbb{N}_0,\, k \le (L-1)n_y + i\},$$

where sets $\Omega_{\mathrm{a},i}$ and $\Omega_{\mathrm{s},i}$ specify the columns to be selected from the corresponding matrices. Then, we introduce *fault dictionaries* as

$$\text{Dictionary} : \begin{cases} \mathbf{D}_L^{\mathrm{a}_i} = \mathbf{K}_L^y \mathbf{T}_L^{\mathrm{a}_i}; & \text{if } i\text{th actuator is faulty,} \\ \mathbf{D}_L^{\mathrm{s}_i} = \mathbf{K}_L^y \mathbf{T}_L^{\mathrm{s}_i}; & \text{if } i\text{th sensor is faulty,} \end{cases} \tag{3.8}$$

in which $\mathbf{D}_L^{\mathrm{a}_i}, \mathbf{D}_L^{\mathrm{s}_i} \in \mathbb{R}^{(Ln_y-n)\times L}$. The total set of dictionaries are collected in $\mathcal{D}_L = \{\mathbf{D}_L^{\mathrm{a}_i}\}_{i=1}^{n_u} \cup \{\mathbf{D}_L^{\mathrm{s}_i}\}_{i=1}^{n_y}$. In addition, denote by $\mathcal{A} := \{\mathrm{a}_1, \ldots, \mathrm{a}_{n_u}\}$ and $\mathcal{S} := \{\mathrm{s}_1, \ldots, \mathrm{s}_{n_y}\}$ the sets of actuators and sensors, respectively. Note that learning the dictionaries uses only input–output data, thus not relying on the underlying system matrices.

3.3.2 Geometric Classifier

In the proposed framework, classification takes place in the subspace $\mathbb{R}^{Ln_y-n}$. In this space, hyperplane i corresponds to the span of the columns in $\mathbf{D}_L^{(i)} \in \mathcal{D}_L$. The residual signal is expected to belong to the subspace that shares the same basis vectors as π_L; that is, if only one fault is active, the signal should lie entirely within the corresponding subspace for an appropriate choice of L. The geometry of the problem suggests that projecting the residual signal onto each hyperplane should provide the necessary information for classification. In other words, the angle between the residual signal and its projection serves as the primary decision variable in the proposed classifier (see Fig 3.2). As a result, the problem can be formulated as

$$\cos\theta_t^{(i)} = \frac{\langle \boldsymbol{r}(t), \mathbf{P}_{\mathbf{D}_L^{(i)}}[\boldsymbol{r}(t)]\rangle}{\|\boldsymbol{r}(t)\|\,\|\mathbf{P}_{\mathbf{D}_L^{(i)}}[\boldsymbol{r}(t)]\|}, \tag{3.9}$$

with $\mathbf{P}_{\mathbf{D}_L^{(i)}}[\boldsymbol{r}(t)] := \mathbf{D}_L^{(i)}(\mathbf{D}_L^{(i)^\top}\mathbf{D}_L^{(i)})^{-1}\mathbf{D}_L^{(i)^\top}\boldsymbol{r}(t)$. The multidimensional time-varying signal $\boldsymbol{\theta}(t)$ is defined as $\boldsymbol{\theta}(t) := [\theta_t^{(1)} \quad \ldots \quad \theta_t^{(n_u+n_y)}]^\top$. To simplify the exposition, we assume that only *a single fault is present* at time instant t (i.e., $n_f = 1$), and the classifier is proposed as

$$\text{faulty mode} := \arg \max_{i=1,\ldots,n_u+n_y} \cos\theta_t^{(i)}; \qquad 0 \le \theta_t^{(i)} \le \pi/2.$$

Note that $\cos x$ is monotone in the closed interval $[0, \frac{\pi}{2}]$.

Remark 3.2. The classifier can be extended to handle simultaneous faults, provided the fault subsystem remains left-invertible. This is done by iteratively testing combinations of dictionaries using direct sums of their column spaces, until one yields a zero angle.

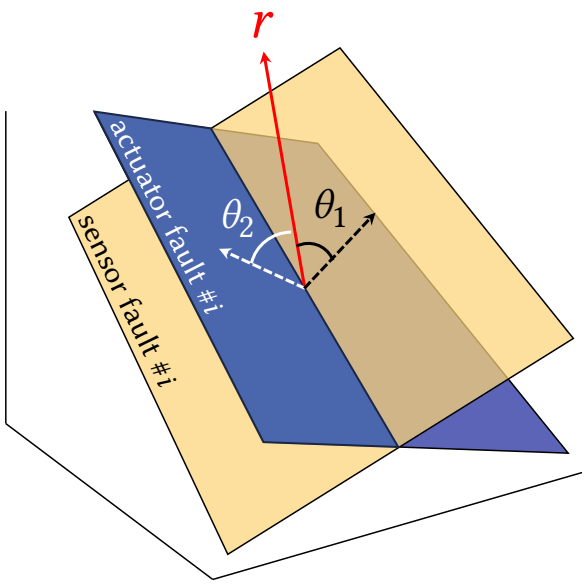

Figure 3.2: Geometric interpretation of the fault isolation problem. Each plane represents a distinct fault subspace in the residual space. At each time instant, the residual vector (red) forms an angle with each candidate fault subspace, and these angles serve as the decision variables for the proposed classification method.

3.4 Fault Discernibility

By introducing the FI scheme, we can determine the conditions under which faults can be perfectly isolated and identify the limiting factors. To emphasize its importance, consider the scenario where the system is subject to only one fault. From Figure 3.2, it follows that if the resulting residual signal resides exactly on the intersection of two planes, the angles will be zero for both possible faults. Consequently, the classifier cannot distinguish between them. In the following, we establish the link between fault discernibility and hyperplane intersections based on the filter horizon and the dynamical system properties.

First, we formally define the concept of *mutual discernibility of faults* in terms of the system output behavior.

Definition 3.2 (Mutual discernibility)**.** Let $\boldsymbol{f}^1(t) \in \mathbb{R}^{n_1}$ and $\boldsymbol{f}^2(t) \in \mathbb{R}^{n_2}$ be two nonzero fault signals with $\boldsymbol{f}^1(t) \neq \boldsymbol{f}^2(t)$. $\boldsymbol{f}^1(t)$ and $\boldsymbol{f}^2(t)$ are said to be indiscernible for a given L if there exist $\boldsymbol{x}^1(t), \boldsymbol{x}^2(t)$ such that $\mathbf{y}^2_{[t,t+L-1]} = \mathbf{y}^2_{[t,t+L-1]}$, where $\mathbf{y}^i_{[t,t+L-1]} = \mathbf{O}_L \boldsymbol{x}^i(t) + \mathbf{T}^u_L \mathbf{u}_{[t,t+L-1]} + \mathbf{T}^{f_i}_L \mathbf{f}^i_{[t,t+L-1]} + \mathbf{T}^e_L \mathbf{e}_{[t,t+L-1]}$. Otherwise, $\boldsymbol{f}^1(t)$ and $\boldsymbol{f}^2(t)$ are discernible.

Assumption 3.3 (Minimality of fault subsystem)**.** The fault subsystem $(\boldsymbol{A}, \boldsymbol{B}_f, \boldsymbol{C}, \boldsymbol{D}_f)$ is minimal with order n.

Next, the null space of $\begin{bmatrix} \mathbf{O}_L & \mathbf{T}^f_L \end{bmatrix}$ is related to the transmission zeros of the fault subsystem, as shown in [158]:

Theorem 3.4. *Suppose Assumption 3.3 holds. Let τ be the smallest integer such that $(\boldsymbol{A}, \boldsymbol{B}_f, \boldsymbol{C}, \boldsymbol{D}_f)$ is τ-delay left invertible, and ζ be the number of finite and infinite transmission zeros counting multiplicity. Then, if $L \geq \max(\tau, n)$, we have* $\dim(\ker \begin{bmatrix} \mathbf{O}_L & \mathbf{T}_L^f \end{bmatrix}) = \zeta$.

Proof. See Appendix A. ∎

Lemma 3.5. *For any $\boldsymbol{f}_0 \in \mathbb{C}^{Ln_f}$, $\mathbf{K}_L^y \mathbf{T}_L^f \boldsymbol{f}_0 = \mathbf{0}$ if and only if there exists $\boldsymbol{x}_0 \in \mathbb{C}^n$ such that* $\begin{bmatrix} \mathbf{O}_L & \mathbf{T}_L^f \end{bmatrix} \begin{bmatrix} \boldsymbol{x}_0 \\ \boldsymbol{f}_0 \end{bmatrix} = \mathbf{0}$.

Proof. See Appendix A. ∎

A direct consequence of Lemma 3.5 and Theorem 3.4 is

$$\dim(\ker(\mathbf{K}_L^y \mathbf{T}_L^f)) = \dim(\ker \begin{bmatrix} \mathbf{O}_L & \mathbf{T}_L^f \end{bmatrix}) = \zeta, \tag{3.10}$$

where ζ denotes the number of transmission zeros of $(\boldsymbol{A}, \boldsymbol{B}_f, \boldsymbol{C}, \boldsymbol{D}_f)$. Thus, we call a nonzero $\boldsymbol{f}_0$ satisfying Lemma 3.5 a *zero dynamics input*. Moreover, *indiscernible faults* relate to zero dynamics input directions as follows:

Proposition 3.6. *Let $\mathbf{f}^1_{[t,t+L-1]} \neq \mathbf{f}^2_{[t,t+L-1]}$ be indiscernible faults. Denote by $\mathbf{f}^{\text{aug}}_{[t,t+L-1]} := [\boldsymbol{f}^1(t) \quad -\boldsymbol{f}^2(t) \quad \cdots \quad \boldsymbol{f}^1((L-1)n_1) \quad -\boldsymbol{f}^2((L-1)n_2)]^\top$ the augmented fault. Then, $\mathbf{f}^{\text{aug}}_{[t,t+L-1]}$ is the zero dynamics input of the augmented system $(\boldsymbol{A}, [\boldsymbol{B}_f^1, \boldsymbol{B}_f^2], \boldsymbol{C}, [\boldsymbol{D}_f^1, \boldsymbol{D}_f^2])$.*

Proof. See Appendix A. ∎

3.4.1 Intersection of Two Dictionaries

Since a fault cannot be isolated when its residual belongs to two different dictionaries, here we characterize the intersection between two dictionaries. In what follows, we present the necessary lemmas and propositions to quantify the intersection in terms of $\mathbf{O}_L$ and $\mathbf{T}_L^f$, enabling the application of the result in Lemma 3.5.

Lemma 3.7. *Let $\boldsymbol{P}_1 \in \mathbb{R}^{m \times n}$ and $\boldsymbol{P}_2 \in \mathbb{R}^{m \times n}$. Then,* $\dim(\operatorname{im} \boldsymbol{P}_1 \cap \operatorname{im} \boldsymbol{P}_2)$ *is equal to:*

(i) $\operatorname{rank} \boldsymbol{P}_1 + \operatorname{rank} \boldsymbol{P}_2 - \operatorname{rank} [\boldsymbol{P}_1 \quad \boldsymbol{P}_2]$.

(ii) $\dim(\ker [\boldsymbol{P}_1 \quad \boldsymbol{P}_2]) - \dim(\ker \boldsymbol{P}_1) - \dim(\ker \boldsymbol{P}_2)$.

Proof. For the proof of (i), see [159, Fact 3.14.15]. Applying the rank-nullity theorem to (i) gives (ii). ∎

Lemma 3.8. *Let* $\operatorname{im}(\mathbf{K}_L^y)^\top = \ker \mathbf{O}_L^\top$ *and $\boldsymbol{P} \in \mathbb{R}^{Ln_y \times L}$. Then,*

$$\operatorname{rank}(\mathbf{K}_L^y \boldsymbol{P}) = L - \dim(\ker \begin{bmatrix} \mathbf{O}_L & \boldsymbol{P} \end{bmatrix})$$

Proof. See Appendix A. ∎

The following lemma characterizes the common subspace spanned by the columns of two distinct fault dictionaries. For this, let $c, c' \in \mathcal{A} \cup \mathcal{S}$ and assume that $\mathbf{D}_L^c$, $\mathbf{D}_L^{c'}$ with $c \neq c'$ follow (3.8). Define $d_\cap^{c,c'} := \dim\left(\operatorname{im} \mathbf{D}_L^c \cap \operatorname{im} \mathbf{D}_L^{c'}\right)$.

Lemma 3.9. *The dimension of intersection of subspaces* $\mathbf{D}_L^c$ *and* $\mathbf{D}_L^{c'}$ *is given as*

$$d_\cap^{c,c'} = \dim(\ker\begin{bmatrix}\mathbf{O}_L & \mathbf{T}_L^c & \mathbf{T}_L^{c'}\end{bmatrix}) - \dim(\ker\begin{bmatrix}\mathbf{O}_L & \mathbf{T}_L^c\end{bmatrix}) - \dim(\ker\begin{bmatrix}\mathbf{O}_L & \mathbf{T}_L^{c'}\end{bmatrix}). \quad (3.11)$$

Proof. See Appendix A. ∎

Assumption 3.4. The pair $(\boldsymbol{A}, \boldsymbol{C}_{\mathcal{J}_y})$ is observable for any subset $\mathcal{J}_y \subseteq \{1, \ldots, n_y\}$, where $\boldsymbol{C}_{\mathcal{J}_y}$ consists of the rows of $\boldsymbol{C}$ corresponding to the outputs in $\mathcal{J}_y$.

The main result is presented in the following theorem, where the dimension of the intersection is derived for different combination of fault dictionaries. Each case is defined by c and c', denoting either an ith actuator a_i or a ith sensor s_i.

Theorem 3.10. *Suppose that Assumptions 3.1, 3.3 and 3.4 hold, and let* $L \geq n$. *Define* $\mathcal{J}_u \subseteq \{1, \ldots, n_u\}$ *and* $\mathcal{J}_y \subseteq \{1, \ldots, n_y\}$ *to be subsets of the inputs and outputs, respectively. Denote by* ζ^m, $\zeta^{\mathcal{J}_u}$, *and* $\zeta^{m,\mathcal{J}_y}$ *the total number of finite and infinite transmission zeros in the subsystem: from the* m*th input to all outputs, from all inputs in* $\mathcal{J}_u$ *to all outputs, and from the* m*th input to all outputs in* $\mathcal{J}_y$, *respectively. Then, for any two different channels* c *and* c'

$$d_\cap^{c,c'} = \begin{cases} \zeta^{\{i,j\}} - \zeta^i - \zeta^j & \text{if } c = \mathrm{a}_i, c' = \mathrm{a}_j, i \neq j, \\ \zeta^{i,\{1,\ldots,n_y\}\setminus j} & \text{if } c = \mathrm{a}_i, c' = \mathrm{s}_j, \\ 0 & \text{if } c = \mathrm{s}_i, c' = \mathrm{s}_j, i \neq j, n_y > 2, \\ n & \text{if } c = \mathrm{s}_i, c' = \mathrm{s}_j, i \neq j, n_y = 2. \end{cases}$$

Proof. See Appendix A. ∎

Remark 3.3. When the underlying system has only two outputs ($n_y = 2$), the dimension of intersections in all cases of Theorem 3.10 coincides with the system order, i.e., for any two distinct channels $c, c' \in \mathcal{A} \cup \mathcal{S}$, we have $d_\cap^{c,c'} = n$.

3.5 Computing the Diagnosis Filter with Noisy Data

This section provides a numerical approach to compute $\mathbf{K}_L^y$ and fault dictionaries $\mathbf{D}_L^{\mathrm{a}_i}$ when $\boldsymbol{e}(t) \neq \mathbf{0}$. To this end, we need to make the following assumptions for the underlying stochastic setting:

Assumption 3.5. Let $\boldsymbol{x}_0$ be a random vector. The signals $\boldsymbol{x}(t), \boldsymbol{u}(t), \boldsymbol{e}(t)$ are ergodic stochastic processes, where $\boldsymbol{e}(t)$ is zero-mean white noise with covariance matrix Σ_e and uncorrelated with $\boldsymbol{u}(t)$ and $\boldsymbol{x}_0$.

Assumption 3.6. Let $\mathbf{Z}_N$ denote an instrumental variable of compatible dimensions, satisfying the following conditions:

(i) $\lim\limits_{N\to\infty} \frac{1}{N} \overline{\overline{\mathbf{E}}}_{t,L,N} \boldsymbol{P}_{\bar{U}}^{\perp} \mathbf{Z}_N^\top = \mathbf{0}$,

(ii) $\operatorname{rank}\left(\lim\limits_{N\to\infty} \frac{1}{N} \mathbf{X}_{[t,t+N-L]} \boldsymbol{P}_{\bar{U}}^{\perp} \mathbf{Z}_N^\top \right) = n$,

in which $\boldsymbol{P}_U^{\perp}$ is the projection onto the null space of $\overset{/\!/}{\mathbf{U}}_{t,L,N}$, i.e., $\overset{/\!/}{\mathbf{U}}_{t,L,N}\boldsymbol{P}_U^{\perp} = \mathbf{0}$.

We now turn to the asymptotically unbiased computation of the left null space of $\mathbf{O}_L$ and the fault dictionaries, as summarized in the following proposition:

Proposition 3.11. *Let Assumptions 3.5 and 3.6 hold. Given fault-free data* $\{\boldsymbol{u}(t), \boldsymbol{y}(t)\}_{t=0}^{N-1}$ *with* $N \to \infty$, *we have*

$$\operatorname{im}(\mathbf{K}_L^y)^\top = \ker\left(\lim_{N\to\infty} \frac{1}{N} \boldsymbol{L}_{22}\boldsymbol{L}_{32}^\top\right), \quad \mathbf{K}_L^y \mathbf{T}_L^u = \mathbf{K}_L^y \boldsymbol{L}_{31}\boldsymbol{L}_{11}^{-1},$$

where $\boldsymbol{L}_{11}$, $\boldsymbol{L}_{22}$, $\boldsymbol{L}_{31}$, *and* $\boldsymbol{L}_{32}$ *are derived from the following LQ decomposition*

$$\begin{bmatrix} \overset{/\!/}{\mathbf{U}}_{0,L,N} \\ \mathbf{Z}_N \\ \overset{/\!/}{\mathbf{Y}}_{0,L,N} \end{bmatrix} = \begin{bmatrix} \boldsymbol{L}_{11} & \mathbf{0} & \mathbf{0} \\ \boldsymbol{L}_{21} & \boldsymbol{L}_{22} & \mathbf{0} \\ \boldsymbol{L}_{31} & \boldsymbol{L}_{32} & \boldsymbol{L}_{33} \end{bmatrix} \begin{bmatrix} \boldsymbol{Q}_1^\top \\ \boldsymbol{Q}_2^\top \\ \boldsymbol{Q}_3^\top \end{bmatrix}.$$

Proof. See Appendix A. ∎

As a consequence of Proposition 3.11, in order to compute $\mathbf{D}_L^{\mathrm{a}_i}$, we use $\mathbf{T}_L^{\mathrm{a}_i} = \left(\boldsymbol{L}_{31}\boldsymbol{L}_{11}^{-1}\right)_{\Omega_{\mathrm{a},i}}$ in the presence of noise.

Remark 3.4. Define $\mathbf{U}_\mathrm{p} := \overset{/\!/}{\mathbf{U}}_{0,L,N}, \mathbf{U}_\mathrm{f} := \overset{/\!/}{\mathbf{U}}_{L,L,N}, \mathbf{Y}_\mathrm{p} := \overset{/\!/}{\mathbf{Y}}_{0,L,N}, \mathbf{Y}_\mathrm{f} := \overset{/\!/}{\mathbf{Y}}_{L,L,N}$. If the following stochastic persistently exciting condition holds

$$\operatorname{rank} \lim_{N\to\infty} \frac{1}{N} \begin{bmatrix} \mathbf{X}_{[0,N-L]} \\ \overset{/\!/}{\mathbf{U}}_{0,2L,N} \end{bmatrix} \begin{bmatrix} \mathbf{X}_{[0,N-L]}^\top & \overset{/\!/}{\mathbf{U}}_{0,2L,N}^\top \end{bmatrix} = n + 2Ln_u,$$

a practical choice for the instrumental variable in Proposition 3.11 is $\mathbf{Z}_N := \begin{bmatrix} \mathbf{U}_\mathrm{p} \\ \mathbf{Y}_\mathrm{p} \end{bmatrix}$, which satisfies Assumption 3.6. Then, we perform the following decomposition

$$\begin{bmatrix} \mathbf{U}_\mathrm{f} \\ \mathbf{Z}_N \\ \mathbf{Y}_\mathrm{f} \end{bmatrix} = \begin{bmatrix} \boldsymbol{L}_{11} & \mathbf{0} & \mathbf{0} \\ \boldsymbol{L}_{21} & \boldsymbol{L}_{22} & \mathbf{0} \\ \boldsymbol{L}_{31} & \boldsymbol{L}_{32} & \boldsymbol{L}_{33} \end{bmatrix} \begin{bmatrix} \boldsymbol{Q}_1^\top \\ \boldsymbol{Q}_2^\top \\ \boldsymbol{Q}_3^\top \end{bmatrix}.$$

With this choice of $\mathbf{Z}_N$, the left null space computation amounts to [48, Theorem 9.4]

$$\operatorname{im}(\mathbf{K}_L^y)^\top = \ker\left(\lim_{N\to\infty} \frac{1}{\sqrt{N}} \boldsymbol{L}_{32}^\top\right).$$

3.6 Numerical Results

To showcase the theoretical results, we design experiments under both noise free and noise-contaminated conditions. Consider an observable LTI system as follows[1]:

$$A = \begin{bmatrix} 0 & 1 & 0 & 0 \\ 0 & 0 & 1 & 0 \\ 0 & 0 & 0 & 1 \\ -0.136 & 0.956 & -2.406 & 2.580 \end{bmatrix}, \; B_u = \begin{bmatrix} 2.520 \\ 3.147 \\ 2.945 \\ 2.458 \end{bmatrix}$$

$$C = \begin{bmatrix} 1 & 0 & 0 & 0 \\ -0.027 & 0.083 & -0.038 & -0.030 \\ 0.194 & -0.868 & 1.234 & -0.566 \end{bmatrix}, \; D_u = \begin{bmatrix} 1 \\ 1 \\ 1 \end{bmatrix}.$$

In this system, only the channels from the input to the outputs $\{1,3\}$ share a transmission zero at $z = 0.95$, i.e., $\zeta^{1,\{1,3\}} = 1$.

Scenario 1. In a noise-free setting, the considered system is subject to only an actuator fault throughout the simulation. To highlight some of the key findings in Theorem 3.10, it is assumed that the fault dictionaries are computed with nominal values. The input signal is a multi-step signal taking values from $\{1, 2, 1.5\}$. We aim to design a fault signal that leads to an isolation confusion. To this end, consider the fault signal as

$$f(t) := \begin{cases} 0 & \text{if } t < 10, \\ \sin(0.2\pi t) & \text{if } 10 \le t \le 70, \\ (0.95)^{t-70} & \text{if } 70 \le t \le 130, \\ -0.5 & \text{otherwise}. \end{cases}$$

The isolation performance is illustrated in Fig. 3.3 for $L = 5$. From the figure, it can be seen that the classifier cannot distinguish between the actuator and sensor #2 faults during the shaded period (i.e., $\cos\theta = 1$ for both). This is because the residual signal exactly resides at the intersection of the corresponding hyperplanes in this period. This non-trivial intersection corresponds to the second case of Theorem 3.10, where an actuator and a sensor fault become indiscernible if the subsystem from the actuator to the considered sensor does not contain the transmission zero shared by the other output channels.

Scenario 2. In a more realistic setting, the faulty subsystem switches between multiple fault modes under a noisy condition. The perturbed healthy input–output data is collected using a PRBS signal, generating $N = 1000$ samples. The innovation signal is considered to be zero-mean white noise with a nonzero covariance matrix, and the signal-to-noise ratio (SNR) is 25. Setting $L = 15$ to estimate fault dictionaries and to obtain $\mathbf{K}_L$ by Proposition 3.11. The FI performance is evaluated through a Monte Carlo simulation. The average FI accuracy across simulations is 91.28%. The result for one particular realization is shown in Figure 3.4. Apart from some transient behavior, the results demonstrate the effectiveness of the proposed method.

[1]The details of the system matrices can be found at https://github.com/amiiigen/DDFI.git.

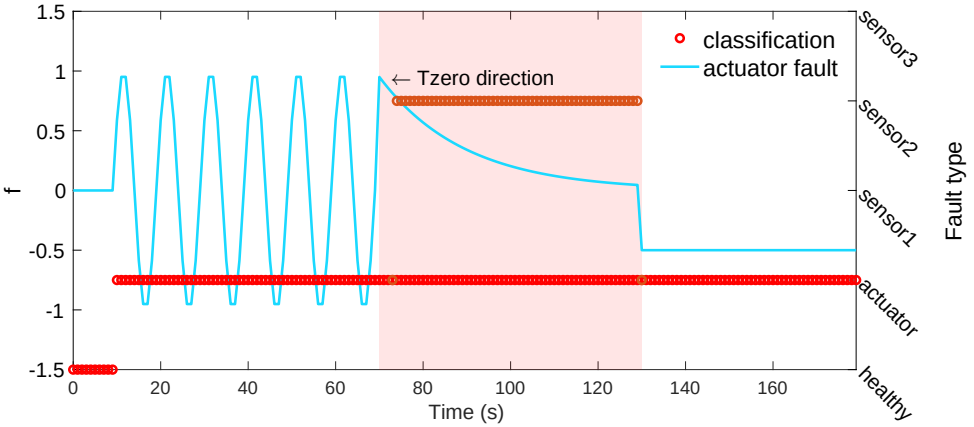

Figure 3.3: Noise-free actuator-fault scenario. The left y-axis indicates the fault magnitude, while the right y-axis shows the classification result. The blue line represents the actuator fault signal, and the red circles indicate the fault isolation outcome at each time instant. The shaded red region denotes the interval during which the fault evolves according to a transmission-zero direction.

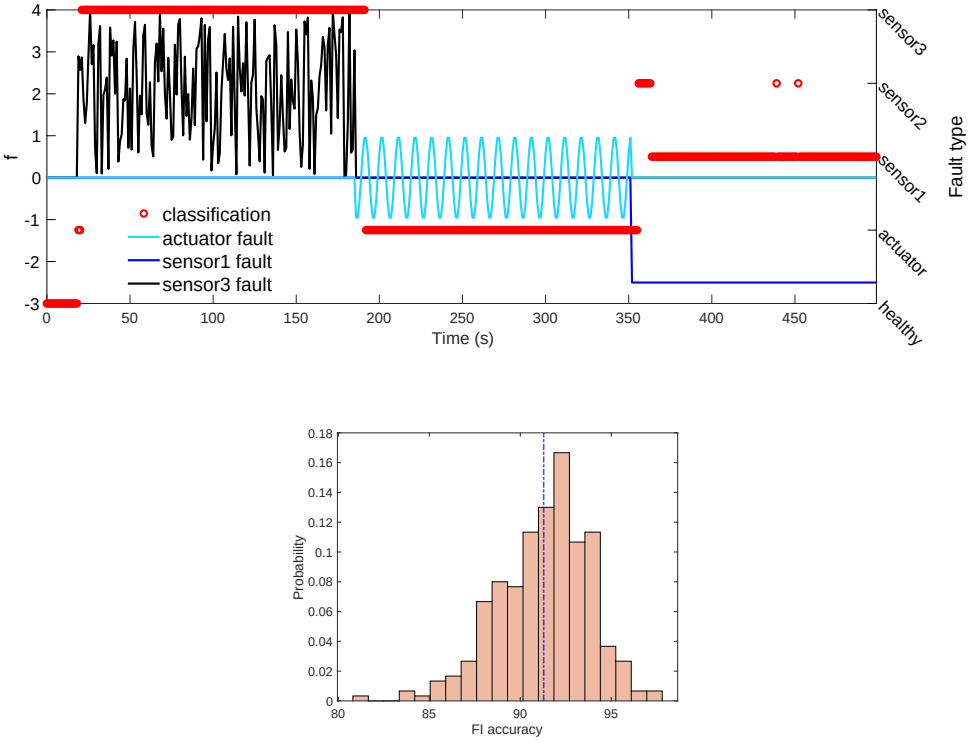

Figure 3.4: The proposed fault isolation performance in the presence of noise for different fault types. (Top) The left y-axis indicates the fault magnitude, while the right y-axis shows the classification result for one specific noise realization. The black, light blue, and blue lines represent the third sensor, first sensor, and actuator fault signals, respectively, and the red circles indicate the fault isolation outcome at each time instant. (Bottom) The corresponding fault isolation accuracy histogram across all the experiments.

3.7 Conclusions

The proposed FI approach achieves perfect isolation under noise-free conditions when the faults are discernible. Although simple, the geometric classifier demonstrates the effectiveness of partitioning the residual space for fault isolation. More advanced subspace classification methods could be employed to develop more sophisticated diagnosis filters, although this lies beyond the scope of this chapter. The analysis also establishes a connection between intersections of the fault subspaces and the zero structure of the underlying system, revealing a fundamental source of fault indiscernibility. On another note, despite the fact that the presence of noise degrades the classification performance, the filter still performs satisfactorily. A formal investigation of filter performance under noisy conditions remains an interesting direction for future work.

4

Data-Driven Characterization of Multivariable LTI Systems Zeros

The previous chapter revealed that the performance of null-space-based fault isolation filters is fundamentally constrained by the zero structure of the fault subsystem. Motivated by this finding, the present chapter investigates the zero structure of general linear time-invariant systems, with particular emphasis on data-driven settings. The zero structure of multivariable linear time-invariant systems, with particular emphasis on data-driven characterization. The zero structure is studied through a finite-horizon output-zeroing problem formulated in terms of the null space of the data equation, which naturally arises in data-driven control and estimation. Drawing on classical results from multivariable system theory and geometric control theory, we establish connections between this null space, system zeros, and structural properties such as invertibility. Fundamental invariant subspaces provide the theoretical foundation for the analysis, while connections to other system descriptions are also examined. The main findings hold for general non-minimal and degenerate systems with arbitrary input–output dimensions. Furthermore, leveraging this characterization, we develop a data-driven method for computing system zeros and the associated output-zeroing input sequences directly from input–output measurements for left-invertible systems. Illustrative numerical examples evaluate the proposed method in the presence of noise and compare its performance with existing approaches.

This chapter is partly based on *Data-driven Characterization of Multivariable LTI System Zeros* [160].

4.1 Introduction

Despite having been studied extensively for decades, the zero structure of linear multivariable systems remains of interest owing to its relevance to many modern systems and control problems. These include disturbance decoupling [161], model matching [162], performance limitations in tracking and feedback control [163], non-interacting control [164], estimation problems (e.g., unknown-input reconstruction [38, 85]), as well as fault diagnosis [25, 42, 165] and cybersecurity [166]. The theory of system zeros encompasses a variety of (not necessarily equivalent) definitions and characterizations formulated under different perspectives and system representations. For comprehensive historical accounts and discussions, see the surveys in [31, 167].

The presence of zeros is associated with the *output-zeroing problem* [168, 169], which is to find non-trivial pairs of initial conditions and input trajectories leading to an identically zero output. Any solution to this problem is referred to as a zero direction, whereas the zero dynamics describe the internal state trajectories of the system induced by such solutions [170]. Through this connection, studying the output-zeroing problem provides insight into the underlying zero structure.

Related literature. The most well-accepted characterization of system zeros was provided in [30] and relies on finding the complex values at which the so-called Rosenbrock system matrix loses rank. An advantage is that it directly links the frequency-response and state-space descriptions of the system. However, this null-space characterization is not sufficient to recover the complete set of zero directions corresponding to invariant zeros whose algebraic multiplicities exceed their geometric multiplicities. In such cases, the remaining zero directions must be computed by solving a generalized eigenvalue-type problem [168].

In parallel, geometric notions were developed for the output-zeroing problem using controlled invariant and reachability subspaces within the framework of geometric control theory [157, 171]. It has been shown that the zero directions span the maximal output-nulling controlled invariant and reachability subspaces of the state space, where the number of invariant zeros, counting algebraic multiplicities, is related to the dimensions of these subspaces [172–174]. Nevertheless, as mentioned earlier, these invariant subspaces characterize only the state trajectories associated with the zero directions and provide no explicit description of the corresponding input trajectories in contrast to the Rosenbrock system matrix approach.

More recently, the discrete-time output-zeroing problem has been alternatively characterized in terms of the null space of the extended observability and the block Toeplitz matrix of the Markov parameters [115]. This characterization becomes apparent by expressing the output data equation over a finite horizon and is hereafter referred to as the data equation approach. Unlike the previous approaches, the corresponding zeroing problem in the data equation approach requires the output to remain identically zero only over a finite horizon. Therefore, it represents a weaker form of the output-zeroing problem, which we refer to as the *restricted output-zeroing problem.*

This restricted problem is especially relevant in data-driven control and estimation, where only a finite amount of input–output data is available. For instance, in behavioral system theory, trajectories are typically considered over finite time intervals, and both

direct methods based on the fundamental lemma [21] and indirect methods based on subspace identification [47, 48]—such as data-enabled predictive control [175] and subspace predictive control [176]— rely on the data equation. Likewise, unknown-input estimation and perfect tracking consider a similar setting, where the input can be reconstructed with a finite delay provided that the system is invertible [84, 115]. In fault diagnosis, the null space of the data equation determines fault detectability [34, 68], while in cybersecurity, zero dynamics attacks exploit this null space to manipulate the underlying state while being undetected [166]. Hence, the data equation approach concerns a broad class of modern systems and control problems.

This chapter adopts the data equation characterization, focusing particularly on solutions to the restricted output-nulling problem, whose connection with the classical system-theoretic results (see, e.g., [167, 168, 174]) remains largely unexplored. In particular, the connection between the null space of the output data equation and the complete system zero structure is not yet fully understood. To the best of our knowledge, [158] provides the first analysis linking the dimension of this null space to that of the maximal output-nulling controlled invariant subspace. However, the result is limited to left invertible systems with a minimal realization, for which transmission and invariant zeros coincide. A complete characterization based on the null space of the data equation is still lacking in the literature, particularly for non-minimal systems with arbitrary input and output dimensions. Furthermore, it remains unclear whether the complete zero structure, including invariant decoupling zeros and assignable zeros, can be recovered from this null space.

Direct computation of system zeros and zero directions from input–output data has also received limited attention. Existing works [177, 178] compute invariant zeros using the Rosenbrock system matrix and a state-space realization. Alternatively, they can be computed using recursive subspace operations performed over a finite number of iterations [157, 172, 179, 180]. More recently, the authors of [181, 182] proposed a nonrecursive method for computing output-nulling invariant subspaces using the extended observability matrix, the block Toeplitz matrix of Markov parameters, and the Rosenbrock system matrix. These approaches, however, require the exact knowledge of the system realization matrices, limiting their applicability primarily to model-based settings. In contrast, a recent work in [183] presents a data-driven method for computing fundamental invariant subspaces from multiple input–state–output trajectories collected through separate experiments. Nevertheless, the proposed method requires access to the initial and final states of every experiment, which are often unavailable in data-driven applications. Besides, the method is restricted to systems with a zero feedthrough matrix. Hence, the direct computation of invariant subspaces, system zeros, and the corresponding zero directions from input–output data is still an open problem.

Contributions. This chapter aims at a complete characterization of the restricted output-nulling problem in connection to the system zero structure and other system-theoretic properties. The provided treatment extends the state of the art to general non-minimal and degenerate systems with arbitrary numbers of inputs and outputs. The main contributions can be summarized as follows:

- Theorem 4.16, which shows that, with sufficiently large horizon L, the dimension of input set that solves the restricted output-nulling problem is the sum of the number

of output-nulling zeros and L times the degree of input redundancy [184]. This result relies on novel characterizations of invariant subspaces in terms of extended observability, reachability, and Markov parameter matrices (Theorem 4.13) as well as the characterization of the kernel dimensions of said matrices (Theorem 4.15).

- A direct data-driven method for computing the degree of input redundancy in general systems through rank inspection (Proposition 4.17).
- The notion of finite-zero input (Definition 4.13) characterizing solutions to the restricted output-zeroing problem that can be extended beyond the horizon L while keeping the output at zero, as well as the subspace characterization of the set of finite-zero inputs (Theorem 4.18).
- A direct data-driven algorithm for computing system zeros and the corresponding output-zeroing input sequences in left-invertible systems from a single input–output trajectory (Theorem 4.22). Moreover, unlike existing algorithms, the proposed method does not require prior knowledge of the true state-space dimension.
- The evaluation of the proposed approach against the conventional two-step method, which applies model-based techniques to an identified system, via numerical simulations in the presence of noise. The results demonstrate that our approach significantly improves estimation performance.

For clarity of exposition, several established definitions from the classical literature are refined and adapted to the setting.

4.2 Preliminaries

A general discrete-time finite-dimensional linear time-invariant system Σ is governed by the following state-space representation

$$\Sigma : \quad \begin{aligned} \boldsymbol{x}(t+1) &= \boldsymbol{A}\boldsymbol{x}(t) + \boldsymbol{B}\boldsymbol{u}(t), \\ \boldsymbol{y}(t) &= \boldsymbol{C}\boldsymbol{x}(t) + \boldsymbol{D}\boldsymbol{u}(t), \end{aligned} \tag{4.1}$$

where $t \in \mathbb{Z}_{\geq 0}$, $\boldsymbol{x}(t) \in \mathcal{X} = \mathbb{R}^{n_x}$, $\boldsymbol{u}(t) \in \mathcal{U} = \mathbb{R}^{n_u}$, and $\boldsymbol{y}(t) \in \mathcal{Y} = \mathbb{R}^{n_y}$ represent the time index, the system states, the control inputs, and the measured outputs, respectively. The matrices $\boldsymbol{A} \in \mathbb{R}^{n_x \times n_x}$, $\boldsymbol{B} \in \mathbb{R}^{n_x \times n_u}$, $\boldsymbol{C} \in \mathbb{R}^{n_y \times n_x}$, and $\boldsymbol{D} \in \mathbb{R}^{n_y \times n_u}$ define the linear mappings $\boldsymbol{A} : \mathcal{X} \to \mathcal{X}$, $\boldsymbol{B} : \mathcal{U} \to \mathcal{X}$, $\boldsymbol{C} : \mathcal{X} \to \mathcal{Y}$, and $\boldsymbol{D} : \mathcal{U} \to \mathcal{Y}$, respectively. These form a state-space realization of the dynamical system, which is not necessarily reachable or observable, and yield the transfer function $\boldsymbol{G}(\mathfrak{q})$ as

$$\boldsymbol{G}(\mathfrak{q}) := \boldsymbol{D} + \boldsymbol{C}(\mathfrak{q}\mathbf{I}_{n_x} - \boldsymbol{A})^{-1}\boldsymbol{B}$$

in which $\mathfrak{q} \in \mathbb{C}$. The corresponding Markov parameters are defined by

$$\boldsymbol{M}_i = \begin{cases} \boldsymbol{D} & i = 0 \\ \boldsymbol{C}\boldsymbol{A}^{i-1}\boldsymbol{B} & i > 0 \end{cases},$$

and the (Rosenbrock) system matrix has the form

$$P(\mathfrak{q}) \coloneqq \begin{bmatrix} A - \mathfrak{q}\mathbf{I}_{n_x} & B \\ C & D \end{bmatrix}.$$

The dual system is denoted by $\Sigma^\top$, with the state-space realization $(A^\top, C^\top, B^\top, D^\top)$ and transfer function $G^\top(\mathfrak{q})$. Unless stated otherwise, all subspaces introduced in the following refer to the system Σ. As an example, a subspace $\mathcal{V} \subseteq \mathcal{X}$ is associated with the system Σ, whereas $\mathcal{V}(\Sigma^\top)$ corresponds to the dual system $\Sigma^\top$.

Definition 4.1 (State-Space Minimality)**.** The state-space system Σ is said to be minimal if $n_x = n$, the smallest dimension of a state-space realization (i.e., reachable and observable). Denote by the quadruple $(A_\mathrm{m}, B_\mathrm{m}, C_\mathrm{m}, D_\mathrm{m})$ a minimal realization of the system Σ.

Using the Kalman canonical decomposition, it can be shown that the transfer function $G(\mathfrak{q})$ and Markov parameters M_i of the system Σ are uniquely determined and invariant under the choice of state-space realization, that is,

$$\begin{aligned} &D + C(\mathfrak{q}\mathbf{I}_{n_x} - A)^{-1}B = D_\mathrm{m} + C_\mathrm{m}(\mathfrak{q}\mathbf{I}_n - A_\mathrm{m})^{-1}B_\mathrm{m}, \\ &D = D_\mathrm{m}, \quad CA^{i-1}B = C_\mathrm{m}A_\mathrm{m}^{i-1}B_\mathrm{m}. \end{aligned}$$

4.2.1 System Properties from a Geometrical Perspective

This subsection leverages geometric control theory, as established in [157, 171, 179, 185], to characterize the fundamental structural properties of the system Σ. The geometric notions defined herein form the theoretical basis for the subsequent results presented in this paper.

Definition 4.2 (Output-nulling subspace)**.** The *output-nulling* subspace $\mathcal{Z} \subseteq \mathcal{X}$ of the system Σ is defined as

$$\mathcal{Z} \coloneqq \{x \in \mathcal{X} \mid \text{there exists } u \in \mathcal{U} \text{ such that } Cx + Du = 0\} = C^{-1}\operatorname{im} D.$$

Definition 4.3 (Output-nulling controlled invariant subspace)**.** A subspace $\mathcal{V} \subseteq \mathcal{X}$ is called an *output-nulling controlled invariant subspace* for the system Σ if, for all $x(0) \in \mathcal{V}$, there exists an input sequence $\{u(t)\}_{t\geq 0}$ such that $y(t) = 0$ for all $t \geq 0$. Equivalently, the following inclusion holds:

$$\begin{bmatrix} A \\ C \end{bmatrix} \mathcal{V} \subseteq \begin{bmatrix} \mathbf{I}_{n_x} \\ 0 \end{bmatrix} \mathcal{V} + \operatorname{im} \begin{bmatrix} B \\ D \end{bmatrix}. \tag{4.2}$$

The maximal output-nulling invariant subspace, denoted by $\mathcal{V}^\star$, is the supremum of all subspaces $\mathcal{V}$ satisfying (4.2). For a given $k \in \mathbb{Z}_{\geq 0}$, the notation $\mathcal{V}_k$ is used for the finite-time counterpart, in which the requirement $y(t) = 0$ is imposed only for $t \in [0, k]$ (see [172, Lemma 1]).

Definition 4.4 (Input-containing conditioned invariant subspace)**.** A subspace $\mathcal{S} \subseteq \mathcal{X}$ is called an *input-containing conditioned invariant subspace* for the system Σ if, for all $x(k) \in \mathcal{S}$ at some finite time $k \in \mathbb{Z}_{>0}$, there exists an input sequence $\{u(t)\}_{t\in[0,k-1]}$ such that $x(k)$ is reachable from the origin while $y(t) = 0$ for all $t \in [0, k-1]$. Equivalently, $\mathcal{S}$ satisfies [179, Theorem 8.19]

$$\begin{bmatrix} A & B \end{bmatrix} \left((\mathcal{S} \times \mathcal{U}) \cap \ker \begin{bmatrix} C & D \end{bmatrix} \right) \subseteq \mathcal{S}. \tag{4.3}$$

The minimal input-containing conditioned invariant subspace, denoted by $\mathcal{S}^\star$, is the infimal $\mathcal{S}$ satisfying (4.3).

Definition 4.5 (Output-nulling reachable subspace)**.** The subspace $\mathcal{R}^\star \subseteq \mathcal{X}$ is defined as the *maximal output-nulling reachable subspace* from the origin for the system Σ if and only if it satisfies the relation $\mathcal{R}^\star = \mathcal{V}^\star \cap \mathcal{S}^\star$.

Remark 4.1. The space $\mathcal{S}^\star$ is a dual space of $\mathcal{V}^\star$ in the following way. Let $\Sigma^\top$ be the dual system. Then $\mathcal{S}^\star = \left(\mathcal{V}^\star(\Sigma^\top)\right)^\perp$ [179, Theorem 8.20], which gives

$$\begin{bmatrix} \boldsymbol{A}^\top \\ \boldsymbol{B}^\top \end{bmatrix} \mathcal{S}^\perp \subseteq \begin{bmatrix} \mathbf{I}_{n_x} \\ \mathbf{0} \end{bmatrix} \mathcal{S}^\perp + \operatorname{im} \begin{bmatrix} \boldsymbol{C}^\top \\ \boldsymbol{D}^\top \end{bmatrix}. \tag{4.4}$$

A rigorous proof for (4.4) is provided in Section B.1.

The sum of maximal reachable and controlled invariant output-nulling subspaces $\mathcal{N}^\star := \mathcal{V}^\star + \mathcal{S}^\star = \mathcal{V}^\star + \mathcal{R}^\star/\mathcal{V}^\star$ can be interpreted in discrete-time as the set of all states that can either be reached or controlled while keeping the output zero.[1] For this reason, we shall call $\mathcal{N}^\star$ the *finite-time weakly unobservable subspace*.

Next, we examine the system properties using rank conditions and the fundamental invariant subspaces.

Definition 4.6 (System degeneracy)**.** A system Σ is said to be *degenerate* if the following rank condition holds:

$$\operatorname{normalrank} \boldsymbol{P}(\mathfrak{q}) < n_x + \min\{n_u, n_y\};$$

otherwise, the system is said to be *non-degenerate*.

Definition 4.7 (System invertibility)**.** A system Σ with the transfer function $\boldsymbol{G}(\mathfrak{q})$ is *left-invertible* (respectively, *right invertible*) if there exists a proper transfer function $\boldsymbol{G}^+(\mathfrak{q})$ and a delay $\tau \in \mathbb{Z}_{\geq 0}$ such that $\boldsymbol{G}^+(\mathfrak{q})\boldsymbol{G}(\mathfrak{q}) = \mathfrak{q}^{-\tau}\mathbf{I}_{n_u}$ (respectively, $\boldsymbol{G}(\mathfrak{q})\boldsymbol{G}^+(\mathfrak{q}) = \mathfrak{q}^{-\tau}\mathbf{I}_{n_y}$) for almost all $\mathfrak{q} \in \mathbb{C}$. The system is said to be *invertible* if it is both left invertible and right invertible.

Related to degeneracy and left invertibility is the notion of input redundancy, for which we borrow the definition from [184]:

Definition 4.8 (Input redundancy)**.** System Σ is said to be *input-redundant* if there exists an output $\boldsymbol{y} : \mathbb{Z}_{\geq 0} \to \mathcal{Y}$ that can be produced by at least two distinct input sequences for some $\boldsymbol{x}(0)$. The *degree of input redundancy* of Σ is denoted by $\nu := \dim(\boldsymbol{B}^{-1}\mathcal{V}^\star \cap \ker \boldsymbol{D})$, based on Theorem 4.1 and following [184].

Theorem 4.1 ([184, Theorem 3.1])**.** *The following statements are equivalent:*

(i) Σ *is input-redundant;*

(ii) $\dim(\mathcal{R}^\star) > 0$*;*

[1] In continuous-time, $\mathcal{N}^\star$ has been called *distributionally weakly unobservable subspace* due to the connection to impulsive inputs, see [179, Chap. 8]

(iii) $\dim(\boldsymbol{B}^{-1}\mathcal{V}^{\star} \cap \ker \boldsymbol{D}) > 0$;

(iv) Σ *is not left invertible.*

The normal ranks of $\boldsymbol{P}(\mathfrak{q})$ and $\boldsymbol{G}(\mathfrak{q})$, system invertibility, and system degeneracy are closely interrelated. These connections are formalized in a proposition, the proof of which relies on the following lemma:

Lemma 4.2 ([159, Proposition 16.10.3])**.** *The following identities hold for any system* Σ*:*

$$\begin{aligned} \operatorname{rank} \boldsymbol{P}(\mathfrak{q}) &= n_x + \operatorname{rank} \boldsymbol{G}(\mathfrak{q}); \quad \forall \mathfrak{q} \in \mathbb{C} \backslash \sigma(\boldsymbol{A}), \\ \operatorname{normal\,rank} \boldsymbol{P}(\mathfrak{q}) &= n_x + \operatorname{normal\,rank} \boldsymbol{G}(\mathfrak{q}). \end{aligned}$$

Proposition 4.3. *The following statements are equivalent:*

(i) The system Σ *is (left/right) invertible.*

(ii) $\operatorname{normal\,rank} \boldsymbol{G}(\mathfrak{q}) = \min\{n_u, n_y\}$.

(iii) The system Σ *is non-degenerate.*

(iv) At least one of the following holds:

(a) $\mathcal{V}^{\star} \cap \boldsymbol{B} \ker \boldsymbol{D} = \mathcal{R}^{\star} = \{\mathbf{0}\}$ *and* $\operatorname{rank} \begin{bmatrix} \boldsymbol{B} \\ \boldsymbol{D} \end{bmatrix} = n_u$ *(left invertibility);*

(b) $\mathcal{S}^{\star} + \boldsymbol{C}^{-1} \operatorname{im} \boldsymbol{D} = \mathcal{S}^{\star} + \mathcal{V}^{\star} = \mathcal{X}$ *and* $\operatorname{rank} \begin{bmatrix} \boldsymbol{C} & \boldsymbol{D} \end{bmatrix} = n_y$ *(right invertibility).*

Proof. The equivalence of statements (i)–(iii) follows from [32, Theorem 2] and Lemma 4.2. See [179, Theorems 8.26 and 8.27] for the proof of (i) $\iff$ (iv). ∎

4.2.2 System Zeros

In what follows, we introduce a series of definitions concerning the conventional types of zeros associated with a general system Σ. The main results will be developed based on these definitions.

Definition 4.9 (System zeros)**.** Let $\mathfrak{q}_0 \in \mathbb{C}$ be a complex scalar. With respect to the system Σ, $\mathfrak{q}_0$ is called:

(a) an *invariant zero* if $\operatorname{rank} \boldsymbol{P}(\mathfrak{q}_0) < \operatorname{normal\,rank} \boldsymbol{P}(\mathfrak{q})$;

(b) a *finite transmission zero* if it is an invariant zero of a minimal realization of Σ. Equivalently, $\operatorname{rank} \boldsymbol{G}(\mathfrak{q}_0) < \operatorname{normal\,rank} \boldsymbol{G}(\mathfrak{q})$ provided that $\mathfrak{q}_0 \notin \sigma(\boldsymbol{A}_{\mathrm{m}})$;

(c) an *infinite transmission zero* if $\operatorname{rank} \lim_{\mathfrak{q}_0 \to \infty} \boldsymbol{G}(\mathfrak{q}_0) < \operatorname{normal\,rank} \boldsymbol{G}(\mathfrak{q})$.

(d) an *input-decoupling zero* if $\operatorname{rank} \begin{bmatrix} \boldsymbol{A} - \mathfrak{q}_0 \mathbf{I} & \boldsymbol{B} \end{bmatrix} < \operatorname{normal\,rank} \begin{bmatrix} \boldsymbol{A} - \mathfrak{q} \mathbf{I} & \boldsymbol{B} \end{bmatrix}$;

(e) an *output-decoupling zero* if $\operatorname{rank} \begin{bmatrix} \boldsymbol{A} - \mathfrak{q}_0 \mathbf{I} \\ \boldsymbol{C} \end{bmatrix} < \operatorname{normal\,rank} \begin{bmatrix} \boldsymbol{A} - \mathfrak{q} \mathbf{I} \\ \boldsymbol{C} \end{bmatrix}$;

(f) an *input-output-decoupling zero* if it is an output-decoupling zero that disappears after eliminating the input-decoupling zeros according to the procedure prescribed in [30, pp. 60–63];

(g) a *system zero* if it is a zero of the greatest common divisor (GCD) of all nonzero minors of order $n_x + k$ of $\boldsymbol{P}(\mathfrak{q})$ containing its first n_x rows and columns, where k is the largest integer for which such a minor exists.

Definition 4.10. Denote by ζ the number of finite invariant zeros, counting algebraic multiplicities, and by ζ_∞ the number of infinite zeros, defined as the algebraic multiplicity of the transmission zero at $\mathfrak{q} = 0$ of $\boldsymbol{G}(1/\mathfrak{q})$.

Remark 4.2. If the system Σ is non-degenerate, then $k = \min(n_u, n_y)$ in Definition 4.9(g).

Zeros of a multivariable system characterize combinations of inputs and state trajectories that lead to a zero output (which we call hereafter *output-nulling zeros*) or combinations of outputs and states that emerge from a zero input. A complete characterization of the output-nulling zeros requires the notion of assignable zeros, which we adapt from [186].

Definition 4.11 (Assignable output-nulling zero)**.** A complex scalar $\mathfrak{q}_0 \in \mathbb{C}$ is an assignable output-nulling zero if it is not an invariant zero and there exists a *friend* $\boldsymbol{F} \in \mathscr{F}(\mathcal{V}^\star)$ such that $\mathfrak{q}_0 \in \sigma(\boldsymbol{A} + \boldsymbol{B}\boldsymbol{F}|_{\mathcal{V}^\star})$.

As discussed in [171, p. 115] and shown in general cases in [180, 186], the assignable output-nulling zeros are restricted to $\mathcal{R}^\star$, while $\mathcal{V}^\star/\mathcal{R}^\star$ contains only invariant zeros. Aling and Schumacher [174] thoroughly described the different zeros of LTI systems and their relation with the invariant subspaces $\mathcal{C}, \bar{\mathcal{O}}, \mathcal{V}^\star, \mathcal{S}^\star$, where $\mathcal{C}$ and $\bar{\mathcal{O}}$ denote, respectively, the reachable and unobservable subspaces to be defined in Section 4.3. These relations are summarized in a lattice diagram [174, Figure 4], hereafter called Aling–Schumacher diagram. We summarize the most important relations for this work in the following theorem:

Theorem 4.4 (Output-nulling zero count)**.** *For any system* Σ*,*

(a) the number of zeros at infinity, counting algebraic multiplicity, is $\dim(\mathcal{S}^\star/\mathcal{R}^\star)$*;*

(b) the number of finite invariant zeros, counting algebraic multiplicity, is $\dim(\mathcal{V}^\star/\mathcal{R}^\star)$*;*

(c) the number of assignable output-nulling zeros is $\dim(\mathcal{R}^\star)$*.*[2]

(d) the total number of output-nulling zeros is given by $\dim(\mathcal{N}^\star)$*.*

Proof. See Appendix B.3. ∎

The following proposition describes the implications of infinite zeros for the structural properties of the system.

Proposition 4.5. *Suppose* Σ *is non-degenerate. The following statements are equivalent:*

[2] The multiplicity of assignable zeros is not relevant here, since they can always be assigned to be different, see [181].

(i) The system Σ has a zero at infinity.

(ii) $\operatorname{rank} \boldsymbol{D} < \operatorname{normalrank} \boldsymbol{G}(\mathfrak{q})$.

(iii) $\operatorname{rank} \lim_{\mathfrak{q}\to\infty} \boldsymbol{P}(\mathfrak{q}) < \operatorname{normalrank} \boldsymbol{P}(\mathfrak{q})$.

(iv) The system Σ is (left/right) invertible with the smallest delay $\tau_0 \geq 1$.

Proof. See Appendix B.3. ∎

We are now in a position to formally state the output-zeroing problem and characterize its solutions in terms of the system-theoretic notions introduced so far.

4.3 Output-Zeroing Problem

First, a formal definition of the output-zeroing problem is provided within the established framework, after which the formulation is extended to a data-driven setting.

Definition 4.12. (Output-zeroing problem) The output-zeroing problem is said to have a non-trivial solution if there exist an initial state $\boldsymbol{x}(0)$ and an input sequence $\{\boldsymbol{u}(t)\}_{t\geq 0}$, not both identically zero, such that the resulting output satisfies $\boldsymbol{y}(t) = \boldsymbol{0}$ for all $t \geq 0$, i.e., $\boldsymbol{y}(t) \equiv \boldsymbol{0}$. It is called a *restricted* output-zeroing problem if the condition $\boldsymbol{y}(t) = \boldsymbol{0}$ is required only on the finite time interval $t \in [t_1, t_2]$ for some $t_1, t_2 \in \mathbb{Z}_{\geq 0}$ with $t_1 \leq t_2$.

Without loss of generality, consider the L-long time interval $[0, L-1]$ for which the system data equation is given by

$$\boldsymbol{y}_{[0,L-1]} = \mathbf{O}_L \boldsymbol{x}(0) + \mathbf{T}_L \boldsymbol{u}_{[0,L-1]}, \tag{4.5}$$

where the extended observability matrix $\mathbf{O}_L$ and the block-Toeplitz matrix $\mathbf{T}_L$ are defined as

$$\mathbf{O}_L := \begin{bmatrix} \boldsymbol{C} \\ \boldsymbol{CA} \\ \vdots \\ \boldsymbol{CA}^{L-1} \end{bmatrix}, \quad \mathbf{T}_L := \begin{bmatrix} \boldsymbol{M}_0 & \boldsymbol{0} & \cdots & \boldsymbol{0} \\ \boldsymbol{M}_1 & \boldsymbol{M}_0 & \ddots & \vdots \\ \vdots & \ddots & \ddots & \boldsymbol{0} \\ \boldsymbol{M}_{L-1} & \cdots & \boldsymbol{M}_1 & \boldsymbol{M}_0 \end{bmatrix}.$$

Moreover, the following state reachability data equation will be useful:

$$\boldsymbol{x}(L) = \boldsymbol{A}^L \boldsymbol{x}(0) + \mathbf{K}_L \boldsymbol{u}_{[0,L-1]} \tag{4.6}$$

where $\mathbf{K}_L := \begin{bmatrix} \boldsymbol{A}^{L-1}\boldsymbol{B} & \cdots & \boldsymbol{AB} & \boldsymbol{B} \end{bmatrix}$. From the data equations, the reachable and unobservable subspaces are given by $\mathcal{C} = \operatorname{im} \mathbf{K}_L$ and $\bar{\mathcal{O}} = \ker \mathbf{O}_L$ for a sufficient large L, respectively.

Lemma 4.6. *Let $L > \dim \mathcal{Z}$ and $M > \dim \mathcal{Z}(\Sigma^\top)$. Then,*

$$\ker \mathbf{O}_L = \ker \mathbf{O}_{n_x} = \bar{\mathcal{O}},$$
$$\operatorname{im} \mathbf{K}_M = \operatorname{im} \mathbf{K}_{n_x} = \mathcal{C},$$

and consequently, $\operatorname{rank} \mathbf{O}_L = \operatorname{rank} \bar{\mathcal{O}}$ *and* $\operatorname{rank} \mathbf{K}_M = \operatorname{rank} \mathcal{C}$.

Proof. See Appendix B.3. ∎

Remark 4.3. In the proof of Lemma 4.6, the condition $\bar{\mathcal{O}}_i = \bar{\mathcal{O}}_{i+1}$ also implies $\bar{\mathcal{O}}_i$ is $\boldsymbol{A}$-invariant. To verify, we must show $\boldsymbol{A}\bar{\mathcal{O}}_i \subseteq \bar{\mathcal{O}}_i$. Indeed, $\bar{\mathcal{O}}_{i+1} = \bar{\mathcal{O}}_0 \cap \boldsymbol{A}^{-1}\bar{\mathcal{O}}_i \implies \bar{\mathcal{O}}_i = \bar{\mathcal{O}}_0 \cap \boldsymbol{A}^{-1}\bar{\mathcal{O}}_i$, since $\bar{\mathcal{O}}_i = \bar{\mathcal{O}}_{i+1}$. This further implies $\bar{\mathcal{O}}_i \subseteq \boldsymbol{A}^{-1}\bar{\mathcal{O}}_i \implies \boldsymbol{A}\bar{\mathcal{O}}_i \subseteq \boldsymbol{A}(\boldsymbol{A}^{-1}\bar{\mathcal{O}}_i) \subseteq \bar{\mathcal{O}}_i$.

Remark 4.4. It is worth mentioning that Lemma 4.6 exploits the geometry of the output-zeroing problem to establish a new sufficient condition on the horizon L for retrieving the observable and reachable subspaces. If $\dim \mathcal{Z}$ of either Σ or $\Sigma^\top$ is strictly less than $n_x - 1$, the proposed condition is less conservative than the conventional worst-case bound given by the system order n_x. In particular, $\dim \mathcal{Z} < n_x$ only when $\operatorname{im} \boldsymbol{C} \nsubseteq \operatorname{im} \boldsymbol{D}$.

The null space of $\begin{bmatrix}\mathbf{O}_L & \mathbf{T}_L\end{bmatrix}$ is closely related to the restricted output-zeroing problem. To see this, we show that every element of the null space of $\begin{bmatrix}\mathbf{O}_L & \mathbf{T}_L\end{bmatrix}$ results in an identically zero output over a finite L-step time window, and that the converse also holds.

Proposition 4.7. *Let $L \in \mathbb{Z}_{\geq 0}$, $\bar{\boldsymbol{x}} \in \mathcal{X}$ and $\bar{\boldsymbol{u}} \in \mathcal{U}^L$. Define $\boldsymbol{x}(0) = \bar{\boldsymbol{x}}$ and $\boldsymbol{u}_{[0,L-1]} = \bar{\boldsymbol{u}}$. Then, for all $t \in [0, L-1]$, $\boldsymbol{y}(t) = 0$ if and only if $\begin{bmatrix}\bar{\boldsymbol{x}} \\ \bar{\boldsymbol{u}}\end{bmatrix} \in \ker \begin{bmatrix}\mathbf{O}_L & \mathbf{T}_L\end{bmatrix}$.*

Proof. The result follows immediately from the definition of the null space and the data equation (4.5). ∎

Any pair $(\bar{\boldsymbol{x}}, \bar{\boldsymbol{u}}) \in \mathcal{X} \times \mathcal{U}^L$, with $L \in \mathbb{Z}_{\geq 0}$, satisfying Proposition 4.7 is referred to as an *output-zeroing direction*. In light of this relationship, addressing the output-zeroing problem in data-driven settings primarily involves characterizing the null space of $\begin{bmatrix}\mathbf{O}_L & \mathbf{T}_L\end{bmatrix}$ through the structural and frequency properties of the system. For this purpose, we resort to the geometric and system-theoretic notions introduced in Section 4.2. The matrices $\mathbf{O}_L$ and $\mathbf{T}_L$ are fundamental components of subspace identification methods and data-driven solutions to linear systems and control problems [47, 48, 68, 166, 175].

4.3.1 Characterization of Data Equation Null Space

In this section, we show that the null space of $\begin{bmatrix}\mathbf{O}_L & \mathbf{T}_L\end{bmatrix}$ reveals the complete zero structure of the system Σ.

As shown in [179, Theorem 7.12], the finite-time invariant subspace $\mathcal{V}_k$ admits a recurrence relation, leading to the following result:

Lemma 4.8. *There exists $k_0 \leq \dim \mathcal{Z} \leq n_x$ such that, for all $k \geq k_0$, $\mathcal{V}_{k_0} = \mathcal{V}_k = \mathcal{V}^\star$.*

Lemma 4.9. *Let $L \in \mathbb{Z}_{\geq 0}$ with $L > \dim \mathcal{Z}$. Then $\bar{\boldsymbol{x}} \in \mathcal{V}^\star$ if and only if there exists $\bar{\boldsymbol{u}} \in \mathcal{U}^L$ such that $(\bar{\boldsymbol{x}}, \bar{\boldsymbol{u}}) \in \ker \begin{bmatrix}\mathbf{O}_L & \mathbf{T}_L\end{bmatrix}$.*

Proof. See Appendix B.3. ∎

Remark 4.5. In light of Lemmas 4.8 and 4.9, one can compute $\mathcal{V}^\star$ by computing $\ker \begin{bmatrix}\mathbf{O}_{L>\dim \mathcal{Z}} & \mathbf{T}_{L>\dim \mathcal{Z}}\end{bmatrix}$ and projecting the resulting null space back onto the state space $\mathcal{X}$. This approach provides an alternative to the iterative algorithms typically proposed in the geometric control literature [157, 171, 179]. Furthermore, Lemma 4.9 shows that a

horizon of length at least $L = \dim \mathcal{Z} + 1$ is sufficient to uniquely determine $\mathcal{V}^\star$. This condition is not necessary; however, in the absence of the restriction $\mathcal{V} \subseteq \mathcal{Z}$ in Definition 4.3, the sufficient horizon changes to $L \geq \dim \mathcal{X} + 1$.

Lemma 4.10. *Let $L \in \mathbb{Z}_{\geq 0}$ with $L > \dim \mathcal{Z}$. Then*

$$\dim(\ker \begin{bmatrix} \mathbf{O}_L & \mathbf{T}_L \end{bmatrix}) = \dim \mathcal{V}^\star + \dim(\ker \mathbf{T}_L).$$

Proof. See Appendix B.3. ∎

As a consequence of Lemma 4.10, the following result can be obtained:

Lemma 4.11. *Let $L \in \mathbb{Z}_{\geq 0}$ with $L > \dim \mathcal{Z}$. Then*

$$\dim \mathcal{V}^\star = \dim(\ker \mathbf{O}_L) + \dim(\operatorname{im} \mathbf{O}_L \cap \operatorname{im} \mathbf{T}_L).$$

Proof. From [159, Fact 3.14.15], we have

$$\dim(\ker \begin{bmatrix} \mathbf{O}_L & \mathbf{T}_L \end{bmatrix}) = \dim(\ker \mathbf{O}_L) + \dim(\ker \mathbf{T}_L) + \dim(\operatorname{im} \mathbf{O}_L \cap \operatorname{im} \mathbf{T}_L).$$

The result then follows by substituting the identity with the one in Lemma 4.10. ∎

The characterizations in Lemmas 4.10 and 4.11 are inherently linked to system zeros. Several intermediate theoretical results are needed to make this connection explicit. As a first step, the following lemma establishes a relation between the Toeplitz matrices of Σ and its dual $\Sigma^\top$.

Lemma 4.12. *Denote by $\tilde{\mathbf{T}}_L$ the block Toeplitz matrix corresponding to the transposed transfer function matrix $\boldsymbol{G}^\top(\mathfrak{q})$. We have that*

$$\mathbf{T}_L^\top = \boldsymbol{P}_1 \tilde{\mathbf{T}}_L \boldsymbol{P}_2, \tag{4.7}$$

with suitable block-flipper matrices

$$\boldsymbol{P}_1 = \begin{bmatrix} \mathbf{0} & & \mathbf{I}_{n_u} \\ & \iddots & \\ \mathbf{I}_{n_u} & & \mathbf{0} \end{bmatrix}, \quad \boldsymbol{P}_2 = \begin{bmatrix} \mathbf{0} & & \mathbf{I}_{n_y} \\ & \iddots & \\ \mathbf{I}_{n_y} & & \mathbf{0} \end{bmatrix}.$$

Consequently, $\dim(\ker \mathbf{T}_L^\top) = \dim(\ker \tilde{\mathbf{T}}_L)$.

Proof. The identity (4.7) holds by exploiting the block-Toeplitz structure of $\mathbf{T}_L, \tilde{\mathbf{T}}_L$. Using this identity, we get

$$\mathbf{T}_L^\top \boldsymbol{P}_2 = \boldsymbol{P}_1 \tilde{\mathbf{T}}_L \implies \ker(\mathbf{T}_L^\top \boldsymbol{P}_2) = \ker(\boldsymbol{P}_1 \tilde{\mathbf{T}}_L) = \ker \tilde{\mathbf{T}}_L,$$

by invertibility of the matrices $\boldsymbol{P}_1, \boldsymbol{P}_2$, which in turn gives the dimension equality. ∎

Theorem 4.13. *Let $L > \dim \mathcal{Z}$ and $M > \dim \mathcal{Z}(\Sigma^\top)$. Then, the following holds:*

$$\mathcal{V}^\star = \mathbf{O}_L^{-1} \operatorname{im} \mathbf{T}_L, \tag{4.8}$$

$$\mathcal{S}^\star = \mathbf{K}_M \ker \mathbf{T}_M. \tag{4.9}$$

Proof. See Appendix B.3. ∎

Remark 4.6. The expression (4.9) also follows from [182, Theorem 3.1], but proved with a different approach.

Corollary 4.14. *For $L > \dim \mathcal{Z}$ and $M > \dim \mathcal{Z}(\Sigma^\top)$, we have $\bar{\mathcal{O}} = \ker \mathbf{O}_L \subseteq \mathcal{V}^\star$ and $\mathcal{S}^\star \subseteq \operatorname{im} \mathbf{K}_M$.*

Proof. The result is a direct consequence of Theorem 4.13 (see also [174]). ∎

Assumption 4.1. The horizon $L \in \mathbb{Z}_{\geq 0}$ is chosen such that $L > \max\{\dim \mathcal{Z}, \dim \mathcal{Z}(\Sigma^\top)\}$.

To express $\dim(\ker \begin{bmatrix} \mathbf{O}_L & \mathbf{T}_L \end{bmatrix})$ in terms of system zeros, the following theorem is important.

Theorem 4.15. *Under Assumption 4.1, $\dim \ker \mathbf{T}_L = \zeta_\infty + Lv$, where v denotes the degree of input redundancy as introduced in Definition 4.8. Moreover,*

$$\dim \ker \mathbf{T}_L = \begin{cases} \zeta_\infty & \text{if } \Sigma \text{ is left-invertible,} \\ \zeta_\infty + L(n_u - n_y) & \text{if } \Sigma \text{ is right-invertible} \end{cases}.$$

Proof. See Appendix B.3. ∎

Remark 4.7. Note that [158, Theorem IV.8] is stated for a minimal realization of the system Σ with a full column rank transfer function matrix $G(\mathfrak{q})$, i.e., a left-invertible system. In this sense, Theorem 4.15 generalizes Theorem IV.8 in [158] to non-minimal systems that may be left-invertible, right-invertible, or both. Moreover, when $n_u > n_y$, the null space of $\mathbf{T}_L$ contains additional basis vectors arising from its block structure, beyond those associated with zeros at infinity.

We are now ready to state the main theorem connecting the null space of $\begin{bmatrix} \mathbf{O}_L & \mathbf{T}_L \end{bmatrix}$ to the system zero structure and other structural properties:

Theorem 4.16. *Under Assumption 4.1,*

$$\dim \ker \begin{bmatrix} \mathbf{O}_L & \mathbf{T}_L \end{bmatrix} = \dim \mathcal{N}^\star + Lv.$$

Moreover,

$$\dim \ker \begin{bmatrix} \mathbf{O}_L & \mathbf{T}_L \end{bmatrix} = \begin{cases} \zeta + \zeta_\infty & \text{if } \Sigma \text{ is left-invertible,} \\ \dim \mathcal{N}^\star + L(n_u - n_y) & \text{if } \Sigma \text{ is right-invertible.} \end{cases}$$

Proof. See Appendix B.3. ∎

To conclude this section, we revisit the insightful lattice diagram, originally presented by Aling and Schumacher [174, Figure 4], to illustrate the connection between the system zero structure and the fundamental invariant subspaces characterized in a data-driven setting.

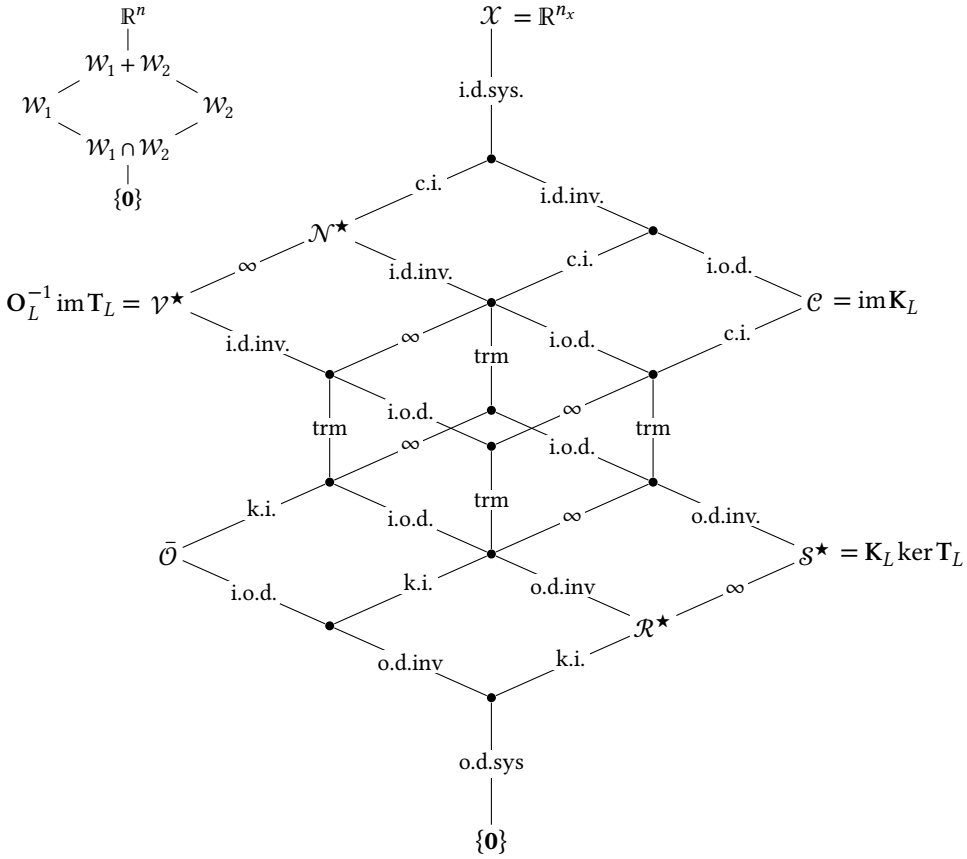

Figure 4.1: Middle: Lattice diagram of invariant subspaces from [174], and their computation via Theorem 4.13. The acronyms and symbols i.d.sys., o.d.sys., c.i., k.i., i.o.d., i.d.inv., o.d.inv., trm, and ∞ respectively refer to input-decoupling system zeros that are not invariant, output-decoupling system zeros that are not invariant, co-range indices, kernel indices, input-output-decoupling invariant zeros, input-decoupling invariant zeros which are not i.o.d., output-decoupling invariant zeros which are not i.o.d., finite transmission zeros, and infinite transmission zeros. Top left: An example of how to interpret a subspace lattice diagram, where $\mathcal{W}_1$ and $\mathcal{W}_2$ are subspaces of $\mathbb{R}^n$.

4.4 Data-Driven Computation of Zeros

In this section we use the previously established results to determine a formula for data-driven computation of invariant zeros from input-output data. For this, given N data points of an arbitrary signal $\boldsymbol{s}(k)$, define the family of block-Hankel matrices constructed as follows:

$$\overset{///}{\mathrm{S}}_{t,L,N} := \begin{bmatrix} \boldsymbol{s}(t) & \boldsymbol{s}(t+1) & \cdots & \boldsymbol{s}(N-L) \\ \boldsymbol{s}(t+1) & \boldsymbol{s}(t+2) & \cdots & \boldsymbol{s}(N-L+1) \\ \vdots & \vdots & \ddots & \vdots \\ \boldsymbol{s}(t+L-1) & \boldsymbol{s}(t+L) & \cdots & \boldsymbol{s}(N-1) \end{bmatrix}.$$

Similarly, the state trajectory over an interval $[t_1, t_2]$ is gathered in the matrix $X_{[t_1,t_2]} := \begin{bmatrix} \boldsymbol{x}(t_1) & \boldsymbol{x}(t_1+1) & \cdots & \boldsymbol{x}(t_2) \end{bmatrix}$. This gives the block-Hankel version of the data-equation (4.5)

$$\overset{///}{\mathrm{Y}}_{t,L,N} = \begin{bmatrix} \mathbf{O}_L & \mathbf{T}_L \end{bmatrix} \begin{bmatrix} X_{[t,t+N-L]} \\ \overset{///}{\mathrm{U}}_{t,L,N} \end{bmatrix}. \tag{4.10}$$

We start by using a standard identifiability assumption on the data:

Assumption 4.2. The matrix $\begin{bmatrix} X_{0,N-L} \\ \overset{///}{\mathrm{U}}_{0,L,N} \end{bmatrix}$ is full row rank.

This is the case when, e.g., $(\boldsymbol{A}, \boldsymbol{B})$ in (3.1) is controllable and $\boldsymbol{u}$ is persistently exciting (PE) of sufficiently high order [17], provided N and L are appropriately chosen.

Under these conditions, all sequences of inputs and outputs $\boldsymbol{u}, \boldsymbol{y}$ of an LTI system can be generated from a single trajectory by solving $\begin{bmatrix} \overset{///}{\mathrm{U}}_{0,L,N} \\ \overset{///}{\mathrm{Y}}_{0,L,N} \end{bmatrix} \boldsymbol{g} = \begin{bmatrix} \boldsymbol{u}_{[t,t+L-1]} \\ \boldsymbol{y}_{[t,t+L-1]} \end{bmatrix}$. Therefore, in the data-driven case, the output zeroing problem can be solved without the need to identify the system, by computing $\overset{///}{\mathrm{U}}_{0,L,N} \overset{///}{\mathrm{Y}}^{\ker}_{0,L,N}$. This provides a basis, in the input trajectory space, for all input sequences for which there exists an initial state giving $\overset{///}{\mathrm{Y}}_{0,L,N} = \mathbf{0}$. As we see next, $\overset{///}{\mathrm{U}}_{0,L,N} \overset{///}{\mathrm{Y}}^{\ker}_{0,L,N}$ is connected to Theorem 4.16.

Proposition 4.17. *Let Assumptions 4.1 and 4.2 hold. Then*

$$\operatorname{rank}\left(\overset{///}{\mathrm{U}}_{0,L,N} \overset{///}{\mathrm{Y}}^{\ker}_{0,L,N}\right) = \dim(\mathcal{N}^{\star}/\bar{\mathcal{O}}) + Lv.$$

Proof. See Appendix B.3. ∎

The subspace of solutions spanned by the standard restricted output-zeroing problem, $\ker\begin{bmatrix} \mathbf{O}_L & \mathbf{T}_L \end{bmatrix}$ may include inputs that are not necessarily extendable; that is, after applying one such input for L steps, it might be impossible to find an input for after L that holds a zero output. As an example, consider the simple scalar single-input single-output system $\Sigma = (0,1,1,0)$, the unit-delay. Picking $L = 1$ gives $\ker\begin{bmatrix} \mathbf{O}_L & \mathbf{T}_L \end{bmatrix} = \operatorname{im}\begin{bmatrix} 0 \\ 1 \end{bmatrix}$. From $x(0) = 0$ and $u(0) = 1$, we get $x(1) = 1$, from which it is impossible to obtain $y(1) = 0$. Clearly, this input is associated with the system's zero at infinity.

To characterize these extendable inputs we use the following definition.

Definition 4.13 (Finite-zero input sequence)**.** The sequence $\{\boldsymbol{u}^{\mathrm{fz}}(t)\}_{t\geq 0}$, where $\boldsymbol{u}^{\mathrm{fz}} : \mathbb{Z}_{\geq 0} \to \mathcal{U}$, is called a *finite-zero input sequence* for system Σ if there exists an initial state $\boldsymbol{x}(0)$ such that $\boldsymbol{y}(t) = \mathbf{0}$ for all $t \geq 0$. The set of all finite-zero input sequences of Σ is denoted by $\mathcal{U}^{\mathrm{fz}}(\Sigma)$. The corresponding state trajectory satisfies $\boldsymbol{x}(t) \in \mathcal{V}^{\star}$ for all $t \geq 0$ by maximality and controlled-invariance of $\mathcal{V}^{\star}$.

The following theorem characterizes all finite-zero input subsequences of length L, with L satisfying Assumption 4.1, as a subspace, and provides a reason to call them finite-zero sequences. For this, let us use the following partitions and notations for $\mathbf{T}_{L+M}$:

$$\mathbf{T}_{L+M} = \left[\begin{array}{c|c} \mathbf{T}_L & \mathbf{0} \\ \mathbf{O}_M \mathbf{K}_L & \mathbf{T}_M \end{array}\right] =: \begin{bmatrix} \mathbf{T}_{L+M,L} & \mathbf{0} \\ & \mathbf{T}_M \end{bmatrix}.$$

Theorem 4.18. *Let $L, M \in \mathbb{Z}_{\geq 0}$ satisfy the condition in Assumption 4.1. Then, the sequence $\{\boldsymbol{u}^{\mathrm{fz}}(t)\}_{t\geq 0}$ is a finite-zero input sequence for Σ if, for every $t \in \mathbb{Z}_{\geq 0}$,*

$$\boldsymbol{u}^{\mathrm{fz}}_{[t,t+L-1]} \in \mathcal{U}^{\mathrm{fz}}_L := \mathbf{T}^{-1}_{L+M,L} \operatorname{im} \begin{bmatrix} \mathbf{O}_{L+M} & \mathbf{0} \\ & \mathbf{T}_M \end{bmatrix}. \tag{4.11}$$

Additionally, $\mathcal{U}^{\mathrm{fz}}_L$ is a basis for all L-long subsequences of $\mathcal{U}^{\mathrm{fz}}(\Sigma)$. Moreover,

$$\dim \mathcal{U}^{\mathrm{fz}}_L = \dim(\mathcal{V}^{\star}/\bar{\mathcal{O}}) + Lv = \zeta + \dim \mathcal{R}^{\star} - \dim \bar{\mathcal{O}} + Lv, \tag{4.12}$$

and, in particular,

$$\dim \mathcal{U}^{\mathrm{fz}}_L = \begin{cases} \zeta - \dim \bar{\mathcal{O}} & \text{if } \Sigma \text{ is left-invertible,} \\ \zeta + \dim \mathcal{R}^{\star} - \dim \bar{\mathcal{O}} + L(n_u - n_y) & \text{if } \Sigma \text{ is right-invertible.} \end{cases} \tag{4.13}$$

Proof. See Appendix B.3. ∎

Under a stronger assumption, the necessary condition in Theorem 4.18 becomes necessary and sufficient, as stated in the following proposition:

Proposition 4.19. *Under the assumptions of Theorem 4.18, with $L > \dim \mathcal{Z} + 1$, the sequence $\{\boldsymbol{u}^{\mathrm{fz}}(t)\}_{t\geq 0}$ belongs to $\mathcal{U}^{\mathrm{fz}}(\Sigma)$ if and only if, for every $t \in \mathbb{Z}_{\geq 0}$, $\boldsymbol{u}^{\mathrm{fz}}_{[t,t+L-1]} \in \mathcal{U}^{\mathrm{fz}}_L$.*

Proof. See Appendix B.3 ∎

By Theorem 4.18, the difference between the dimension of $\mathcal{U}^{\mathrm{fz}}_L$, compared to the dimension of the general output nulling solution (Proposition 4.17) is precisely the number of zeros at infinity of Σ, hence the term "finite-zero" input. Theorem 4.18 admits an input–output version as formulated next.

Lemma 4.20. *Let $L, M \in \mathbb{Z}_{\geq 0}$ satisfy the condition in Assumption 4.1, and let Assumption 4.2 hold. Then,*

$$\operatorname{im}(\overset{/\!/}{\mathbf{U}}_{0,L,N-M} \overset{/\!/}{\mathbf{Y}}^{\ker}_{0,L+M,N}) = \mathcal{U}^{\mathrm{fz}}_L. \tag{4.14}$$

Proof. See Appendix B.3. ∎

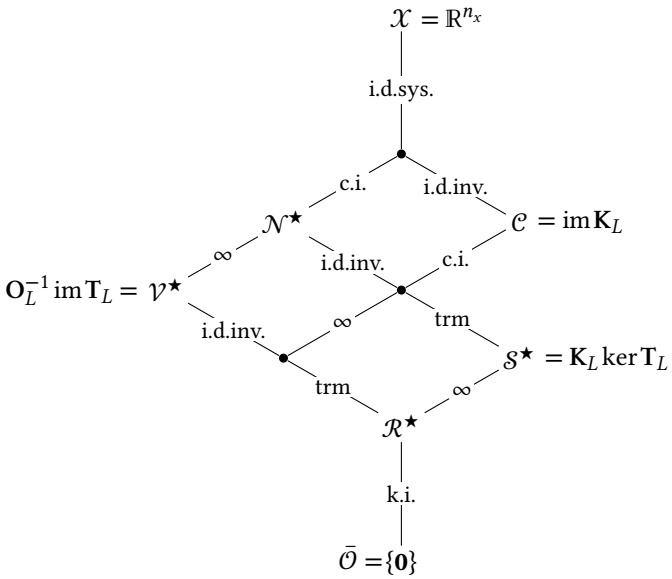

Figure 4.2: Lattice diagram of invariant subspaces reduced to observable systems.

Since unobservable modes do not appear in the data, the zeros that are revealed with a data-driven approach exclude those related to unobservable modes: namely, the output-decoupling zeros and the input-output decoupling zeros. As a result, denote by $\zeta_o = \zeta - \dim \bar{\mathcal{O}}$ the number of such zeros counting algebraic multiplicities. This is also consistent with characterizations provided in Proposition 4.17 and Lemma 4.20. Figure 4.2 shows the diagram in Figure 4.1 for observable systems, obtained by setting $\bar{\mathcal{O}} = \{\mathbf{0}\}$.

The following lemma reveals a characterization of finite-zero inputs of left-invertible systems as the output of an autonomous system.

Lemma 4.21. *Let Σ be left-invertible. Then, there exist matrices $\boldsymbol{C}_\zeta, \boldsymbol{A}_\zeta$ such that $\boldsymbol{u}^{\mathrm{fz}} : \mathbb{Z}_{\geq 0} \to \mathcal{U}$ is a finite-zero input of Σ if and only if it is of the form $\boldsymbol{u}^{\mathrm{fz}}(t) = \boldsymbol{C}_\zeta \boldsymbol{A}_\zeta^t z$ for some $z \in \mathbb{R}^\zeta$. Moreover, $\sigma(\boldsymbol{A}_\zeta)$ is the multiset of invariant zeros of Σ.*

Proof. See Appendix B.3. ∎

Theorem 4.18 and Lemmas 4.20–4.21 enable the following theorem on how to determine the finite invariant zeros of the system directly from input–output data in the case of left-invertible systems. Before stating it, let $\boldsymbol{U} \in \mathbb{R}^{Ln_u \times p}$ be the basis for some subspace of L-long input sequences vertically concatenated as $\boldsymbol{u}_{[0,L-1]} \in \operatorname{im} \boldsymbol{U}$. We denote by $\boldsymbol{U}_{[i]}$ its i-th block row ('zero-indexed', corresponding to rows $in_u + 1$ through $(i+1)n_u$) and by $\boldsymbol{U}_{[i:j]}$ its submatrix comprised of all block rows from i up to and including j.

Theorem 4.22. *Let Σ be left-invertible. Suppose that $L, M \in \mathbb{Z}_{\geq 0}$ satisfy the condition in Assumption 4.1 and Assumption 4.2 holds. Let $\boldsymbol{U}$ be a full-column-rank basis for $\overline{\overline{\mathbf{U}}}_{0,L+1,N-M} \ker \overline{\overline{\mathbf{Y}}}_{0,L+M+1,N}$. Then, there exists a unique matrix $\boldsymbol{A}_{\zeta_o}$ satisfying $\boldsymbol{U}_{[0:L-1]} \boldsymbol{A}_{\zeta_o} =$*

$U_{[1:L]}$ such that, for any vector $z \in \mathbb{R}^{\zeta_o}$, the sequence $u(t) = U_{[0]} A_{\zeta_o}^t z$ is an output-zeroing sequence for Σ. Moreover, $\sigma(A_{\zeta_o})$ is the multiset of finite invariant zeros of Σ, excluding the output-decoupling zeros.

Proof. See Appendix B.3. ∎

4.5 Numerical Examples and Applications

In this section, we examine an implications of Theorem 4.16 for fault diagnosis, followed by an application of Theorem 4.18 and Lemma 4.21 to input reconstruction. Lastly, two numerical examples illustrate the main theoretical findings[3].

4.5.1 Fault Discernibility

A direct implication of the developments in Section 4.3, particularly Theorem 4.16, arises in fault diagnosis as discussed in Chapter 3. In this context, fault discernibility characterizes the fundamental extent to which different faulty modes can be distinguished from the input–output behavior. For simplicity, neglect the control input and suppose that the fault signal $f(t)$ affects the output $y(t)$ of a system via the following dynamics:

$$x(t+1) = Ax(t) + \underbrace{\begin{bmatrix} B_f^{(1)} & B_f^{(2)} \end{bmatrix}}_{=:B_f} \underbrace{\begin{bmatrix} f_1(t) \\ f_2(t) \end{bmatrix}}_{=:f(t)}, \quad y(t) = Cx(t) + \underbrace{\begin{bmatrix} D_f^{(1)} & D_f^{(2)} \end{bmatrix}}_{=:D_f} \begin{bmatrix} f_1(t) \\ f_2(t) \end{bmatrix},$$

where $f_1(t) \in \mathbb{R}^{n_{f_1}}$ and $f_2(t) \in \mathbb{R}^{n_{f_2}}$ denote fault inputs and $y(t) \in \mathbb{R}^{n_y}$ the output. The state-space realization (A, B_f, C, D_f) has order n and is not necessarily minimal. In the following, the total fault subsystem and the fault subsystems associated with the pairs $(B_f^{(1)}, D_f^{(1)})$ and $(B_f^{(2)}, D_f^{(2)})$ are indicated by superscripts f, f_1 and f_2, respectively. Focusing on null-space-based diagnosis filters [40, 68, 149], the residual signal is generated using the left null space of the extended observability matrix. Let $\mathbf{O}_L^{\mathrm{lker}}$ be a basis for the left null space of $\mathbf{O}_L$, i.e., $\ker \mathbf{O}_L^\top = \operatorname{im}(\mathbf{O}_L^{\mathrm{lker}})^\top$. Following the design in Chapter 3, the residual subspaces generated by $f_1(t)$ and $f_2(t)$ are given by $r_1(t) \in \operatorname{im} \mathbf{O}_L^{\mathrm{lker}} \mathbf{T}_L^{f_1}$ and $r_2(t) \in \operatorname{im} \mathbf{O}_L^{\mathrm{lker}} \mathbf{T}_L^{f_2}$, respectively. In Lemma 3.9, it is shown that the intersection of the residual subspaces is directly related to fault discernibility and its dimension can be characterized by

$$\begin{aligned} \dim\left(\operatorname{im} \mathbf{O}_L^{\mathrm{lker}} \mathbf{T}_L^{f_1} \cap \operatorname{im} \mathbf{O}_L^{\mathrm{lker}} \mathbf{T}_L^{f_2}\right) = \dim \ker \begin{bmatrix} \mathbf{O}_L & \mathbf{T}_L^{f} \end{bmatrix} \\ - \dim \ker \begin{bmatrix} \mathbf{O}_L & \mathbf{T}_L^{f_1} \end{bmatrix} - \dim \ker \begin{bmatrix} \mathbf{O}_L & \mathbf{T}_L^{f_2} \end{bmatrix}. \end{aligned}$$

The intersection characterization in Theorem 3.10 requires the minimality of every fault subsystem and, in the case of sensor faults, its observability with respect to each individual output. Unfortunately, the latter is not guaranteed by the former, making these assumptions rather restrictive in practical applications. In contrast to state-space minimality, left invertibility is preserved by every subsystem obtained by removing a subset

[3] The examples here can be reproduced by using the code in https://gitlab.tudelft.nl/ggleizer/dd-zeros.git.

of fault inputs. Consequently, the generality of the statement in Theorem 4.16 allows the minimality assumption in Theorem 3.10 to be relaxed, leading to

Theorem 4.23. *Let* $(\boldsymbol{A}, [\boldsymbol{B}_f^{(1)} \quad \boldsymbol{B}_f^{(2)}], \boldsymbol{C}, [\boldsymbol{D}_f^{(1)} \quad \boldsymbol{D}_f^{(2)}])$ *be a left-invertible system. Then,*

$$\dim\left(\operatorname{im}\mathbf{O}_L^{\mathrm{lker}}\mathbf{T}_L^{f_1} \cap \operatorname{im}\mathbf{O}_L^{\mathrm{lker}}\mathbf{T}_L^{f_2}\right) = (\zeta^{f} + \zeta_\infty^{f}) - (\zeta^{f_1} + \zeta_\infty^{f_1}) - (\zeta^{f_2} + \zeta_\infty^{f_2}).$$

The characterization in Theorem 4.23 demonstrates that the dimension of intersection depends on the number of invariant zeros, including both transmission zeros and decoupling invariant zeros.

4.5.2 Input Reconstruction

The input reconstruction problem is inherent in several problem classes, including inverse problems [43], prefect tracking control [163], additive fault estimation [25], and output matching [21]. In this section, we study the reconstruction error dynamics and its connection to system zeros in linear cases using our results. Left-invertibility is a necessary condition for well-posedness; here, we provide an equivalent characterization of left-invertibility in Definition 4.7, which is particularly useful in data-driven settings:

Definition 4.14 ([187])**.** Let $\tau \in \mathbb{Z}_{\geq 0}$. System Σ is left-invertible with the delay τ if and only if $\operatorname{rank}\mathbf{T}_\tau - \operatorname{rank}\mathbf{T}_{\tau-1} = n_u$ (Note that $\operatorname{rank}\mathbf{T}_{-1} = 0$ by definition).

Thus, we assume Σ is left-invertible for some delay $\tau \geq \tau_0 \in \mathbb{Z}_{>0}$ where τ_0 is the minimum delay for which Σ is left-invertible. Then, for any $t \in \mathbb{Z}_{\geq 0}$, the data is generated according to

$$\boldsymbol{y}_{[t,t+L-1]} = \mathbf{O}_L\boldsymbol{x}^\star(t) + \mathbf{T}_L\boldsymbol{u}^\star_{[t,t+L-1]} = \mathbf{T}_{L,L-\tau}\boldsymbol{u}^\star_{[t,t+L-\tau-1]} + \begin{bmatrix}\mathbf{O}_L & \mathbf{0} \\ & \mathbf{T}_\tau\end{bmatrix}\begin{bmatrix}\boldsymbol{x}(t) \\ \boldsymbol{u}^\star_{[t+L-\tau,t+L-1]}\end{bmatrix}.$$

By Definition 4.14, the inherent delay τ_0 guarantees that $\mathbf{T}_\tau$ is column-rank deficient, that is, it is impossible to uniquely reconstruct $\boldsymbol{u}^\star_{[t+L-\tau,t+L-1]}$ even with known $\boldsymbol{x}(t)$, as discussed in [84]. However, in practice, $\boldsymbol{x}(t)$ is also unknown and, in particular, cannot be uniquely determined in data-driven applications either. Therefore, the goal is to obtain an unbiased reconstruction of $\boldsymbol{u}^\star_{[t,t+L-\tau-1]}$ regardless of the value of $\boldsymbol{x}(t)$ and $\boldsymbol{u}^\star_{[t+L-\tau,t+L-1]}$. Given only linear causal estimators, we define the estimator $\hat{\boldsymbol{u}}_{t,\tau,L} = \boldsymbol{\Theta}\boldsymbol{y}_{[t,t+L-1]}$ with $\boldsymbol{\Theta} \in \mathbb{R}^{(L-\tau)n_u \times Ln_y}$. For an unbiased estimator, the parameter $\boldsymbol{\Theta}$ must satisfy the following conditions:

$$\left.\begin{aligned}\boldsymbol{\Theta}\begin{bmatrix}\mathbf{O}_L & \mathbf{0} \\ & \mathbf{T}_\tau\end{bmatrix} = \mathbf{0} \\ \boldsymbol{\Theta}\mathbf{T}_{L,L-\tau} = \mathbf{I}\end{aligned}\right\} \Longrightarrow \boldsymbol{\Theta} = (\boldsymbol{Q}\mathbf{T}_{L,L-\tau})^+\boldsymbol{Q} \text{ with } \operatorname{im}\boldsymbol{Q}^\top = \ker\begin{bmatrix}\mathbf{O}_L & \mathbf{0} \\ & \mathbf{T}_\tau\end{bmatrix}^\top,$$

where $(\cdot)^+$ denotes the Moore–Penrose pseudoinverse. Note that $\tau_0 > 0$ ensures the existence of matrix $\boldsymbol{Q}$. Substituting into $\hat{\boldsymbol{u}}_{t,\tau,L}$ gives

$$\hat{\boldsymbol{u}}_{t,\tau,L} = (\boldsymbol{Q}\mathbf{T}_{L,L-\tau})^+\boldsymbol{Q}\boldsymbol{y}_{[t,t+L-1]},$$

which is also a solution of the following optimization:

$$\hat{\boldsymbol{u}}_{t,\tau,L} = \min_{\bar{\boldsymbol{u}} \in \mathcal{U}^{L-\tau}} \|\boldsymbol{Q}\boldsymbol{y}_{[t,t+L-1]} - \boldsymbol{Q}\mathbf{T}_{L,L-\tau}\bar{\boldsymbol{u}}\|.$$

Using this estimator, we characterize the reconstruction error as

$$\begin{aligned}
&\hat{\boldsymbol{u}}_{t,\tau,L} = (\boldsymbol{Q}\mathbf{T}_{L,L-\tau})^{+}\boldsymbol{Q}\boldsymbol{y}_{[t,t+L-1]} = (\boldsymbol{Q}\mathbf{T}_{L,L-\tau})^{+}\boldsymbol{Q}\mathbf{T}_{L,L-\tau}\boldsymbol{u}^{\star}_{[t,t+L-\tau-1]} \\
\Longrightarrow\ &\boldsymbol{Q}\mathbf{T}_{L,L-\tau}\hat{\boldsymbol{u}}_{t,\tau,L} = \boldsymbol{Q}\mathbf{T}_{L,L-\tau}\boldsymbol{u}^{\star}_{[t,t+L-\tau-1]} \\
\Longrightarrow\ &\hat{\boldsymbol{u}}_{t,\tau,L} - \boldsymbol{u}^{\star}_{[t,t+L-\tau-1]} \in \ker(\boldsymbol{Q}\mathbf{T}_{L,L-\tau}),
\end{aligned}$$

where the first implication follows from the Moore-Penrose pseudoinverse property. Define the reconstruction error $\boldsymbol{e}_{t,\tau,L} \coloneqq \hat{\boldsymbol{u}}_{t,\tau,L} - \boldsymbol{u}^{\star}_{[t,t+L-\tau-1]}$. For any unbiased estimator $\hat{\boldsymbol{u}}_{t,\tau,L}$, we have

$$\boldsymbol{e}_{t,\tau,L} \in \ker(\boldsymbol{Q}\mathbf{T}_{L,L-\tau}) = \mathbf{T}^{-1}_{L,L-\tau}\ker\boldsymbol{Q} = \mathbf{T}^{-1}_{L,L-\tau}\operatorname{im}\begin{bmatrix}\mathbf{O}_L & \mathbf{0} \\ & \mathbf{T}_\tau\end{bmatrix}.$$

Applying Theorem 4.18 characterizes the error as an output-zeroing input direction for sufficiently large τ and L, as formalized in the following proposition:

Proposition 4.24. *Let Σ be left-invertible and $L-\tau, \tau$ satisfy Assumption 4.1. Then, for any fixed $t \in \mathbb{Z}_{\geq 0}$ and any unbiased estimator $\hat{\boldsymbol{u}}_{t,\tau,L}$, the reconstruction error $\boldsymbol{e}_{t,\tau,L} \in \mathcal{U}^{\mathrm{fz}}_{L-\tau}$.*

We now established $\boldsymbol{e}_{t,\tau,L} \in \mathcal{U}^{\mathrm{fz}}_{L-\tau}$ by Proposition 4.24. Based on Theorem 4.18, $\mathcal{U}^{\mathrm{fz}}_{L-\tau}$ forms a basis for the space of all $(L-\tau)$-long trajectories of $\mathcal{U}^{\mathrm{fz}}(\Sigma)$. Moreover, from Lemma 4.21, there exist matrices $\boldsymbol{C}_\zeta, \boldsymbol{A}_\zeta$ such that any trajectory of $\mathcal{U}^{\mathrm{fz}}(\Sigma)$ admits a representation of the form $\boldsymbol{C}_\zeta \boldsymbol{A}_\zeta^t \boldsymbol{z}$ at time t, for some $\boldsymbol{z} \in \mathbb{R}^\zeta$. Putting altogether, we can conclude that $\boldsymbol{e}^{[L-\tau-1]}_{t,\tau,L} = \boldsymbol{C}_\zeta \boldsymbol{A}_\zeta^{L-\tau-1}\boldsymbol{A}_\zeta^t \boldsymbol{z}$ for a given t, where $\boldsymbol{e}^{[j]}_{t,\tau,L}$ denotes its j-th n_u-block component ('zero-indexed', corresponding to rows jn_u+1 through $(j+1)n_u$). As a consequence, the error is governed by $\boldsymbol{A}_\zeta$, whose eigenvalues are finite invariant zeros of Σ. Therefore, for systems with finite invariant zeros, we have

$$\lim_{L\to\infty} \boldsymbol{e}^{[L-\tau-1]}_{t,\tau,L} = \mathbf{0} \quad \Longleftrightarrow \quad \rho(\boldsymbol{A}_\zeta) < 1 \text{ and } (\boldsymbol{A}, \boldsymbol{C}) \text{ observable}$$

for every initial error $\boldsymbol{e}^{[0]}_{t,\tau,L}$. If Σ possesses any non-minimum phase zero, the reconstruction error grows exponentially with the horizon L even in the noise-free case with full knowledge of system matrices. This fact has also been pointed out in [25, 84], whereas our statement is more general in the sense that it is expressed in terms of $\boldsymbol{A}_\zeta$ and does not require the minimality assumption on Σ.

4.5.3 Data-driven Invariant Zero Computation

Here we demonstrate the efficacy of Theorem 4.22 in retrieving zeros from input–output data, and also illustrate how to adapt it to cases with measurement noise. For the latter, we evaluate the relative error of an estimated zero z_{est} with respect to the true zero z_{true} by $e = \|z_{\mathrm{est}} - z_{\mathrm{true}}\|/\|z_{\mathrm{true}}\|$.

Consider the system Σ with

$$\begin{bmatrix} \boldsymbol{A} & \boldsymbol{B} \\ \boldsymbol{C} & \boldsymbol{D} \end{bmatrix} = \left[\begin{array}{ccccccccc} -7/8 & -7/4 & 0 & -7/4 & 0 & -7/4 & 53/24 & 0 & -53/24 \\ 0 & 7/8 & 0 & 13/8 & 0 & 13/8 & -2 & 0 & 1 \\ 27/16 & 27/16 & 13/16 & 27/16 & 0 & 27/16 & -77/24 & -1 & 77/24 \\ 0 & 0 & 0 & -3/4 & 0 & -3/2 & 3 & 1 & -2 \\ 1/8 & 1/8 & 1/8 & 1/8 & 15/16 & 1/8 & 0 & 0 & 0 \\ 0 & 0 & 0 & 0 & 0 & 3/4 & -1 & -1 & 1 \\ \hline -2 & -1 & 2 & 2 & 1 & 0 & 4 & 0 & -4 \\ 0 & 2 & 2 & 3 & 1 & 1 & 2 & 0 & -2 \\ 2 & 2 & 2 & 2 & 1 & 0 & 0 & 0 & 0 \\ 1 & 1 & 1 & 1 & 1 & 0 & 0 & 0 & 0 \end{array}\right],$$

4

where $n_x = 6, n_u = 3, n_y = 4$. The system is observable, left-invertible ($\dim \mathcal{R}^\star = 0$), but has an uncontrollable mode corresponding to an input-decoupling invariant zero at $\mathfrak{q} = 7/8$. Its other invariant zeros are a non-minimum phase transmission zero at $\mathfrak{q} = 4/3$ and three zeros at infinity, $\zeta_\infty = 3$, computed via $\dim \mathcal{S}^\star/\mathcal{R}^\star = \dim \mathcal{S}^\star = 3$ (see Theorem 4.4 and Figure 4.2). Since the number of finite invariant zeros is 2, we get $\dim \mathcal{V}^\star = 2$. We computed $\begin{bmatrix} \mathbf{O}_L & \mathbf{T}_L \end{bmatrix}$ for $L = 1, ..., n_x$ and found that, for $L = 2$, we already get $\dim\ker \begin{bmatrix} \mathbf{O}_L & \mathbf{T}_L \end{bmatrix} = \dim \mathcal{N}^\star = 5, \dim\ker \mathbf{T}_L = 3$, and $\dim \mathbf{O}_L^{-1} \operatorname{im} \mathbf{T}_L = 2$, which corroborates Theorems 4.16, 4.15 and 4.13, respectively. Indeed, the smallest number of iterations to compute both $\mathcal{V}^\star$ and $\mathcal{S}^\star$ with the fixed-point convergence is 2.

We generated 100 data points with inputs comprised of a combination of sinusoids and pseudo-random numbers, and a random initial condition, and verified that Assumption 4.2 holds. First, we applied Theorem 4.22 to this noise-free data, indeed confirming that $\operatorname{rank} \hat{\mathbf{U}}_{0,L+1,N} \hat{\mathbf{Y}}^{\ker}_{0,2L+1,N} = 2 = \zeta$, and finding that the spectrum of $\boldsymbol{A}_\zeta$ is 7/8 and 4/3, as expected.

To evaluate how noise affects the outlined approach, we added pseudo-random Gaussian white noise to the output with mean zero and variance 0.005, giving output signal-to-noise ratios between 50 and 71 dB. Denote by $\hat{\mathbf{Z}}_{0,L+M+1,N}$ the output block-Hankel matrix corrupted by noise. Then, we set $L = 5$ and followed Theorem 4.22 to compute $\hat{\boldsymbol{U}} := \hat{\mathbf{U}}_{0,L+1,N} \hat{\mathbf{Z}}^{\ker}_{0,2L+1,N}$. Due to the noise, this matrix was full rank. We used two criteria to deal with this. First, we inspected the singular values of $\hat{\boldsymbol{U}}$ (Figure 4.3) to estimate its approximate rank. Second, denoting by $\hat{\boldsymbol{U}}^{(k)}$ the top k singular vectors of $\hat{\boldsymbol{U}}$, we investigated the angle between the subspaces spanned by $\hat{\boldsymbol{U}}^{(k)}_{[0:L]}$ and $\hat{\boldsymbol{U}}^{(k)}_{[1:L+1]}$ (Figure 4.4); in the noise-free case, Theorem 4.22 gives that this angle should be zero. Based on the inspection of these two plots, it is apparent that $k = 2 = \zeta$ is a good estimate of the number of finite invariant zeros. Using $\hat{\boldsymbol{U}}^{(2)}$ to compute $\boldsymbol{A}_\zeta$, we obtained the spectrum $\{0.8773, 1.3244\}$, giving relative errors of less than 0.7%.

To establish a baseline to our approach, we also performed a two-step approach: subspace identification followed by invariant zero computation on the model. We applied N4SID [47] on the noisy data using the correct state-space dimension[4]. We ran 1000 simulations and used our proposed approach to retrieve the zeros using $\zeta = 2$. On the same

[4]We used the Matlab routine `n4sid` with `Feedthrough` set to 1 and `DisturbanceModel` set to `none`. The latter setting corresponds to assuming white noise, as is the case of our numerical experiment.

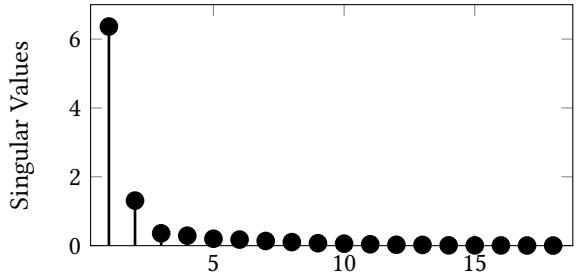

Figure 4.3: Singular values of $\hat{U} = \hat{\mathscr{U}}_{0,L+1,N}\hat{\mathscr{Z}}^{\ker}_{0,L+M+1,N}$ in the numerical example.

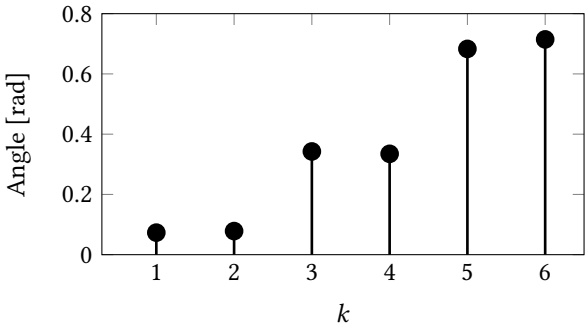

Figure 4.4: Angle between the subspaces spanned by $\hat{U}^{(k)}_{[0:L]}$ and $\hat{U}^{(k)}_{[1:L+1]}$ in the numerical example, for different guesses k for the number of finite invariant zeros ζ.

simulations, the two-step approach failed to retrieve zeros in all of them. For this reason, we conducted a line search over the tolerance of Matlab's invariant zero algorithm `tzero` until we got two transmission zeros. Still, in most of these cases the transmission zeros found were very far from the true values, whereas our proposed approach retrieves zeros with relative errors below 10% in almost all cases, see Table 4.1. Importantly, the non-minimum-phase zero could rarely be identified via the two-step approach, leaving, e.g., the system's vulnerability towards zero-dynamic attacks unnoticed.

Table 4.1: System zero estimation error performance comparison between the direct approach provided in Theorem 4.22 and the two-step approach via N4SID [47]. The values reported in the relative error ('Rel. error') column indicate the success rate across all simulations, while 'Std. dev.' denotes standard deviation.

Method	Mean	Std. dev.	Rel. error $\leq 10\%$
Proposed method	0.026	0.019	99.6%
N4SID [47] + `tzero`	0.493	1.769	3.8%

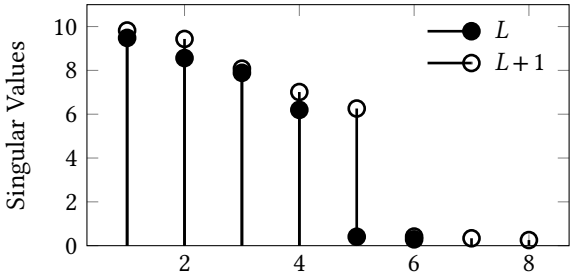

Figure 4.5: Singular values of $\mathscr{U}_{0,L+1,N}\mathscr{Y}^{\ker}_{0,L+1,N}$ and $\mathscr{U}_{0,L,N}\mathscr{Y}^{\ker}_{0,L,N}$ in the numerical example of Section 4.5.4.

4

4.5.4 Data-Driven Input Redundancy Detection

As a corollary of Proposition 4.17, we have $\nu = \operatorname{rank}\mathscr{U}_{0,L+1,N}\mathscr{Y}^{\ker}_{0,L+1,N} - \operatorname{rank}\mathscr{U}_{0,L,N}\mathscr{Y}^{\ker}_{0,L,N}$ under Assumption 4.1. This fact can be used to detect input redundancy directly from input-output data.

Consider the system Σ extracted from [123] with approximate values reported below[5]

$$\begin{bmatrix} A & B \\ C & D \end{bmatrix} = \left[\begin{array}{ccc|cc} 0 & 1 & 0 & 0 & 0.938 \\ 0 & 0 & 1 & 0 & 0.328 \\ -0.25 & 0.75 & 0.25 & 0 & 0.115 \\ \hline 1 & 0 & 0 & -0.944 & 0 \\ 0 & 1 & 0 & -0.33 & 0 \end{array}\right],$$

which is not controllable and is input-redundant with $\nu = 1$. Like in the previous example, we generated 100 data points with inputs and random initial condition satisfying Assumption 4.2. With $L = 3$, we confirmed that $\operatorname{rank}\mathscr{U}_{0,L+1,N}\mathscr{Y}^{\ker}_{0,L+1,N} - \operatorname{rank}\mathscr{U}_{0,L,N}\mathscr{Y}^{\ker}_{0,L,N} = 1$. Next, we added pseudo-random Gaussian white noise to the output with mean zero and variance 0.05, giving output signal-to-noise ratios between 21 and 28 dB. Inspecting the singular values of $\mathscr{U}_{0,L+1,N}\mathscr{Y}^{\ker}_{0,L+1,N}$ and $\mathscr{U}_{0,L,N}\mathscr{Y}^{\ker}_{0,L,N}$ (see Figure 4.5) shows an abrupt increase from L to $L+1$ at index 5, from nearly zero to about 6. Since this occurs at a single index, we can confirm that the degree of redundancy is 1.

Again, for the sake of comparison, we have identified the system using N4SID. The identified system $\widehat{\Sigma}$ was not detected as output redundant (by computing $\mathcal{R}^{\star}(\widehat{\Sigma}) = \{\mathbf{0}\}$), but had a maximal number of transmission zeros ($\zeta = n_x = 3$). This is again expected, as the system is square, and small perturbations to the parameters in A, B, C, D should render the system with the same number of finite zeros as poles.

4.6 Conclusion

This work provides a complete characterization of multivariable system zeros in data-driven settings by establishing a link to the output-zeroing problem. The results extend the existing theories to general non-minimal and degenerate systems with arbitrary numbers of inputs and outputs. In this regard, fundamental invariant subspaces from geometric

[5]For the precise matrices, see the code at https://gitlab.tudelft.nl/ggleizer/dd-zeros.git.

control provide the theoretical basis connecting system zeros, structural properties, and the output-zeroing problem. Associated with these zeros are finite output-zeroing input sequences that maintain a zero output, with practical relevance to applications such as fault diagnosis and cybersecurity. Building on this characterization, we propose a direct data-driven approach to compute system zeros and corresponding output-zeroing input sequences, as opposed to the conventional two-step procedure of system identification followed by model-based computation. Importantly, the proposed method does not require the exact state-space dimension a priori. Numerical simulations with noisy data demonstrate its effectiveness and show its superior performance over the two-step approach. The analysis in this paper focused exclusively on the deterministic setting. It would be interesting to extend our analysis to stochastic systems. Moreover, while the proposed zero computation is restricted to left-invertible systems, the underlying principle can be developed more generally for invertible systems; we leave this direction for future work.

5

Data-Driven Fault Estimation

This chapter considers the problem of fault estimation in linear time-invariant systems when actuators are subject to unknown additive faults. A data-driven approach is proposed to design an inverse-system-based filter for reconstructing fault signals when the underlying fault subsystem can be either a minimum phase or non-minimum phase system. Unlike traditional two-step data-driven methods in the literature, the proposed method directly computes the filter parameters from input–output data to avoid the propagation of identification errors through an inverse operation into the fault estimates, which is the case in state-of-the-art filter designs. Furthermore, regarding out-of-sample performance of the filter, a kernel-based regularization is exploited to not only reduce the model complexity but also enable the design scheme to take advantage of available prior knowledge on the underlying system behavior. This knowledge can be incorporated into basis functions, promoting the desired solution to the optimization problem. To validate the effectiveness of the proposed method, a simulation study is conducted, demonstrating a notable reduction in estimation error compared to state-of-the-art methods.

This chapter is partly based on *A Kernel-Based Approach to Data-Driven Actuator Fault Estimation* [122].

5.1 Introduction

During the past decades, fault diagnosis techniques on detection and isolation tasks have been extensively studied [188]; however, fault estimation (FE) has been less investigated, which is the main focus of this chapter. On the one hand, FE is a more challenging task, requiring the diagnosis system to detect, isolate, and determine the size and shape of faults. On the other hand, the outcomes of FE would provide more informative insights for control objectives, particularly in fault-tolerant design and predictive maintenance. Model-based residual generation approaches, such as unknown input observers [34, 97] and null-space-based filters [58, 189] under certain conditions can track fault signals. However, in practice, an explicit and accurate model of the real system often is not available, which promotes the adoption of data-driven methods.

As far as fault estimation problem is concerned, it is inherently tied to inverting the underlying fault subsystem, for which the model is unavailable in data-driven applications. As a result, inversion-based filters have recently garnered attention [25, 190]. The principal obstacle in this class of problems is the presence of transmission zeros, causing the system to become input–state unobservable [84]. This signifies that exact reconstruction is impossible within a finite time horizon if the underlying system possesses any transmission zero [85, 115], since there exists a nonzero pair of initial conditions and inputs for which the output is identically zero, leading to a nonempty unobservable input space. In [44], a subspace-based data-driven fault estimation filter is developed based on predictor Markov parameters (MPs). This result is further extended for additive actuator/sensor fault signals in minimum phase open-loop unstable systems [25, 120]. Stable system-inversion is the fundamental requirement in these methods to ensure asymptotically unbiased estimation. Most of the recent developments in data-driven fault estimation methods share the restrictive minimum phase condition of the fault subsystem; otherwise, the reconstruction error grows exponentially. Hence, achieving stable inversion of non-minimum phase (NMP) systems remains a significant challenge across various contexts, especially FE problems. In this regard, few model-based methods have been proposed in recent literature, although their applications in real scenarios are limited. In [82], a geometric approach is proposed in a noise-free condition, where the system matrices are assumed to be known. The model-based approach in [190] is only unbiased for either step or ramp fault signals. A more general model-based solution is provided in [191] by introducing a retrospective cost function for unknown input reconstruction. Inspired by preview-based techniques in control tracking problems of NMP systems, two methods were developed recently for fault estimation in model-based [192] and data-driven [45] fashions. The major issue with these methods is the high sensitivity of the reconstruction error to the correct location of zeros, especially in a data-driven framework due to identification errors. Furthermore, the closer the invariant zeros are to the unit circle, the larger the horizon required, leading to a considerable delay in fault estimation.

Contributions. This chapter addresses the fault estimation problem for non-minimum phase systems within a data-driven framework, while naturally accommodating minimum phase systems as a special case. A bilateral finite-impulse-response filter is proposed for the fault subsystem inverse, directly parameterized by corresponding Markov parameters of the inverse system, in contrast to the approach in [45]. As a result, identification errors bypass the inversion operation, thereby improving the estimation performance. More-

over, the proposed scheme allows for using kernel-based regularization to enforce prior knowledge about the filter characteristics at the design stage.

5.2 Problem Statement

Consider the following general linear time-invariant system

$$\begin{aligned} \boldsymbol{x}(t+1) &= \boldsymbol{A}\boldsymbol{x}(t) + \boldsymbol{B}_u\boldsymbol{u}(t) + \boldsymbol{B}_f\boldsymbol{f}(t) + \boldsymbol{B}_w\boldsymbol{w}(t), \\ \boldsymbol{y}(t) &= \boldsymbol{C}\boldsymbol{x}(t) + \boldsymbol{D}_u\boldsymbol{u}(t) + \boldsymbol{D}_f\boldsymbol{f}(t) + \boldsymbol{v}(t), \end{aligned} \tag{5.1}$$

in which $\boldsymbol{x}(t) \in \mathbb{R}^n$, $\boldsymbol{y}(t) \in \mathbb{R}^{n_y}$, $\boldsymbol{u}(t) \in \mathbb{R}^{n_u}$, and $\boldsymbol{f}(t) \in \mathbb{R}^{n_f}$ denote the state, the output measurement, the control input, and the unknown fault signal at discrete-time instant $t \in \mathbb{Z}_{\geq 0}$, respectively. The disturbances are represented by the process noise $\boldsymbol{w}(t) \in \mathbb{R}^{n_w}$ and the measurement noise $\boldsymbol{v}(t) \in \mathbb{R}^{n_v}$, both of which are considered to be white noises with zero-mean, without loss of generality, and the known corresponding bounded covariance matrix $\begin{bmatrix} \boldsymbol{w}(t) \\ \boldsymbol{v}(t) \end{bmatrix} \sim \begin{bmatrix} \boldsymbol{Q} & \boldsymbol{S} \\ \boldsymbol{S}^\top & \boldsymbol{R} \end{bmatrix}$. It is further assumed that $\boldsymbol{w}(t)$ and $\boldsymbol{v}(t)$ are uncorrelated with $\boldsymbol{u}(t)$ and $\boldsymbol{f}(t)$. $(\boldsymbol{A}, \boldsymbol{B}_u, \boldsymbol{B}_f, \boldsymbol{B}_w, \boldsymbol{C}, \boldsymbol{D}_u, \boldsymbol{D}_f)$ are minimal state-space realization matrices with compatible dimensions. Under detectability assumption of pair $(\boldsymbol{A}, \boldsymbol{C})$, the system in (5.1) admits the following one-step ahead prediction form as [150]

$$\begin{aligned} \hat{\boldsymbol{x}}(t+1) &= \tilde{\boldsymbol{A}}\hat{\boldsymbol{x}}(t) + \tilde{\boldsymbol{B}}_u\boldsymbol{u}(t) + \tilde{\boldsymbol{B}}_f\boldsymbol{f}(t) + \boldsymbol{K}\boldsymbol{y}(t) \\ \hat{\boldsymbol{y}}(t) &= \boldsymbol{C}\hat{\boldsymbol{x}}(t) + \boldsymbol{D}_u\boldsymbol{u}(t) + \boldsymbol{D}_f\boldsymbol{f}(t) + \boldsymbol{e}(t) \end{aligned} \tag{5.2}$$

with $\tilde{\boldsymbol{A}} = \boldsymbol{A} - \boldsymbol{K}\boldsymbol{C}$, $\tilde{\boldsymbol{B}}_u = \boldsymbol{B}_u - \boldsymbol{K}\boldsymbol{D}_u$, $\tilde{\boldsymbol{B}}_f = \boldsymbol{B}_f - \boldsymbol{K}\boldsymbol{D}_f$. $\boldsymbol{K} \in \mathbb{R}^{n \times n_y}$ represents the steady-state Kalman gain, and $\boldsymbol{e}(t) \in \mathbb{R}^{n_y}$ is the zero-mean innovation process with covariance matrix Σ_e.

Definition 5.1 (Transmission zero)**.** For a system with minimal state-space realization $(\boldsymbol{A}, \boldsymbol{B}, \boldsymbol{C}, \boldsymbol{D})$ with $\boldsymbol{u}(t) \in \mathbb{R}^{n_u}$, $\boldsymbol{x}(t) \in \mathbb{R}^n$, $\boldsymbol{y}(t) \in \mathbb{R}^{n_y}$, $\mathfrak{q}_0 \in \mathbb{C}$ is called a transmission zero if the associated Rosenbrock system matrix loses rank, i.e.,

$$\operatorname{rank}\left(\mathbf{R}(\mathfrak{q}_0) \triangleq \begin{bmatrix} \boldsymbol{A} - \mathfrak{q}_0\mathbf{I} & \boldsymbol{B} \\ \boldsymbol{C} & \boldsymbol{D} \end{bmatrix}\right) < n + \min\{n_y, n_u\}.$$

Remark 5.1. The transmission zeros of the original system (5.1) are equivalent to its observer form (5.2). In fact, the system zeros are not being modified by the output feedback, which can be verified by investigating the relation between both system matrices and Definition 5.1.

$$\begin{bmatrix} \tilde{\boldsymbol{A}} - \mathfrak{q}\mathbf{I} & [\tilde{\boldsymbol{B}}_u & \tilde{\boldsymbol{B}}_f] \\ \boldsymbol{C} & [\boldsymbol{D}_u & \boldsymbol{D}_f] \end{bmatrix} = \begin{bmatrix} \mathbf{I} & -\boldsymbol{K} \\ \mathbf{0} & \mathbf{I} \end{bmatrix} \begin{bmatrix} \boldsymbol{A} - \mathfrak{q}\mathbf{I} & [\boldsymbol{B}_u & \boldsymbol{B}_f] \\ \boldsymbol{C} & [\boldsymbol{D}_u & \boldsymbol{D}_f] \end{bmatrix}$$

The observer form is linked to the original system through a full rank matrix that does not affect the rank of Rosenbrock matrix.

According to Theorem 3.1, $n_y \geq n_u$ is a necessary condition for system 5.1 to be a left invertible system, i.e., the system must have at least as many outputs as inputs. As a matter of fact, this condition usually holds in most practical systems, and it is not restrictive.

Assumption 5.1 (Detectability)**.** . The fault matrices $\boldsymbol{B}_f$ and $\boldsymbol{D}_f$ satisfy the rank condition $\max(\text{rank}\,[\boldsymbol{B}_f^\top \quad \boldsymbol{D}_f^\top]) = n_f$, which is a necessary condition for the fault detectability.

The fault subsystem $(\boldsymbol{A}, \boldsymbol{B}_f, \boldsymbol{C}, \boldsymbol{D}_f)$ satisfies Assumption 5.1, and is τ-delay left invertible, where τ represents the corresponding relative degree. It is worth to note that for strictly proper fault subsystems with nonzero relative degree ($\boldsymbol{D}_f = \boldsymbol{0}$), left invertibility implies that the underlying time-shifted system is a bi-proper system that can be inverted. Furthermore, fault estimation in the presence of transmission zeros is a significant challenge in actuator fault scenarios. Consequently, we shall consider the problematic case of actuator fault throughout the rest of chapter, that is,

$$j\text{-th actuator fault: } \boldsymbol{B}_f = \boldsymbol{B}_u^{(:,j)}, \quad \boldsymbol{D}_f = \boldsymbol{D}_u^{(:,j)}$$

where $X^{(:,j)}$ denotes the j-th column of the matrix X. For the sake of brevity in subsequent analysis, we further assume that the fault signals affect all the input component/channels, i.e., $n_f = n_u$, while recovering the general case is straightforward.

As faulty datasets are often not available in practice, the following assumption is required to be made on the collected data.

Assumption 5.2 (Data regularity)**.** Fault-free input–output (input–output) data obtained from the system is available for the proposed data-driven design. Moreover, the input signal $u(k)$ is persistently exciting of sufficient order.

Problem. Given only the fault-free input–output data from system (3.1), provide a stable data-driven fault estimator for the unknown actuator fault signal $\boldsymbol{f}(t)$ in the presence of disturbances without knowing the system matrices, where the underlying fault subsystem can be an NMP system. No assumption on the fault signal evolution over time has been made.

5.2.1 Model

Since the proposed method is developed for a data-driven application, the system (5.2) can be expressed from input–output perspective. To do so, the prediction form (5.2) can be consistently represented by a VARX (vector autoregressive with exogenous inputs) model of sufficiently large order p [147]:

$$\mathrm{A}(\mathfrak{q}^{-1})\boldsymbol{y}(t) = \mathrm{B}(\mathfrak{q}^{-1})(\boldsymbol{u}(t) + \boldsymbol{f}(t)) + \boldsymbol{\varepsilon}(t), \tag{5.3}$$

where $\mathfrak{q}^{-1}$ is the backward shift operator, $\mathrm{A}(\mathfrak{q}^{-1}) = \mathbb{I}_{n_y} - \sum_{i=1}^{p} \boldsymbol{M}_i^y \mathfrak{q}^{-i}$, $\mathrm{B}(\mathfrak{q}^{-1}) = \sum_{i=0}^{p} \boldsymbol{M}_i^u \mathfrak{q}^{-i}$, and $\boldsymbol{\varepsilon}(t) \in \mathbb{R}^{n_y}$ represents noise signals as a sequence of independent and identically distributed (*i.i.d.*) multivariate random variable. $\boldsymbol{M}_i^u$ and $\boldsymbol{M}_i^y$ are associated predictor Markov parameters defined as follows

$$\boldsymbol{M}_i^u = \begin{cases} \boldsymbol{D} & i = 0 \\ \boldsymbol{C}\tilde{\boldsymbol{A}}^{i-1}\tilde{\boldsymbol{B}}_u & i > 0 \end{cases}, \; \boldsymbol{M}_i^y = \begin{cases} \boldsymbol{0} & i = 0 \\ \boldsymbol{C}\tilde{\boldsymbol{A}}^{i-1}\boldsymbol{K} & i > 0 \end{cases}.$$

Motivation: The existing data-driven FE solutions in the literature [25, 45, 120] are fully parameterized by the estimated MPs of the VARX model (5.3) using fault-free input–output data collected from (3.1). The identified model is followed by an inversion operation to reconstruct the fault signal. In this chapter, these approaches are referred to as *indirect methods* for FE. However, they give raise to two issues that can be highlighted. Firstly, in practice, identification errors are inevitable in the presence of noise, leading to nonlinear propagation of errors into the fault estimation. Secondly, the identification process should align with the intended use of the model. In FE, the ultimate goal of the identification step is to be inverted as a cascade filter with the original system. Thus, the estimated model in indirect methods may not be necessarily optimal for the purpose of inverse model. To overcome the aforementioned issues, we propose directly identifying the underlying inverse system from the real input–output data, and reconstructing the fault signal subsequently called the *direct method* in this study (see Figure 5.1). More importantly, this approach optimizes the identified model specifically for FE.

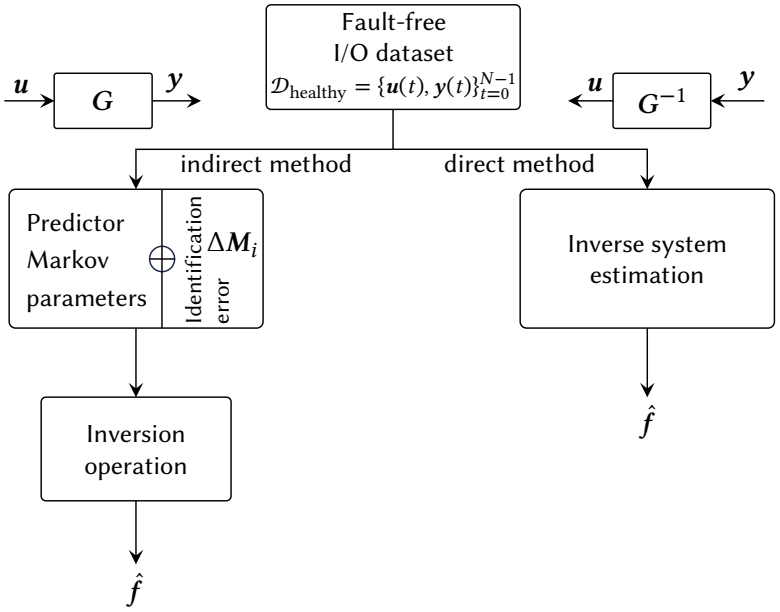

Figure 5.1: Comparison of the proposed direct and indirect (two-steps) fault estimation methods.

5.3 Main Result

In this section, an inverse-system-based filter is developed for the data-driven fault estimation problem. Figure 5.2 illustrates the general configuration for which the proposed filter is designed, with $\boldsymbol{d}$ encompassing all unknown signals except for the fault signal. This structure underscores the requirement for the underlying system from the fault to the output to be a left invertible system.

Suppose linear maps $\boldsymbol{G} : \mathbb{R}^{n_u} \to \mathbb{R}^{n_y}$ and $\boldsymbol{G}^{-1} : \mathbb{R}^{n_y} \to \mathbb{R}^{n_u}$ represent the nominal sys-

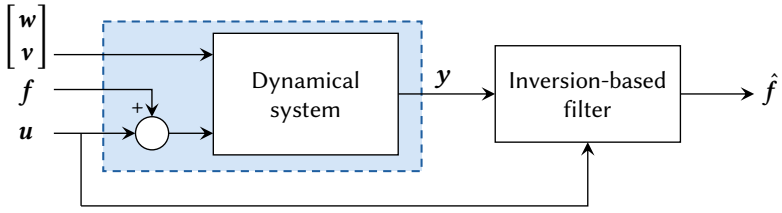

Figure 5.2: Fault estimation scheme based on system inversion, with the actuator fault modeled as an additive signal.

tem and its left inverse, respectively. In the absence of process and measurement noises, i.e., $(\boldsymbol{w}, \boldsymbol{v}) = \mathbf{0}$, the estimation performance $\boldsymbol{f} - \hat{\boldsymbol{f}}$ can be quantified as

$$\boldsymbol{f} - \hat{\boldsymbol{f}} = (\mathbf{I} - G^{-1}G)(\boldsymbol{u} + \boldsymbol{f}). \tag{5.4}$$

Based on (5.4), perfect fault estimation is achieved if $\mathbf{I} - G^{-1}G = \mathbf{0}$. This condition depends on the accuracy of the system inversion to the true inverse of the system. The main goal of the proposed filter is to minimize this difference in order to enhance the reconstruction of fault signals, which is a challenging task when both the actual system parameters and the fault signal are unknown. Regarding the data-driven design, the problem should be parameterized, where Markov parameters are the well-known choice to describe the linear dynamical systems (see Equation (5.3)). In contrast to the available indirect methods, we propose to directly estimate the corresponding Markov parameters of the inverse system from input–output data. More precisely, the estimated model in the direct approach considers the system output $y(k)$ as the input, and the input signal $\boldsymbol{u}(t)$ as the output, i.e., $\boldsymbol{y}(t) \overset{G^{-1}}{\longmapsto} \boldsymbol{u}(t)$.

To develop the direct approach, the inverse system can also be described based on the predictor Markov parameters of a VARX model if we rearrange the model in (5.3) with respect to the input signal in a fault-free condition.

$$\begin{aligned} \mathrm{B}(\mathrm{q}^{-1})\boldsymbol{u}(t) &= \mathrm{A}(\mathrm{q}^{-1})\boldsymbol{y}(t) - \boldsymbol{\varepsilon}(t) \\ &= \mathrm{A}(\mathrm{q}^{-1})\boldsymbol{y}(t) + \boldsymbol{\varepsilon}'(t) \end{aligned} \tag{5.5}$$

This implies that the inverse of a VARX model is another VARX model. There are, however, two major differences. Unlike the model in (5.3), the stability of the inverse model relies on the characteristics of $\mathrm{B}(\mathrm{q}^{-1})$, while simultaneously, the autoregressive behavior of the stochastic noise term is also dictated by $\mathrm{B}(\mathrm{q}^{-1})$. Hence, ensuring stability in the inverse system is a crucial aspect to be taken into account in the proposed scheme. For systems with NMP transmission zeros, the inverse VARX model results in an unstable filter with poles outside the unit circle. Additionally, strictly proper systems feature an improper inverse model, leading to the amplification of high-frequency components, including noise signals.

5.3.1 Inverse-System-Based Filter

We aim at providing a stable inverse-system-based filter (ISF) to be used for fault estimation in the presence of NMP zeros. To this end, stable inversion techniques are developed

in which the central idea involves treating the unstable internal dynamics as stable noncausal operators in order to produce bounded responses [193]. The noncausality viewpoint implies that the desired trajectory must be known ahead of time over a preview horizon. Since the proposed filter parameters are derived from only the fault-free input–output data, the preview information of the trajectory is available to the design scheme and is not a limitation. In turn, the preview window would naturally cause estimation delay that should be minimized. Hence, the resulting filter is a combination of causal and noncausal components of the inverse system. In order to take advantage of preview-based methods, the following assumption has to be made.

Assumption 5.3 (No transmission zeros on the unit circle)**.** The system $(\boldsymbol{A}, \boldsymbol{B}_u, \boldsymbol{C}, \boldsymbol{D}_u)$ has no transmission zeros on the unit circle, i.e.,

$$\operatorname{rank}\left(\begin{bmatrix} \boldsymbol{A}-\mathfrak{q}\mathbf{I} & \boldsymbol{B}_u \\ \boldsymbol{C} & \boldsymbol{D}_u \end{bmatrix}\right) = n + n_u, \quad \forall \mathfrak{q} \in \mathbb{C},\ |\mathfrak{q}| = 1.$$

Most of the solutions in the literature explicitly decouple stable and unstable dynamics of the inverted system in the state-space representation through an eigenvalue decomposition [45, 192, 193], whereas the states of the system are not readily accessible in data-driven applications. Moreover, these filters are parameterized by the left inverse of matrix $\boldsymbol{D}$, which is not invertible in non-square systems. On the contrary, we describe the inverse system by a bilateral expansion of impulse responses, entirely independent of any knowledge of system states. The proposed method is completely realized based on the available input–output data points. In addition, it can handle non-square NMP systems without any further modification compared to [192, 194]. This parameterization will be presented in the following.

The inverse of any linear system that satisfies Assumption 5.3 can be described using the following two-sided representation based on the Laurent Series:

$$G^{-1}: \quad G^{\text{inv}}(\mathfrak{q}, \mathbf{H}) = \sum_{i=-\infty}^{\infty} \boldsymbol{H}_i \mathfrak{q}^{-i}; \quad i \in \mathbb{Z}, \tag{5.6}$$

where $G^{\text{inv}}(\mathfrak{q}, \mathbf{H})$ represents a bilateral impulse response expansion of the nominal left inverse system G^{-1}. In this representation, $H_i \in \mathbb{R}^{n_u \times n_y}$ is a matrix of expansion coefficients in the impulse response sequence $\mathbf{H} = \{\boldsymbol{H}_i\}_{i=-\infty}^{\infty}$, and the time shift operator $\mathfrak{q}$ allows the manipulation of multi-dimensional signals either forward or backward in time.

Remark 5.2. It is worth mentioning that the coefficients of the bilateral model (5.6) are in fact the Markov parameters associated with causal ('c') and noncausal ('nc') dynamics of the inverse system after eigenvalue decomposition, that is, a sequence of $\{\bar{\boldsymbol{C}}_{\text{c}} \bar{\boldsymbol{A}}_{\text{c}}^{i-1} \bar{\boldsymbol{B}}_{\text{c}}, \bar{\boldsymbol{C}}_{\text{nc}} \bar{\boldsymbol{A}}_{\text{nc}}^{i-1} \bar{\boldsymbol{B}}_{\text{nc}}, \bar{\boldsymbol{D}}\}$ form.

Given the model (5.6), the input–output relation in a noise-free condition can be written as

$$\boldsymbol{u}(k) = \mathbf{H} * \boldsymbol{y}(t) = \sum_{i=-\infty}^{\infty} \boldsymbol{H}_i \boldsymbol{y}(t-i); \quad i \in \mathbb{Z}, \tag{5.7}$$

where $*$ denotes discrete convolution, and the input signal at time t is a convolution of the output signal with the bilateral Markov parameter sequence $\mathbf{H}$. Therefore, negative time-delays $i \in \{\ldots, -2, -1, 0, 1, \ldots\}$ are acceptable, making the model noncausal and dependent

on both past and future input data at each instant. As a result, the fault estimation filter parameterized by $\mathbf{H}$ can be proposed as

$$\text{ISF filter: } \boldsymbol{f}(t) = \sum_{i=-\infty}^{\infty} \boldsymbol{H}_i \boldsymbol{u}^{\text{ISF}}(t-i) - \boldsymbol{u}(t); \quad i \in \mathbb{Z}, \tag{5.8}$$

with $\boldsymbol{u}^{\text{ISF}}$ as the input of the filter. Hence, the filter design boils down to estimating the sequence $\mathbf{H}$ from healthy data. Let $\mathcal{D}_{\text{healthy}}$ be the set of fault-free measurement data as $\mathcal{D}_{\text{healthy}} := \{\boldsymbol{u}(t), \boldsymbol{y}(t)\}_{t=0}^{N-1}$. To estimate the parameters of bilateral model (5.6) in terms of mean-squared error criterion, the following optimization problem can be considered

$$\hat{\mathbf{H}} := \arg \min_{\{\boldsymbol{H}_i\}_{i=-\infty}^{\infty} \in \mathbb{R}^{n_u \times n_y}} \frac{1}{N} \sum_{t=0}^{N-1} \left\| \boldsymbol{u}(t) - \sum_{i=-\infty}^{\infty} \boldsymbol{H}_i \boldsymbol{y}(t-i) \right\|_2^2$$

This problem can be reformulated as

$$\hat{\boldsymbol{\theta}} := \arg \min_{\{\boldsymbol{\theta}_i\}_{i=-\infty}^{\infty} \in \mathbb{R}^{n_u n_y}} \frac{1}{N} \sum_{t=0}^{N-1} \left\| \boldsymbol{u}(t) - \sum_{i=-\infty}^{\infty} (\boldsymbol{y}^\top(t-i) \otimes \mathbf{I}_{n_u}) \boldsymbol{\theta}_i \right\|_2^2 \tag{5.9}$$

with $\boldsymbol{\theta}_i = \text{vec}(\boldsymbol{H}_i)$. Examining (5.9) shows that an infinite dimensional optimization problem should be solved to retrieve the parameters of model (5.6). This is because the VARX model (5.5) is described by a two-sided infinite impulse response model, wherein the set of corresponding Markov parameters has no compact support. Consequently, achieving the exact inverse of the system from a finite number of noisy measurements in the learning phase is an ill-posed problem leading to high estimation variance. To address ill-posedness and overfitting, regularization should be introduced into the regression problem. Kernel-based regularization is a technique commonly employed in the machine learning theory to robustify the prediction model performance against unseen data by making a trade-off between bias and variance. Moreover, it provides a flexible framework to incorporate prior knowledge about the system behavior into the decision variables [195]. This approach can capture aspects including stability, smoothness, noncausality, and model complexity.

5.3.2 Kernel-Based Regularization

In order to introduce regularization, we limit the hypothesis space to a class of reproducing kernel Hilbert space (RKHS) $\mathcal{H}_\kappa$ that can be uniquely characterized by a positive semidefinite kernel function κ [196]. As a result, designing the kernel function is at the core of kernel-based methods, as it directly influences the representation and generalization capabilities of the model. In this regard, we penalize the feasible solutions that do not align with the prior knowledge by including a regularization term associated with the induced norm on $\mathcal{H}_\kappa$ in the optimization problem (5.9)

$$\begin{aligned} \hat{\boldsymbol{\theta}} := \arg \min_{\boldsymbol{\theta} \in \mathcal{H}_\kappa} \frac{1}{N} \sum_{t=0}^{N-1} \left\| u(t) - \sum_{i=-\infty}^{\infty} (\boldsymbol{y}^\top(t-i) \otimes \mathbf{I}_{n_u}) \boldsymbol{\theta}_i \right\|_2^2 \\ + \mu \|\boldsymbol{\theta}\|_{\mathcal{H}_\kappa}^2. \end{aligned} \tag{5.10}$$

in which $\theta = \begin{bmatrix} \theta_{-\infty}^\top & \cdots & \theta_{\infty}^\top \end{bmatrix}^\top$ is the column stack of θ_i, and the positive scalar $\mu > 0$ is the regularization parameter to create a bias–variance balance. An immediate result of adopting RKHS function space is that the infinite-dimensional problem (5.10) has a finite-dimensional solution according to the representer theorem [195]. In the proposed optimization problem (5.10), kernels also accounts for noncausal terms in the impulse response expansion (5.7) for general NMP systems. Noncausal kernels are recently introduced in [197], where negative indices are allowed for kernels as well. Henceforth, we define the (i, j) element of the kernel matrix $[\mathbf{K}_\kappa]_{ij}$ corresponds to the real-valued kernel function κ as $\kappa(t_i, t_j; \boldsymbol{\alpha}) : \mathbb{Z} \times \mathbb{Z} \to \mathbb{R}$ in contrast to the conventional input space $\mathbb{Z}_{\geq 0} \times \mathbb{Z}_{\geq 0}$. The kernel matrix $\mathbf{K}_\kappa(\boldsymbol{\alpha})$ is a positive semidefinite matrix ($\mathbf{K}_\kappa(\boldsymbol{\alpha}) \succeq 0$) parameterized in terms of $\boldsymbol{\alpha}$, a set of hyperparameters that depends on the type of kernels in use. In [195], it is shown that taking the kernel matrix $\mathbf{K}_\kappa = \theta_{\text{true}} \theta_{\text{true}}^\top$ is the optimal choice in terms of mean-squared error in the presence of noise, where θ_{true} denotes "true" model parameters. This implies that kernels can be designed in the sense of reflecting the optimal kernel behavior even though θ_{true} is not known in practice.

Remark 5.3. It is notable that the way the optimization problem is formulated in (5.10) paves the way of using a scalar type of basis functions for MIMO systems, which are more commonly utilized in kernel-based regularization problems.

Rational Orthonormal Basis Functions

Orthonormal basis functions (OBFs) kernels have been demonstrated to be effective in describing a wide range of linear dynamical systems, as well as estimating impulse responses [198]. Since the proposed fault estimation filter is formulated on the basis of bilateral impulse responses, OBF-based kernels are considered for the ISF. These basis functions are essentially a network of interconnected transfer functions in a cascading fashion. Whereas a finite number of bases is often required in practice, each basis function has an infinite impulse response sequence that enables the design scheme to effectively capture slow dynamics with a relatively small number of basis functions compared to other methods [199]. These advantages motivate the use of rational OBFs recently presented in [197], which is an extension of the so-called Takenaka-Malmquist basis functions for noncausal systems. Let $G^{\text{inv}}(\mathfrak{q}) \in \mathcal{RL}_2^{n_u \times n_y}(\mathbb{T})$ denotes the inverse system. Under Assumption 5.3, $G^{\text{inv}}(\mathfrak{q})$ can be decomposed with a complete set of scalar orthonormal basis functions for $\mathcal{RL}_2(\mathbb{T})$ as

$$G^{\text{inv}}(\mathfrak{q}) = \sum_{i=-\infty}^{\infty} G_i \psi_i(\mathfrak{q}) \tag{5.11}$$

where $G_i \in \mathbb{R}^{n_u \times n_y}$ is a sequence of matrices whose (m, n) entry $G_i^{[m,n]}$ is computed from $G_i^{[m,n]} = \langle \psi_i, G_{[m,n]}^{\text{inv}} \rangle_{\mathcal{L}_2}$ in which $G_{[m,n]}^{\text{inv}}$ denotes the mth input and nth output channel of $G^{\text{inv}}(\mathfrak{q})$. This expansion can be viewed as a generalization of the bilateral impulse response model in (5.6) with the time shift operator $\{\mathfrak{q}^{-i}\}_{i=-\infty}^{\infty}$. In this regard, we define noncausal

OBF kernels as

$$\psi_i(\mathfrak{q}) = \begin{cases} \psi_i^{\mathrm{c}}(\mathfrak{q}) = \dfrac{\sqrt{1-|\lambda_{\mathrm{c},i}|^2}}{\mathfrak{q}-\lambda_{\mathrm{c},i}} \displaystyle\prod_{j=1}^{i-1} \frac{1-\overline{\lambda_{\mathrm{c},j}}\,\mathfrak{q}}{\mathfrak{q}-\lambda_{\mathrm{c},j}} & i>0\,, \\ \psi_i^{\mathrm{ac}}(\mathfrak{q}) = \dfrac{\sqrt{1-|\lambda_{\mathrm{ac},i}|^2}}{1-\overline{\lambda_{\mathrm{ac},i}}\,\mathfrak{q}} \displaystyle\prod_{j=-1}^{i+1} \frac{\mathfrak{q}-\lambda_{\mathrm{ac},j}}{1-\overline{\lambda_{\mathrm{ac},j}}\,\mathfrak{q}} & i<0\,, \\ \psi_i^{\mathrm{ac}}(\mathfrak{q}) = \{0,1\} & i=0\,, \end{cases} \tag{5.12}$$

in which $\{\lambda_{\mathrm{c},i}\}_{i\in\mathbb{Z}_{\geq 0}}, \{\lambda_{\mathrm{ac},i}\}_{i\in\mathbb{Z}\setminus\mathbb{Z}_{\geq 0}} \subset \mathbb{D}$ are sequences of generating poles that play the role of hyperparameters in the kernel design, i.e., $\boldsymbol{\alpha} = \{\lambda_{\mathrm{c}}, \lambda_{\mathrm{ac}}\}$. To guarantee real-valued impulse responses, the set of poles should appear as either real numbers or pairs of complex conjugate numbers to span $\mathcal{RL}_2(\mathbb{T})$. For the sake of completeness of basis, the conditions I)$\sum_{i=1}^{\infty}(1-|\lambda_{\mathrm{c},i}|)=\infty$, II)$\sum_{i=-\infty}^{-1}(1-|\lambda_{\mathrm{ac},i}|)=\infty$ have to be satisfied. Direct feedthrough can be included in basis functions by setting $\psi_0^{\mathrm{ac}}=1$. The proposed noncausal OBFs are orthonormal with respect to the unit circle in the sense that

$$\frac{1}{2\pi}\oint_{\mathbb{T}} \psi_i(e^{j\omega})\,\overline{\psi_j(e^{j\omega})}\,\mathrm{d}\omega = \delta_{i,j}$$

$\{\psi_i^{\mathrm{c}}\}_{i>0}$ and $\{\psi_i^{\mathrm{ac}}\}_{i\leq 0}$ form causal and anti-causal basis functions, respectively. As we aim at estimating impulse responses of the inverse system, the time-domain counterpart of the proposed basis should be derived. To do so, the corresponding basis functions in time-domain can be computed by taking the inverse z-transform $\mathrm{Z}^{-1}\{\cdot\}$ of the rational OBFs with respect to the valid region of convergence. Therefore, $\phi_i(t) = \mathrm{Z}^{-1}\{\psi_i(\mathfrak{q})\}$ denotes the corresponding basis function in the time-domain. Since $\{\psi_i\}_{i=-\infty}^{\infty}$ is a complete basis of Hilbert space $\mathcal{RL}_2$, a similar argument applies to the time-domain basis functions $\{\phi_i\}_{i=-\infty}^{\infty}$ to verify that they are complete in $\mathcal{R}\ell_2(\mathbb{Z})$ and orthonormal:

$$\sum_{t=-\infty}^{\infty} \phi_i(t)\,\overline{\phi_j(t)} = \delta_{i,j}$$

Accordingly, the bilateral impulse response $g(t)\in\mathcal{R}\ell_2(\mathbb{Z})$ associated with $\boldsymbol{G}^{\mathrm{inv}}(\mathfrak{q})$ in (5.11) can be equivalently expressed by

$$g(t) = \sum_{i=-\infty}^{\infty} g_i\phi_i(t),$$

Hence, the following kernel function is built

$$\kappa_{\mathrm{OBF}}(t_i,t_j;\{\lambda_{\mathrm{c}},\lambda_{\mathrm{ac}}\}) = \sum_{i=-\infty}^{\infty} \phi_i(t_i)\,\overline{\phi_i(t_j)}. \tag{5.13}$$

It can be shown that it is a reproducing kernel for the RKHS space spanned by $\{\phi_i\}_{i=-\infty}^{\infty}$. In practice, a finite number of basis functions is used for the estimation while accepting a certain level of error, which can be made arbitrarily small by increasing the model order. For an efficient implementation, see Chapter C. To ensure a specified level of approximation error, the required preview time is determined by the closest NMP zero of the original system to the unit circle [45, 193]. Denote by n_{ac} and n_{c} the number of anti-causal and causal terms in (5.6), respectively. Then define the stacked vector of data over N measurements as

$$\mathbf{u}_N := \begin{bmatrix} \boldsymbol{u}^\top(n_{\mathrm{c}}+1) & \boldsymbol{u}^\top(n_{\mathrm{c}}+2) & \cdots & \boldsymbol{u}^\top(N-n_{\mathrm{ac}}) \end{bmatrix}^\top,$$

and the block-Toeplitz structure of output data

$$\overset{\approx}{\mathbf{Y}}_N := \begin{bmatrix} \boldsymbol{y}^\top(n_{\mathrm{c}}+n_{\mathrm{ac}}+1) & \boldsymbol{y}^\top(n_{\mathrm{c}}+n_{\mathrm{ac}}) & \cdots & \boldsymbol{y}^\top(1) \\ \boldsymbol{y}^\top(n_{\mathrm{c}}+n_{\mathrm{ac}}+2) & \boldsymbol{y}^\top(n_{\mathrm{c}}+n_{\mathrm{ac}}+1) & \cdots & \boldsymbol{y}^\top(2) \\ \vdots & \vdots & \ddots & \vdots \\ \boldsymbol{y}^\top(N) & \boldsymbol{y}^\top(N-1) & \cdots & \boldsymbol{y}^\top(N-n_{\mathrm{c}}-n_{\mathrm{ac}}) \end{bmatrix}.$$

Consider $\boldsymbol{\theta} = \mathrm{vec}\big(\begin{bmatrix} \boldsymbol{H}_{-n_{\mathrm{ac}}} & \cdots & \boldsymbol{H}_0 & \cdots & \boldsymbol{H}_{n_{\mathrm{c}}} \end{bmatrix}\big) \in \mathbb{R}^{n_\theta}$ with $n_\theta = n_y n_u (n_{\mathrm{ac}} + n_{\mathrm{c}} + 1)$. Using (5.10) and the kernel matrix $\mathbf{K}_\kappa(\boldsymbol{\alpha}) \in \mathbb{R}^{n_\theta \times n_\theta}$ associated with (5.13), the model parameters are the solution of the following optimization problem

$$\begin{aligned} \hat{\boldsymbol{\theta}} &:= \arg\min_{\boldsymbol{\theta}\in\mathbb{R}^{n_\theta}} \frac{1}{N}\|\mathbf{u}_N - X\boldsymbol{\theta}\|_2^2 + \frac{\mu}{N}\boldsymbol{\theta}^\top \mathbf{K}_\kappa(\boldsymbol{\alpha})^{-1}\boldsymbol{\theta} \;\text{ with }\; X = \overset{\approx}{\mathbf{Y}}_N \otimes \mathbf{I}_{n_u}, \\ &= (\mathbf{K}_\kappa(\boldsymbol{\alpha})X^\top X + \mu \mathbf{I}_{n_\theta})^{-1}\mathbf{K}_\kappa(\boldsymbol{\alpha})X^\top \mathbf{u}_N. \end{aligned} \tag{5.14}$$

In case the kernel matrix is rank deficient, the optimization problem can be modified based on the singular value decomposition of kernel matrix, as suggested in [195, Remark 1]. In view of $\mathbf{K}_\kappa = \boldsymbol{\theta}_{\mathrm{true}}\boldsymbol{\theta}_{\mathrm{true}}^\top$, the poles of rational OBF, $\{\lambda_{\mathrm{c}}, \lambda_{\mathrm{ac}}\}$, can be designed to approximate the true dynamics of the inverse system G^{-1}. Since the inverse fault subsystem is estimated by solving the optimization problem (5.14), the fault estimator of $\boldsymbol{f}(t)$ is given without performing any further operation as

$$\hat{\boldsymbol{f}}(t) = \sum_{i=-n_{\mathrm{ac}}}^{n_{\mathrm{c}}} \hat{\boldsymbol{H}}_i^\theta \, \boldsymbol{u}^{\mathrm{ISF}}(t-i) - \boldsymbol{u}(t). \tag{5.15}$$

The proposed fault estimation design scheme is summarized in Algorithm 1.

Algorithm 1 Fault Estimation Cycle

Require: $\mathcal{D}_{\text{healthy}} = \{\boldsymbol{u}(t), \boldsymbol{y}(t)\}_{t=0}^{N-1}, n_{\text{c}}, n_{\text{ac}}, \{\lambda_{\text{c}}, \lambda_{\text{ac}}\}, \mu$.

1: Compute kernel matrix $\mathbf{K}_{\kappa}$ elements based on OBF basis functions (5.12) and kernel function (5.13) in the time domain.
2: Solve the convex optimization problem (5.14) using $\mathcal{D}_{\text{healthy}}$.
3: Construct the estimation of bilateral Markov parameter sequence $\{\hat{\boldsymbol{H}}_i^{\theta}\}_{i=-n_{\text{ac}}}^{n_{\text{c}}}$ by rearranging $\hat{\boldsymbol{\theta}}$.
4: $\boldsymbol{u}^{\text{ISF}} \leftarrow$ real output $\boldsymbol{y}_{\text{real}}$ ▷ Online implementation
5: Estimate fault signal using filter (5.15) in the real-time.

Ensure: $\hat{f}(t)$.

5.4 Simulation Results

To show the effectiveness of the proposed method compared to the state-of-the-art method [45], the following Monte Carlo experiment is provided.

Consider a linear dynamical system with the following minimal realization of state-space representation

$$\begin{aligned} \boldsymbol{A} &= \begin{bmatrix} 2.000 & 1.000 & 0 \\ -1.230 & 0 & 1.000 \\ 0.216 & 0 & 0 \end{bmatrix}, \quad \boldsymbol{B}_u = \begin{bmatrix} -0.100 \\ 0.370 \\ -0.334 \end{bmatrix} \\ \boldsymbol{C} &= \begin{bmatrix} 1 & 0 & 0 \end{bmatrix}, \quad \boldsymbol{D}_u = 1, \end{aligned} \tag{5.16}$$

where the associated transfer function is given by

$$\boldsymbol{G}(\mathfrak{q}) = \frac{(\mathfrak{q}^2 - \mathfrak{q} + 0.5)(\mathfrak{q} - 1.1)}{(\mathfrak{q} - 0.3)(\mathfrak{q} - 0.8)(\mathfrak{q} - 0.9)}.$$

This system possesses an NMP zero at $\mathfrak{q} = 1.1$ while the rest of zeros are inside the unit circle ($\mathfrak{q} = 0.5 \pm 0.5i$). The fault matrix is $\boldsymbol{B}_f = \boldsymbol{B}_u$, and $\boldsymbol{B}_w = \mathbf{I}_3$ for the process noise. The process and measurement noises are zero mean white noises generated from Gaussian distributions as $\boldsymbol{w}(t) \sim \mathcal{N}(0, 0.01\mathbf{I}_3)$ and $\boldsymbol{v}(t) \sim \mathcal{N}(0, 0.01)$, respectively. In addition, the following fault signal is considered in these experiments

$$f(t) = \begin{cases} 0 & t \leq 50 \\ \sin(0.1\pi t) & 50 < t \leq 200 \\ 2 & t > 200 \end{cases}.$$

To design the fault estimation filter, a data set of $\{\boldsymbol{u}(t), \boldsymbol{y}(t)\}_{t=0}^{N-1}$ healthy input–output samples with $N = 1000$ is collected after applying a persistently exciting input signal. The signal-to-noise ratio (SNR) is kept at the high level of SNR = 20 dB. A bilateral impulse response model for the inverse system will be estimated using (5.10). The model order in the proposed direct approach is selected as $n_{\text{c}} = 20$ and $n_{\text{ac}} = 40$. The hyper parameters of OBF kernels are designed according to $\{\lambda_{\text{c},i}\} = \texttt{linspace}(0.4, 0.6, n_{\text{c}})$ and

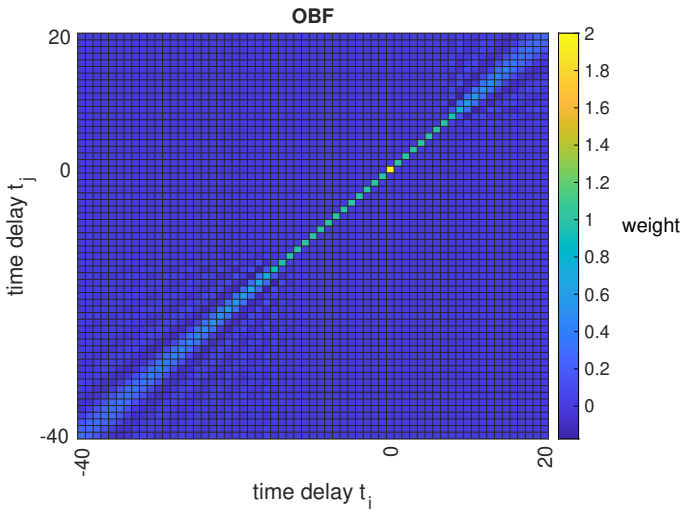

Figure 5.3: Realization of the kernel matrix associated with the orthonormal basis function kernels designed in Section 5.4.

$\{\lambda_{\mathrm{ac},i}\} = \texttt{linspace}(0.8, 0.9, n_{\mathrm{ac}})$ together with a nonzero direct feedthrough. The corresponding Kernel matrix is illustrated in Figure 5.3. The true two-sided expansion of the inverse system and its estimation is provided in Figure 5.4. The Markov parameters of VARX model (5.3) related to (5.16) are estimated using the predictor-based subspace identification (PBSID) method in [147]. These MPs are building blocks of the receding horizon filter proposed in [45]. A VARX model of order $3L$ with $L = 50$ is identified for the system (Figure 5.5).

5.4.1 Comparison Study

The fault reconstruction performance of the proposed ISF filter and the result of [45] are assessed in terms of normalized estimation error $\frac{\|f-\hat{f}\|^2}{\|f\|^2}$ and VAF (variance accounted for). A Monte Carlo simulation involving 300 runs is conducted with *i.i.d.* realization for process and measurement noises, following the specified distributions. A multi-step input signal is considered, which is more realistic in operational conditions. Both approaches are compared in Figure 5.6. Despite the perfect performance of MPs identification, a clear bias in the estimation can be seen using the filter in [45]. In contrast, the proposed ISF filter leads to an almost unbiased estimation. This result resonates with the fact that nonlinear propagation of identification errors via an inversion operation can introduce a noticeable bias in indirect approaches, even when they are small. This issue is addressed in the proposed method by directly designing the filter parameters from the input–output data, where the identification errors are linear with respect to FE error. The estimation bias due to truncation can be controlled through regularization trade-off. Figure 5.7 presents the estimated fault signals along with their corresponding estimation errors for a specific noise realization. In this simulation, we also demonstrate that receding horizon filter [45] based on the true MPs is unbiased. In addition, the proposed filter offers two more advantages over

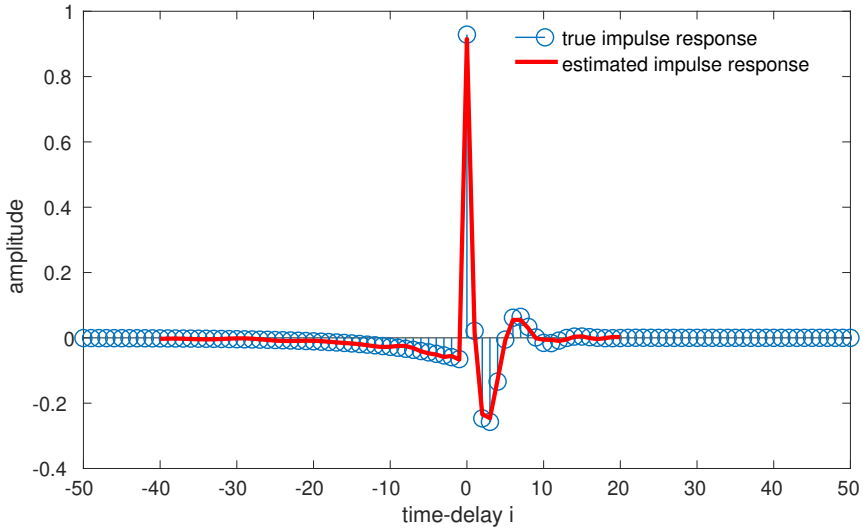

Figure 5.4: Bilateral impulse response estimation performance. The blue circles indicate the ground-truth impulse responses, while the red circles represent their truncated estimates.

the recent literature. First, the ISF filter order is much lower than the receding horizon filter with time window length of $3L+1 = 151$. This sliding window in the ISF filter is only 60. This implies less delay in the estimation of the fault signal from practical point of view. For a fair comparison, L is chosen small enough to obtain an unbiased estimation with the true MPs. Second, computational efficiency for online applications. The indirect approach demands computational complexity of $\mathcal{O}(3L+1)^3$ in each iteration because of the inversion operation, whereas the proposed direct filter does not require any inversion.

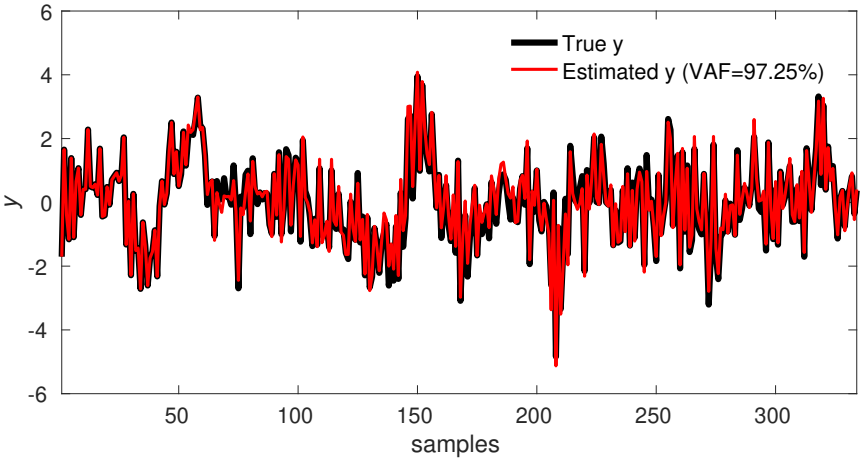

Figure 5.5: The output prediction performance of the identified VARX model.

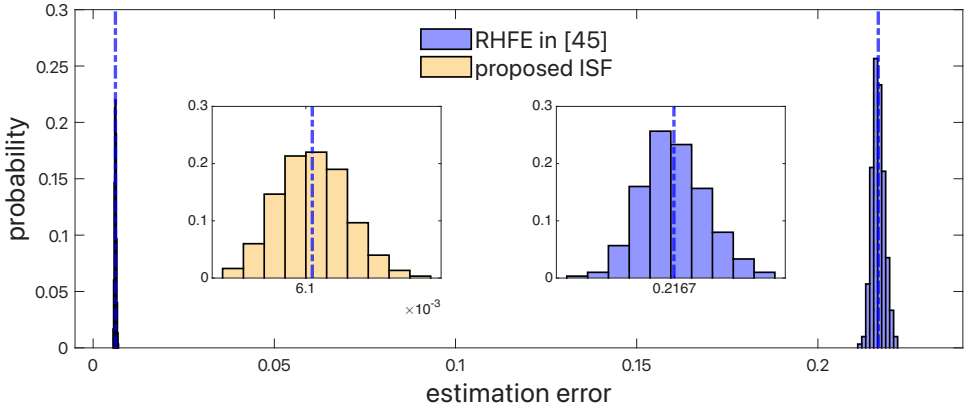

Figure 5.6: Fault estimation error distributions for the proposed direct inverse-based filter (light yellow) and the state-of-the-art indirect two-step approach proposed in [45] (purple).

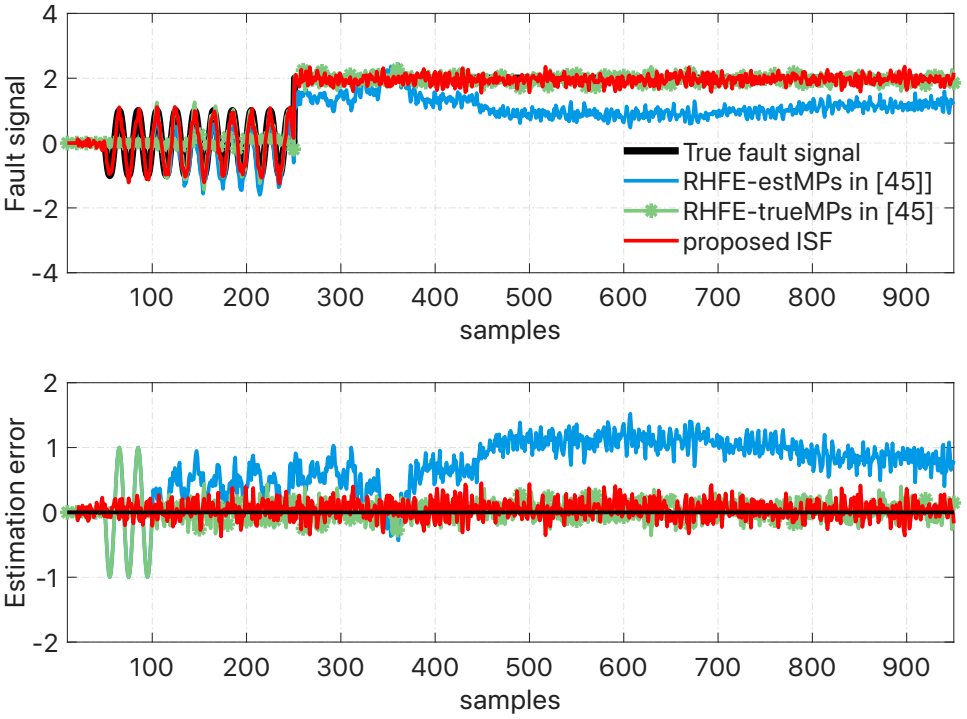

Figure 5.7: The proposed fault estimation performance in comparison with the state-of-the-art method in [45] for one specific noise realization. (Top) The black line denotes the ground truth fault signal, while the red, blue, and green lines represent estimates obtained using the proposed direct filter, the indirect method in [45] with an estimated truncated forward model, and the same method with the true truncated forward model, respectively. (Bottom) The corresponding estimation errors.

5.5 Conclusions

This chapter presents a data-driven fault estimation method for linear systems, including those with unstable transmission zeros. The challenges posed by NMP zeros are addressed by representing the inverse system through bilateral impulse responses, resulting in a mixed causal and noncausal model. Unlike existing inversion-based approaches, the proposed method identifies the inverse fault subsystem directly from input–output data, avoiding the propagation of forward-model identification errors through inversion. Moreover, it employs kernel-based regularization with OBF kernels not only to reduce the filter order but also to incorporate prior knowledge of the inverse system, enhancing performance on unseen data. Simulation studies demonstrate that the proposed direct approach can outperform existing indirect methods.

6

Active Learning

Even though system identification of linear time-invariant systems is well established, determining their true order based purely on data remains a longstanding challenge. In this chapter, we address this via a novel input design method, which consists of two loops. In the outer loop, a hypothesized system order r is tested in the real system through an input designed in the inner loop. The input is designed to maximize the minimal singular value of the data matrices of the r-th order model approximation coming from standard identification methods. The design is enabled by a tractable optimization problem formulation that exploits the structure of the data, for which we propose an efficient first-order algorithm. We show that our proposed method not only increases the spectral gap used for order estimation, but also reduces identification error. Finally, numerical studies are provided to validate the effectiveness of the proposed method.

This chapter is partly based on *Input Design for System Order Estimation* [200].

6.1 Introduction

One of the most fundamental parameters of LTI systems is its order; yet, it is notoriously difficult to estimate it from raw input–output data. In fact, most identification methods either require prior knowledge of the system order or benefit substantially from it. For example, parametric identification methods generally require it as an input, while subspace methods circumvent this requirement by estimating the order of the system via a spectral gap analysis on relevant data matrices [48, 50]. However, successfully determining the order is highly dependent on the experiment that generated the data. Standard randomized inputs such as pseudo-random binary sequences sometimes fail to excite the right directions or dynamics to make them stand out against the noise, as reported for example by [201].

Several theoretical results exist on experiment design in the absence of noise. Initially this was achieved by the seminal paper [17] and its persistency of excitation (PE) lemma: in the absence of noise and with the input satisfying PE conditions, the spectral gap analysis reduces to a rank computation, which retrieves the correct system order. This framework has been relaxed when the goal is control instead of complete identification [202]. Classically, determining the order of an LTI system under noise is possible in the limit case of infinite data, by the consistency results in, e.g., [47, 48, 203]. In this limit case, the contribution of the noise vanishes in the spectral analysis. In the more realistic case of finite data, the qualitative notion of PE has been expanded to a quantitative version [49], which finds sufficient conditions on the input power so that the order is distinguishable during the spectral analysis. Given that the order is known, a substantial body of literature covers experiment design in order to maximize the accuracy of the obtained parameters, see [204–206] for the early works and [207–210] for a comprehensive list of more recent developments.

So far, the literature lacks a systematic method to design optimally exciting inputs to obtain the correct order of an LTI system in the presence of noise, in the realistic case of limited data availability from controlled experiments. In this work, we propose a method of designing a series of experiments to determine the order of an LTI system subject to noise. For that, we build on the subspace approach for model order determination, which is a spectral gap analysis.

Contributions. The method relies on the principle that input can be designed to both *confirm a model order* and *falsify a model order*. Given an input that improves the spectral gap for a given model, this improvement should also be reflected in the real system if the order is right. If the model order is larger than the real system's, no statistically relevant improvement in the spectral gap should be seen. To realize this method, we develop a first-order algorithm to design inputs that maximize the spectral gap given a model. We test our method on a simple example that already showcases the difficulty of using spectral analysis for order determination under random inputs. Our method consistently determines the right order of the system, and also results in a more accurate identification than that obtained from the baseline random input. Moreover, despite solving an inherently non-convex optimization problem, our input design algorithm is remarkably fast and stable, making it potentially useful as a tool on its own.

6.2 Problem Statement

Consider a finite-dimensional discrete-time LTI system subject to additive noise described as

$$\begin{aligned} \boldsymbol{x}(t+1) &= \boldsymbol{A}\boldsymbol{x}(t) + \boldsymbol{B}\boldsymbol{u}(t), \\ \boldsymbol{y}(t) &= \boldsymbol{C}\boldsymbol{x}(t) + \boldsymbol{D}\boldsymbol{u}(t) + \boldsymbol{e}(t), \end{aligned} \tag{6.1}$$

where, for $t \in \mathbb{Z}_{\geq 0}$, $\boldsymbol{x}(t) \in \mathbb{R}^n$, $\boldsymbol{u}(t) \in \mathbb{R}^{n_u}$, $\boldsymbol{y}(t) \in \mathbb{R}^{n_y}$, and $\boldsymbol{e}(t) \in \mathbb{R}^{n_y}$ denote the system states, input (control) signal, output signal, and additive measurement noise, respectively. The quadruple $(\boldsymbol{A}, \boldsymbol{B}, \boldsymbol{C}, \boldsymbol{D})$ is the minimal state-space realization with compatible dimensions. The additive noise $\boldsymbol{e}(k)$ is zero-mean, independent and identically distributed (i.i.d) white noise with variance ε_e^2, and is statistically independent of the input signal $\boldsymbol{u}(k)$. The corresponding Markov parameters are given by

$$\boldsymbol{M}_i = \begin{cases} \boldsymbol{D} & i = 0 \\ \boldsymbol{C}\boldsymbol{A}^{i-1}\boldsymbol{B} & i > 0 \end{cases}.$$

The first step in any subspace identification method requires the estimation of system's minimal order or the McMillan degree. To this end, we collect input–output (I/O) data points $\mathcal{D} := \{\boldsymbol{u}(t), \boldsymbol{y}(t)\}_{t=0}^{N-1}$ generated according to the system (6.1), which are the only measurable signals (states cannot be measured directly). Consequently, the data collected over $[0, N-1]$ can be arranged into the following Hankel form for time horizon L

$$\overset{///}{\mathbf{Y}}_{0,L,N} = \mathbf{O}_L \overset{///}{\mathbf{X}}_{0,1,N} + \overset{\gg}{\mathbf{M}}_L \overset{///}{\mathbf{U}}_{0,L,N} + \overset{///}{\mathbf{E}}_{0,L,N}, \tag{6.2}$$

where the extended observability $\mathbf{O}_L$ and the lower-triangular block-Toeplitz matrix of Markov parameters $\overset{\gg}{\mathbf{M}}_L$ are defined as

$$\mathbf{O}_L := \begin{bmatrix} \boldsymbol{C} \\ \boldsymbol{C}\boldsymbol{A} \\ \vdots \\ \boldsymbol{C}\boldsymbol{A}^{L-1} \end{bmatrix}, \quad \overset{\gg}{\mathbf{M}}_L := \begin{bmatrix} \boldsymbol{M}_0 & 0 & \cdots & 0 \\ \boldsymbol{M}_1 & \boldsymbol{M}_0 & \ddots & \vdots \\ \vdots & \ddots & \ddots & 0 \\ \boldsymbol{M}_{L-1} & \cdots & \boldsymbol{M}_1 & \boldsymbol{M}_0 \end{bmatrix}.$$

In subspace identification, one need the system minimal order to identify $(\boldsymbol{A}, \boldsymbol{B}, \boldsymbol{C}, \boldsymbol{D})$. This step typically involves reconstruction of $\operatorname{col}(\mathbf{O}_L)$, since $\operatorname{rank}(\mathbf{O}_L) = n$ for an observable system (6.1). We briefly revisit the fundamentals of system order determination to set the stage for the main result.

6.2.1 Order Determination in Subspace Identification

To estimate $\operatorname{col}\mathbf{O}_L$, a suitable linear transformation $\boldsymbol{P}_{\mathcal{D}}$ can be found that maps $\overset{///}{\mathbf{Y}}_{0,L,N}$ into a subspace preserving the information on the column space of observability. While the specific form of this transformation varies across subspace identification methods, the underlying idea remains the same. For example, the N4SID method [47] employs an oblique projection to define $\boldsymbol{P}_{\mathcal{D}}$, whereas the MOESP approach uses an orthogonal projection for this purpose [203]. The next assumption is required to ensure that $\operatorname{col}\mathbf{O}_L$ remains recoverable after projection.

Assumption 6.1 (Data rank condition)**.** The data is recorded such that the following holds:

$$\operatorname{rank}\begin{bmatrix} \overset{\mathscr{H}}{\mathbf{X}}_{0,1,N} \\ \overset{\mathscr{H}}{\mathbf{U}}_{0,L,N} \end{bmatrix} = n + Ln_u\,.$$

Although Assumption 6.1 is general, it can be guaranteed under certain practical conditions, namely: 1) the input signal is persistently exciting (PE) of sufficient order, and 2) the system operates in open-loop, or, in the closed-loop case, the feedback loop contains at least a unit delay. A time-domain description of PE for a signal is provided as follows [17]:

Definition 6.1 (Persistently exciting)**.** A signal $\boldsymbol{u}_k$ for k in time interval $[0, N-1]$ is persistently exciting of order L if $\overset{\mathscr{H}}{\mathbf{U}}_{0,L,N}$ has full row rank.

The fundamental lemma states that an input $\boldsymbol{u}_{[0,N-1]}$ with PE of order $L+n$ is sufficient to ensure that Assumption 6.1 is satisfied. Additionally, under the ergodicity of the process, the following holds:

$$\mathbb{E}\left[(\overset{\mathscr{H}}{\mathbf{Y}}_{0,L,N}\boldsymbol{P}_{\mathcal{D}})\right] = \lim_{N\to\infty}\frac{1}{N}(\overset{\mathscr{H}}{\mathbf{Y}}_{0,L,N}\boldsymbol{P}_{\mathcal{D}})$$

6

Suppose the data is collected such that Assumption 6.1 is satisfied. Then, it can be shown that, as $N \to \infty$, the reduced singular value decomposition (SVD) of $\overset{\mathscr{H}}{\mathbf{Y}}_{0,L,N}\boldsymbol{P}_{\mathcal{D}}$ takes the form

$$\operatorname{SVD}\left(\lim_{N\to\infty}\frac{1}{N}(\overset{\mathscr{H}}{\mathbf{Y}}_{0,L,N}\boldsymbol{P}_{\mathcal{D}})\right) = \begin{bmatrix}\boldsymbol{Q}_n & \boldsymbol{Q}_{\tilde{n}}^\top\end{bmatrix}\begin{bmatrix}\sqrt{\Sigma_n^2+\varepsilon_e^2\mathbf{I}} & \mathbf{0} \\ \mathbf{0} & \varepsilon_e\mathbf{I}\end{bmatrix}\begin{bmatrix}\boldsymbol{V}_n^\top \\ \boldsymbol{V}_{\tilde{n}}^\top\end{bmatrix} \tag{6.3}$$

From this decomposition, the underlying system information is captured by ($\boldsymbol{Q}_n$, $\sqrt{\Sigma_n^2+\varepsilon_e^2\mathbf{I}}$, $\boldsymbol{V}_n$), where $\operatorname{col}\mathbf{O}_L = \operatorname{col}\boldsymbol{Q}_n$. Therefore, the number of nonzero singular values contained in the block $\sqrt{\Sigma_n^2+\varepsilon_e^2\mathbf{I}}$ reveals the system order. However, since all singular values are perturbed by noise, recovering the true separation requires inspection of the singular value spectrum. Under a sufficiently high signal-to-noise ratio (SNR), a significant drop—often exhibiting an 'elbow' shape—is expected at n, indicating the true order. Another approach is introduced in the Ho-Kalman realization algorithm [211], where the spectral analysis performs on a specific matrix defined as follows:

$$\begin{bmatrix}\boldsymbol{M}_1 & \boldsymbol{M}_2 & \cdots & \boldsymbol{M}_L \\ \boldsymbol{M}_2 & \boldsymbol{M}_3 & \cdots & \boldsymbol{M}_{L+1} \\ \vdots & \vdots & & \vdots \\ \boldsymbol{M}_L & \boldsymbol{M}_{L+1} & \cdots & \boldsymbol{M}_{2L}\end{bmatrix}.$$

This matrix is uniquely parameterized by Markov parameters $\boldsymbol{M}_i$ that can be identified from the least squares approach in subspace identification [147, 212]. Since this matrix can be decomposed as product of extended observability and controllability matrices, it presents low rank structure of order n. Following the same principle as before, we expect the spectral analysis demonstrates a significant drop at index n. In addition to the MOESP, N4SID, and Ho-Kalman approaches, this drop can also be revealed in another way which

will be utilized for our proposed method. Under Assumption 6.1, the singular values of the augmented Hankel matrix of input–output data $\mathbf{W}_L$ also demonstrate a similar spectral pattern, that is,

$$\mathrm{SVD}(\mathbf{W}_L); \quad \mathbf{W}_L := \begin{bmatrix} \mathbf{U}_{0,L,N} \\ \mathbf{Y}_{0,L,N} \end{bmatrix}. \tag{6.4}$$

However, the drop occurs at the $(Ln_u + n)$-th singular value rather than at the n-th. Once the system order n is determined, the state-space realization matrices $(\boldsymbol{A}, \boldsymbol{B}, \boldsymbol{C}, \boldsymbol{D})$ can be estimated using the existing subspace identification methods [47, 203]. Nevertheless, a clear spectral separation is not always guaranteed, as it depends on several factors, including system properties, the input signal, and noise perturbations, making order estimation challenging. Moreover, the SVD in (6.3) is valid only asymptotically ($N \to \infty$), whereas in practice only finite samples are available. The following example highlights these challenges.

Example 6.1. In this example, synthetic data are generated according to the following stable LTI system[1]:

$$\begin{aligned} \boldsymbol{A} &= \begin{bmatrix} 2.8005 & -2.6973 & 0.8958 \\ 1 & 0 & 0 \\ 0 & 1 & 0 \end{bmatrix}, \boldsymbol{B} = \begin{bmatrix} 1 \\ 0 \\ 0 \end{bmatrix}, \\ \boldsymbol{C} &= \begin{bmatrix} 0.0194 & -0.0366 & 0.0182 \end{bmatrix}, \boldsymbol{D} = \mathbf{0}, \end{aligned} \tag{6.5}$$

with minimal order $n = 3$, which serves as the benchmark throughout the paper. The dataset satisfies Assumption 6.1. Following standard subspace identification methods, the singular values are plotted on a logarithmic scale to highlight the spectral drop.

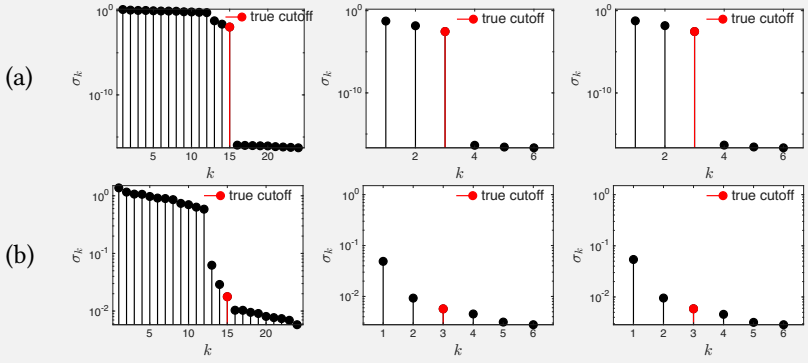

Figure 6.1: Each column (left to right) shows the augmented Hankel input–output data, MOESP, and N4SID methods. Singular values, obtained via an order-revealing technique, are shown as black circles for the noise-free case in (a) and the noisy case in (b), while the ground-truth cutoff is marked by a red circle with respect to the method.

[1] https://github.com/amiiinsheikhi/input_design_ifacwc.git

Using MOESP, N4SID, and the augmented Hankel matrix to reveal the system order, Figure 6.1a first presents the noise-free case, followed by the noisy case in Figure 6.1b. While the correct drop is observed in the noise-free setting, noise perturbations significantly affect the spectrum. In particular, the MOESP and N4SID exhibit an earlier drop ($k = 2$), leading to underestimation of the system order. The augmented Hankel approach performs even worse. This raises the question of whether the singular value separation can be improved. Unlike intrinsic system properties and noise, the input signal provides a design degree of freedom when experiment design is permitted.

Problem. Given an unknown finite-order system (3.1), design a collection of finite-length input sequences $\{\boldsymbol{u}(t)\}_{t=0}^{N-1}$ that enhances singular value separation and enables correct determination of the true system order.

Remark 6.1 (Bounded input). Naturally, the higher the input power, the higher the resulting output SNR. Hence, to ensure that the problem is well posed and practically meaningful, we also impose a bound on the power of admissible input signals.

6.3 Proposed Method

In this section we present our main contribution: a method to successively generate a series of experiments to determine the order of the unknown system (6.1). The method is composed of an outer loop and an inner loop. The inner loop (Section 6.3.1) generates optimized inputs for the next experiment, given information from the previous experiment. The outer loop (Section 6.3.2) executes experiments using the input generated in the inner loop and decides whether (i) the system order has been established, or (ii) if a new experiment is needed. This decision is based on the following pair of principles:

- **Input design to confirm the order.** Suppose system (6.1) has order $n \geq r$, and consider its r-th order approximation obtained from any system identification method. If an input sequence $\{\boldsymbol{u}(t)\}_{t=0}^{N-1}$ increases $\sigma_{Ln_u+r}(\mathbf{W}_L)$, then the corresponding singular value in real data should also attain a similar improvement, since the r-th order dynamics are physically present and can be excited.
- **Input design to falsify the order.** Conversely, suppose system (6.1) has order $n < r$, and consider an r-th order model. Any input sequence $\{\boldsymbol{u}(t)\}_{t=0}^{N-1}$ that improves $\sigma_{Ln_u+r}(\mathbf{W}_L)$ should not make any statistically significant change in the corresponding singular value from real data, since the r-th mode is inexistent, and $\sigma_{Ln_u+r}(\mathbf{W}_L)$ from real data only captures spurious input–noise correlations.

6.3.1 Optimal Input Design

The inner loop receives a model of order r, and its goal is to design an input that maximizes the spectral gap for this model. We propose an optimal input design aimed at maximizing the $(Ln_u + r)$-th singular value of the matrix $\mathbf{W}_L$ generated by the model.

Since the primary degree of freedom in input design is the input signal itself, we express the output explicitly as a function of the input by first expanding the state sequence

as follows:

$$\overset{\diagup\!\!\!\!\diagup\!\!\!\!\diagup}{\mathbf{X}}_{0,1,N} = \underbrace{\begin{bmatrix}\mathbf{I}_n & A & A^2 & \cdots & A^{N-L}\end{bmatrix}}_{=:\bar{A}_L}(\mathbf{I}_{N-L+1} \otimes \boldsymbol{x}_0)$$
$$+ \begin{bmatrix} \mathbf{0} & B\boldsymbol{u}_0 & \begin{bmatrix}AB & B\end{bmatrix}\begin{bmatrix}\boldsymbol{u}_0\\ \boldsymbol{u}_1\end{bmatrix} & \begin{bmatrix}A^2B & AB & B\end{bmatrix}\begin{bmatrix}\boldsymbol{u}_0\\ \boldsymbol{u}_1\\ \boldsymbol{u}_2\end{bmatrix} & \cdots \end{bmatrix}.$$

Using this expansion, the term $\mathbf{O}_L\overset{\diagup\!\!\!\!\diagup\!\!\!\!\diagup}{\mathbf{X}}_{0,1,N}$ turns out to admit an interesting representation as a function of the input sequence:

$$\mathbf{O}_L\overset{\diagup\!\!\!\!\diagup\!\!\!\!\diagup}{\mathbf{X}}_{0,1,N} = \mathbf{O}_L\bar{\mathrm{A}}_L(\mathbf{I}_{N-L+1} \otimes \boldsymbol{x}_0) + \overset{\diagup\!\!\!\!\diagup\!\!\!\!\diagup}{\mathbf{M}}_{1,L,N-1}\begin{bmatrix}\mathbf{0} & \overset{\diagdown\!\!\!\!\diagdown\!\!\!\!\diagdown}{\mathbf{U}}_{N-L}\end{bmatrix}, \tag{6.6}$$

where the block-Hankel matrix of Markov parameters, $\overset{\diagup\!\!\!\!\diagup\!\!\!\!\diagup}{\mathbf{M}}_{1,L,N-1}$, is defined as follows:

$$\overset{\diagup\!\!\!\!\diagup\!\!\!\!\diagup}{\mathbf{M}}_{1,L,N-1} := \begin{bmatrix} M_1 & M_2 & \cdots & M_{N-L} \\ M_2 & M_3 & \cdots & M_{N-L+1} \\ \vdots & \vdots & & \vdots \\ M_L & M_{L+1} & \cdots & M_{N-1} \end{bmatrix},$$

and the upper-triangular block-Toeplitz matrix of input sequence $\overset{\diagdown\!\!\!\!\diagdown\!\!\!\!\diagdown}{\mathbf{U}}_{N-L}$ is given by

$$\overset{\diagdown\!\!\!\!\diagdown\!\!\!\!\diagdown}{\mathbf{U}}_{N-L} := \begin{bmatrix} \boldsymbol{u}(0) & \boldsymbol{u}(1) & \cdots & \boldsymbol{u}(N-L-1) \\ \mathbf{0} & \boldsymbol{u}(0) & \cdots & \boldsymbol{u}(N-L-2) \\ \vdots & \ddots & \ddots & \vdots \\ \mathbf{0} & \cdots & \mathbf{0} & \boldsymbol{u}(0) \end{bmatrix}.$$

Remark 6.2. The block-Hankel matrix $\overset{\diagup\!\!\!\!\diagup\!\!\!\!\diagup}{\mathbf{M}}_{1,L,N-1}$ is the celebrated Ho-Kalman matrix [211] that can be decomposed as the product of extended observability and controllability matrices, i.e.,

$$\overset{\diagup\!\!\!\!\diagup\!\!\!\!\diagup}{\mathbf{M}}_{1,L,N-1} = \begin{bmatrix} CB & CAB & \cdots & CA^{N-L-1}B \\ CAB & CA^2B & \cdots & CA^{N-L}B \\ \vdots & \vdots & & \vdots \\ CA^{L-1}B & CA^LB & \cdots & CA^{N-2}B \end{bmatrix}$$
$$= \begin{bmatrix} C \\ CA \\ \vdots \\ CA^{L-1} \end{bmatrix}\begin{bmatrix}B & AB & \cdots & A^{N-L-1}B\end{bmatrix}.$$

Using (6.6), the augmented Hankel matrix of input–output sequences can be expressed

as

$$\begin{aligned}\begin{bmatrix}\overbrace{\mathbf{U}}^{}_{0,L,N}\\ \overbrace{\mathbf{Y}}^{}_{0,L,N}\end{bmatrix} &= \begin{bmatrix}\mathbf{0} & \mathbf{I}_{Ln_u}\\ \mathbf{O}_L & \overbrace{\mathbf{M}}^{}_L\end{bmatrix}\begin{bmatrix}\overbrace{\mathbf{X}}^{}_{0,1,N}\\ \overbrace{\mathbf{U}}^{}_{0,L,N}\end{bmatrix} + \begin{bmatrix}\mathbf{0}\\ \overbrace{\mathbf{E}}^{}_{0,L}\end{bmatrix},\\ &= \begin{bmatrix}\mathbf{0} & \mathbf{I}_{Ln_u}\\ \mathbf{I}_{Ln_y} & \overbrace{\mathbf{M}}^{}_L\end{bmatrix}\left(\begin{bmatrix}\mathbf{O}_L\bar{\mathbf{A}}_L(\mathbf{I}_{N-L+1}\otimes \boldsymbol{x}_0)\\ \mathbf{0}\end{bmatrix}\right.\\ &\quad \left. + \begin{bmatrix}\overbrace{\mathbf{M}}^{}_{1,L,N-1}\begin{bmatrix}\mathbf{0} & \overbrace{\mathbf{U}}^{}_{N-L}\end{bmatrix}\\ \overbrace{\mathbf{U}}^{}_{0,L,N}\end{bmatrix}\right) + \begin{bmatrix}\mathbf{0}\\ \overbrace{\mathbf{E}}^{}_{0,L}\end{bmatrix}.\end{aligned}$$

After some mathematical manipulations, the final expression takes the following form

$$\begin{aligned}\mathbf{W}_L = \begin{bmatrix}\overbrace{\mathbf{U}}^{}_{0,L,N}\\ \overbrace{\mathbf{Y}}^{}_{0,L,N}\end{bmatrix} &= \underbrace{\begin{bmatrix}\mathbf{0}\\ \mathbf{O}_L\bar{\mathbf{A}}_L(\mathbf{I}_{N-L+1}\otimes \boldsymbol{x}_0)\end{bmatrix}}_{\Xi_0}\\ &\quad + \underbrace{\begin{bmatrix}\mathbf{0} & \mathbf{I}_{Ln_u}\\ \overbrace{\mathbf{M}}^{}_{1,L,N-1} & \overbrace{\mathbf{M}}^{}_L\end{bmatrix}}_{\mathbf{F}}\underbrace{\begin{bmatrix}\mathbf{0}\,\overbrace{\mathbf{U}}^{}_{N-L}\\ \overbrace{\mathbf{U}}^{}_{0,L,N}\end{bmatrix}}_{\boldsymbol{\Theta}(\boldsymbol{u}_{[0,N-1]})} + \underbrace{\begin{bmatrix}\mathbf{0}\\ \overbrace{\mathbf{E}}^{}_{0,L}\end{bmatrix}}_{\mathbf{E}(\boldsymbol{e}_{[0,N-1]})} \qquad (6.7)\\ &= \Xi_0 + \mathbf{F}\boldsymbol{\Theta} + \mathbf{E}. \qquad (6.8)\end{aligned}$$

This representation offers two advantages: first, the contribution of input signal is completely encompassed in the $\mathbf{F}\boldsymbol{\Theta}$; second, it shows that the matrices Ξ_0 and $\mathbf{E}$ depend only on the initial condition and the noise perturbation, respectively, and not on the input signal. Since the optimization is performed on the model, no noise is present and the initial state can be selected zero, giving $\Xi_0 = \mathbf{E} = \mathbf{0}$. Therefore, $\mathbf{W}_L$ only retains the component linear in $\boldsymbol{u}$. These properties will be leveraged in the proposed optimal input design.

Our proposed optimization problem is given by

$$\boldsymbol{u}^{\star}_{[0,N-1]} \coloneqq \arg\max_{\boldsymbol{u}_{[0,N-1]} \in \mathcal{U}} \ell_r; \quad \ell_r \coloneqq \sigma_r(\mathbf{W}_L), \qquad (6.9)$$

where the set $\mathcal{U}$ of bounded-energy inputs is defined by

$$\mathcal{U}(\gamma_u) \coloneqq \{\boldsymbol{u}_{[0,N-1]} \in \mathbb{R}^{Nn_u} : \sum_{t=0}^{N-1} \boldsymbol{u}^{\top}(t)\boldsymbol{u}(t) \le \gamma_u^2\}.$$

The original optimization (6.9) can be reformulated using (6.7)

$$\begin{aligned}\underset{\boldsymbol{\Theta}}{\text{maximize}} \quad & \sigma_r(\mathbf{F}\boldsymbol{\Theta})\\ \text{subject to} \quad & \boldsymbol{\Pi}\,\mathrm{vec}(\boldsymbol{\Theta}) = \mathbf{0},\\ & \|\boldsymbol{u}_{[0,N-1]}(\boldsymbol{\Theta})\| \le \gamma_u.\end{aligned} \qquad (6.10)$$

In this reformulation, the specific structure of the matrix $\boldsymbol{\Theta} \in \mathbb{R}^{Nn_u \times (N-L+1)}$ is enforced by the matrix $\boldsymbol{\Pi}$ through a set of linear constraints; namely, (i) setting the block-diagonal

elements of $\overset{\diagdown\diagdown}{\mathbf{U}}_{N-L}$ to be equal, (ii) setting the block-antidiagonal elements of $\overset{\diagup\diagup}{\mathbf{U}}_{0,L,N}$ to be equal, and (iii) setting the remaining elements to zero. Since $\boldsymbol{\Theta}$ satisfies the structure, a unique $\boldsymbol{u}_{[0,N-1]}$ can be determined from it by using the first column and last row of $\overset{\diagup\diagup}{\mathbf{U}}_{0,L,N}$, thereby enabling the power constraint.

The cost function ℓ_r is generally non-concave and non-smooth. Consequently, maximizing a constrained non-concave problem is prone to convergence to a local optimum. Nevertheless, we can still employ a gradient ascent-based method to solve the optimization problem in (6.10), since the subgradient of the cost function has a closed-form solution. Applying the chain rule together with the subgradient of a singular value yields the following subgradient of the cost function at $\boldsymbol{\Theta}$:

$$\nabla \ell_r \coloneqq \mathbf{F}^\top(\boldsymbol{q}_r \boldsymbol{v}_r^\top), \tag{6.11}$$

where $\boldsymbol{q}_r$ and $\boldsymbol{v}_r$ denote the left and right singular vectors corresponding to the r-th largest singular value of the SVD in (6.4).

Remark 6.3. The cost function in (6.10) is non-differentiable when the r-th largest singular value σ_r has multiplicity $m > 1$. In this general case, the subdifferential $\partial \ell_r$ at $\boldsymbol{\Theta}$ can be computed as [213, Theorem 7.1]

$$\begin{aligned} \partial \ell_r &\coloneqq \operatorname{conv}\left\{\mathbf{F}^\top(\boldsymbol{q}\boldsymbol{v}^\top) \,:\, \mathbf{W}_L \boldsymbol{v} = \sigma_r \boldsymbol{q}\right\}, \\ &= \left\{\mathbf{F}^\top(\boldsymbol{Q}\operatorname{diag}(\boldsymbol{\alpha})\boldsymbol{V}^\top) \,:\, \mathbf{W}_L \boldsymbol{V} = \sigma_r \boldsymbol{Q},\ \sum_{i=1}^{m} \alpha_i = 1\right\}, \end{aligned} \tag{6.12}$$

in which $\boldsymbol{\alpha} \coloneqq \left[\alpha_1, \ldots, \alpha_m\right]^\top$ is a vector of positive scalar components, i.e., $\alpha_i \geq 0$. All left and right singular vectors associated with σ_r are collected in $\boldsymbol{Q}$ and $\boldsymbol{V}$, respectively. The subgradient in (6.11) belongs to this set, hence it can be used even at points of non-differentiability.

The problem in (6.9) can be solved using Algorithm 2, which provides the function `OptimalInput`.

Algorithm 2. It takes as input a model parameterized by the matrix $\mathbf{F}$; see (6.7). Additionally, it receives an initial input sequence $\boldsymbol{u}_{[0,N-1]}$ and iterates over it. By applying this input to the model [Line 5], the matrix $\mathbf{W}_L$ is built and its singular value decomposition is computed [Line 6]. From this and the matrix $\mathbf{F}$, the subgradient (6.11) is computed [Line 7]; diminishing step sizes are chosen due to the non-smooth nature of the problem. Lines 8–12 perform a projected subgradient step: Line 8 starts with a standard subgradient step. This is followed by the orthogonal projection onto the subspace dictating the Toeplitz–Hankel structure in (6.7) [Line 9], then by a projection onto the γ_u-sphere [Lines 10–11], which is simply done by normalization. In Line 12, the projected $\boldsymbol{\Theta}$ is obtained. This loop iterates until convergence or until the maximum number of allowed iterations is reached.

6.3.2 Experiment Application Loop

Following the principles outlined in the beginning of this section, Algorithm 2 is integrated into the main loop, which executes experiments in succession for system order estimation. This iterative scheme is summarized in Algorithm 3, with the corresponding flowchart presented in Figure 6.2.

Algorithm 3. It iterates on the order of the system, starting at $r = 1$ or any valid lower bound $r_0 \leq n$, obtained using an arbitrary low-rank estimation method [214, 215]. The input is initialized such that Assumption 6.1 holds, and is applied on the real system [Line 2]. The singular values from the data matrix $\mathbf{W}_L$ are then collected [line 3], and the main iteration begins. At every step of the iteration, a subspace identification method is applied on the data for the fixed order r [Line 5], and its resulting Markov parameters are used to build $\mathbf{F}$ via (6.7) [Line 6]. Given the identified model of order r, Algorithm 2 is executed to obtain the input the maximizes the $(Ln_u + r)$-th singular value of $\mathbf{W}_L$ [Line 7]. This input is tested in the real system [Line 8], and the new vector of singular values is computed [Line 9]. Lines 10–13 provide the stopping criterion: in Line 10, the relative improvement in the $(Ln_u + r)$-th singular value of the real data matrix $\mathbf{W}_L$ is compared to a pre-established threshold; if the improvement falls below the prescribed threshold or negative, the model is falsified and the order is chosen to be $r - 1$. Otherwise, the loop continues by updating the singular values [Line 14] and incrementing r [Line 15].

Algorithm 2 Optimal Input Design to Solve (6.9)

1: **function** `OptimalInput`($\boldsymbol{u}_{[0,N-1]}$,`Model`,$\mathbf{F}$,$\boldsymbol{\Pi}$,L,r,γ_u, η, ϵ_Θ)
2: $k \leftarrow 1$
3: **repeat**
4: $\boldsymbol{\Theta} \leftarrow$ construct $\boldsymbol{\Theta}$ based on (6.7) using $\boldsymbol{u}_{[0,N-1]}$
5: $\boldsymbol{y}_{[0,N-1]} \leftarrow \texttt{Model}(\boldsymbol{u}_{[0,N-1]})$
6: $\boldsymbol{q}_r, \boldsymbol{v}_r, \sigma_r \leftarrow \mathrm{SVD}(\mathbf{W}_L)$ ▷ based on (6.4)
7: $\nabla \ell_r \leftarrow \mathbf{F}^\top(\boldsymbol{q}_r \boldsymbol{v}_r^\top)$
8: $\boldsymbol{\Theta}_{\text{new}} \leftarrow \boldsymbol{\Theta} + \frac{\eta}{\sqrt{k}} \nabla \ell_r$
9: $\boldsymbol{\Theta}_{\text{new}} \leftarrow \mathrm{project}_{\boldsymbol{\Pi}^\perp} \mathrm{vec}(\boldsymbol{\Theta}_{\text{new}})$
10: $\boldsymbol{u}_{[0,N-1]} \leftarrow$ read off $\boldsymbol{u}_{[0,N-1]}$ from $\boldsymbol{\Theta}_{\text{new}}$
11: $\boldsymbol{u}_{[0,N-1]} \leftarrow \mathrm{project}_{\mathcal{U}(\gamma_u)} \boldsymbol{u}_{[0,N-1]}$
12: $\boldsymbol{\Theta}_{\text{new}} \leftarrow$ construct $\boldsymbol{\Theta}$ based on (6.7) using $\boldsymbol{u}_{[0,N-1]}$
13: $k \leftarrow k + 1$
14: **until** $\|\boldsymbol{\Theta}_{\text{new}} - \boldsymbol{\Theta}\| \leq \epsilon_\Theta$
15: $\boldsymbol{u}^\star_{[0,N-1]} \leftarrow \boldsymbol{u}_{[0,N-1]}$
16: **return** $\boldsymbol{u}^\star_{[0,N-1]}$

Algorithm 3 Experiment Design for Order Estimation

Input: $\boldsymbol{u}_{[0,N-1]}$, $\boldsymbol{\Pi}$, L, γ_u, η, ϵ_Θ, ϵ_σ

Output: $\hat{n}$

$r \leftarrow 1$ or any known lower bound of system order, i.e., $r_0 \leq n$
$\boldsymbol{y}_{[0,N-1]} \leftarrow \texttt{System}(\boldsymbol{u}_{[0,N-1]})$ ▷ System (6.1)
$\sigma \leftarrow \mathrm{SVD}(\mathbf{W}_L)$ ▷ based on (6.4)
while $r \leq Ln_y$ **do**
  $\{\boldsymbol{M}_i\}_{i=0}^{N-1}, \texttt{Model} \leftarrow \texttt{SysId}(\{\boldsymbol{u}(t), \boldsymbol{y}(t)\}_{t=0}^{N-1}, r)$
  $\mathbf{F} \leftarrow$ construct $\mathbf{F}$ based on (6.7) using $\{\boldsymbol{M}_i\}_{i=0}^{N-1}$
  $\boldsymbol{u}_{[0,N-1]} \leftarrow \texttt{OptimalInput}(\boldsymbol{u}_{[0,N-1]}, \texttt{Model}, \mathbf{F}, \boldsymbol{\Pi}, L, Ln_u + r, \gamma_u, \eta, \epsilon_\Theta)$
  $\boldsymbol{y}_{[0,N-1]} \leftarrow \texttt{System}(\boldsymbol{u}_{[0,N-1]})$ ▷ System (6.1)
  $\sigma^{\text{new}} \leftarrow \mathrm{SVD}(\mathbf{W}_L)$ ▷ based on (6.4)
  if $\sigma^{\text{new}}_{Ln_u+r} - \sigma_{Ln_u+r} \leq \epsilon_\sigma \sigma_{Ln_u+r}$ **then**
    $\hat{n} \leftarrow r - 1$
    return
  end if
  $\sigma \leftarrow \sigma^{\text{new}}$.
  $r \leftarrow r + 1$
end while

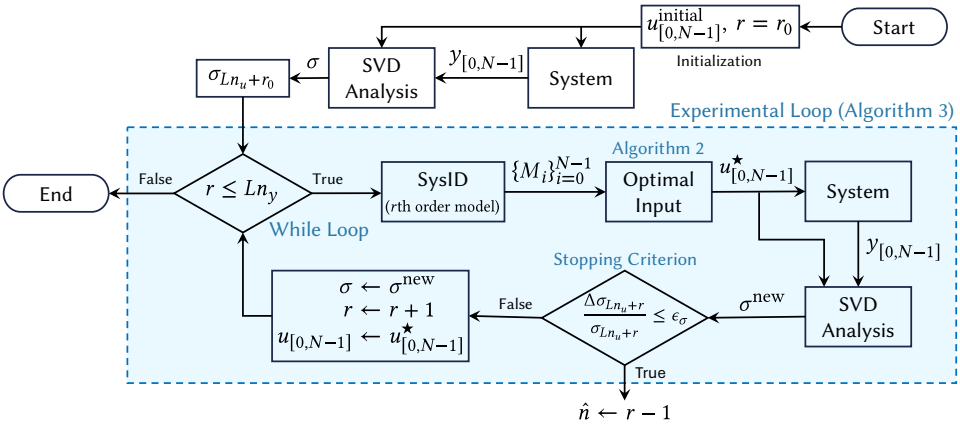

Figure 6.2: The flowchart of proposed experiment design for system order estimation (Algorithm 3).

6.4 Numerical Simulation

To demonstrate the proposed method, we present two simulation studies on the system (6.5). In the first part, we focus on the effectiveness of Algorithm 2 in increasing the singular value at the true cutoff index. In contrast, in the second part, the true system order is assumed to be unknown, and Algorithm 3 is executed to estimate the order.

Scenario: Optimal Input Design

This study aims to show that a random input is not optimal for increasing the spectral gap, whereas an optimal input can excite the system in a desired manner. The optimization parameters are set as $N = 100$, $L = 13$, $\gamma_u = 1$, $\epsilon_\Theta = 10^{-8}$, $\eta = 100$, with zero-mean i.i.d. Gaussian noise of variance $\varepsilon_e^2 = 10^{-7}$. The SNR level is approximately 20. The initial input is chosen as a bounded random Gaussian sequence with zero-mean and unit variance. The true order $n = 3$ is assumed to be known. The optimal input is designed based on the identified model via N4SID using Algorithm 2. As demonstrated in Fig. 6.3, it significantly improves the spectral gap, that is, the singular value at $Ln_u + n$ increases by about 363% relative to a random input, despite both satisfying Assumption 6.1. This indicates that the PE condition alone does not ensure reliable identification. Furthermore, the optimal input reduces impulse response estimation error by about 70% and improves subspace accuracy, measured via principal angles of $\operatorname{col} \mathbf{O}_L$, by 13%. Notably, the resulting input has periodic nature, with frequency content aligned to the underlying system dynamics, even though no periodicity is enforced in the optimization. Another noteworthy observation is the periodic nature of the optimal input, whose frequency content aligns with that of the underlying system. It is worth recalling that, in the optimization, no assumption is made regarding input periodicity beyond boundedness. To make the scenario more realistic, the next section assumes the true order is unknown and requires conducting experiments to determine the underlying order.

Scenario: System Order Estimation

Maintaining the same setup as in the previous scenario, we now assume that the true order $n = 3$ is unknown. Algorithm 3 is applied to determine the system order. Robustness is assessed over 200 experiments with different noise realizations. The confidence threshold ϵ_σ is chosen as 20%. The histogram of the estimated orders is shown in Figure 6.4, achieving an accuracy of 90%. Figure 6.4 also illustrates the evolution of the singular value growth for a given r at each trial. A sharp decline in the growth rate is evident at the true order $n = 3$ across the trials, which is consistent with the theoretical expectations.

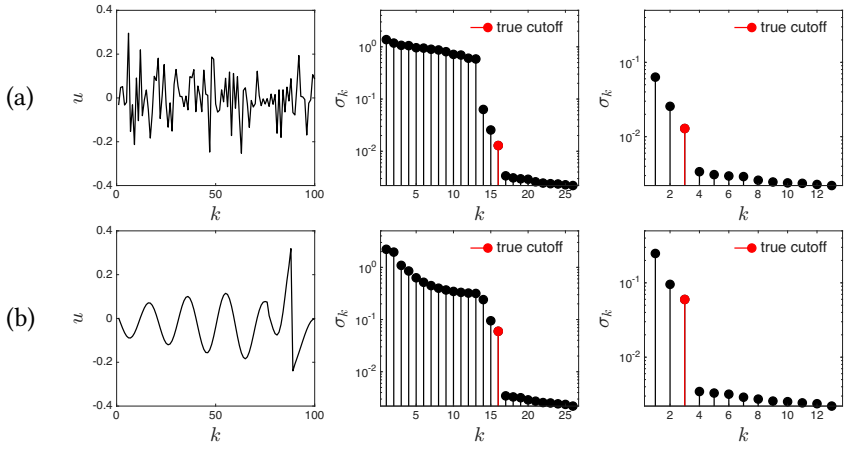

Figure 6.3: This figure compares random (a) and optimal (b) inputs. From left to right, the plots show the input signal, $\mathbf{W}_L$ singular values, and MOESP singular values, with the true cutoff marked in red depending on the method.

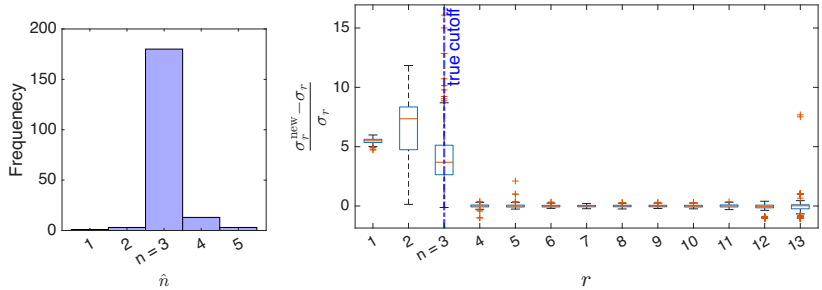

Figure 6.4: The left panel shows the histogram of system order estimates obtained using Algorithm 3, while the right panel presents the box plot of the singular value growth rate for each r across all trials.

6.5 Conclusions

Accurately identifying the true system order is directly linked to the accuracy of system identification. For this reason, we have proposed an iterative approach to determine the order that best explains the perturbed data. This approach is enabled through an optimal input design that maximizes a particular singular value associated with a low-rank data representation, enhancing the distinguishability of system information from noise. Thanks to relying on the identified model rather than the true system, it leads to a minimal number of experiments required for estimation. Since our optimal input design depends only on the identified model rather than the true system, it leads to a minimal number of experiments required for estimation. We would like to stress that, despite being presented as an algorithm, our method also serves as a guideline for experiment design; e.g., inspecting the relative improvements in singular value over a range of orders a posteriori may be beneficial. Future work will be dedicated to the problem of minimizing the number of experiments by using, e.g., bisection instead of linear search over r, and determining guarantees of the proposed method.

7

Conclusion

Fault diagnosis is an indispensable component of modern health-monitoring systems in high-tech industries. It supports two critical requirements: safety and predictability, for which companies are willing to make substantial investments to prevent catastrophic failures and unplanned downtime. In response to these industrial needs, this thesis develops fault diagnosis methods for more reliable and efficient monitoring solutions. Its main contributions advance data-driven fault diagnosis for applications where only input–output data are accessible and an accurate system model is unavailable or difficult to obtain. Three key assumptions are adopted throughout the thesis: (i) the system is linear time-invariant, (ii) faults enter the system additively, and (iii) fault-free data are available for diagnosis filter design. Even though linear systems are the most studied class of dynamical systems, the findings of this thesis demonstrate that several fundamental questions remain unresolved, giving rise to new technical challenges and research opportunities.

In Chapter 2, we provide an overview of recent advances in fault diagnosis and estimation from a system-theoretic perspective. Beside examining the classical diagnosis problems in a unified DAE-based framework, we also discuss emerging research directions, including model-free fault diagnosis and active design. Inspired by the survey, we formulate the research questions regarding the data-driven fault diagnosis in Chapters 3 to 5 and active design for system identification and diagnosis in Chapter 6.

The first research question, RQ1, investigates the fundamental performance limits of null-space-based diagnosis filters, which represent a major class of solutions in the literature. In Chapter 3, we address this question by formulating fault isolation as a subspace classification problem and introducing the notion of fault discernibility. Our results show that achievable isolation performance is determined by the system zero structure and the geometry of the fault subspaces partitioning the residual space, both of which are intrinsic to the structural properties of system and independent of the chosen diagnosis method. To formalize the discussion, we introduce the notion of fault discernibility. The simulations illustrate how an actuator fault may become indiscernible from a sensor fault, imposing a fundamental limitation on fault isolation. Conventional DAE-, UIO-, and parity-based approaches (e.g.,[24, 34, 40, 51]) typically construct a bank of filters, each generating a scalar residual dedicated to a particular fault. Such a design may be infeasible when the

fault subsystem is not left invertible, as illustrated by a single-input single-output system subject to both sensor and actuator faults. On the contrary, the geometric classifier proposed in Chapter 3 exploits a multidimensional residual and remains applicable without left invertibility. The implications of noise for this geometric approach needs further discussion.

Although the explicit connection between intersections of fault dictionaries and transmission zeros holds only in the noise-free condition, the underlying principle remains applicable in the presence of noise. Noise affects the accuracy of identifying these subspaces, while trajectories lying in their intersections are still difficult to distinguish. To showcase the relevance of zeros in the presence of noise, consider fault signals designed along output-zeroing directions. For a Schur stable system, the contribution from the deterministic residual components decay exponentially even with mismatched initial conditions, eventually becoming dominated by noise. This leads to an unreliable classification, which is also demonstrated in our numerical simulations. Thus, the characterization remains useful for revealing the noise sensitivity of the diagnosis method and the limitations of classifiers relying on angles between residuals and subspaces. As a practical note, to account for noise, the geometric classifier can determine the faulty mode provided that the residual magnitude exceeds a certain threshold.

As established in Chapter 3, system zeros impose fundamental limitations on fault isolation performance. The next research question, RQ2, therefore focuses on characterizing the system zero structure in a data-driven setting. Drawing on the extensive literature on the output-zeroing problem, Chapter 4 tackles this question from an output-zeroing perspective. Its first contribution is to establish a general connection between the null space of the data equation and the system zero structure. Geometric control theory—and, in particular, the fundamental output-nulling invariant subspaces—provides the appropriate tools for this analysis. The chapter characterizes different types of system zeros, including invariant, decoupling, and infinite zeros, in terms of these geometric subspaces and, more importantly, relates them to the null space of the data equation. This characterization does not require system minimality and accommodates degenerate systems with arbitrary input and output dimensions. Furthermore, the chapter shows how these geometric objects can be computed from the components of the data equation, namely the extended observability matrix and the block Toeplitz matrix of Markov parameters. Drawing on these findings, we provide a method to compute system zeros directly from input–output data. In data-driven settings, the zeros can be identified up to a minimal realization of system. The theoretical contributions hold for noise-free settings. Extending the results to noisy settings or systems with model uncertainties, whether bounded or stochastic, boils down to solving the output-zeroing problem for the underlying uncertain system and accounting for the effects of these uncertainties on the computation of zeros.

Fault isolation is a prerequisite for fault estimation, which seeks to track and reconstruct fault signals for effective predictive maintenance. In data-driven settings, conventional methods first identify the forward fault subsystem and then invert the identified model. The research question RQ3 challenges this two-step scheme, arguing that the resulting inverse model may not be optimal for fault estimation. This is because the identification criterion is formulated for the forward model rather than the ultimate estimation objective. In particular, the identification errors propagate nonlinearly through inversion.

A further challenge arises for nonminimum phase systems, whose inverses are unstable. Chapter 5 addresses both issues by learning the inverse system directly from input–output data, without an intermediate inversion step. Stable estimation is achieved using a noncausal diagnosis filter based on a bilateral impulse-response expansion. Kernel-based regularization is proposed that incorporates prior knowledge, with rational orthonormal basis function (ROBF) kernels encoding the inverse dynamics when approximate zero locations are available. Since efficient time-domain implementation of these kernels is not straightforward, an accompanying toolbox is developed; see Chapter C.

The research question RQ4 investigates the use of the input signal as a design variable to improve identification and diagnosis accuracy. Accordingly, Chapter 6 shifts from the passive setting of the preceding chapters to an active design regime. The chapter focuses on determining the order of a minimal realization, which remains challenging under noisy conditions. Conventional subspace identification methods infer the order from the singular-value cutoff of a Hankel data matrix; however, noise obscures its low-rank structure and makes this cutoff difficult to identify. To address this issue, the chapter develops an input design scheme that reveals the appropriate cutoff by maximizing a selected singular value of the Hankel matrix. Although the resulting objective is nonconvex and nonsmooth, its subgradient admits a closed-form expression, enabling an efficient first-order algorithm that converges to a locally optimal solution. The proposed input design is embedded in a hypothesis-testing procedure that confirms or falsifies candidate system orders. Simulations demonstrate clear improvements over random excitation. A key takeaway is that, in the presence of noise, persistence of excitation alone does not guarantee accurate system identification.

Returning to the main research question posed at the beginning of this thesis, the contributions presented herein not only establish the theoretical foundations for quantifying the performance of data-driven fault diagnosis methods for linear dynamical systems, but also leverage these insights to develop new methods for improving diagnosis performance. While further methodological development and validation under real-world operating conditions are needed, these contributions represent a step toward reliable and accurate predictive maintenance in modern manufacturing systems. Moreover, although motivated primarily by fault diagnosis, several findings from Chapters 4 to 6 have broader implications in system theory and control, system identification, estimation, and experiment design.

Regarding the motivating examples provided in Section 1.1.1, a linear diagnosis filter can still perform satisfactorily in applications such as industrial printing, autonomous vehicles, and power systems. Although almost all real systems are nonlinear, nonlinear dynamics can be dealt with as external disturbances in these use cases, allowing the diagnosis filter to be robustified against nonlinearities using training data. Mechatronics systems, on the other hand, often require ultra-precision diagnosis performance, demanding the development of accurate models. Consequently, unmodeled dynamics can compromise the desired diagnostic accuracy. The additivity of faults is another assumption underlying this thesis. In autonomous vehicles, mechatronic systems and industrial printing, faults can also be multiplicative, limiting the applicability of our methods. Nevertheless, certain multiplicative faults can be represented as equivalent additive faults, enabling the latter to be used for diagnosis up to modeling factors. Additionally, designing diagnosis filters us-

ing only fault-free data makes it challenging to account for multiplicative faults. However, this limitation may be overcome if faulty datasets are also available. Hence, model-based approaches are often employed to handle multiplicative faults [10, 63, 100, 107].

7.1 Future Research Recommendations

This section outlines potential research directions building on the contributions of this thesis. These directions follow two complementary paths: addressing the limitations of the proposed methods and extending them to broader settings and applications. We begin with the methodological limitations, each of which presents an opportunity for future research.

Two factors are particularly important for the practical deployment of data-driven diagnosis methods in this thesis: the presence of noise, and limited training data. Each poses distinct challenges to the analysis and design of data-driven solutions. Although noise was included in the problem formulations through the innovation signal, its effects were largely excluded from the theoretical analysis and examined mainly through numerical simulations. A rigorous characterization of these effects using tools from stochastic process theory is therefore an important direction for future research. Limited data present a related challenge. While many classical results rely on asymptotic assumptions, modern data-driven applications increasingly require non-asymptotic guarantees based on finite samples. Neither aspect was studied comprehensively in this thesis and thus warrants dedicated investigation. It is worth noting that tools from high-dimensional probability have only relatively recently been adopted in systems and control [216], with many existing results still focusing on idealized settings [214] rather than practical applications. For instance, extending the estimation problem in Chapter 5 to the finite-sample regime hinges on non-asymptotic concentration inequalities. Among these, the result in [217] is instrumental in deriving finite-sample bounds for linear estimation problems. Nevertheless, its application requires establishing that the relevant noise terms form a martingale difference sequence, which is nontrivial in inverse problems. Furthermore, deriving such guarantees may require additional assumptions, such as sub-Gaussian distributions for the control inputs and fault signals that can be unrealistic, particularly for faults. Hence, finite-sample analysis of the developments in this thesis also requires further advances in these techniques.

Other method-specific limitations also motivate the research directions discussed below. The following list is not exhaustive but highlights several promising avenues for future work.

Sparse fault isolation for large scale applications

The promising results of the geometric classifier developed in Chapter 3 motivate formulating fault isolation as a sparse subspace classification problem, following related developments in image processing; see, e.g., [218]. By representing the effects of candidate faults on the residual signal as bases for distinct fault subspaces, the active faults can be identified through the nonzero entries of a sparse decision vector. Such a formulation naturally accommodates simultaneous faults and is particularly relevant to large-scale systems with many inputs and outputs, where only a small subset of faults is typically active at any given time. The geometric insights from

Chapter 3 can further support performance analysis, as the relative angles between fault subspaces determine fundamental classification limits. In particular, principal angles provide a suitable tool for quantifying the relative geometry and discernibility of these subspaces.

Finite-sample analysis of direct vs. indirect inverse system identification
Chapter 5 introduced a regularized inverse system identification method for actuator fault estimation. Although the simulation results indicate that the direct approach achieves lower fault reconstruction errors than its indirect counterpart, it remains unclear whether this advantage holds generally and, if not, under which conditions either approach is preferable. A formal comparison could be established through a non-asymptotic analysis based on finite training data. Both schemes are affected by finite-sample identification errors; however, in the indirect approach, these errors additionally propagate nonlinearly through the inversion step. Recent advances in high-dimensional probability and statistical learning provide promising tools for deriving finite-sample guarantees and comparing the reconstruction errors of the two schemes. The techniques developed in [216] may provide a useful starting point for this investigation.

Quantifying suboptimality in input design
The input design algorithm proposed in Chapter 6 may converge to locally optimal solutions. Even when computing a globally optimal solution is computationally intractable, quantifying the suboptimality gap is important for assessing the quality of the designed input and establishing a principled stopping criterion from a practical viewpoint. An interesting direction is to construct a tractable convex relaxation that provides nontrivial upper or lower bounds on the globally optimal value. These bounds could then be used to certify the quality of locally optimal solutions by quantifying their optimality gap, for instance through a computable primal-dual gap.

Fault tolerant control
Beyond predictive maintenance, fault estimates can be used by reconfigurable controllers to accommodate faults, potentially at the expense of degraded nominal control performance. As a natural extension, the fault estimation method developed in Chapter 5 could be integrated with a reconfigurable control mechanism to form a fault-tolerant control framework. The relevant literature suggests that existing subspace-based diagnosis methods have not yet been fully explored for this purpose [219]. Two key challenges are to ensure timely recovery before the fault destabilizes the system and to maintain a nonempty feasible set following fault occurrence. Since the recovery time depends partly on the estimation delay induced by the noncausal bilateral filter, this requirement should be incorporated into the diagnosis filter design. Computational efficiency is another important consideration for real-time implementation.

Extension to nonlinear systems
Real-world systems often exhibit nonlinear behavior. To address a broader class of systems, the diagnosis methods developed in this thesis could be extended using models that remain linear-in-parameters, allowing the corresponding diagno-

sis problems to retain a regression-based formulation. Three families of nonlinear models are particularly relevant. First, block-oriented models, such as Hammerstein and Hammerstein–Wiener models, cascading linear dynamics with static nonlinearities, whereas Volterra models represent nonlinear input–output behavior through polynomial kernel expansions. Recent developments in data-driven control using nonlinear ARX models [220] may provide a foundation for pursuing this direction. Second, nonlinear dynamics can be represented using a linear combination of predefined basis functions, such as Fourier bases, with their coefficients serving as the decision variables. Such representations are typically overparameterized and can benefit from sparsity-promoting methods. A notable example is sparse identification of nonlinear dynamics (SINDy) [221], which selects a few active terms from a large library of candidate functions. Finally, recent Koopman-based generalizations of Willems' fundamental lemma could support the development of direct data-driven diagnosis methods for nonlinear systems. A preliminary result along this line have been reported in [222].

7.2 Societal Impact

The transition toward proactive and increasingly automated health management of high-tech systems can deliver a range of societal benefits by improving the resilience, accessibility, and safety of the technological infrastructure and supply chains on which modern society depends. These impacts can be grouped into three categories:

- **Operational and economic resilience.** Early detection of anomalous behavior, supported by health-monitoring systems and digital twins, can reduce unplanned downtime, maintenance costs, and production losses. It can also improve the sustainability and resilience of manufacturing operations and their associated supply chains.

- **Scalable deployment.** The data-driven solutions provided in this thesis make diagnostic tools more accessible to high-tech manufacturing systems compared to traditional model-based approaches, where obtaining accurate models may be costly or impractical for complex manufacturing systems. Furthermore, their adaptability across different machines and processes may facilitate scalable and flexible deployment, supporting the broader digitalization of the manufacturing sector.

- **Enhanced industrial safety.** Automated health monitoring can identify system degradation and abnormal operating conditions before they develop into hazardous failures, reducing risks to personnel, equipment, and the surrounding environment.

A

Technical Proofs of Chapter 3

This chapter provides the required theoretical foundations to establish the proof of our main claim in Theorem 3.10.

Proof of Proposition 3.3

Multiplying the data-equation (3.4) on the right by $\boldsymbol{Q}_2$ gives $\mathbf{O}_L \mathbf{X}_{[0,N-L]} \boldsymbol{Q}_2 = \boldsymbol{L}_{22}$, following from the orthogonality condition, i.e., $\boldsymbol{Q}_1^\top \boldsymbol{Q}_2 = \mathbf{0}$. Assumption 3.2 ensures that $\mathbf{X}_{[0,N-L]} \boldsymbol{Q}_2$ has full row rank, implying $\operatorname{im} \mathbf{O}_L = \operatorname{im} \boldsymbol{L}_{22}$. Thus, $\operatorname{im}(\mathbf{K}_L^y)^\top = \ker \mathbf{O}_L^\top = \ker \boldsymbol{L}_{22}^\top$. Next, pre-multiply the data-equation (3.4) by $\mathbf{K}_L^y$ and post-multiplying it by $\boldsymbol{Q}_1$ leads to $\mathbf{K}_L^y \mathbf{T}_L^u \boldsymbol{L}_{11} = \mathbf{K}_L^y \boldsymbol{L}_{21}$, since $\boldsymbol{Q}_1^\top \boldsymbol{Q}_1 = \mathbf{I}$. By Assumption 3.2, $\overset{\#}{\mathbf{U}}_{t,L,N}$ has full row rank, which guarantees the invertibility of $\boldsymbol{L}_{11}$. Consequently, $\mathbf{K}_L^y \mathbf{T}_L^u = \mathbf{K}_L^y \boldsymbol{L}_{21} \boldsymbol{L}_{11}^{-1}$, completing the proof.

Proof of Theorem 3.4

Let ζ_{fi} be the number of finite transmission zeros counting algebraic multiplicity and ζ_{inf} be the number of infinite transmission zeros, so that $\zeta = \zeta_{\text{fi}} + \zeta_{\text{inf}}$. By Theorem III.4 of [158], if $L \geq n$, then $\dim(\ker \begin{bmatrix} \mathbf{O}_L & \mathbf{T}_L^f \end{bmatrix}) - \dim(\ker \mathbf{T}_L^f) = \zeta_{\text{fi}}$. By Theorem IV.8 of [158], if $L \geq \tau$, $\dim(\ker \mathbf{T}_L^f) = \zeta_{\text{inf}}$. Combining the two expressions gives the desired result.

Proof of Lemma3.5

($\Longrightarrow$) Suppose $\mathbf{K}_L^y \mathbf{T}_L^f \boldsymbol{f}_0 = \mathbf{0}$. This implies $\mathbf{T}_L^f \boldsymbol{f}_0 \in \ker \mathbf{K}_L^y = \operatorname{im} \mathbf{O}_L$. Thus, $\mathbf{T}_L^f \boldsymbol{f}_0 = \mathbf{O}_L \boldsymbol{v}$ for some $\boldsymbol{v}$, and taking $\boldsymbol{x}_0 = -\boldsymbol{v}$ yields $\mathbf{O}_L \boldsymbol{x}_0 = -\mathbf{T}_L^f \boldsymbol{f}_0$. ($\Longleftarrow$) Left multiplying the zero equation by $\mathbf{K}_L^y$ gives the result.

A

Proof of Proposition 3.6

From Definition 3.2, indiscernible faults yield identical residuals, i.e., $\boldsymbol{r}^1(t) = \boldsymbol{r}^2(t)$. This implies

$$\mathbf{K}_L^y[\mathbf{T}_L^{f_1}\ \mathbf{T}_L^{f_2}]\begin{bmatrix}\mathbf{f}^1_{[t,t+L-1]}\\ \\ -\mathbf{f}^2_{[t,t+L-1]}\end{bmatrix} = \mathbf{0};$$

and it can be rewritten as $\mathbf{K}_L^y\mathbf{T}_L^{f\text{aug}}\mathbf{f}^{\text{aug}}_{[t,t+L-1]} = 0$, where $\mathbf{T}_L^{f\text{aug}}$ defines the augmented system, obtained by reordering the columns and entries of the associated matrices. By Lemma 3.5, $\mathbf{f}^{\text{aug}}_{[t,t+L-1]}$ lies in the zero dynamics input space of the augmented system.

Proof of Lemma 3.8

By [159, Proposition 3.6.10], $\operatorname{rank}(\mathbf{K}_L^y\boldsymbol{P}) = \operatorname{rank}\boldsymbol{P} - \dim\big(\ker\mathbf{K}_L^y \cap \operatorname{im}\boldsymbol{P}\big)$. From the fundamental theorem for subspaces, it can be established that $\ker\mathbf{K}_L^y = \operatorname{im}\mathbf{O}_L$. Combining this with the second part of the findings in Lemma 3.7, we can express the rank as follows

$$\operatorname{rank}(\mathbf{K}_L^y\boldsymbol{P}) = \operatorname{rank}\boldsymbol{P} + \dim(\ker\boldsymbol{P}) - \dim\left(\ker\begin{bmatrix}\mathbf{O}_L & \boldsymbol{P}\end{bmatrix}\right).$$

In this derivation, the fact that $\dim(\ker\mathbf{O}_L) = \mathbf{0}$ is already taken into account. Using the rank-nullity theorem then yields the desired result.

Proof of Lemma 3.9

In light of Lemma 3.7, we have

$$\begin{aligned} d_\cap^{c,c'} &= \operatorname{rank}\mathbf{D}_L^c + \operatorname{rank}\mathbf{D}_L^{c'} - \operatorname{rank}\begin{bmatrix}\mathbf{D}_L^c & \mathbf{D}_L^{c'}\end{bmatrix}\\ &= \operatorname{rank}(\mathbf{K}_L^y\mathbf{T}_L^c) + \operatorname{rank}(\mathbf{K}_L^y\mathbf{T}_L^{c'}) - \operatorname{rank}(\mathbf{K}_L^y\mathbf{T}_L).\end{aligned}$$

By applying Lemma 3.8 to each term individually, the final result is achieved.

Proof of Theorem 3.10

To prove this, we primarily rely on the dimension of the intersection (3.11) in Lemma 3.9. The key aspect is computing the dimension of each null space, where Theorem 3.4 connects it to transmission zeros.

(First case): In this case, fault dictionaries correspond to actuator faults. Direct application of Theorem 3.4 yields $\dim(\ker\begin{bmatrix}\mathbf{O}_L & \mathbf{T}_L^{\mathrm{a}_i}\end{bmatrix}) = \zeta^i$ and $\dim(\ker\begin{bmatrix}\mathbf{O}_L & \mathbf{T}_L^{\mathrm{a}_j}\end{bmatrix}) = \zeta^j$. To obtain $\dim(\ker\begin{bmatrix}\mathbf{O}_L & \mathbf{T}_L^{\mathrm{a}_i} & \mathbf{T}_L^{\mathrm{a}_j}\end{bmatrix})$, we rearrange the columns so that Theorem 3.4 can be invoked for the subsystem from $\{i, j\}$th inputs to all outputs. Note that the rank of a matrix remains invariant under column-wise permutations. Consequently, the nullity for this subsystem is equal to $\zeta^{\{i,j\}}$. Substituting each part into (3.11) gives the result.

(Second case): This case considers an actuator fault versus a sensor fault. We analyze each term separately. According to Theorem 3.4, $\dim(\ker\begin{bmatrix}\mathbf{O}_L & \mathbf{T}_L^{\mathrm{a}_i}\end{bmatrix}) = \zeta^i$. On the other hand, Assumption 3.1 implies that $\begin{bmatrix}\mathbf{O}_L & \mathbf{T}_L^{\mathrm{s}_j}\end{bmatrix}$ is full column rank, and therefore

$\dim(\ker\begin{bmatrix}\mathbf{O}_L & \mathbf{T}_L^{\mathrm{s}_j}\end{bmatrix}) = 0$. To simplify computation of $\dim(\ker\begin{bmatrix}\mathbf{O}_L & \mathbf{T}_L^{\mathrm{a}_i} & \mathbf{T}_L^{\mathrm{s}_j}\end{bmatrix})$, we break it down to a few steps. Since one of the dictionaries corresponds to an actuator fault, we can always find at least ζ^i nonzero linear combinations of columns in $\begin{bmatrix}\mathbf{O}_L & \mathbf{T}_L^{\mathrm{a}_i} & \mathbf{T}_L^{\mathrm{s}_j}\end{bmatrix}$ that produce zero based on Theorem 3.4, implying $\dim(\ker\begin{bmatrix}\mathbf{O}_L & \mathbf{T}_L^{\mathrm{a}_i} & \mathbf{T}_L^{\mathrm{s}_j}\end{bmatrix}) \geq \zeta^i$. We now show that there exists another set of linear combinations that leads to rank deficiency. Let j represent the jth output of the system and Ω denote the set $\{1,\ldots,n_y\}\backslash j$. Consider $z_0 \in \mathbb{C}$ to be a transmission zero for the subsystem from ith input to all outputs in Ω. For notational clarity, we introduce $\mathbf{O}_L^{\mathcal{I}_y}$ to represent the extended observability matrix for the outputs in $\mathcal{I}_y$, and $\mathbf{T}_L^{m,\mathcal{I}_y}$ to represent the Toeplitz matrix corresponding to subsystem from the mth input to the outputs in $\mathcal{I}_y$. Then, according to Theorem 3.4, there exist pairs $(\boldsymbol{x}_0^{(\omega)}, \boldsymbol{u}_0)$ for all $\omega \in \Omega$ such that $\begin{bmatrix}\mathbf{O}_L^1 & \mathbf{T}_L^{i,1}\end{bmatrix}\begin{bmatrix}\boldsymbol{x}_0^{(1)} \\ \boldsymbol{u}_0\end{bmatrix} = \cdots = \begin{bmatrix}\mathbf{O}_L^{n_y} & \mathbf{T}_L^{i,n_y}\end{bmatrix}\begin{bmatrix}\boldsymbol{x}_0^{(n_y)} \\ \boldsymbol{u}_0\end{bmatrix} = \mathbf{0}$ and $\begin{bmatrix}\mathbf{O}_L^j & \mathbf{T}_L^{i,j}\end{bmatrix}\begin{bmatrix}\boldsymbol{x}_0^{(j)} \\ \boldsymbol{u}_0\end{bmatrix} \neq \mathbf{0}$. Permuting rows, which does not affect rank, results in

$$\operatorname{perm}[\mathbf{O}_L \quad \mathbf{T}_L^{\mathrm{a}_i} \quad \mathbf{T}_L^{\mathrm{s}_j}] = \left[\begin{array}{ccc} \mathbf{O}_L^{\Omega} & \mathbf{T}_L^{i,\Omega} & \mathbf{0} \\ \hline \mathbf{O}_L^{j} & \mathbf{T}_L^{i,j} & \mathbf{I}_L \end{array}\right].$$

Our goal is to demonstrate the existence of a nonzero tuple $\boldsymbol{\lambda} := (\boldsymbol{\lambda}_1, \boldsymbol{\lambda}_2, \boldsymbol{\lambda}_3)$ satisfying

$$\left[\begin{array}{ccc} \mathbf{O}_L^{\Omega} & \mathbf{T}_L^{i,\Omega} & \mathbf{0} \\ \hline \mathbf{O}_L^{j} & \mathbf{T}_L^{i,j} & \mathbf{I}_L \end{array}\right]\begin{bmatrix}\boldsymbol{\lambda}_1 \\ \boldsymbol{\lambda}_2 \\ \boldsymbol{\lambda}_3\end{bmatrix} = 0\,.$$

Since z_0 is also a transmission zero for the subsystem (i,Ω), it is always possible to find a nonzero $(\boldsymbol{\lambda}_1, \boldsymbol{\lambda}_2)$ such that the top partition becomes zero, i.e., $\mathbf{O}_L^{\Omega}\boldsymbol{\lambda}_1 + \mathbf{T}_L^{i,\Omega}\boldsymbol{\lambda}_2 = \mathbf{0}$. Substituting the solution of the top partition into the bottom partition gives $\boldsymbol{\lambda}_3 = -\mathbf{O}_L^{y_j}\boldsymbol{\lambda}_1 - \mathbf{T}_L^{(u_i,y_j)}\boldsymbol{\lambda}_2 \neq \mathbf{0}$ as z_0 is not a transmission zero for subsystem from the ith to the jth output; this argument holds for all $\zeta^{i,\Omega}$ transmission zeros. It is easy to show that if there were another output channel not sharing z_0 as a transmission zero, the given system of equations would have no nonzero solution, but the proof is omitted for brevity. Assumption 3.1 guarantees that no additional linear dependencies exist. Thus, $\dim(\ker\begin{bmatrix}\mathbf{O}_L & \mathbf{T}_L^{\mathrm{a}_i} & \mathbf{T}_L^{\mathrm{s}_j}\end{bmatrix}) = \zeta^i + \zeta^{i,\Omega}$. The desired result follows from (3.11).

(Third case): In case of two distinct sensor fault dictionaries, $\mathbf{T}_L^{\mathrm{s}_i}$ and $\mathbf{T}_L^{\mathrm{s}_i}$ have independent columns by construction. Moreover, Assumption 3.1 ensures that $\begin{bmatrix}\mathbf{O}_L & \mathbf{T}_L^{\mathrm{s}_i}\end{bmatrix}$ and $\begin{bmatrix}\mathbf{O}_L & \mathbf{T}_L^{\mathrm{s}_j}\end{bmatrix}$ are full column rank, resulting in a null space of zero dimension. Using similar notations as in the second case, but with Ω being $\{1,\ldots,n_y\}\backslash\{i,j\}$, and applying row-wise permutations, we obtain

$$\operatorname{perm}[\mathbf{O}_L \quad \mathbf{T}_L^{\mathrm{s}_i} \quad \mathbf{T}_L^{\mathrm{s}_j}] = \left[\begin{array}{ccc} \mathbf{O}_L^{\Omega} & \mathbf{0} & \mathbf{0} \\ \hline \mathbf{O}_L^{i} & \mathbf{I}_L & \mathbf{0} \\ \mathbf{O}_L^{j} & \mathbf{0} & \mathbf{I}_L \end{array}\right]. \tag{A.1}$$

A

Assumption 3.4 implies that $\dim(\ker\begin{bmatrix}\mathbf{O}_L & \mathbf{T}_L^{s_i} & \mathbf{T}_L^{s_j}\end{bmatrix}) = \mathbf{0}$ if $n_y > 2$ based on the structure in (A.1). In case of $n_y = 2$, it follows from (A.1) that $\dim(\ker\begin{bmatrix}\mathbf{O}_L & \mathbf{T}_L^{s_i} & \mathbf{T}_L^{s_j}\end{bmatrix})$ reduces to $\dim(\ker\begin{bmatrix}\mathbf{O}_L^i \\ \mathbf{O}_L^j\end{bmatrix}) = n$. This concludes the proof.

Proof of Proposition 3.11

The proof of left null space computation follows from [48, Lemma 9.4]. We show $\mathbf{K}_L^y\mathbf{T}_L^u = \mathbf{K}_L^y\boldsymbol{L}_{31}\boldsymbol{L}_{11}^{-1}$ and is asymptotically unbiased. With this in mind, pre-multiplying the data-equation (3.4) by $\mathbf{K}_L^y$ leads to

$$\mathbf{K}_L^y\overset{///}{\mathbf{Y}}_{0,L,N} = \mathbf{K}_L^y\mathbf{T}_L^u\overset{///}{\mathbf{U}}_{0,L,N} + \mathbf{K}_L^y\mathbf{T}_L^e\overset{///}{\mathbf{E}}_{0,L,N}\,.$$

After replacing $\overset{///}{\mathbf{U}}_{0,L,N}$ with $\boldsymbol{L}_{11}\boldsymbol{Q}_1^\top$ from the LQ decomposition and post-multiplying by $\boldsymbol{Q}_1$, the following holds

$$\mathbf{K}_L^y\overset{///}{\mathbf{Y}}_{0,L,N}\boldsymbol{Q}_1 = \mathbf{K}_L^y\mathbf{T}_L^u\boldsymbol{L}_{11} + \mathbf{K}_L^y\mathbf{T}_L^e\overset{///}{\mathbf{E}}_{0,L,N}\boldsymbol{Q}_1\,,$$

since $\boldsymbol{Q}_1^\top\boldsymbol{Q}_1 = \mathbf{0}$. Moreover, using the alternative expression for $\overset{///}{\mathbf{Y}}_{0,L,N}$ from the LQ decomposition, we obtain

$$\mathbf{K}_L^y\boldsymbol{L}_{31} = \mathbf{K}_L^y\mathbf{T}_L^u\boldsymbol{L}_{11} + \mathbf{K}_L^y\mathbf{T}_L^e\overset{///}{\mathbf{E}}_{0,L,N}\boldsymbol{Q}_1\,. \tag{A.2}$$

We have to examine the influence of $\mathbf{K}_L^y\mathbf{T}_L^e\overset{///}{\mathbf{E}}_{0,L,N}\boldsymbol{Q}_1$ when $N \to \infty$. Since condition (ii) of Assumption 3.6 holds, it implicitly imposes

$$\begin{aligned}&\operatorname{rank}\left(\lim_{N\to\infty}\frac{1}{N}\mathbf{X}_{[t,t+N-L]}\boldsymbol{P}_U^\perp\right) = n\\ \implies &\lim_{N\to\infty}\frac{1}{N}\begin{bmatrix}\mathbf{X}_{[t,t+N-L]}\mathbf{X}_{[t,t+N-L]}^\top & \mathbf{X}_{[t,t+N-L]}\overset{///}{\mathbf{U}}_{0,L,N}^\top\\ \overset{///}{\mathbf{U}}_{0,L,N}\mathbf{X}_{[t,t+N-L]}^\top & \overset{///}{\mathbf{U}}_{0,L,N}\overset{///}{\mathbf{U}}_{0,L,N}^\top\end{bmatrix} \succ 0\,.\end{aligned}$$

By the Schur complement, the matrix $\overset{///}{\mathbf{U}}_{0,L,N}$ has full row rank, and therefore $\boldsymbol{L}_{11}$ is invertible. Consequently, $\boldsymbol{Q}_1 = \overset{///}{\mathbf{U}}_{0,L,N}^\top(\boldsymbol{L}_{11}^{-1})^\top$. Substitution in (A.2) and taking the limit as $N \to \infty$ lead to

$$\begin{aligned}\lim_{N\to\infty}\frac{1}{N}\mathbf{K}_L^y\boldsymbol{L}_{31} &= \lim_{N\to\infty}\frac{1}{N}\mathbf{K}_L^y\mathbf{T}_L^u\boldsymbol{L}_{11} + \lim_{N\to\infty}\frac{1}{N}\mathbf{K}_L^y\mathbf{T}_L^e\overset{///}{\mathbf{E}}_{0,L,N}\overset{///}{\mathbf{U}}_{0,L,N}^\top(\boldsymbol{L}_{11}^{-1})^\top\\ \lim_{N\to\infty}\frac{1}{N}\mathbf{K}_L^y\boldsymbol{L}_{31} &\overset{\text{(i)}}{=} \lim_{N\to\infty}\frac{1}{N}\mathbf{K}_L^y\mathbf{T}_L^u\boldsymbol{L}_{11}\\ \mathbf{K}_L^y\boldsymbol{L}_{31} &= \mathbf{K}_L^y\mathbf{T}_L^u\boldsymbol{L}_{11} \implies \mathbf{K}_L^y\mathbf{T}_L^u = \mathbf{K}_L^y\boldsymbol{L}_{31}\boldsymbol{L}_{11}^{-1}\,,\end{aligned}$$

in which step (i) holds due to $\lim_{N\to\infty}\frac{1}{N}\mathbf{K}_L^y\mathbf{T}_L^e\overset{///}{\mathbf{E}}_{0,L,N}\overset{///}{\mathbf{U}}_{0,L,N}^\top(\boldsymbol{L}_{11}^{-1})^\top = \mathbf{0}$ with probability 1 by ergodicity and Assumption 3.5. This completes the proof.

B

Appendices to Chapter 4

B.1 Duality Between Subspaces

Here we show the equivalence between (4.3) and (4.4). For this, the following fact is useful.

Proposition B.1. *For any two subspaces $\mathcal{V}, \mathcal{W}$ and any matrix $\boldsymbol{A}$ with compatible dimensions, $\mathcal{W} \subseteq \boldsymbol{A}^{-1}\mathcal{V} \iff \boldsymbol{A}\mathcal{W} \subseteq \mathcal{V}$.*

Proof. ($\implies$) $\forall \boldsymbol{w} \in \mathcal{W}$, we have $\boldsymbol{w} \in \{\boldsymbol{v} \mid \boldsymbol{A}\boldsymbol{v} \in \mathcal{V}\} \implies \forall \boldsymbol{w} \in \mathcal{W}, \boldsymbol{A}\boldsymbol{w} \in \mathcal{V} \implies \boldsymbol{A}\mathcal{W} \subseteq \mathcal{V}$.
($\impliedby$) $\forall \boldsymbol{w} \in \mathcal{W}$, we have $\boldsymbol{A}\boldsymbol{w} \in \mathcal{V} \implies \forall \boldsymbol{w} \in \mathcal{W}, \boldsymbol{w} \in \boldsymbol{A}^{-1}\mathcal{V} \implies \mathcal{W} \subseteq \boldsymbol{A}^{-1}\mathcal{V}$. ∎

Now, using $\mathcal{V} \subseteq \mathcal{W} \iff \mathcal{V}^\perp \supseteq \mathcal{W}^\perp$, and the formulas $(\boldsymbol{A}^\top \mathcal{V})^\perp = \boldsymbol{A}^{-1}\mathcal{V}^\perp$ and $(\mathcal{V} \cap \mathcal{W})^\perp = \mathcal{V}^\perp + \mathcal{W}^\perp$, we get

$$\mathcal{S}^\perp \subseteq \begin{bmatrix} \boldsymbol{A}^\top \\ \boldsymbol{B}^\top \end{bmatrix}^{-1} \left((\mathcal{S} \times \mathcal{U})^\perp \cap (\ker \begin{bmatrix} \boldsymbol{C} & \boldsymbol{D} \end{bmatrix})^\perp\right) = \begin{bmatrix} \boldsymbol{A}^\top \\ \boldsymbol{B}^\top \end{bmatrix}^{-1} \left((\mathcal{S}^\perp \times \{\boldsymbol{0}\}) + \operatorname{im} \begin{bmatrix} \boldsymbol{C}^\top \\ \boldsymbol{D}^\top \end{bmatrix}\right).$$

Using Proposition B.1 gives

$$\begin{bmatrix} \boldsymbol{A}^\top \\ \boldsymbol{B}^\top \end{bmatrix} \mathcal{S}^\perp \subseteq (\mathcal{S}^\perp \times \{\boldsymbol{0}\}) + \operatorname{im} \begin{bmatrix} \boldsymbol{C}^\top \\ \boldsymbol{D}^\top \end{bmatrix} = \begin{bmatrix} \mathbf{I}_{n_x} \\ \boldsymbol{0} \end{bmatrix} \mathcal{S}^\perp + \operatorname{im} \begin{bmatrix} \boldsymbol{C}^\top \\ \boldsymbol{D}^\top \end{bmatrix},$$

which is the same as (4.4).

B.2 Auxiliary Results

This section presents several auxiliary results used in the theoretical developments of Chapter 4.

Proposition B.2. *Let $\boldsymbol{A} \in \mathbb{R}^{n \times m}$ be a matrix and $\mathcal{V} \subseteq \mathbb{R}^n$ be a linear subspace. Then*

$$\dim(\boldsymbol{A}^{-1}\mathcal{V}) = \dim \ker \boldsymbol{A} + \dim(\operatorname{im} \boldsymbol{A} \cap \mathcal{V}). \tag{B.1}$$

Proof. Let $T : \boldsymbol{A}^{-1}\mathcal{V} \to \mathbb{R}^n$ be the restriction of $\boldsymbol{x} \to \boldsymbol{A}\boldsymbol{x}$ to the domain $\boldsymbol{A}^{-1}\mathcal{V}$. The kernel of T is $\{\boldsymbol{x} \mid \boldsymbol{A}\boldsymbol{x} = 0, \boldsymbol{A}\boldsymbol{x} \in \mathcal{V}\} = \ker \boldsymbol{A}$ and the image is $\{\boldsymbol{A}\boldsymbol{x} \mid \boldsymbol{x} \in \boldsymbol{A}^{-1}\mathcal{V}\} = \{\boldsymbol{A}\boldsymbol{x} \mid \boldsymbol{A}\boldsymbol{x} \in \mathcal{V}\} = \operatorname{im} \boldsymbol{A} \cap \mathcal{V}$. The result then arrives from the rank-nullity theorem. ∎

Proposition B.3. $\dim\ker\begin{bmatrix}A & B\end{bmatrix} = \dim\ker B + \dim(A^{-1}\operatorname{im}B) = \dim\ker A + \dim(B^{-1}\operatorname{im}A)$.

Proof. It follows from [159, Fact 3.14.15] and Proposition B.2. ∎

B

Lemma B.4. *Let Z be a basis for* $\ker(AX+BY)$*, where* $\begin{bmatrix}X^\top & Y^\top\end{bmatrix}^\top$ *is right-invertible. Then,* $\operatorname{im}YZ = B^{-1}\operatorname{im}A$.

Proof. Let $\begin{bmatrix}U^\top & V^\top\end{bmatrix}^\top$ be a basis for $\ker\begin{bmatrix}A & B\end{bmatrix}$. Then, $\operatorname{im}V = B^{-1}\operatorname{im}A$. Hence,

$$\operatorname{im}V = \begin{bmatrix}0 & I\end{bmatrix}\ker\begin{bmatrix}A & B\end{bmatrix} = \begin{bmatrix}0 & I\end{bmatrix}\begin{bmatrix}X\\Y\end{bmatrix}\ker\left(\begin{bmatrix}A & B\end{bmatrix}\begin{bmatrix}X\\Y\end{bmatrix}\right),$$

where in the last line we have used [159, Fact 3.13.3]. Continuing,

$$\operatorname{im}V = Y\ker(AX+BY) = Y\operatorname{im}Z.$$

∎

B.3 Technical Proofs

This appendix collects the proofs of the main formal results stated in the main text, in their order of appearance.

Proof of Theorem 4.4

Item (a) comes from [174, Theorem 4], which gives that the number of zeros at infinity is $\dim(\mathcal{V}^\star+\mathcal{S}^\star)-\dim(\mathcal{V}^\star)$, and using the fact that $(\mathcal{V}^\star+\mathcal{S}^\star)/\mathcal{V}^\star = \mathcal{S}^\star/\mathcal{R}^\star$. Fix any friend $F \in \mathscr{F}(\mathcal{V}^\star)$. We have that $\sigma(A+BF|_{\mathcal{V}^\star/\mathcal{R}^\star})$ are the invariant zeros of the system [174, Theorem 2(f)], implying (b). Similarly for (c), we have [186, p. 965] that all assignable zeros inside $\mathcal{V}^\star$ are $\sigma(A+BF|_{\mathcal{R}^\star})$. Finally, the summing of (a), (b), (c) gives the total number of output-nulling zeros, which is $\dim(\mathcal{V}^\star/\mathcal{R}^\star)+\dim(\mathcal{S}^\star/\mathcal{R}^\star)+\dim(\mathcal{R}^\star) = \dim(\mathcal{V}^\star)+\dim(\mathcal{S}^\star/\mathcal{R}^\star) = \dim\mathcal{N}^\star$.

Proof of Proposition 4.5

(i) $\implies$ (ii) Applying a one-sided Laurent series expansion for $|\mathfrak{q}| > \rho(A)$, the transfer function can be expressed as $G(\mathfrak{q}) = \sum_{i=0}^{\infty} M_i\mathfrak{q}^{-i}$. Consequently, the limit as $\mathfrak{q}\to\infty$ is well-defined and satisfies $\lim_{\mathfrak{q}\to\infty}G(\mathfrak{q}) = M_0 = D$. The implication then follows from Definition 4.9(c).

(ii) $\implies$ (iii) The first identity in Lemma 4.2 implies that

$$\operatorname{rank}\left(\lim_{\mathfrak{q}\to\infty}P(\mathfrak{q})\right) = n_x + \operatorname{rank}\left(\lim_{\mathfrak{q}\to\infty}G(\mathfrak{q})\right) = n_x + \operatorname{rank}D$$

with well-defined limits due to $|\mathfrak{q}| > \rho(A)$. Assuming (ii) holds, the second identity in Lemma 4.2 yields (iii).

(iii) $\implies$ (iv) Since Σ is non-degenerate, Proposition 4.3 implies that $G(\mathfrak{q})$ is (left/right) invertible for some delay $\tau \geq \tau_0 \in \mathbb{Z}_{\geq 0}$. We prove by contradiction that τ_0 must be at

least one. Suppose $\tau_0 = 0$. Then, by Definition 4.7, there exists a proper transfer function $G^+(\mathfrak{q})$ such that either $G^+(\mathfrak{q})G(\mathfrak{q}) = \mathbf{I}_{n_u}$ or $G(\mathfrak{q})G^+(\mathfrak{q}) = \mathbf{I}_{n_y}$ must hold. It suffices to consider the left-invertible case, as the right-invertible case follows analogously. Let $G^+(\mathfrak{q}) = \sum_{i=0}^{\infty} \tilde{M}_i \mathfrak{q}^{-i}$. According to [84, Theorem 2], $\tilde{M}_0 M_0 = \mathbf{I}_{n_u}$, implying that $M_0 = D$ is full column rank. However, statement (iii) yields $\operatorname{rank}(D) < \operatorname{normalrank} G(\mathfrak{q}) = n_u$, which contradicts the full column rank property of D. Hence, $\tau_0 = 0$ is impossible, and therefore $\tau_0 \geq 1$.

(iv) $\implies$ (i) For a contradiction, suppose that the system Σ has no zero at infinity, i.e., $\operatorname{rank} \lim_{\mathfrak{q}\to\infty} G(\mathfrak{q}) = \operatorname{normalrank} G(\mathfrak{q})$, implying D is full rank due to (left/right) invertibility of Σ. Hence, there exists a real matrix D^+ satisfying $D^+D = \mathbf{I}_{n_u}$ in the left-invertible case or $DD^+ = \mathbf{I}_{n_y}$ in the right invertible case. We show that D^+ can be used to construct a proper transfer function $G^+(\mathfrak{q})$ satisfying the invertibility condition in Definition 4.7 for $\tau_0 = 0$. To do so, consider the left-invertible case. Define the proper transfer function

$$\begin{aligned} G^+(\mathfrak{q}) &= D^+ - D^+C\big(\mathfrak{q}\mathbf{I}_{n_x} - (A - BD^+C)\big)^{-1}BD^+, \\ &= D^+\big(\mathbf{I}_{n_y} + C(\mathfrak{q}\mathbf{I}_{n_x} - A)^{-1}BD^+\big)^{-1}, \end{aligned}$$

where the second equality follows from the matrix inversion lemma. Moreover, the transfer function $G(\mathfrak{q})$ can be expressed as $G(\mathfrak{q}) = \big(\mathbf{I}_{n_y} + C(\mathfrak{q}\mathbf{I}_{n_x} - A)^{-1}BD^+\big)D$. Consequently, $G^+(\mathfrak{q})G(\mathfrak{q}) = D^+D = \mathbf{I}_{n_u}$, implying $\tau_0 = 0$. This contradicts $\tau_0 \geq 1$. One can similarly design $G^+(\mathfrak{q})$ for the right invertible case, completing the proof.

Proof of Lemma 4.6

We begin by proving the equality for the observability matrix. To this end, it suffices to show $\ker \mathbf{O}_L = \ker \mathbf{O}_{n_x}$ due to the rank-nullity theorem. Since the equality holds for any $L \geq n_x$ by the Cayley–Hamilton theorem, we only consider the case $\dim \mathcal{Z} + 1 \leq L < n_x$ without loss of generality.

($\ker \mathbf{O}_L \supseteq \ker \mathbf{O}_{n_x}$) Since $\ker \mathbf{O}_{n_x} = \ker \mathbf{O}_L \cap \big(\bigcap_{i=L}^{n_x-1} \ker(CA^i)\big)$, the desired inclusion follows by construction.

($\ker \mathbf{O}_L \subseteq \ker \mathbf{O}_{n_x}$) Note that $\ker C \subseteq \mathcal{Z}$ by Definition 4.2, leading to $\dim \ker C \leq \dim \mathcal{Z}$. Moreover, rewriting the observability matrix as $\ker \mathbf{O}_L = \bigcap_{i=0}^{L-1} \ker(CA^i)$, we obtain $\ker \mathbf{O}_L \subseteq \ker C \subseteq \mathcal{Z}$. To establish the desired inclusion, define $\bar{\mathcal{O}}_i := \bar{\mathcal{O}}_{i-1} \cap \ker(CA^i)$ with $\bar{\mathcal{O}}_0 = \ker C$ for $i \geq 1$. We split the proof into two main parts: the fixed-point convergence of the sequence $\{\bar{\mathcal{O}}_i\}_{i\geq 0}$ and the sufficiency of the condition $i \geq \dim \mathcal{Z}$ for this convergence.

Convergence: We prove that, given $i \geq 0$, the condition $\bar{\mathcal{O}}_i = \bar{\mathcal{O}}_{i+1}$ implies $\bar{\mathcal{O}}_i = \bar{\mathcal{O}}_{i+j}$ for all $j \geq 1$. To achieve this, expressing $\bar{\mathcal{O}}_i$ alternatively as $\bar{\mathcal{O}}_i = \bar{\mathcal{O}}_0 \cap A^{-1}\bar{\mathcal{O}}_{i-1}$ simplifies the proof. To see this, consider $\bar{\mathcal{O}}_1 = \ker C \cap \ker(CA) = \bar{\mathcal{O}}_0 \cap A^{-1}\bar{\mathcal{O}}_0$ using the property $\ker(CA) = A^{-1}\ker C$, and

$$\bar{\mathcal{O}}_2 = \ker C \cap \ker(CA) \cap \ker(CA^2) = \bar{\mathcal{O}}_0 \cap A^{-1}\big(\ker C \cap \ker(CA)\big) = \bar{\mathcal{O}}_0 \cap A^{-1}\bar{\mathcal{O}}_1,$$

where the general expression follows by induction. As a result, if $\bar{\mathcal{O}}_i = \bar{\mathcal{O}}_{i+1}$, then $\bar{\mathcal{O}}_{i+2} = \bar{\mathcal{O}}_0 \cap A^{-1}\bar{\mathcal{O}}_{i+1} = \bar{\mathcal{O}}_0 \cap A^{-1}\bar{\mathcal{O}}_i = \bar{\mathcal{O}}_{i+1}$. Thus, by induction, $\bar{\mathcal{O}}_i = \bar{\mathcal{O}}_{i+j}$ holds for all $j \geq 1$.

B

Sufficiency: We show $\bar{\mathcal{O}}_i = \bar{\mathcal{O}}_{i+1}$ for $i \geq \dim \mathcal{Z}$ (equivalently, $L \geq \dim \mathcal{Z} + 1$), where $i = L-1$. The inclusion $\bar{\mathcal{O}}_i \supseteq \bar{\mathcal{O}}_{i+1}$ holds by definition, which leads to showing only $\bar{\mathcal{O}}_i \subseteq \bar{\mathcal{O}}_{i+1}$ when $i \geq \dim \mathcal{Z}$. Since $\ker \mathbf{O}_L \subseteq \mathcal{Z}$, we have $\bar{\mathcal{O}}_i \subseteq \mathcal{Z}$ from the identity $\bar{\mathcal{O}}_i = \ker \mathbf{O}_{i+1}$. Thus, $\dim \bar{\mathcal{O}}_i \leq \dim \mathcal{Z}$. Furthermore, by construction, the sequence $\{\bar{\mathcal{O}}_i\}_{i \geq 0}$ is monotonically non-increasing, therefore $\dim \bar{\mathcal{O}}_i$ decreases by at least one or remains the same at each step, i.e., $\dim \bar{\mathcal{O}}_{i+1} \leq \dim \bar{\mathcal{O}}_i$. Suppose $\bar{\mathcal{O}}_j \neq \bar{\mathcal{O}}_{j+1}$ for $j = 0, \ldots, i-1$ with $\bar{\mathcal{O}}_0 = \mathcal{Z}$. Then, the monotonicity and $\dim \bar{\mathcal{O}}_0 \leq \dim \mathcal{Z}$ imply $\dim \bar{\mathcal{O}}_i \leq 0$ since $i \geq \dim \mathcal{Z}$; hence $\bar{\mathcal{O}}_i = \{\mathbf{0}\} \subseteq \bar{\mathcal{O}}_{i+1}$. On the other hand, if $\bar{\mathcal{O}}_j = \bar{\mathcal{O}}_{j+1}$ at any step $j < i$, the inclusion $\bar{\mathcal{O}}_i \subseteq \bar{\mathcal{O}}_{i+1}$ follows immediately from the convergence argument.

The equality for the reachability matrix can be proved by applying the preceding argument to the dual system $\Sigma^\top$ and using the invariance of matrix rank under transposition and permutation; finishing the proof.

Proof of Lemma 4.9

($\Longrightarrow$) The proof of this direction is similar to that in [158, Lemma III.3]. Let $\boldsymbol{x}(0) = \bar{\boldsymbol{x}} \in \mathcal{V}^\star$. By Definition 4.3, there exists $\boldsymbol{u}(0)$ such that

$$\begin{aligned} \boldsymbol{x}(1) &= \boldsymbol{A}\bar{\boldsymbol{x}} + \boldsymbol{B}\boldsymbol{u}(0), \\ \mathbf{0} &= \boldsymbol{C}\bar{\boldsymbol{x}} + \boldsymbol{D}\boldsymbol{u}(0), \end{aligned}$$

in which $\boldsymbol{x}(1) \in \mathcal{V}^\star$ follows from (4.2). By iterating the system dynamics for $L-1$ additional steps, the state sequence $\{\boldsymbol{x}(t)\}_{t=0}^{L-1}$ remains in $\mathcal{V}^\star$ due to the invariance property. Consequently, the corresponding input sequence $\{\boldsymbol{u}(t)\}_{t=0}^{L-1}$ defines the vector $\bar{\boldsymbol{u}} = \boldsymbol{u}_{[0,L-1]}$. It then follows from Proposition 4.7 that $(\bar{\boldsymbol{x}}, \bar{\boldsymbol{u}}) \in \ker \begin{bmatrix} \mathbf{O}_L & \mathbf{T}_L \end{bmatrix}$.

($\Longleftarrow$) Assume, for the sake of contradiction, that $\boldsymbol{x}(0) = \bar{\boldsymbol{x}} \notin \mathcal{V}^\star$, and $\boldsymbol{u}_{[0,L-1]} = \bar{\boldsymbol{u}}$. Since $(\bar{\boldsymbol{x}}, \bar{\boldsymbol{u}}) \in \ker \begin{bmatrix} \mathbf{O}_L & \mathbf{T}_L \end{bmatrix}$ and $L \geq \dim \mathcal{Z} + 1$, it follows that $\boldsymbol{y}(t) = \mathbf{0}$ for all $t = 0, 1, \ldots, \dim \mathcal{Z}, \ldots, L-1$. Consequently, $\bar{\boldsymbol{x}} \in \mathcal{V}_{\dim \mathcal{Z}}$, which equals $\mathcal{V}^\star$ by Lemma 4.8. This contradicts the assumption that $\bar{\boldsymbol{x}} \notin \mathcal{V}^\star$, and hence $\bar{\boldsymbol{x}} \in \mathcal{V}^\star$.

Proof of Lemma 4.10

Let $\pi_x : \ker \begin{bmatrix} \mathbf{O}_L & \mathbf{T}_L \end{bmatrix} \to \mathcal{X}$ be the coordinate projection onto the first component restricted to $\ker \begin{bmatrix} \mathbf{O}_L & \mathbf{T}_L \end{bmatrix}$, defined by $\pi_x(\bar{\boldsymbol{x}}, \bar{\boldsymbol{u}}) = \bar{\boldsymbol{x}}$. By Lemma 4.9, it is immediate that $\operatorname{im} \pi_x = \mathcal{V}^\star$. Therefore, $\dim(\operatorname{im} \pi_x) = \operatorname{rank} \pi_x = \dim \mathcal{V}^\star$. In addition, the associated null space to the linear map π_x is defined as $\ker \pi_x := \{(\bar{\boldsymbol{x}}, \bar{\boldsymbol{u}}) \in \ker \begin{bmatrix} \mathbf{O}_L & \mathbf{T}_L \end{bmatrix} \mid \pi_x(\bar{\boldsymbol{x}}, \bar{\boldsymbol{u}}) = \mathbf{0}\}$. Since $(\bar{\boldsymbol{x}}, \bar{\boldsymbol{u}}) \in \ker \pi_x$ if and only if $\bar{\boldsymbol{u}} \in \ker \mathbf{T}_L$ (by definition), $\dim(\ker \pi_x) = \dim(\ker \mathbf{T}_L)$. From the rank-nullity theorem, we have

$$\dim(\ker \begin{bmatrix} \mathbf{O}_L & \mathbf{T}_L \end{bmatrix}) = \operatorname{rank} \pi_x + \dim \ker \pi_x = \dim \mathcal{V}^\star + \dim(\ker \mathbf{T}_L).$$

This concludes the proof.

Proof of Theorem 4.13

The expression (4.8) is a direct consequence of Lemma 4.9. To prove (4.9), substituting (4.8) into the dual expression of $\mathcal{S}^\star$ in Remark 4.1 gives

$$\mathcal{S}^\star = \left(\begin{bmatrix} B^\top \\ B^\top A^\top \\ \vdots \end{bmatrix}^{-1} \operatorname{im} \tilde{\mathbf{T}}_L \right)^\perp,$$

where $\tilde{\mathbf{T}}_L$ is as in Lemma 4.12, and $L > \dim \mathcal{Z}(\Sigma^\top)$ according to Lemma 4.8. Setting $M = L > \dim \mathcal{Z}(\Sigma^\top)$ and applying the formula $(A^\top \mathcal{V})^\perp = A^{-1}\mathcal{V}^\perp$ then lead to

$$\mathcal{S}^\star = \begin{bmatrix} B & AB & \cdots \end{bmatrix} \ker \tilde{\mathbf{T}}_M^\top.$$

From Lemma 4.12, we have that $\tilde{\mathbf{T}}_M^\top = P_2 \mathbf{T}_L P_1 \implies \ker(\tilde{\mathbf{T}}_M^\top) = \ker(P_2 \mathbf{T}_M P_1) = \ker(\overiii{[}_M] P_1)$ (by invertibility of P_2). Now, using $P_1^{-1} = P_1$,

$$\ker(\mathbf{T}_M P_1) = \{x \mid \mathbf{T}_M P_1 x = \mathbf{0}\} = \{P_1^{-1} z \mid \mathbf{T}_M z = \mathbf{0}\} = P_1 \ker \mathbf{T}_M,$$

which leads to

$$\mathcal{S}^\star = \begin{bmatrix} B & AB & \cdots \end{bmatrix} P_1 \ker \mathbf{T}_M = \begin{bmatrix} \cdots & AB & B \end{bmatrix} \ker \mathbf{T}_M = \mathbf{K}_M \ker \mathbf{T}_M.$$

Proof of Theorem 4.15

In order to prove Theorem 4.15, the following lemmas are necessary:

Lemma B.5. *For any $L, M \in \mathbb{Z}_{\geq 0}$ satisfying the condition in Assumption 4.1,* $\dim \ker \mathbf{T}_{L+M} = \dim \ker \mathbf{T}_L + \dim \ker \mathbf{T}_M - \zeta_\infty$.

Lemma B.6. *For any $L > \dim \mathcal{Z}$,*

$$\dim \ker \mathbf{T}_{L+1} - \dim \ker \mathbf{T}_L = \nu.$$

Note that the proofs of Lemmas B.5 and B.6 are deferred until after the proof of the main claim.

Proof of the main claim. For any positive integer $M \geq L$, Lemma B.6 yields

$$\dim \ker \mathbf{T}_{M+1} - \dim \ker \mathbf{T}_M = \nu.$$

Applying this recursively L times gives

$$\dim \ker \mathbf{T}_{M+L} - \dim \ker \mathbf{T}_M = L\nu.$$

Now, from Lemma B.5, we get

$$\dim \ker \mathbf{T}_{L+M} - \dim \ker \mathbf{T}_M = \dim \ker \mathbf{T}_L - \zeta_\infty.$$

Subtracting these last two equations gives

$$0 = \dim \ker \mathbf{T}_L - L\nu - \zeta_\infty,$$

which is equivalent to the desired expression.

The left-invertible case (which is proven in [223]) is a consequence of Proposition 4.3(iv)(a), which gives $\dim(\mathcal{V}^\star \cap \boldsymbol{B}\ker \boldsymbol{D}) = 0$.

For the right-invertible case, observe that $\dim\ker \mathbf{T}_L + \operatorname{rank}\mathbf{T}_L = Ln_u$. Moreover, since the rank is invariant under transposition, $\operatorname{rank}\mathbf{T}_L = \operatorname{rank}\mathbf{T}_L^\top = Ln_y - \dim\ker\mathbf{T}_L^\top$. Denote by $\tilde{\mathbf{T}}_L$ the block Toeplitz matrix corresponding to the transposed transfer function matrix $G^\top(\mathfrak{q})$. Then $\tilde{\mathbf{T}}_L$ satisfies the structural condition of [158, Theorem IV.8], giving $\dim\ker\tilde{\mathbf{T}}_L = \zeta_\infty(G^\top(\mathfrak{q}))$. Furthermore, the number of infinite zeros is invariant with respect to the transposed system from Definition 4.9(c). Applying Lemma 4.12, we get $\dim\ker\mathbf{T}_L^\top = \dim\ker\tilde{\mathbf{T}}_L = \zeta_\infty$. Hence, if $n_u > n_y$, $\dim\ker\mathbf{T}_L = Ln_u - (Ln_y - \zeta_\infty)$, proving the result.

Proof of Lemma B.5

Fix L, M according to Assumption 4.1. From

$$\mathbf{T}_{L+M} = \begin{bmatrix} \mathbf{T}_L & \mathbf{0} \\ \mathbf{O}_M\mathbf{K}_L & \mathbf{T}_M \end{bmatrix},$$

we use Proposition B.3 to get

$$\begin{aligned}\dim\ker\mathbf{T}_{L+M} &= \dim\ker\begin{bmatrix}\mathbf{0}\\ \mathbf{T}_M\end{bmatrix} + \dim\begin{bmatrix}\mathbf{T}_L\\ \mathbf{O}_M\mathbf{K}_L\end{bmatrix}^{-1}\operatorname{im}\begin{bmatrix}\mathbf{0}\\ \mathbf{T}_M\end{bmatrix}\\ &= \dim\ker\mathbf{T}_M + \dim\begin{bmatrix}\mathbf{T}_L\\ \mathbf{O}_M\mathbf{K}_L\end{bmatrix}^{-1}\operatorname{im}\begin{bmatrix}\mathbf{0}\\ \mathbf{T}_M\end{bmatrix} =: \dim\ker\mathbf{T}_M + \dim\mathcal{U}_L,\end{aligned}$$

giving the formula

$$\dim\ker\mathbf{T}_{L+M} = \dim\mathcal{U}_L + \dim\ker\mathbf{T}_M. \tag{B.2}$$

By its definition, the subspace $\mathcal{U}_L$ is that set of all $\boldsymbol{u}$ for which there exists a vector $\boldsymbol{v}$ giving

$$\mathbf{T}_L\boldsymbol{u} = 0, \qquad \mathbf{T}_M\boldsymbol{v} = -\mathbf{O}_M\mathbf{K}_L\boldsymbol{u}.$$

By Theorem 4.13, we have that $\mathcal{V}^\star = \mathbf{O}_M^{-1}\operatorname{im}\mathbf{T}_M$. Therefore, the second equation is equivalent to $\mathbf{K}_L\boldsymbol{u} \in \mathcal{V}^\star$. At the same time, $\boldsymbol{u} \in \ker\mathbf{T}_L$, giving, by Theorem 4.13, that $\mathbf{K}_L\boldsymbol{u} \in \mathcal{S}^\star$. As such, we have that $\mathbf{K}_L\boldsymbol{u} \in \mathcal{V}^\star \cap \mathcal{S}^\star = \mathcal{R}^\star$, which gives that

$$\mathcal{U}_L = \{\boldsymbol{u} \in \ker\mathbf{T}_L \mid \mathbf{K}_L\boldsymbol{u} \in \mathcal{R}^\star\}.$$

To determine the dimension of $\mathcal{U}_L$, consider the map

$$\phi : \ker\mathbf{T}_L \to \mathcal{S}^\star, \qquad \phi(\boldsymbol{u}) = \mathbf{K}_L\boldsymbol{u},$$

and its restriction to $\mathcal{U}_L$, $\phi|_{\mathcal{U}_L}$. Both maps are surjective, and their kernels satisfy (see [224, p. 63])

$$\ker\phi = \ker\mathbf{T}_L \cap \ker\mathbf{K}_L = \ker\mathbf{T}_L \cap \mathbf{K}_L^{-1}\{\mathbf{0}\} = \ker\mathbf{T}_L \cap \mathbf{K}_L^{-1}\{\mathbf{0}\} \cap \mathbf{K}_L^{-1}\mathcal{R}^\star = \ker\phi|_{\mathcal{U}_L}.$$

Applying the rank-nullity theorem on both ϕ and $\phi|_{\mathcal{U}_L}$ gives

$$\begin{aligned}\dim\ker\mathbf{T}_L &= \dim\ker\phi + \dim\mathcal{S}^\star,\\ \dim\mathcal{U}_L &= \dim\ker\phi + \dim\mathcal{R}^\star.\end{aligned}$$

Subtracting, we get that

$$\dim \mathcal{U}_L = \dim\ker \mathbf{T}_L - (\dim \mathcal{S}^\star - \dim \mathcal{R}^\star) = \dim\ker \mathbf{T}_L - (\dim \mathcal{S}^\star/\mathcal{R}^\star) = \dim\ker \mathbf{T}_L - \zeta_\infty,$$

where in the last step we used Theorem 4.4. Substituting in (B.2), we achieve the desired result.

Proof of Lemma B.6

We use again Proposition B.3 on

$$\mathbf{T}_{L+1} = \begin{bmatrix} \boldsymbol{D} & \mathbf{0} \\ \mathbf{O}_L \boldsymbol{B} & \mathbf{T}_L \end{bmatrix},$$

to get

$$\begin{aligned} \dim\ker \mathbf{T}_{L+1} &= \dim\ker \begin{bmatrix} \mathbf{0} \\ \mathbf{T}_L \end{bmatrix} + \dim \begin{bmatrix} \boldsymbol{D} \\ \mathbf{O}_L \boldsymbol{B} \end{bmatrix}^{-1} \operatorname{im} \begin{bmatrix} \mathbf{0} \\ \mathbf{T}_L \end{bmatrix} \\ &= \dim\ker \mathbf{T}_L + \dim \begin{bmatrix} \boldsymbol{D} \\ \mathbf{O}_L \boldsymbol{B} \end{bmatrix}^{-1} \operatorname{im} \begin{bmatrix} \mathbf{0} \\ \mathbf{T}_L \end{bmatrix} =: \dim\ker \mathbf{T}_L + \dim \mathcal{W}. \end{aligned} \tag{B.3}$$

With similar arguments as in Lemma B.5, we get that $\mathcal{W} = \boldsymbol{B}^{-1}\mathcal{V}^\star \cap \ker \boldsymbol{D}$. Replacing in (B.3) and using Theorem 4.1 gives the desired result.

Proof of Theorem 4.16

Applying Lemma 4.10 and Theorem 4.15, we obtain

$$\dim\ker \begin{bmatrix} \mathbf{O}_L & \mathbf{T}_L \end{bmatrix} = \dim \mathcal{V}^\star + \zeta_\infty + Lv.$$

From Theorem 4.4, we see that $\dim \mathcal{V}^\star + \zeta_\infty = \dim \mathcal{V}^\star + \dim \mathcal{S}^\star/\mathcal{R}^\star = \mathcal{N}^\star$, which provides the main result. The right-invertible case in Theorem 4.15 gives $v = n_u - n_y$, providing the respective expression in this theorem.

Finally, the expression for the left-invertible case follows likewise from Lemma 4.10 and Theorem 4.15, and using the fact that $\mathcal{R}^\star = \{\mathbf{0}\}$, so that $\dim \mathcal{V}^\star = \dim \mathcal{V}^\star/\mathcal{R}^\star = \zeta$ (Theorem 4.4).

Proof of Proposition 4.17

The null space of $\dddot{\mathbf{Y}}_{0,L,N}$ forms a basis for the null space of the right-hand side of the data equation (4.10). Therefore, using Assumption 4.2 and applying Lemma B.4 gives

$$\operatorname{im}(\dddot{\mathbf{U}}_{0,L,N} \dddot{\mathbf{Y}}^{\ker}_{0,L,N}) = \mathbf{T}_L^{-1} \operatorname{im} \mathbf{O}_L.$$

Applying Proposition B.3, we achieve

$$\dim \mathbf{T}_L^{-1} \operatorname{im} \mathbf{O}_L = \dim\ker \begin{bmatrix} \mathbf{O}_L & \mathbf{T}_L \end{bmatrix} - \dim \bar{\mathcal{O}} = \dim(\mathcal{N}^\star/\bar{\mathcal{O}}) + Lv,$$

where the last equality follows from Theorem 4.16, the inclusion $\bar{\mathcal{O}} \subseteq \mathcal{V}^\star$ established in Corollary 4.14, and the fact that $\mathcal{V}^\star \subseteq \mathcal{N}^\star$.

B

Proof of Theorem 4.18

By time-invariance, we can constrain the analysis by setting $t = 0$. Fix a trajectory, call $\boldsymbol{u}_\mathrm{p} \coloneqq \boldsymbol{u}^\mathrm{fz}_{[0,L-1]}$ and $\boldsymbol{u}_\mathrm{f} \coloneqq \boldsymbol{u}^\mathrm{fz}_{[L,L+M-1]}$. By Definition 4.13, there exists an initial state $\boldsymbol{x}(0)$ such that $\boldsymbol{y}(t) = 0$ for all $t \geq 0$. Fix any such $\boldsymbol{x}(0) =: \boldsymbol{x}_0$. Since $\boldsymbol{x}(L) = \boldsymbol{A}^L\boldsymbol{x}_0 + \mathbf{K}_L\boldsymbol{u}_\mathrm{p}$, zero output for $t \geq 0$ gives

$$\mathbf{O}_L\boldsymbol{x}_0 + \mathbf{T}_L\boldsymbol{u}_\mathrm{p} = \mathbf{0}, \tag{B.4a}$$

$$\mathbf{O}_M\boldsymbol{A}^L\boldsymbol{x}_0 + \mathbf{O}_M\mathbf{K}_L\boldsymbol{u}_\mathrm{p} + \mathbf{T}_M\boldsymbol{u}_\mathrm{f} = \mathbf{0}. \tag{B.4b}$$

Combining these two equations gives

$$-\mathbf{T}_{L+M,L}\boldsymbol{u}_\mathrm{p} = \mathbf{O}_{L+M}\boldsymbol{x}_0 + \begin{bmatrix}\mathbf{0}\\ \mathbf{T}_M\end{bmatrix}\boldsymbol{u}_\mathrm{f},$$

which implies

$$\mathbf{T}_{L+M,L}\boldsymbol{u}_\mathrm{p} \in \operatorname{im}\begin{bmatrix}\mathbf{O}_{L+M} & \mathbf{0}\\ & \mathbf{T}_M\end{bmatrix} \implies \boldsymbol{u}_\mathrm{p} \in \mathcal{U}^\mathrm{fz}_L.$$

This concludes the proof of necessity for (4.11).

To show that $\mathcal{U}^\mathrm{fz}_L$ is a basis for all L-long subsequences of $\mathcal{U}^\mathrm{fz}(\Sigma)$, choose $\boldsymbol{u}_\mathrm{p} \in \mathcal{U}^\mathrm{fz}_L$. By time invariance, it suffices to show that there exist $\boldsymbol{x}(0), \{\boldsymbol{u}(t)\}_{t\geq 0}$ such that $\{\boldsymbol{u}(t)\}_{t=0}^{L-1} = \boldsymbol{u}_p$ leads to $\boldsymbol{y}(t) = \mathbf{0}$ for all $t \in \mathbb{Z}_{\geq 0}$.

Since $\boldsymbol{u}_\mathrm{p} \in \mathcal{U}^\mathrm{fz}_L$, there exist $\boldsymbol{x}_0 \in \mathcal{V}^\star, \boldsymbol{u}_\mathrm{f} \in \mathcal{U}^M$ satisfying (B.4). Therefore, setting $\boldsymbol{x}(0) = \boldsymbol{x}_0$ and $\{\boldsymbol{u}(t)\}_{t=0}^{L-1} = \boldsymbol{u}_\mathrm{p}$, which satisfy (B.4b), gives $\mathbf{O}_M\boldsymbol{x}(L) + \mathbf{T}_M\boldsymbol{u}_\mathrm{f} = \mathbf{0}$, implying $\boldsymbol{x}(L) \in \mathcal{V}^\star$ and $\boldsymbol{y}(t) = \mathbf{0}, t = 0, 1, ..., L-1$ by M satisfying Assumption 4.1 and Lemma 4.9. By controlled-invariance of $\mathcal{V}^\star$, there exists $\{\boldsymbol{u}(t)\}_{t\geq L}$ such that $\boldsymbol{y}(t) = \mathbf{0}$ for all $t \geq L$. This concludes the proof of (4.11).

To compute the dimension $\dim \mathcal{U}^\mathrm{fz}_L$, we start by computing

$$\begin{aligned}
\dim\operatorname{im}\begin{bmatrix}\mathbf{O}_{L+M} & \mathbf{T}_{L+M}\end{bmatrix} &= \dim\left(\operatorname{im}\mathbf{T}_{L+M,L} + \operatorname{im}\begin{bmatrix}\mathbf{O}_{L+M} & \mathbf{0}\\ & \mathbf{T}_M\end{bmatrix}\right)\\
&= \dim\operatorname{im}\mathbf{T}_{L+M,L} + \dim\operatorname{im}\begin{bmatrix}\mathbf{O}_{L+M} & \mathbf{0}\\ & \mathbf{T}_M\end{bmatrix} - \dim\left(\operatorname{im}\mathbf{T}_{L+M,L} \cap \operatorname{im}\begin{bmatrix}\mathbf{O}_{L+M} & \mathbf{0}\\ & \mathbf{T}_M\end{bmatrix}\right)\\
&\overset{\text{(i)}}{=} Ln_u - \dim\ker\overbrace{[}^{}_L + M, L] - \dim\left(\operatorname{im}\mathbf{T}_{L+M,L} \cap \operatorname{im}\begin{bmatrix}\mathbf{O}_{L+M} & \mathbf{0}\\ & \mathbf{T}_M\end{bmatrix}\right)\\
&\quad + \dim\operatorname{im}\begin{bmatrix}\mathbf{O}_{L+M} & \mathbf{0}\\ & \mathbf{T}_M\end{bmatrix}\\
&\overset{\text{(ii)}}{=} Ln_u - \dim\mathbf{T}^{-1}_{L+M,L}\begin{bmatrix}\mathbf{O}_{L+M} & \mathbf{0}\\ & \mathbf{T}_M\end{bmatrix} + \dim\operatorname{im}\begin{bmatrix}\mathbf{O}_{L+M} & \mathbf{0}\\ & \mathbf{T}_M\end{bmatrix}\\
&= Ln_u - \dim\mathcal{U}^\mathrm{fz}_L + \dim\operatorname{im}\begin{bmatrix}\mathbf{O}_{L+M} & \mathbf{0}\\ & \mathbf{T}_M\end{bmatrix},
\end{aligned}$$

where equality (i) holds by the rank nullity theorem, and equality (ii) follows from Proposition B.2. Applying the rank nullity theorem on Theorem 4.16, we get

$$\dim\operatorname{im}\begin{bmatrix}\mathbf{O}_{L+M} & \mathbf{T}_{L+M}\end{bmatrix} = n_x + (L+M)n_u - \dim\mathcal{V}^\star - \zeta_\infty - (L+M)\nu.$$

Therefore,

$$\begin{aligned}\dim \mathcal{U}_L^{\mathrm{fz}} &= \dim \mathcal{V}^\star + \zeta_\infty + \dim \operatorname{im}\begin{bmatrix}\mathbf{O}_{L+M} & \mathbf{0}\\ & \mathbf{T}_M\end{bmatrix} + (L+M)\nu - (n_x + Mn_u)\\ &= \dim \mathcal{V}^\star + \zeta_\infty + (L+M)\nu - \dim\ker\begin{bmatrix}\mathbf{O}_{L+M} & \mathbf{0}\\ & \mathbf{T}_M\end{bmatrix}. \end{aligned} \tag{B.5}$$

Now we inspect $\ker\begin{bmatrix}\mathbf{O}_{L+M} & \mathbf{0}\\ & \mathbf{T}_M\end{bmatrix}$. These are the solutions $(\boldsymbol{x}_0, \boldsymbol{u}_{\mathrm{f}})$ such that

$$\mathbf{O}_L \boldsymbol{x}_0 = \mathbf{0} \tag{B.6a}$$

$$\mathbf{O}_M \boldsymbol{A}^L \boldsymbol{x}_0 + \mathbf{T}_M \boldsymbol{u}_{\mathrm{f}} = \mathbf{0}. \tag{B.6b}$$

Equation (B.6a) imposes $\boldsymbol{x}_0 \in \ker \mathbf{O}_L$, which equals $\bar{\mathcal{O}}$ by Lemma 4.6 since $L > \dim \mathcal{Z}$. Now, Lemma 4.6 also gives $\ker \mathbf{O}_{L+M} = \bar{\mathcal{O}}$. Hence, $\ker \mathbf{O}_{L+M} = \ker \mathbf{O}_L \cap \ker(\mathbf{O}_M \boldsymbol{A}^L) = \bar{\mathcal{O}} \cap \ker(\mathbf{O}_M \boldsymbol{A}^L) \iff \bar{\mathcal{O}} = \bar{\mathcal{O}} \cap \ker(\mathbf{O}_M \boldsymbol{A}^L)$, which implies that $\ker(\mathbf{O}_M \boldsymbol{A}^L) \supseteq \bar{\mathcal{O}}$. Thus, $\boldsymbol{x}_0 \in \ker \mathbf{O}_L \implies \boldsymbol{x}_0 \in \ker(\mathbf{O}_M \boldsymbol{A}^L)$, which means that (B.6) is equivalent to

$$\begin{aligned}\mathbf{O}_L \boldsymbol{x}_0 &= \mathbf{0},\\ \mathbf{T}_M \boldsymbol{u}_{\mathrm{f}} &= \mathbf{0}.\end{aligned}$$

These are independent equations, whose solution dimensions are $\dim \bar{\mathcal{O}}$ and $\dim\ker \mathbf{T}_M$, respectively. Hence,

$$\dim\ker\begin{bmatrix}\mathbf{O}_{L+M} & \mathbf{0}\\ & \mathbf{T}_M\end{bmatrix} = \dim \bar{\mathcal{O}} + \dim\ker \mathbf{T}_M.$$

Substitution in (B.5) leads to

$$\begin{aligned}\dim \mathcal{U}_L^{\mathrm{fz}} &= \dim \mathcal{V}^\star + \zeta_\infty + (L+M)\nu - \dim \bar{\mathcal{O}} - \dim\ker \mathbf{T}_M\\ &\overset{\text{(i)}}{=} \dim(\mathcal{V}^\star/\bar{\mathcal{O}}) + L\nu = \zeta - \dim \bar{\mathcal{O}} + \dim \mathcal{R}^\star\\ &= \zeta - \dim \bar{\mathcal{O}} + \dim \mathcal{R}^\star + L\nu,\end{aligned}$$

in which step (i) follows from $\dim\ker \mathbf{T}_M = \zeta_\infty + M\nu$, and the last equality is due to the alternative expression $\dim \mathcal{V}^\star = \dim \mathcal{V}^\star/\mathcal{R}^\star + \dim \mathcal{R}^\star = \zeta + \dim \mathcal{R}^\star$ by Theorem 4.4. For invertible systems, Theorem 4.15 gives $\nu = n_u - n_y$ in the right-invertible case. Substitution in (B.5) yields the desired expression. Finally, when Σ left-invertible, $\mathcal{R}^\star = \{\mathbf{0}\}$ (Proposition 4.3), thereby concluding the proof.

Proof of Proposition 4.19

Since ($\implies$) has already been established in Theorem 4.18, it remains to prove ($\impliedby$). Given that $\boldsymbol{u}^{\mathrm{fz}}_{[t,t+L-1]} \in \mathcal{U}^{\mathrm{fz}}_L$ for all $t \in \mathbb{Z}_{\geq 0}$, fixing $t = 0$ gives $\boldsymbol{u}_{\mathrm{p}} \coloneqq \boldsymbol{u}^{\mathrm{fz}}_{[0,L-1]} \in \mathcal{U}^{\mathrm{fz}}_L$, implying there exist $\boldsymbol{x}_0 \in \mathcal{V}^\star, \boldsymbol{u}_{\mathrm{f}} \in \mathcal{U}^M$ satisfying (B.4). Therefore, setting $\boldsymbol{x}(0) = \boldsymbol{x}_0$ and applying $\boldsymbol{u}_{\mathrm{p}}$ leads to $\boldsymbol{x}(t) \in \mathcal{V}^\star$ for $t = 0, \dots, L$ and $\boldsymbol{y}(t) = \mathbf{0}$ for $t = 0, \dots, L-1$ by Lemma 4.9 and

B

Assumption 4.1. It suffices to show that applying the shifted input $\boldsymbol{u}'_{\mathrm{p}} \coloneqq \boldsymbol{u}^{\mathrm{fz}}_{[1,L]}$ to $\boldsymbol{x}(1) = \boldsymbol{A}\boldsymbol{x}_0 + \boldsymbol{B}\boldsymbol{u}^{\mathrm{fz}}(0)$ also results in $\boldsymbol{x}(t) \in \mathcal{V}^\star$ for $t = 1,\dots,L+1$ and $\boldsymbol{y}(t) = \boldsymbol{0}$ for $t = 1,\dots,L$. This is because the same argument can be applied inductively to $\boldsymbol{u}^{\mathrm{fz}}_{[2,L+1]}, \boldsymbol{u}^{\mathrm{fz}}_{[3,L+2]},\dots$, due to time invariance, while the output remains zero throughout. As a consequence, if the argument holds for t, it also holds for $t+1$. Accordingly, we now turn to proving the claim by focusing on the time-window overlap of $(L-1)$-length between $\boldsymbol{u}_{\mathrm{p}}$ and $\boldsymbol{u}'_{\mathrm{p}}$. Since $\boldsymbol{u}'_{\mathrm{p}} \in \mathcal{U}^{\mathrm{fz}}_L$ by assumption, there exist $\boldsymbol{x}'_0 \in \mathcal{V}^\star, \boldsymbol{u}'_{\mathrm{f}} \in \mathcal{U}^M$ satisfying (B.4). Then, we have

$$\left.\begin{aligned} \boldsymbol{u}_{\mathrm{p}} \text{ satisfies (B.4a)} &\implies \mathbf{O}_{L-1}\boldsymbol{x}(1) + \mathbf{T}_{L-1}\boldsymbol{u}^{\mathrm{fz}}_{[1,L-1]} = \boldsymbol{0} \\ \boldsymbol{u}'_{\mathrm{p}} \text{ satisfies (B.4a)} &\implies \mathbf{O}_{L-1}\boldsymbol{x}'_0 + \mathbf{T}_{L-1}\boldsymbol{u}^{\mathrm{fz}}_{[1,L-1]} = \boldsymbol{0} \end{aligned}\right\} \implies \boldsymbol{x}(1) - \boldsymbol{x}'_0 \in \ker \mathbf{O}_{L-1} = \bar{\mathcal{O}},$$

following from $L-1$ satisfying Assumption 4.1, since $L > \dim Z + 1$. Consequently, in order for $\mathbf{O}_L\boldsymbol{x}(1) + \mathbf{T}_L\boldsymbol{u}'_{\mathrm{p}} = \boldsymbol{0}$ to hold, we only need to show

$$\boldsymbol{C}\boldsymbol{A}^{L-1}\boldsymbol{x}(1) + \sum_{i=0}^{L-1} \boldsymbol{M}_i \boldsymbol{u}^{\mathrm{fz}}(L-i) = \boldsymbol{0}. \tag{B.8}$$

In this regard, from $\boldsymbol{u}'_{\mathrm{p}}$ satisfying (B.4a), we obtain $\sum_{i=0}^{L-1} \boldsymbol{M}_i \boldsymbol{u}^{\mathrm{fz}}(L-i) = -\boldsymbol{C}\boldsymbol{A}^{L-1}\boldsymbol{x}'_0$. Substitution in (B.8) leads to $\boldsymbol{C}\boldsymbol{A}^{L-1}\boldsymbol{x}(1) + \sum_{i=0}^{L-1} \boldsymbol{M}_i \boldsymbol{u}^{\mathrm{fz}}(L-i) = \boldsymbol{C}\boldsymbol{A}^{L-1}(\boldsymbol{x}(1) - \boldsymbol{x}'_0) = \boldsymbol{0}$ due to $\boldsymbol{x}(1) - \boldsymbol{x}'_0 \in \bar{\mathcal{O}}$ and $\boldsymbol{A}$-invariance of $\bar{\mathcal{O}}$. This establishes that $(\boldsymbol{x}(1), \boldsymbol{u}'_{\mathrm{p}})$ satisfies (B.4a). Furthermore, we show (B.4b) also holds for $(\boldsymbol{x}(1), \boldsymbol{u}'_{\mathrm{p}}, \boldsymbol{u}'_{\mathrm{f}})$ by the following implications

$$\begin{aligned} \boldsymbol{u}'_{\mathrm{p}} \text{ satisfies (B.4b)} &\implies \mathbf{O}_M\boldsymbol{A}^L\boldsymbol{x}'_0 + \mathbf{O}_M\mathbf{K}_L\boldsymbol{u}'_{\mathrm{p}} + \mathbf{T}_M\boldsymbol{u}'_{\mathrm{f}} = \boldsymbol{0} && \text{(I)} \\ \boldsymbol{x}'_0 - \boldsymbol{x}(1) \in \mathbf{O}_L &\implies \mathbf{O}_M\boldsymbol{A}^L(\boldsymbol{x}'_0 - \boldsymbol{x}(1)) = \boldsymbol{0} && \text{(II)} \\ \text{(I) and (II)} &\implies \mathbf{O}_M\boldsymbol{A}^L\boldsymbol{x}'_0 + \mathbf{O}_M\mathbf{K}_L\boldsymbol{u}'_{\mathrm{p}} + \mathbf{T}_M\boldsymbol{u}'_{\mathrm{f}} = \mathbf{O}_M\boldsymbol{A}^L(\boldsymbol{x}'_0 - \boldsymbol{x}(1)) \\ &\implies \mathbf{O}_M\boldsymbol{A}^L\boldsymbol{x}(1) + \mathbf{O}_M\mathbf{K}_L\boldsymbol{u}'_{\mathrm{p}} + \mathbf{T}_M\boldsymbol{u}'_{\mathrm{f}} = \boldsymbol{0}. \end{aligned}$$

Hence, $(\boldsymbol{x}(1), \boldsymbol{u}'_{\mathrm{p}}, \boldsymbol{u}'_{\mathrm{f}})$ satisfies (B.4b) and therefore (B.4), leading to $\boldsymbol{x}(t) \in \mathcal{V}^\star$ for $t = 1,\dots,L+1$ and $\boldsymbol{y}(t) = \boldsymbol{0}$ for $t = 1,\dots,L$. This proves the sufficiency for (4.11).

Proof of Lemma 4.20

By the data equation we have

$$\begin{aligned} \overset{/\!/}{\mathbf{Y}}_{0,L+M,N} &= \begin{bmatrix} \mathbf{O}_{L+M} & \mathbf{T}_{L+M,L} & \begin{matrix}\boldsymbol{0}\\ \mathbf{T}_M\end{matrix} \end{bmatrix} \begin{bmatrix} \boldsymbol{X}_{[0,N-L-M]} \\ \overset{/\!/}{\mathbf{U}}_{0,L,N-M} \\ \overset{/\!/}{\mathbf{U}}_{L,M,N} \end{bmatrix} \\ &= \left[\begin{array}{cc|c} \mathbf{O}_{L+M} & \begin{matrix}\boldsymbol{0}\\ \mathbf{T}_M\end{matrix} & \mathbf{T}_{L+M,L} \end{array}\right] \begin{bmatrix} \boldsymbol{X}_{[0,N-L-M]} \\ \overset{/\!/}{\mathbf{U}}_{L,M,N} \\ \overset{/\!/}{\mathbf{U}}_{0,L,N-M} \end{bmatrix} \end{aligned}$$

The null space of $\overset{///}{\mathbf{Y}}_{0,L+M,N}$ is also a null-space basis for the right-hand side. Therefore, using Assumption 4.2, we can apply Lemma B.4 to get

$$\mathbf{T}_{L+M,L}^{-1}\,\mathrm{im}\begin{bmatrix}\mathbf{O}_{L+M} & \mathbf{0}\\ & \mathbf{T}_M\end{bmatrix} = \overset{///}{\mathbf{U}}_{0,L,N-M}\,\ker\overset{///}{\mathbf{Y}}_{0,L+M,N},$$

which, by (4.11) of Theorem 4.18, gives $\mathcal{U}_L^{\mathrm{fz}}$.

Proof of Lemma 4.21

Using [179, Theorem 7.11] and the fact that $\ker \boldsymbol{D}\cap \boldsymbol{B}^{-1}\mathcal{V}^\star = \{\mathbf{0}\}$ for left-invertible systems (Proposition 4.3), we get that any finite-zero input is of the form $\boldsymbol{u}^{\mathrm{fz}}(t) = \boldsymbol{F}(\boldsymbol{A}+\boldsymbol{BF})^t\boldsymbol{x}(0)$ for some $\boldsymbol{x}(0)\in\mathcal{V}^\star$, where $\boldsymbol{F}\in\mathscr{F}(\mathcal{V}^\star)$.

Now, since $(\boldsymbol{A}+\boldsymbol{BF})$ renders $\mathcal{V}^\star$ invariant, then for any full-column-rank $\boldsymbol{V}$ basis of $\mathcal{V}^\star$, there exists a unique square $\boldsymbol{A}_\zeta$ such that $(\boldsymbol{A}+\boldsymbol{BF})\boldsymbol{V} = \boldsymbol{V}\boldsymbol{A}_\zeta \implies (\boldsymbol{A}+\boldsymbol{BF})^t\boldsymbol{V} = \boldsymbol{V}\boldsymbol{A}_\zeta^t$. Hence, let $\boldsymbol{C}_\zeta \coloneqq \boldsymbol{FV}$ and rewrite $\boldsymbol{x}(0) = \boldsymbol{V}\boldsymbol{z}$. We get $\boldsymbol{u}^{\mathrm{fz}}(t) = \boldsymbol{F}(\boldsymbol{A}+\boldsymbol{BF})^t\boldsymbol{x}(0) = \boldsymbol{F}(\boldsymbol{A}+\boldsymbol{BF})^t\boldsymbol{V}\boldsymbol{z} = \boldsymbol{FV}\boldsymbol{A}_\zeta^t\boldsymbol{z} = \boldsymbol{C}_\zeta\boldsymbol{A}_\zeta^t\boldsymbol{z}$, proving the first expression.

Finally, by construction, $\boldsymbol{A}_\zeta$ is a matrix representation of the restriction of $\boldsymbol{A}+\boldsymbol{BF}$ to $\mathcal{V}^\star$. As such, $\sigma(\boldsymbol{A}_\zeta) = \sigma(\boldsymbol{A}+\boldsymbol{BF}|\mathcal{V}^\star) = \sigma(\boldsymbol{A}+\boldsymbol{BF}|\mathcal{V}^\star/\mathcal{R}^\star)$, where the last equality comes from Proposition 4.3, which gives $\mathcal{R}^\star = \{\mathbf{0}\}$ for left-invertible systems. From [174, Theorem 2 (f)], this spectrum is precisely the multiset of invariant zeros of Σ.

Proof of Theorem 4.22

To show existence and uniqueness for $\boldsymbol{U}_{[0:L-1]}\boldsymbol{A}_{\zeta_o} = \boldsymbol{U}_{[1:L]}$, we show that $\mathrm{im}\,\boldsymbol{U}_{[1:L]} \subseteq \mathrm{im}\,\boldsymbol{U}_{[0:L-1]}$ (existence) and $\boldsymbol{U}_{[0:L-1]}$ is full column-rank (uniqueness). We begin by the latter.

By Lemma 4.20, $\boldsymbol{U} = \boldsymbol{U}_{[0,L]}$ is a basis for $\mathcal{U}_{L+1}^{\mathrm{fz}}$. Hence, it follows from Theorem 4.18 that $\boldsymbol{U}$ is also a basis for all $(L+1)$-long subsequences of all finite-zero input sequences for Σ. Now assume $\boldsymbol{U}_{[0:L-1]}$ is column-rank deficient, i.e., $\boldsymbol{u}_{[0:L-1]} \coloneqq \boldsymbol{U}_{[0:L-1]}\boldsymbol{z} = \mathbf{0}$ for some non-zero $\boldsymbol{z}$. Since $\boldsymbol{U}_{[0,L]}$ is full column rank by construction, we have that $\boldsymbol{u}_{[0:L]} \coloneqq \boldsymbol{U}_{[0,L]}\boldsymbol{z} = [\mathbf{0}\ \ \boldsymbol{u}^\top(L)]^\top \neq \mathbf{0}$. We show that $\boldsymbol{u}(L) = \mathbf{0}$.

From the construction of $\boldsymbol{u}(L)$, the corresponding input trajectory $\boldsymbol{u}(t)$ is zero for $t = 0,...,L-1$ and, for some $\boldsymbol{x}(0)\in\mathcal{V}^\star$, gives $\boldsymbol{y}(t) = \mathbf{0}$ for $t = 0,...,L$. Additionally, by Definition 4.13, $\boldsymbol{x}(t)\in\mathcal{V}^\star$ for $t = 0,...,L+1$. Since L satisfying Assumption 4.1, $\boldsymbol{u}_{[0:L-1]} = \mathbf{0}$ implies that $\mathbf{O}_L\boldsymbol{x}(0) = \mathbf{0} \implies \boldsymbol{x}(0)\in\bar{\mathcal{O}}$, meaning $\boldsymbol{C}\boldsymbol{A}^i\boldsymbol{x}(0) = \mathbf{0}$ for all $i\geq 0$. It also follows that $\boldsymbol{x}(L)\in\bar{\mathcal{O}}$ by $\boldsymbol{x}(L) = \boldsymbol{A}^L\boldsymbol{x}(0)$ and $\boldsymbol{A}$-invariance of $\bar{\mathcal{O}}$. On the one hand, $\boldsymbol{y}(L) = \boldsymbol{C}\boldsymbol{x}(L) + \boldsymbol{D}\boldsymbol{u}(L) = \mathbf{0} \implies \boldsymbol{u}(L)\in\ker\boldsymbol{D} \implies \boldsymbol{B}\boldsymbol{u}(L)\in\boldsymbol{B}\ker\boldsymbol{D}$, following from $\boldsymbol{C}\boldsymbol{x}(L) = \boldsymbol{C}\boldsymbol{A}^L\boldsymbol{x}(0) = \mathbf{0}$. On the other hand, $\boldsymbol{x}(L+1) = \boldsymbol{A}\boldsymbol{x}(L) + \boldsymbol{B}\boldsymbol{u}(L)\in\mathcal{V}^\star \implies \boldsymbol{B}\boldsymbol{u}(L)\in\mathcal{V}^\star$, since $\boldsymbol{A}\boldsymbol{x}(L)\in\bar{\mathcal{O}}\subseteq\mathcal{V}^\star$ by $\boldsymbol{A}$-invariance of $\bar{\mathcal{O}}$ and Corollary 4.14. Together, these conditions imply $\boldsymbol{B}\boldsymbol{u}(L)\in\mathcal{V}^\star\cap\boldsymbol{B}\ker\boldsymbol{D} = \{\mathbf{0}\}$ for left-invertible systems by Proposition 4.3, and therefore $\boldsymbol{u}(L)\in\ker\boldsymbol{B}$. We also established that $\boldsymbol{u}(L)\in\ker\boldsymbol{D}$, implying $\boldsymbol{u}(L)\in\ker\begin{bmatrix}\boldsymbol{B}^\top & \boldsymbol{D}^\top\end{bmatrix}^\top = \{\mathbf{0}\}$ by the full column rank condition in Proposition 4.3; hence $\boldsymbol{u}(L) = \mathbf{0}$. This proves uniqueness.

Since $\boldsymbol{U}_{[0:L-1]}$ is full column rank, we have $\mathrm{im}\,\boldsymbol{U}_{[0:L-1]} = \mathcal{U}_L^{\mathrm{fz}}$, leading to $\mathrm{rank}\,\boldsymbol{U}_{[0:L-1]} = \zeta_o$ by Theorem 4.18. By time-invariance, any linear combination of $\boldsymbol{U}_{[1:L]}$ is a subsequence

of $\mathcal{U}_{L+1}^{\mathrm{fz}}$ and thus belongs to $\mathcal{U}_{L}^{\mathrm{fz}}$. Therefore, $\operatorname{im} \boldsymbol{U}_{[1:L]} \subseteq \operatorname{im} \boldsymbol{U}_{[0:L-1]}$, establishing existence.

Now that existence and uniqueness have been proven, we have the recursion $\boldsymbol{U}_{[t+1]} = \boldsymbol{U}_{[t]}\boldsymbol{A}_{\zeta_o}$ and, as such, every finite-zero input of Σ satisfies, for $t = 0, ..., L$, the equation $\boldsymbol{u}(t) = \boldsymbol{U}_{[0]}\boldsymbol{A}_{\zeta_o}^{t}\, \boldsymbol{z}$ for some $\boldsymbol{z} \in \mathbb{R}^{\zeta_o}$. Therefore, Lemma 4.21 implies that $\sigma(\boldsymbol{A}_{\zeta_o})$ is the multiset of invariant zeros of Σ, excluding the output decoupling zeros, concluding the proof.

B

C

Rational Orthonormal Basis Functions Implementation

This chapter provides a tutorial on the efficient implementation of rational orthonormal basis functions introduced in Chapter 5, supported by an accompanying MATLAB toolbox.

C.1 Balanced State-Space Realization

Consider the following LTI system:

$$\mathcal{S}: \quad \begin{cases} \boldsymbol{x}^+(t) = \boldsymbol{A}\boldsymbol{x}(t) + \boldsymbol{B}\boldsymbol{u}(t) \\ \boldsymbol{y}(t) = \boldsymbol{C}\boldsymbol{x}(t) + \boldsymbol{D}\boldsymbol{u}(t) \end{cases},$$

where the superscript ''+' denotes the forward time shift or the differentiation, i.e., $\boldsymbol{x}^+(t) = \boldsymbol{x}(t+1)$ in discrete-time, and $\boldsymbol{x}^+(t) = \mathrm{d}\boldsymbol{x}(t)/\mathrm{d}t$ in continuous-time. Then, the associated *Controllability*/*Reachability* Gramian $\boldsymbol{W}_\mathrm{c}$ can be expressed as

$$\begin{aligned} \boldsymbol{A}\boldsymbol{W}_\mathrm{c}\boldsymbol{A}^\top - \boldsymbol{W}_\mathrm{c} + \boldsymbol{B}\boldsymbol{B}^\top = \boldsymbol{0} \qquad &\text{:discrete-time} \\ \boldsymbol{A}\boldsymbol{W}_\mathrm{c} + \boldsymbol{W}_\mathrm{c}\boldsymbol{A}^\top + \boldsymbol{B}\boldsymbol{B}^\top = \boldsymbol{0} \qquad &\text{:continuous-time} \end{aligned}$$

Also, the associated *Observability*/*Detectability* Gramian $\boldsymbol{W}_\mathrm{o}$ is defined as

$$\begin{aligned} \boldsymbol{A}^T\boldsymbol{W}_\mathrm{o}\boldsymbol{A} - \boldsymbol{W}_\mathrm{o} + \boldsymbol{C}^\top\boldsymbol{C} = \boldsymbol{0} \qquad &\text{:discrete-time} \\ \boldsymbol{A}^\top\boldsymbol{W}_\mathrm{o} + \boldsymbol{W}_\mathrm{o}\boldsymbol{A} + \boldsymbol{C}^\top\boldsymbol{C} = \boldsymbol{0} \qquad &\text{:continuous-time} \end{aligned}$$

Thus, we define the Hankel singular values as

$$\sigma_i \triangleq \sqrt{\lambda_i(\boldsymbol{W}_\mathrm{c}\boldsymbol{W}_\mathrm{o})} \tag{C.1}$$

The controllability and observability Gramians are a measure of controllability and observability of the state-space system model in certain directions.

Remark C.1. The Gramians are not invariant under coordinate (similarity) transformations.

Definition C.1. (*Balanced realization*) Let the quadrupole $(\boldsymbol{A}, \boldsymbol{B}, \boldsymbol{C}, \boldsymbol{D})$ be a minimal state-space realization of the system $\mathcal{S}$. Such a representation is called *balanced* if the associated Gramians are *equal* and *diagonal*, i.e.,

$$\boldsymbol{W}_{\mathrm{c}} = \boldsymbol{W}_{\mathrm{o}} = \Sigma = \mathrm{diag}\{\sigma_1, \sigma_2, \cdots, \sigma_n\} = \begin{bmatrix} \sigma_1 & & & \\ & \sigma_2 & & \\ & & \ddots & \\ & & & \sigma_n \end{bmatrix}$$

Remark C.2. For *stable* systems, Σ is positive semidefinite (p.s.d.) $\Sigma \succeq 0$, that is, $\sigma_1 \geq \sigma_2 \geq \cdots \geq \sigma_n \geq 0$. In addition, the diagonal entries are in fact the Hankel singular values that can be computed from (C.1). However, in case of *unstable* systems, Σ is indefinite and only diagonal [225].

To have a balanced realization of a minimal state-space system model, we would like to obtain a proper coordinate (similarity) transformation $\boldsymbol{T}$ that leads to a realization for which the controllability and observability Gramians are equal and diagonal (Definition C.1), that is,

$$\boldsymbol{G} \sim \left[\begin{array}{c|c} \boldsymbol{A} & \boldsymbol{B} \\ \hline \boldsymbol{C} & \boldsymbol{D} \end{array}\right] = \left[\begin{array}{c|c} \boldsymbol{T}^{-1}\boldsymbol{A}\boldsymbol{T} & \boldsymbol{T}^{-1}\boldsymbol{B} \\ \hline \boldsymbol{C}\boldsymbol{T} & \boldsymbol{D} \end{array}\right] = \left[\begin{array}{c|c} \hat{\boldsymbol{A}} & \hat{\boldsymbol{B}} \\ \hline \hat{\boldsymbol{C}} & \boldsymbol{D} \end{array}\right]; \qquad \boldsymbol{x}(t) = \boldsymbol{T}\hat{\boldsymbol{x}}(t)$$

With this transformation, the controllability and observability Gramians in the new coordinate system are given by

$$\hat{\boldsymbol{W}}_{\mathrm{c}} = \boldsymbol{T}^{-1}\boldsymbol{W}_{\mathrm{c}}(\boldsymbol{T}^{-1})^{\top}$$
$$\hat{\boldsymbol{W}}_{\mathrm{o}} = \boldsymbol{T}^{\top}\boldsymbol{W}_{\mathrm{o}}\boldsymbol{T}$$

For more details, see lecture notes of MIT or these papers [226, 227]

Definition C.2. (*Input Balanced realization*) [227, 228] A state-space realization (A, B, C, D) for which the controllability Gramian equals to the identity matrix, i.e., $\boldsymbol{W}_{\mathrm{c}} = \mathbf{I}$ is called *Input Balanced*. The corresponding input to state transfer functions will then be orthonormal. This state-space realization satisfies the Lyapunov equation

$$\boldsymbol{A}\boldsymbol{A}^{\top} + \boldsymbol{B}\boldsymbol{B}^{\top} = \mathbf{I} \qquad \text{:discrete-time}$$

C.2 Rational Orthonormal Basis Functions

To construct orthonormal rational basis in a scalable manner, consider a cascade structure of *all-pass* filters as shown in Figure C.1, where each filter has a balanced state-space realization. In this structure, a network of all-pass filters are serially connected to each other.

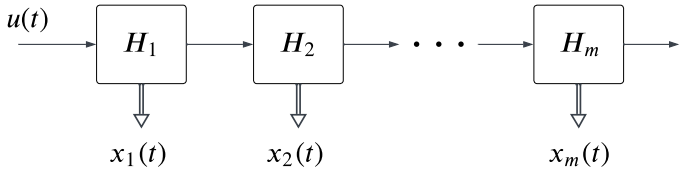

Figure C.1: A cascade network of all-pass filters.

C.2.1 All-Pass Transfer Function

All-pass transfer functions provide a powerful framework for factorization of state covariance matrices (controllability Gramian), as firstly noted by [229].

Definition C.3 (All-Pass)**.** A stable single-input single output LTI system $\mathcal{S}$ with rational transfer function $H(\mathfrak{q})$ is called all-pass if its DTFT (discrete-time Fourier transform) satisfies $|H(e^{j\omega})| = R_0$ for some value $R_0 > 0$ and all ω.

All-pass systems only affect the phase of the signal.

Remark C.3. Some textbooks define all-pass systems such that $|H(e^{j\omega})| = 1$.

Definition C.3 is equivalent to writing

$$\begin{aligned} & |H(e^{j\omega})|^2 = R_0^2 \\ \Leftrightarrow \quad & H(e^{j\omega})\overline{H(e^{j\omega})} = R_0^2 \\ \Leftrightarrow \quad & h[n] * \overline{h[-n]} = R_0^2 \delta[n] \\ \Leftrightarrow \quad & H(\mathfrak{q})\overline{H(1/\overline{z})} = R_0^2 . \end{aligned}$$

Interpretation: $H(\mathfrak{q})$ must have the property that $\overline{H(1/\overline{\mathfrak{q}})}$ is its inverse system (up to a scale factor). This means that $H(\mathfrak{q})$ is all-pass if and only if two conditions hold:

- the poles of $H(\mathfrak{q})$ are canceled by the zeros of $\overline{H(1/\overline{\mathfrak{q}})}$ and
- the zeros of $H(\mathfrak{q})$ are canceled by the poles of $\overline{H(1/\overline{\mathfrak{q}})}$.

In general, all-pass filters have conjugate-reciprocal pole-zero pairs.

C.2.2 Basis Construction

Consider a single-input single-output (SISO) asymptotically stable all-pass transfer function $H(\mathfrak{q})$ of order m with real valued impulse response,

$$H(\mathfrak{q})\overline{H(1/\overline{\mathfrak{q}})} = 1 ,$$

completely determined by its poles $\{\xi_i \in \mathbb{C},\ |\xi_i| < 1\}$,

$$H(\mathfrak{q}) = \prod_{i=1}^{m} \left[\frac{1 - \overline{\xi_i}\mathfrak{q}}{\mathfrak{q} - \xi_i} \right].$$

Let $(\boldsymbol{A}, \boldsymbol{B}, \boldsymbol{C}, D)$ be a minimal input balanced state-space realization of $H(\mathfrak{q})$. With a proper choice of state vector (via the similarity transformation $\boldsymbol{T}$), we can ensure that the controllability Gramian $\boldsymbol{W}_\mathrm{c} = \mathbf{I}$ for the input balanced realization (C.2). Due to the input balanced realization and the all-pass property, we derive the following conditions [228]

$$\begin{aligned} \boldsymbol{A}\boldsymbol{A}^\top + \boldsymbol{B}\boldsymbol{B}^\top &= \mathbf{I}, \\ DD^\top + \boldsymbol{C}\boldsymbol{C}^\top &= 1, \\ \boldsymbol{B}D^\top + \boldsymbol{A}\boldsymbol{C}^\top &= \mathbf{0}, \end{aligned}$$

or more compactly

$$\begin{bmatrix} \boldsymbol{A} & \boldsymbol{B} \\ \boldsymbol{C} & D \end{bmatrix} \begin{bmatrix} \boldsymbol{A} & \boldsymbol{B} \\ \boldsymbol{C} & D \end{bmatrix}^\top = \mathbf{I}, \tag{C.2}$$

implying that the corresponding matrix $\boldsymbol{F} := \begin{bmatrix} \boldsymbol{A} & \boldsymbol{B} \\ \boldsymbol{C} & D \end{bmatrix}$ is orthogonal. Thus, a state-space realization

$$\begin{bmatrix} \boldsymbol{x}(t+1) \\ y(t) \end{bmatrix} = \begin{bmatrix} \boldsymbol{A} & \boldsymbol{B} \\ \boldsymbol{C} & D \end{bmatrix} \begin{bmatrix} \boldsymbol{x}(t) \\ u(t) \end{bmatrix},$$

of $H(\mathfrak{q})$ which satisfies (C.2) is called orthogonal.

The characterization provided above for SISO all-pass filters also holds for multi-input multi-output (MIMO) all-pass filters. A MIMO all-pass system with transfer function $\boldsymbol{H}(\mathfrak{q}) = \boldsymbol{C}(\mathfrak{q}\mathbf{I} - \boldsymbol{A}^{-1})\boldsymbol{B} + \boldsymbol{D}$ is orthogonal if and only if it has an orthogonal realization [228].

In [229], it has been shown that the orthogonality and the all-pass property are preserved through several different connections of all-pass filters (some or all of these filters may have more than one input and/or more than one output). Regarding rational orthonormal basis functions (OBF), we are mostly interested in cascade connections. In the following, we only consider SISO all-pass filters.

Theorem C.1. *Consider two orthogonal all-pass filters $\boldsymbol{H}_1$ and $\boldsymbol{H}_2$ with*

$$\boldsymbol{F}_1 := \begin{bmatrix} \boldsymbol{A}_1 & \boldsymbol{B}_1 \\ \boldsymbol{C}_1 & D_1 \end{bmatrix} \quad \textit{and} \quad \boldsymbol{F}_2 := \begin{bmatrix} \boldsymbol{A}_2 & \boldsymbol{B}_2 \\ \boldsymbol{C}_2 & D_2 \end{bmatrix}$$

and respective state vectors $\boldsymbol{x}_1$ and $\boldsymbol{x}_2$. Then the cascade (serial) connection of H_1 followed by H_2 (H_2H_1) with the combined state vector

$$\begin{bmatrix} \boldsymbol{x}_1 \\ \boldsymbol{x}_2 \end{bmatrix}$$

is also orthogonal and all-pass.

Proof. See [228, 230]. ∎

This follows from the fact that the total matrix for the cascade system is

$$\boldsymbol{F} := \left[\begin{array}{cc|c} \boldsymbol{A}_1 & \mathbf{0} & \boldsymbol{B}_1 \\ \boldsymbol{B}_2\boldsymbol{C}_1 & \boldsymbol{A}_2 & \boldsymbol{B}_2 D_1 \\ \hline D_2\boldsymbol{C}_1 & \boldsymbol{C}_2 & D_2 D_1 \end{array}\right]$$

which is orthogonal if $\boldsymbol{F}_1$ and $\boldsymbol{F}_2$ are orthogonal.

Proposition C.2 ([229]). *Given m all-pass filters $\{H_k\}_{k=1}^m$ and their balanced state-space realizations $(\boldsymbol{A}_k, \boldsymbol{B}_k, \boldsymbol{C}_k, D_k)$ for $k = 1, \cdots, m$. Then for any $k > 1$ it holds that the system $\mathcal{S}_k = \prod_{i=1}^k H_i = H_k \cdots H_2 H_1$ is an all-pass transfer function that has a minimal balanced state-space realization $(\bar{\boldsymbol{A}}_k, \bar{\boldsymbol{B}}_k, \bar{\boldsymbol{C}}_k, \bar{D}_k)$ with the k-th combined state*

$$\bar{\boldsymbol{x}}_k = \begin{bmatrix} \boldsymbol{x}_1 \\ \vdots \\ \boldsymbol{x}_k \end{bmatrix}$$

which satisfies the following recursion:

$$\begin{aligned} \bar{\boldsymbol{A}}_k &:= \begin{bmatrix} \bar{\boldsymbol{A}}_{k-1} & \boldsymbol{0} \\ \boldsymbol{B}_k \bar{\boldsymbol{C}}_{k-1} & \boldsymbol{A}_k \end{bmatrix} \quad \bar{\boldsymbol{B}}_k := \begin{bmatrix} \bar{\boldsymbol{B}}_{k-1} \\ \boldsymbol{B}_k \bar{D}_{k-1} \end{bmatrix} \\ \bar{\boldsymbol{C}}_k &:= \begin{bmatrix} D_k \bar{\boldsymbol{C}}_{k-1} & \boldsymbol{C}_k \end{bmatrix} \quad \bar{D}_k := D_k \bar{D}_{k-1} \end{aligned} \qquad \forall k > 1 \tag{C.3}$$

with the initial condition $(\bar{\boldsymbol{A}}_1, \bar{\boldsymbol{B}}_1, \bar{\boldsymbol{C}}_1, \bar{D}_1) = (\boldsymbol{A}_1, \boldsymbol{B}_1, \boldsymbol{C}_1, D_1)$.

By construction, the *input-to-state* transfer function of the system $\mathcal{S}_k$ is equal to

$$\begin{bmatrix} \boldsymbol{V}_1^\top(\mathfrak{q}) & \boldsymbol{V}_2^\top(\mathfrak{q}) \cdots \boldsymbol{V}_k^\top(\mathfrak{q}) \end{bmatrix}^T$$

where $\boldsymbol{V}_i(\mathfrak{q})$ is a vector valued function defined as

$$\boldsymbol{V}_i(\mathfrak{q}) = \phi_i(\mathfrak{q}) \prod_{j=1}^{i-1} H_j(\mathfrak{q}); \quad \phi_i(\mathfrak{q}) := (\mathfrak{q}\mathbf{I} - \boldsymbol{A}_i)^{-1} B_i .$$

In the time-domain notation, it therefore holds that

$$\boldsymbol{V}_k(t+1) = \left[\begin{array}{c|c} \boldsymbol{B}_k \bar{\boldsymbol{C}}_{k-1} & \boldsymbol{A}_k \end{array}\right] \begin{bmatrix} \boldsymbol{V}_1(t) \\ \boldsymbol{V}_2(t) \\ \vdots \\ \hline \boldsymbol{V}_k(t) \end{bmatrix} + \boldsymbol{B}_k \bar{D}_{k-1} \delta(t),$$

in which $\delta(t)$ denotes the unit pulse signal. This can also be stated as

$$\boldsymbol{V}_k(t+1) = \boldsymbol{B}_k \sum_{j=1}^{k-1} \sum_{i=j+1}^{k-1} D_i \boldsymbol{C}_j \boldsymbol{V}_j(t) + \boldsymbol{A}_k \boldsymbol{V}_k(t) + \boldsymbol{B}_k \prod_{j=1}^{k-1} D_j \delta(t).$$

This equation can be used to calculate the basis functions $\boldsymbol{V}_k$ in an efficient manner [230, 231]. The corresponding representation of the system $\mathcal{S}_k$ is illustrated in Figure C.2.

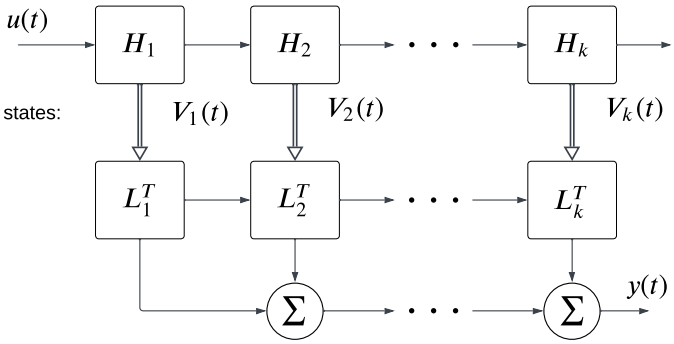

Figure C.2: The cascade representation of the system $\mathcal{S}_k$. The gains L_i^T are row vectors.

C.3 Implementation

In this section, we introduce two sets of orthonormal basis functions to-be-used in the inverse system identification of non-minimum phase systems.

Takenaka-Malmquist functions

Cascading different all-pass blocks of order one or two results in orthonormal basis functions called the Takenaka-Malmquist (TM) functions, covering wide arrays of well-known bases such as pulse basis, *Laguerre* basis, *Kautz* basis, and *Hambo* basis [232]. TM OBFs are defined as

$$\psi_k(\mathfrak{q}) = \frac{\sqrt{1-|\xi_k|^2}}{\mathfrak{q}-\xi_k} \prod_{i=1}^{k-1} \left[\frac{1-\overline{\xi}_i \mathfrak{q}}{\mathfrak{q}-\xi_i} \right]; \quad |\xi_k| < 1 \tag{C.4}$$

with $\{\xi_k\}_{k=1,\dots} \subset \mathbb{D}$ a sequence of poles located inside the unit circle satisfying the *Szasz* condition of $\sum_{i=1}^{\infty} 1-|\xi_i| < \infty$, that is, the sequence of poles does not converge to the unit circle too fast [232]. Notice that for real-valued impulse response, poles should appear as either real numbers or pairs of complex conjugate numbers.

Remark C.4. The argument of $\psi_k(\mathfrak{q})$ is omitted when no confusion arises.

To construct this class of basis functions as a cascade network of all-pass transfer functions, consider the following first-order all-pass filter in the structure of Figure C.1 denoted by

$$H_i(\mathfrak{q}) = \frac{1-\overline{\xi}_i \mathfrak{q}}{\mathfrak{q}-\xi_i}; \quad |\xi_i| < 1 \tag{C.5}$$

An input balanced state-space realization of this filter can be given as

$$\overset{\text{balanced}}{\Longrightarrow} F_i := \begin{bmatrix} A_i & B_i \\ C_i & D_i \end{bmatrix} = \begin{bmatrix} \xi_i & \sqrt{1-|\xi_i|^2} \\ \sqrt{1-|\xi_i|^2} & -\overline{\xi}_i \end{bmatrix},$$

where F_i is a unitary matrix (orthogonal in case of real-valued elements). An interesting observation of this state-space representation is the transfer function from input-to-state

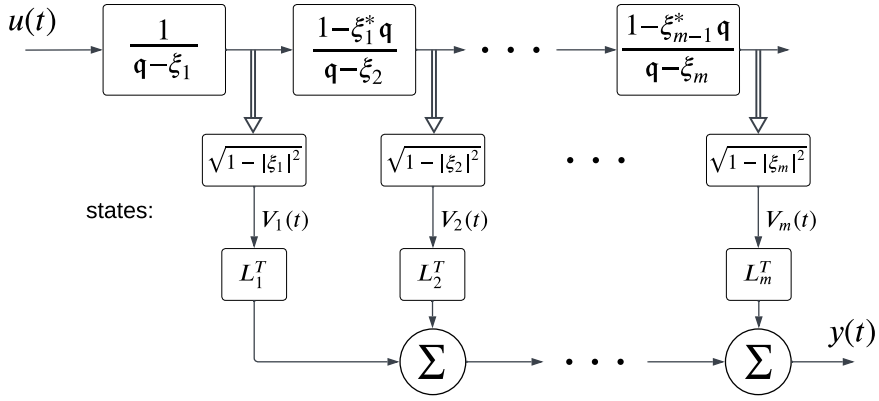

Figure C.3: Block diagram of Takenaka-Malmquist basis functions.

can be obtained as

$$(\mathfrak{q}-A_i)^{-1}B_i = \frac{\sqrt{1-|\xi_i|^2}}{\mathfrak{q}-\xi_i},$$

which directly leads to a construction of $\{\psi_k\}$ in terms of a cascade all-pass network as depicted in Figure C.2, where ψ_i is the transfer function from u to x_i (see Figure C.3). According to Theorem C.1 and the property of balanced realization of all-pass functions, a cascade (serial) connection of all-pass filters (C.5) can be done straightforwardly (by following Proposition C.2). To calculate the coefficient of the basis functions, we can read off based on the scheme provided in Figure C.4.

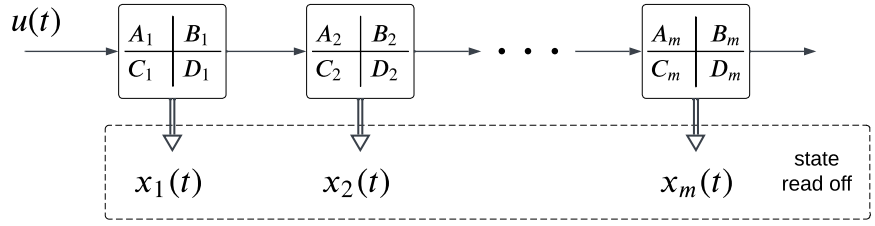

Figure C.4: Coefficient calculation scheme.

Non-Causal Rational Orthonormal Basis Functions

A class of non-causal rational OBFs is introduced in [197] inspired by the Takenaka-Malmquist functions. In this part, we explain how we can efficiently implement these types of non-causal filters. The non-causal rational OBFs are defined as

$$\psi_k(\mathfrak{q}) = \frac{\sqrt{1-|\xi_k|^2}}{1-\overline{\xi}_k\mathfrak{q}} \prod_{i=1}^{k-1}\left[\frac{\mathfrak{q}-\xi_i}{1-\overline{\xi}_i\mathfrak{q}}\right]; \quad |\xi_k|<1 \tag{C.6}$$

where the sequence of poles $\{\xi_k\}_{k=1,\dots} \subset \mathbb{D}$ includes only the ones inside the unit circle. Similarly to TM OBFs, obtaining real-valued impulse responses requires the set of poles

consists of either real numbers or pairs of complex conjugate locations. For a cascade structure, a SISO unstable first-order all-pass filter is proposed as

$$H_i(\mathfrak{q}) = \frac{\mathfrak{q} - \xi_i}{1 - \overline{\xi}_i \mathfrak{q}}; \quad |\xi_i| < 1$$

Note that this filter has a pole at $p = 1/\overline{\xi}_i$ outside of the unit circle ($|p| > 1$) that makes the filter unstable! Later on, we will elaborate on why it is still possible to construct the corresponding state-space representation of this cascade network of unstable filters.

A balanced state-space realization of the filter can be derived as follows, which is not necessarily input balanced and unitary/orthogonal:

$$\overset{\text{balanced}}{\Longrightarrow} F_i := \begin{bmatrix} A_i & B_i \\ C_i & D_i \end{bmatrix} = \begin{bmatrix} \frac{1}{\overline{\xi}_i} & -\frac{1}{\overline{\xi}_i}\sqrt{1-|\xi_i|^2} \\ \frac{1}{\overline{\xi}_i}\sqrt{1-|\xi_i|^2} & -\frac{1}{\overline{\xi}_i} \end{bmatrix}. \tag{C.7}$$

So, the transfer function from input-to-state is

$$(\mathfrak{q} - A_i)^{-1} B_i = \frac{\sqrt{1-|\xi_i|^2}}{1 - \overline{\xi}_i \mathfrak{q}}$$

Remark C.5. Due to instability of the state-space, we cannot guarantee the unitarity/orthogonality property of the cascade (serial) connection of the total system. In other words, Theorem C.1 does not hold in general for unstable all-pass filters, i.e.,

$$F_k F_k^T \overset{?}{\neq} I$$

Given the fact in Remark C.5, however, we can still proceed with the cascade structure to derive a balanced state-space representation of the proposed TM-based OBFs. To do so, the total cascade system will follow the recursion relation explained in Proposition C.2, since the realization in (C.7) is a balanced minimal realization. Thus, the state-space construction procedure is similar to the Takenaka-Malmquist functions in the previous part.

Coefficient Calculation

Since the total system is unstable and all the poles are strictly outside of the unit circle, the inverse system will be *anti-causal* but stable. This method is called *stable inversion* in the literature, for instance, see [194]. To obtain the corresponding coefficients of the basis functions for the anti-causal system, we have to evolve the state vector of the total cascade system *backward in time*. As a result, the *time-reversion* implementation of the total cascade balanced state-space realization (C.3) is given by [45, 194]

$$\mathcal{S}_k^{\text{time-reverse}} : \begin{cases} \bar{\boldsymbol{x}}_k(t) = \bar{\boldsymbol{A}}_k^{-1}\, \bar{\boldsymbol{x}}_k(t+1) - \bar{\boldsymbol{A}}_k^{-1} \bar{\boldsymbol{B}}_k\, u(t) \\ y(t) = \bar{\boldsymbol{C}}_k\, \bar{\boldsymbol{x}}_k(t) + \bar{D}_k\, u(t) \end{cases}.$$

Hence, the coefficients can be retrieved by reading off the state vector $\bar{\boldsymbol{x}}_k$ (see Figure C.4).

Complex Pole Inclusion

As mentioned before, in general, incorporating a complex pole ξ_n into the generating poles set gives rise to complex impulse responses for the $\{\psi_k\}$ for $k \geq n$, which is physically unrealistic (except for specific problems in communications [232]). To avoid this issue, it is required not only to include complex poles as complex conjugate pairs (i.e., $\xi_{n+1} = \overline{\xi_n}$) but also to use certain linear combination of basis functions. In the following, the approach suggested in [232] is sough after for TM OBFs (C.4).

Causal Basis Functions

Suppose $n-1$ real-valued poles $\{\xi_1, \ldots, \xi_{n-1}\}$ have been included in $\{\psi_1, \ldots, \psi_{n-1}\}$ and it is now desired to include a complex pole ξ_n. Two new basis functions, denoted as ψ_n' and ψ_n'', each with real-valued impulse responses, should be constructed as linear combinations of ψ_n and ψ_{n+1}, generated from (C.4). Subsequently, this new pair of basis functions will replace ψ_n and ψ_{n+1} in the set of basis functions $\{\psi_k\}$. This linear combination is given as

$$\begin{bmatrix} \psi_n'(\mathfrak{q}) \\ \psi_n''(\mathfrak{q}) \end{bmatrix} = \begin{bmatrix} c_0 & c_1 \\ c_0' & c_1' \end{bmatrix} \begin{bmatrix} \psi_n(\mathfrak{q}) \\ \psi_{n+1}(\mathfrak{q}) \end{bmatrix}, \quad c_0, c_0', c_1, c_1' \in \mathbb{C}. \tag{C.8}$$

To obtain a proper set of coefficients $\{c_0, c_0', c_1, c_1'\}$, certain conditions should hold such as orthonormality that provides a general guideline on parameters. Details can be found in [232]. By recursion, the basis functions in (C.4) follows

$$\psi_n(\mathfrak{q}) = \sqrt{\frac{1-|\xi_n|^2}{1-|\xi_{n-1}|^2}} \frac{1-\overline{\xi_{n-1}}\mathfrak{q}}{\mathfrak{q}-\xi_n} \psi_{n-1}(\mathfrak{q}) \quad \text{or} \quad \psi_{n+1}(\mathfrak{q}) = \sqrt{\frac{1-|\xi_{n+1}|^2}{1-|\xi_n|^2}} \frac{1-\overline{\xi_n}\mathfrak{q}}{\mathfrak{q}-\xi_{n+1}} \psi_n(\mathfrak{q}). \tag{C.9}$$

Taking complex conjugate poles $\xi_{n+1} = \overline{\xi_n}$ results in

$$\psi_{n+1}(\mathfrak{q}) = \frac{1-\overline{\xi_n}\mathfrak{q}}{\mathfrak{q}-\overline{\xi_n}} \psi_n(\mathfrak{q}).$$

Expressing $\psi_n'(\mathfrak{q})$ according to (C.8) gives

$$\begin{aligned} \psi_n'(\mathfrak{q}) &= c_0 \psi_n(\mathfrak{q}) + c_1 \psi_{n+1}(\mathfrak{q}) \\ \xrightarrow{\xi_{n+1}=\overline{\xi_n}} \quad &= (c_0 + c_1 \frac{1-\overline{\xi_n}\mathfrak{q}}{\mathfrak{q}-\overline{\xi_n}}) \psi_n(\mathfrak{q}) \\ &= (\frac{\beta\mathfrak{q}+\mu}{\mathfrak{q}-\overline{\xi_n}}) \psi_n(\mathfrak{q}), \end{aligned}$$

and by substituting ψ_n from (C.4), we eventually get

$$\psi_n'(\mathfrak{q}) = \frac{\sqrt{1-|\xi_n|^2}(\beta\mathfrak{q}+\mu)}{\mathfrak{q}^2 + (\xi_n + \overline{\xi_n})\mathfrak{q} + |\xi_n|^2} \prod_{i=1}^{n-1} \left[\frac{1-\overline{\xi_i}\mathfrak{q}}{\mathfrak{q}-\xi_i} \right],$$

$$\psi_n''(\mathfrak{q}) = \frac{\sqrt{1-|\xi_n|^2}(\beta'\mathfrak{q}+\mu')}{\mathfrak{q}^2 + (\xi_n + \overline{\xi_n})\mathfrak{q} + |\xi_n|^2} \prod_{i=1}^{n-1} \left[\frac{1-\overline{\xi_i}\mathfrak{q}}{\mathfrak{q}-\xi_i} \right].$$

in which $\beta, \beta', \mu, \mu' \in \mathbb{R}$ are solutions to the following constraints. Let $x \triangleq [\beta, \mu]^T$ and $y \triangleq [\beta', \mu']^T$ be two pairs of choices for basis functions ψ_n' and ψ_n'', respectively. Then, we have

$$\text{(normality)} \quad x^T M x = |1 - \xi_n^2|^2, \quad \text{with } M \triangleq \begin{bmatrix} 1+|\xi_n|^2 & 2\mathrm{Re}\{\xi_n\} \\ 2\mathrm{Re}\{\xi_n\} & 1+|\xi_n|^2 \end{bmatrix} \tag{I}$$

$$\text{(orthogonality)} \quad x^T M y = 0,. \tag{II}$$

As a result, one may find y by rotating x by 90° in the normalized eigenspace of M

$$y = M^{-1/2} \begin{bmatrix} 0 & -1 \\ 1 & 0 \end{bmatrix} M^{1/2} x$$

or,

$$\begin{bmatrix} \beta' \\ \mu' \end{bmatrix} = \frac{1}{\sqrt{1-\alpha^2}} \begin{bmatrix} \alpha & 1 \\ -1 & -\alpha \end{bmatrix} \begin{bmatrix} \beta \\ \mu \end{bmatrix}, \quad \text{with } \alpha \triangleq \frac{\xi_n + \overline{\xi_n}}{1+|\xi_n|^2}$$

In addition, a set of solutions that satisfies both normality (I) and orthogonality (II) constraints can be rendered as [233]

$$x = \frac{1}{\sqrt{2}} \begin{bmatrix} |1-\xi_n|\cos\theta + |1+\xi_n|\sin\theta \\ |1-\xi_n|\cos\theta - |1+\xi_n|\sin\theta \end{bmatrix}, \quad 0 \le \theta < 2\pi,$$
$$y = -\frac{1}{\sqrt{2}} \begin{bmatrix} |1-\xi_n|\sin\theta - |1+\xi_n|\cos\theta \\ |1-\xi_n|\sin\theta + |1+\xi_n|\cos\theta \end{bmatrix}.$$

For $\theta = 0$, the transformed basis functions are obtained as

$$\psi_n'(\mathfrak{q}) = \frac{1}{\sqrt{2}} \frac{\sqrt{1-|\xi_n|^2}|1-\xi_n|(\mathfrak{q}+1)}{\mathfrak{q}^2 + (\xi_n + \overline{\xi_n})\mathfrak{q} + |\xi_n|^2} \prod_{i=1}^{n-1} \left[\frac{1-\overline{\xi_i}\mathfrak{q}}{\mathfrak{q}-\xi_i} \right],$$
$$\psi_n''(\mathfrak{q}) = \frac{1}{\sqrt{2}} \frac{\sqrt{1-|\xi_n|^2}|1+\xi_n|(\mathfrak{q}-1)}{\mathfrak{q}^2 + (\xi_n + \overline{\xi_n})\mathfrak{q} + |\xi_n|^2} \prod_{i=1}^{n-1} \left[\frac{1-\overline{\xi_i}\mathfrak{q}}{\mathfrak{q}-\xi_i} \right].$$

Non-Causal Basis Functions

A similar approach can be exploited to come up with proper linear transformations for non-causal basis functions related to complex conjugate pairs. In this regard, we derive the recursive relation between $\psi_n(\mathfrak{q})$ and $\psi_{n+1}(\mathfrak{q})$ according to (C.6):

$$\psi_n(\mathfrak{q}) = \sqrt{\frac{1-|\xi_n|^2}{1-|\xi_{n-1}|^2}} \frac{\mathfrak{q}-\xi_{n-1}}{1-\overline{\xi_n}\mathfrak{q}} \psi_{n-1}(\mathfrak{q}) \quad \text{or} \quad \psi_{n+1}(\mathfrak{q}) = \sqrt{\frac{1-|\xi_{n+1}|^2}{1-|\xi_n|^2}} \frac{\mathfrak{q}-\xi_n}{1-\overline{\xi_{n+1}}\mathfrak{q}} \psi_n(\mathfrak{q}). \tag{C.10}$$

Choosing complex poles as conjugate pairs $\xi_{n+1} = \overline{\xi_n}$ gives

$$\psi_{n+1}(\mathfrak{q}) = \frac{\mathfrak{q}-\xi_n}{1-\xi_n\mathfrak{q}} \psi_n(\mathfrak{q}).$$

As a result, we can express $\psi_n'(\mathfrak{q})$ as the following linear combination (C.8)

$$\begin{aligned}
&\psi_n'(\mathfrak{q}) = c_0\psi_n(\mathfrak{q}) + c_1\psi_{n+1}(\mathfrak{q}) \\
\xrightarrow{\xi_{n+1}=\overline{\xi_n}} \quad &= (c_0 + c_1\frac{\mathfrak{q}-\xi_n}{1-\xi_n\mathfrak{q}})\psi_n(\mathfrak{q}) \\
&= (\frac{\beta\mathfrak{q}+\mu}{1-\xi_n\mathfrak{q}})\psi_n(\mathfrak{q}) \\
\xrightarrow{\text{using (C.10)}} \quad &= \sqrt{\frac{1-|\xi_n|^2}{1-|\xi_{n-1}|^2}}\frac{(\beta\mathfrak{q}+\mu)(\mathfrak{q}-\xi_{n-1})}{|\xi_n|^2\mathfrak{q}^2-(\xi_n+\overline{\xi_n})\mathfrak{q}+1}\psi_{n-1}(\mathfrak{q}).
\end{aligned}$$

where β, μ are related to c_0, c_1 via

$$c_0 = \frac{\xi_n\beta+\mu}{1-\xi_n^2}, \quad c_1 = \frac{\beta+\xi_n\mu}{1-\xi_n^2}.$$

To ensure normality of bases, β and μ should be chosen according to the constraint $|c_0|^2 + |c_1|^2 = 1$, which can be equivalently expressed as

$$x^T M x = |1-\xi_n^2|^2, \quad \beta, \mu \in \mathbb{R}. \tag{C.11}$$

From the orthogonality constraint, for two pairs of choices (c_0, c_1) and (c_0', c_1'), it is necessary to satisfy $c_0\overline{c_0'} + c_1\overline{c_1'} = 0$, i.e.,

$$x^T M y = 0. \tag{C.12}$$

All solutions to (C.11) are given by [233]

$$x = \frac{1}{\sqrt{2}}\begin{bmatrix} |1-\xi_n|\cos\theta + |1+\xi_n|\sin\theta \\ |1-\xi_n|\cos\theta - |1+\xi_n|\sin\theta \end{bmatrix}, \quad 0 \le \theta < 2\pi.$$

If θ is fixed, a unique y satisfying (C.11) and (C.12) is obtained by substituting $\theta + \pi/2$

$$y = -\frac{1}{\sqrt{2}}\begin{bmatrix} |1-\xi_n|\sin\theta - |1+\xi_n|\cos\theta \\ |1-\xi_n|\sin\theta + |1+\xi_n|\cos\theta \end{bmatrix}.$$

Let $\theta = 0$. The real-valued basis functions can be computed as

$$\begin{aligned}
\psi_n'(\mathfrak{q}) &= \frac{1}{\sqrt{2}}\frac{\sqrt{1-|\xi_n|^2}|1-\xi_n|(q+1)}{1-(\xi_n+\overline{\xi_n})\mathfrak{q}+|\xi_n|^2\mathfrak{q}^2}\prod_{i=1}^{n-1}\left[\frac{1-\overline{\xi_i}\mathfrak{q}}{\mathfrak{q}-\xi_i}\right], \\
\psi_n''(\mathfrak{q}) &= \frac{1}{\sqrt{2}}\frac{\sqrt{1-|\xi_n|^2}|1+\xi_n|(\mathfrak{q}-1)}{1-(\xi_n+\overline{\xi_n})\mathfrak{q}+|\xi_n|^2\mathfrak{q}^2}\prod_{i=1}^{n-1}\left[\frac{1-\overline{\xi_i}\mathfrak{q}}{\mathfrak{q}-\xi_i}\right].
\end{aligned}$$

One solution for y, similar to causal bases, is

$$y = M^{-1/2}\begin{bmatrix} 0 & -1 \\ 1 & 0 \end{bmatrix}M^{1/2}x$$

or,

$$\begin{bmatrix}\beta' \\ \mu'\end{bmatrix} = \frac{1}{\sqrt{1-\alpha^2}}\begin{bmatrix}\alpha & 1 \\ -1 & -\alpha\end{bmatrix}\begin{bmatrix}\beta \\ \mu\end{bmatrix}, \quad \text{with } \alpha \triangleq \frac{\xi_n+\overline{\xi_n}}{1+|\xi_n|^2}$$

Hence, the transformed basis functions with real-valued impulse response are given by

$$\psi_n'(\mathfrak{q}) = \frac{\sqrt{1-|\xi_n|^2}(\beta\mathfrak{q}+\mu)}{1-(\xi_n+\overline{\xi_n})\mathfrak{q}+|\xi_n|^2\mathfrak{q}^2}\prod_{i=1}^{n-1}\left[\frac{1-\overline{\xi_i}\mathfrak{q}}{\mathfrak{q}-\xi_i}\right],$$
$$\psi_n''(\mathfrak{q}) = \frac{\sqrt{1-|\xi_n|^2}(\beta'\mathfrak{q}+\mu')}{1-(\xi_n+\overline{\xi_n})\mathfrak{q}+|\xi_n|^2\mathfrak{q}^2}\prod_{i=1}^{n-1}\left[\frac{1-\overline{\xi_i}\mathfrak{q}}{\mathfrak{q}-\xi_i}\right].$$

C

C.4 Kernel Regularization

The number of bilateral impulse response terms to-be-estimated is denoted by

$$\#\text{IRs} = n_\text{c} + n_\text{ac}$$

The hyperparameter α of the kernel matrix $\mathbf{K}(\alpha) \in \mathbb{R}^{(n_\text{c}+n_\text{ac})\times(n_\text{c}+n_\text{ac})}$ refers to the generating poles of bases in the Rational Orthonormal Basis Functions (ROBF) kernel. Thus, α comprises two different sets of poles, but all of them are causal (inside the unit circle). The first set corresponds to the stable part of the dynamics denoted by p_c, and the other one includes the poles that are related to the anti-causal dynamics and direct feedthrough term represented by p_ac, i.e.,

$$\alpha = \{p_\text{c}, p_\text{ac}\} \quad \text{with} \quad \begin{cases} p_\text{c} = \{p_{\text{c},i}\}_{i\in\mathbb{Z}_+} \subset \mathbb{D} \\ p_\text{ac} = \{p_{\text{ac},i}\}_{i\in\mathbb{Z}_-} \subset \mathbb{D} \end{cases}.$$

We use n_{b_c} for the number of causal basis functions and n_{b_ac} for the anti-causal set, i.e.,

$$\#\text{number of bases } n_\text{b} := n_{\text{b}_\text{c}} + n_{\text{b}_\text{ac}}$$

The set of basis functions in time-domain can be defined by

$$\mathbf{\Phi} \triangleq \{\phi_k(t)\}_{k=1}^{n_\text{b}} = \{\phi_1^\text{ac}, \ldots, \phi_{n_{\text{b}_\text{ac}}}^\text{ac}, \phi_1^\text{c}, \ldots, \phi_{n_{\text{b}_\text{c}}}^\text{c}\}$$

From a system-theoretic point of view, these bases can describe the Hilbert space $\ell_2(\mathbb{Z})$ under completeness condition [197, 234], i.e.,

$$\text{Span}\{\phi_1^\text{ac}, \ldots, \phi_{n_{\text{b}_\text{ac}}}^\text{ac}, \phi_1^\text{c}, \ldots, \phi_{n_{\text{b}_\text{c}}}^\text{c}\} = \ell_2(\mathbb{Z}).$$

In case of real-valued functions, this space will be restricted to $\mathcal{R}\ell_2(\mathbb{Z})$. As a result, the function (hypothesis) space spanned by $\mathbf{\Phi}$ is given as

$$F : \mathcal{X} \triangleq \text{Span}\{\mathbf{\Phi}\} \to \mathbb{C},$$

if real-valued basis functions, then

$$F : \mathcal{X} \triangleq \text{Span}\{\mathbf{\Phi}\} \to \mathbb{R}.$$

In this regard, we construct the kernel matrix $\mathbf{K}$ as

$$[\mathbf{K}]_{(i,j)} = K(t_i, t_j; \alpha) = \sum_{k=1}^{n_\text{b}} \phi_k(t_i)\overline{\phi_k(t_j)},$$

in which $K(t_i, t_j; \alpha)$ is the "reproducing kernel" associated with the RKHS (reproducing kernel Hilbert space) $\mathscr{H}_{\mathbf{K}_\Phi}$ spanned by $\mathbf{\Phi}$. This space can be written as

$$\mathscr{H}_{\mathbf{K}_\Phi} = \text{Span}\{\phi_1, \ldots, \phi_{n_\text{b}}\} = \left\{ h \,|\, h(t) = \sum_{k=1}^{n_\text{b}} c_k \phi_k(t),\ c_k \in \mathbb{R} \right\} \text{ with } c_k = \langle h, \phi_k \rangle_{\mathbf{K}_\Phi}.$$

$h(t)$ represents the impulse response of the inverse system.

If there is no correlation between the causal and anti-causal impulse responses, we have

$$K(t_i, t_j; \alpha) = \sum_{k=1}^{n_{\text{b}_\text{c}}} \phi_k^\text{c}(t_i)\overline{\phi_k^\text{c}(t_j)} + \sum_{k=1}^{n_{\text{b}_\text{ac}}} \phi_k^\text{ac}(t_i)\overline{\phi_k^\text{ac}(t_j)}$$

where $\phi_k^\text{c}(t) \in \ell_2(\mathbb{Z}_{>0})$ takes only positive integers (time indices) and $\phi_k^\text{ac}(t) \in \ell_2(\{0\} \cup \mathbb{Z}_{<0}-)$ is valid for non-positive integers.

Bibliography

References

[1] R. Isermann. *Fault-diagnosis systems: an introduction from fault detection to fault tolerance*. Springer Science & Business Media, 2005.

[2] P. M. Frank. Fault diagnosis in dynamic systems using analytical and knowledge-based redundancy: A survey and some new results. *Automatica*, 26(3):459–474, 1990.

[3] X. J. Zhang. *Auxiliary signal design in fault detection and diagnosis*. Springer, 1989.

[4] J. Gertler and D. Singer. A new structural framework for parity equation-based failure detection and isolation. *Automatica*, 26(2):381–388, 1990.

[5] M. A. Massoumnia, G. C. Verghese, and A. S. Willsky. Failure detection and identification. *IEEE Transactions on Automatic Control*, 34(3):316–321, 2002.

[6] M. Hou and R. J. Patton. Input observability and input reconstruction. *Automatica*, 34(6):789–794, 1998.

[7] Y. Park and J. L. Stein. Closed-loop, state and input observer for systems with unknown inputs. *International Journal of Control*, 48(3):1121–1136, September 1988.

[8] R. V. Beard. *Failure accomodation in linear systems through self-reorganization*. PhD thesis, Massachusetts Institute of Technology, 1971.

[9] Y. Zhang and J. Jiang. Bibliographical review on reconfigurable fault-tolerant control systems. *Annual Reviews in Control*, 32(2):229–252, 2008.

[10] C. van der Ploeg, P. Vieira Oliveira, E. Silvas, P. Mohajerin Esfahani, and N. van de Wouw. Robust fault estimation with structured uncertainty: Scalable algorithms and experimental validation in automated vehicles. *IEEE Transactions on Control Systems Technology*, 33(5):1651–1666, 2025. URL https://mohajerinesfahani.github.io/Publications/journal/2024/FDI_experiment.mp4.

[11] S. de Reij. Multivariate Fault Estimation for a High-Fidelity Model of the AB383 Wire Bonder: A Model-Based Approach. Masters thesis, Delft University of Technology, 2023.

[12] N. Van De Wouw. Digital Twin Research – Project 4, 2025. URL https://www.digital-twin-research.nl/research/research-project-4/.

[13] T. van Esch, F. Ghanipoor, C. Murguia, and N. van de Wouw. Hybrid model-data fault diagnosis for wafer handler robots: Tilt and broken belt cases. *IEEE Transactions on Control Systems Technology*, 34(5):2203–2218, 2026. doi: 10.1109/TCST.2026.3693758.

[14] C. van Peijpe, F. Ghanipoor, Y. de Loore, P. Hacking, N. van de Wouw, and P. Mohajerin Esfahani. Fault isolation for the ink deposition process in high-end industrial printers. *IEEE Transactions on Control Systems Technology*, 34(3):1617–1624, 2026. doi: 10.1109/TCST.2026.3664927.

[15] A. Amini. Fault Diagnosis and Estimation in Inkjet Printers Using Self-Sensing Piezo Actuators. Masters thesis, Delft University of Technology, 2025. URL https://repository.tudelft.nl/record/uuid:88fd0fef-410e-4b12-b74b-7bbb29d2b72e.

[16] P. Mohajerin Esfahani, M. Vrakopoulou, G. Andersson, and J. Lygeros. A tractable nonlinear fault detection and isolation technique with application to the cyber-physical security of power systems. In *IEEE 51st Annual Conference on Decision and Control*, pages 3433–3438, 2012.

[17] J. C. Willems, P. Rapisarda, I. Markovsky, and B. L. De Moor. A note on persistency of excitation. *Systems & Control Letters*, 54(4):325–329, 2005. doi: 10.1016/j.sysconle.2004.09.003.

[18] P. Van Overschee and B. De Moor. *Subspace identification for linear systems: Theory—Implementation—Applications*. Springer Science & Business Media, 1996.

[19] B. Huang and R. Kadali. *Dynamic modeling, predictive control and performance monitoring: a data-driven subspace approach*, volume 374. Springer Science & Business Media, 2008.

[20] C. De Persis and P. Tesi. Formulas for data-driven control: Stabilization, optimality, and robustness. *IEEE Transactions on Automatic Control*, 65(3):909–924, 2019.

[21] I. Markovsky and F. Dörfler. Behavioral systems theory in data-driven analysis, signal processing, and control. *Annual Reviews in Control*, 52:42–64, 2021. doi: 10.1016/j.arcontrol.2021.09.005.

[22] J. Berberich, J. Köhler, M. A. Müller, and F. Allgöwer. Data-driven model predictive control with stability and robustness guarantees. *IEEE Transactions on Automatic Control*, 66(4):1702–1717, 2020.

[23] F. Dörfler. Data-driven control: Part two of two: Hot take: Why not go with models? *IEEE Control Systems Magazine*, 43(6):27–31, 2023.

[24] S. X. Ding, P. Zhang, A. Naik, E. L. Ding, and B. Huang. Subspace method aided data-driven design of fault detection and isolation systems. *Journal of Process Control*, 19 (9):1496–1510, 2009.

[25] Y. Wan, T. Keviczky, M. Verhaegen, and F. Gustafsson. Data-driven robust receding horizon fault estimation. *Automatica*, 71:210–221, 2016. doi: 10.1016/j.automatica.2016.04.020.

[26] J. Yan, I. Markovsky, and J. Lygeros. Secure data reconstruction: A direct data-driven approach. *IEEE Transactions on Automatic Control*, 2025.

[27] I. Markovsky, A. Muixí, S. Zlotnik, and P. Diez. A behavioral approach to direct data-driven fault detection. *Mechanical Systems and Signal Processing*, 245:113802, 2026.

[28] H. Chen, Z. Liu, and B. Huang. Data-driven fault detection for lipschitz nonlinear systems: From open to closed-loop systems. *Automatica*, 155:111161, 2023.

[29] C. Verhoek, J. Berberich, S. Haesaert, R. Tóth, and H. S. Abbas. A linear parameter-varying approach to data predictive control. *IEEE Transactions on Automatic Control*, 2025.

[30] H. H. Rosenbrock. *State-space and multivariable theory*. Nelson, 1970.

[31] A. MacFarlane and N. Karcanias. Poles and zeros of linear multivariable systems: a survey of the algebraic, geometric and complex-variable theory. *International Journal of Control*, 24(1):33–74, 1976.

[32] E. J. Davison and S. Wang. Properties and calculation of transmission zeros of linear multivariable systems. *Automatica*, 10(6):643–658, 1974. doi: 10.1016/0005-1098(74)90085-5.

[33] M. A. Massoumnia. A geometric approach to the synthesis of failure detection filters. *IEEE Transactions on Automatic Control*, 31(9):839–846, 2003.

[34] J. Chen, R. J. Patton, and H.-Y. Zhang. Design of unknown input observers and robust fault detection filters. *International Journal of Control*, 63(1):85–105, 1996. doi: 10.1080/00207179608921833.

[35] H. J. Van Waarde, J. Eising, M. K. Camlibel, and H. L. Trentelman. A behavioral approach to data-driven control with noisy input–output data. *IEEE Transactions on Automatic Control*, 69(2):813–827, 2023.

[36] B. Wolleswinkel, M. Mazo, Jr, and R. Ferrari. Switched zero dynamics attacks on sampled-data systems with non-uniform sampling: Vulnerability and countermeasures. *ACM Transactions on Cyber-Physical Systems*, 9(3):1–23, 2025.

[37] S. Z. Yong, M. Zhu, and E. Frazzoli. A unified filter for simultaneous input and state estimation of linear discrete-time stochastic systems. *Automatica*, 63:321–329, 2016.

[38] J. Shi, Y. Lian, and C. N. Jones. Data-driven input reconstruction and experimental validation. *IEEE Control Systems Letters*, 6:3259–3264, 2022.

[39] R. Anguluri, O. Kosut, and L. Sankar. Localization and estimation of unknown forced inputs: A group LASSO approach. *IEEE Transactions on Control of Network Systems*, 10(4):1997–2009, 2023.

[40] M. Nyberg and E. Frisk. Residual generation for fault diagnosis of systems described by linear differential-algebraic equations. *IEEE Transactions on Automatic Control*, 51(12):1995–2000, 2006.

[41] A. Varga. New computational paradigms in solving fault detection and isolation problems. *Annual Reviews in Control*, 37(1):25–42, 2013.

[42] M. A. Sheikhi, G. d. A. Gleizer, T. Keviczky, and P. M. Esfahani. Fault diagnosis in dynamical systems: Geometric interpretation and tractable algorithms. *Annual Review of Control, Robotics, and Autonomous Systems*, 9, 2026.

[43] P. C. Hansen. *Discrete inverse problems: insight and algorithms*. SIAM, 2010.

[44] J. Dong and M. Verhaegen. Identification of fault estimation filter from i/o data for systems with stable inversion. *IEEE Transactions on Automatic Control*, 57(6): 1347–1361, 2011.

[45] C. Yu and M. Verhaegen. Data-driven fault estimation of non-minimum phase LTI systems. *Automatica*, 92:181–187, June 2018. doi: 10.1016/j.automatica.2018.03.035.

[46] T. A. N. Heirung and A. Mesbah. Input design for active fault diagnosis. *Annual Reviews in Control*, 47:35–50, 2019.

[47] P. Van Overschee and B. De Moor. N4SID: Subspace algorithms for the identification of combined deterministic-stochastic systems. *Automatica*, 30(1):75–93, 1994. doi: 10.1016/0005-1098(94)90230-5.

[48] M. Verhaegen and V. Verdult. *Filtering and system identification: a least squares approach*. Cambridge university press, 2007.

[49] J. Coulson, H. J. Van Waarde, J. Lygeros, and F. Dörfler. A quantitative notion of persistency of excitation and the robust fundamental lemma. *IEEE Control Systems Letters*, 7:1243–1248, 2022.

[50] L. Ljung. *System identification: theory for the user*. Prentice-Hall, 1987.

[51] E. Chow and A. Willsky. Analytical redundancy and the design of robust failure detection systems. *IEEE Transactions on Automatic Control*, 29(7):603–614, 2003.

[52] E. Frisk and M. Nyberg. A minimal polynomial basis solution to residual generation for fault diagnosis in linear systems. *Automatica*, 37(9):1417–1424, 2001.

[53] C. Van der Ploeg, M. Alirezaei, N. Van De Wouw, and P. Mohajerin Esfahani. Multiple faults estimation in dynamical systems: Tractable design and performance bounds. *IEEE Transactions on Automatic Control*, 67(9):4916–4923, 2022.

[54] Q. Zhang. Dynamic system fault diagnosis under sparseness assumption. *IEEE Transactions on Signal Processing*, 69:2499–2508, 2021. doi: 10.1109/TSP.2021.3072004.

[55] C. De Persis and A. Isidori. A geometric approach to nonlinear fault detection and isolation. *IEEE Transactions on Automatic Control*, 46(6):853–865, 2002.

[56] J. Bokor and G. Balas. Detection filter design for LPV systems—a geometric approach. *Automatica*, 40(3):511–518, 2004.

[57] X. Zhang, M. M. Polycarpou, and T. Parisini. Design and analysis of a fault isolation scheme for a class of uncertain nonlinear systems. *Annual Reviews in Control*, 32(1):107–121, 2008.

[58] P. Mohajerin Esfahani and J. Lygeros. A tractable fault detection and isolation approach for nonlinear systems with probabilistic performance. *IEEE Transactions on Automatic Control*, 61(3):633–647, 2015.

[59] C. Shang, S. X. Ding, and H. Ye. Distributionally robust fault detection design and assessment for dynamical systems. *Automatica*, 125:109434, 2021.

[60] S. X. Ding, Y. Yang, Y. Zhang, and L. Li. Data-driven realizations of kernel and image representations and their application to fault detection and control system design. *Automatica*, 50(10):2615–2623, 2014.

[61] K. Pan, P. Palensky, and P. Mohajerin Esfahani. Dynamic anomaly detection with high-fidelity simulators: A convex optimization approach. *IEEE Transactions on Smart Grid*, 13(2):1500–1515, 2021.

[62] K. Pan, P. Palensky, and P. Mohajerin Esfahani. From static to dynamic anomaly detection with application to power system cyber security. *IEEE Transactions on Power Systems*, 35(2):1584–1596, 2019.

[63] G. de Albuquerque Gleizer, P. Mohajerin Esfahani, and T. Keviczky. Active estimation of multiplicative faults in dynamical systems. *Automatica*, 193:113230, 2026. doi: 10.1016/j.automatica.2026.113230.

[64] G. R. Marseglia and D. M. Raimondo. Active fault diagnosis: A multi-parametric approach. *Automatica*, 79:223–230, 2017.

[65] X. Ding, L. Guo, and P. M. Frank. Parameterization of linear observers and its application to observer design. *IEEE Transactions on Automatic Control*, 39(8):1648–1652, 2002.

[66] Q. Zhang, M. Basseville, and A. Benveniste. Fault detection and isolation in nonlinear dynamic systems: A combined input–output and local approach. *Automatica*, 34(11):1359–1373, 1998.

[67] H. Chen, Z. Chai, O. Dogru, B. Jiang, and B. Huang. Data-driven designs of fault detection systems via neural network-aided learning. *IEEE Transactions on Neural Networks and Learning Systems*, 33(10):5694–5705, 2021.

[68] M. A. Sheikhi, G. de Albuquerque Gleizer, P. M. Esfahani, and T. Keviczky. Data-driven fault isolation in linear time-invariant systems: a subspace classification approach. *IEEE Control Systems Letters*, 2025.

[69] X. Ding and P. M. Frank. Fault detection via factorization approach. *Systems & Control Letters*, 14(5):431–436, 1990.

[70] J. Gertler. Fault detection and isolation using parity relations. *Control Engineering Practice*, 5(5):653–661, 1997.

[71] J. Li, Z. Wang, Y. Shen, and L. Xie. Attack detection for cyber-physical systems: A zonotopic approach. *IEEE Transactions on Automatic Control*, 68(11):6828–6835, November 2023. doi: 10.1109/TAC.2023.3240383.

[72] E. Frisk, M. Krysander, and J. Åslund. Sensor placement for fault isolation in linear differential-algebraic systems. *Automatica*, 45(2):364–371, 2009.

[73] V. Cocquempot, T. El Mezyani, and M. Staroswiecki. Fault detection and isolation for hybrid systems using structured parity residuals. In *5th Asian Control Conference*, volume 2, pages 1204–1212, 2004.

[74] D. Wang and K. Y. Lum. Adaptive unknown input observer approach for aircraft actuator fault detection and isolation. *International Journal of Adaptive Control and Signal Processing*, 21(1):31–48, 2007.

[75] J. K. Scott, D. M. Raimondo, G. R. Marseglia, and R. D. Braatz. Constrained zonotopes: A new tool for set-based estimation and fault detection. *Automatica*, 69:126–136, 2016.

[76] B. S. Rego, D. M. Raimondo, and G. V. Raffo. Line zonotopes: A tool for state estimation and fault diagnosis of unbounded and descriptor systems. *Automatica*, 179: 112380, 2025.

[77] J. K. Scott, R. Findeisen, R. D. Braatz, and D. M. Raimondo. Input design for guaranteed fault diagnosis using zonotopes. *Automatica*, 50(6):1580–1589, 2014.

[78] F. Blanchini, D. Casagrande, G. Giordano, S. Miani, S. Olaru, and V. Reppa. Active fault isolation: A duality-based approach via convex programming. *SIAM Journal on Control and Optimization*, 55(3):1619–1640, 2017.

[79] Y. Guo, Q. Liu, Z. Wang, Z. Zhang, and X. He. Active fault diagnosis for linear stochastic systems subject to chance constraints. *Automatica*, 156:111194, 2023.

[80] H. Qiu, F. Xu, B. Liang, and X. Wang. Active fault diagnosis under hybrid bounded and gaussian uncertainties. *Automatica*, 147:110703, 2023.

[81] T. Floquet and J.-P. Barbot. State and unknown input estimation for linear discrete-time systems. *Automatica*, 42(11):1883–1889, 2006.

[82] G. Marro and E. Zattoni. Unknown-state, unknown-input reconstruction in discrete-time nonminimum-phase systems: Geometric methods. *Automatica*, 46(5):815–822, 2010.

[83] S. Gillijns and B. De Moor. Unbiased minimum-variance input and state estimation for linear discrete-time systems. *Automatica*, 43(1):111–116, 2007.

[84] S. Kirtikar, H. Palanthandalam-Madapusi, E. Zattoni, and D. S. Bernstein. l-delay input and initial-state reconstruction for discrete-time linear systems. *Circuits, Systems, and Signal Processing*, 30:233–262, 2011. doi: 10.1007/s00034-010-9214-4.

[85] A. Ansari and D. S. Bernstein. Deadbeat unknown-input state estimation and input reconstruction for linear discrete-time systems. *Automatica*, 103:11–19, 2019.

[86] C. van der Ploeg, E. Silvas, N. van de Wouw, and P. Mohajerin Esfahani. Real-time fault estimation for a class of discrete-time linear parameter-varying systems. *IEEE Control Systems Letters*, 6:1988–1993, 2021.

[87] Q. Zhang. Adaptive Kalman filter for actuator fault diagnosis. *Automatica*, 93:333–342, July 2018. doi: 10.1016/j.automatica.2018.03.075.

[88] S. Venkateswaran, Q. Liu, B. A. Wilhite, and C. Kravaris. Design of linear residual generators for fault detection and isolation in nonlinear systems. *International Journal of Control*, 95(3):804–820, March 2022. doi: 10.1080/00207179.2020.1823020.

[89] F. Boem, R. M. Ferrari, and T. Parisini. Distributed fault detection and isolation of continuous-time non-linear systems. *European Journal of Control*, 17(5-6):603–620, 2011.

[90] R. M. Ferrari, T. Parisini, and M. M. Polycarpou. Distributed fault detection and isolation of large-scale discrete-time nonlinear systems: An adaptive approximation approach. *IEEE Transactions on Automatic Control*, 57(2):275–290, 2011.

[91] F. Boem, S. Riverso, G. Ferrari-Trecate, and T. Parisini. Plug-and-play fault detection and isolation for large-scale nonlinear systems with stochastic uncertainties. *IEEE Transactions on Automatic Control*, 64(1):4–19, 2018.

[92] M. Halimi, G. Millérioux, and J. Daafouz. Model-based modes detection and discernibility for switched affine discrete-time systems. *IEEE Transactions on Automatic Control*, 60(6):1501–1514, 2014.

[93] F. Küsters and S. Trenn. Switch observability for switched linear systems. *Automatica*, 87:121–127, 2018.

[94] D. Mincarelli, A. Pisano, T. Floquet, and E. Usai. Uniformly convergent sliding mode-based observation for switched linear systems. *International Journal of Robust and Nonlinear Control*, 26(7):1549–1564, 2016.

[95] Z. Zhang, S. Li, H. Yan, and Q. Fan. Sliding mode switching observer-based actuator fault detection and isolation for a class of uncertain systems. *Nonlinear Analysis: Hybrid Systems*, 33:322–335, 2019.

[96] J. Dong, A. S. Kolarijani, and P. Mohajerin Esfahani. Multimode diagnosis for switched affine systems with noisy measurement. *Automatica*, 151:110898, 2023.

[97] F. Ghanipoor, C. Murguia, P. Mohajerin Esfahani, and N. van de Wouw. Robust fault estimators for nonlinear systems: An ultra-local model design. *Automatica*, 171:111920, 2025.

[98] M. Witczak, M. Buciakowski, V. Puig, D. Rotondo, and F. Nejjari. An LMI approach to robust fault estimation for a class of nonlinear systems. *International Journal of Robust and Nonlinear Control*, 26(7):1530–1548, 2016.

[99] J.-W. Zhu, G.-H. Yang, H. Wang, and F. Wang. Fault estimation for a class of nonlinear systems based on intermediate estimator. *IEEE Transactions on Automatic Control*, 61(9):2518–2524, September 2016. doi: 10.1109/TAC.2015.2491898.

[100] A. Xu and Q. Zhang. Nonlinear system fault diagnosis based on adaptive estimation. *Automatica*, 40(7):1181–1193, July 2004. doi: 10.1016/j.automatica.2004.02.018.

[101] C. Shang, H. Ye, D. Huang, and S. X. Ding. From generalized Gauss bounds to distributionally robust fault detection with unimodality information. *IEEE Transactions on Automatic Control*, 68(9):5333–5348, 2022.

[102] F. Harirchi and N. Ozay. Guaranteed model-based fault detection in cyber–physical systems: A model invalidation approach. *Automatica*, 93:476–488, 2018.

[103] C.-S. Hsieh. Unbiased minimum-variance input and state estimation for systems with unknown inputs: A system reformation approach. *Automatica*, 84:236–240, 2017.

[104] J. Dong, K. Pan, S. Pequito, and P. Mohajerin Esfahani. Robust multivariate detection and estimation with fault frequency content information. *Automatica*, 173:112049, 2025.

[105] J. Tan, H. Zheng, D. Meng, X. Wang, and B. Liang. Active input design for simultaneous fault estimation and fault-tolerant control of LPV systems. *Automatica*, 151: 110903, 2023.

[106] R. Seliger and P. M. Frank. Fault-diagnosis by disturbance decoupled nonlinear observers. In *Proceedings of the 30th IEEE Conference on Decision and Control*, pages 2248–2253. IEEE, 1991.

[107] L. Li, S. X. Ding, M. Zhong, and K. Peng. Orthogonal projection-based fault detection for linear discrete-time varying systems. *IEEE Transactions on Automatic Control*, 70 (5):3478–3485, 2025. doi: 10.1109/TAC.2024.3519303.

[108] T. Xue, S. X. Ding, M. Zhong, and D. Zhou. An integrated design scheme for SKR-based data-driven dynamic fault detection systems. *IEEE Transactions on Industrial Informatics*, 18(10):6828–6839, 2022.

[109] Q. Jiang, X. Yan, and B. Huang. Performance-driven distributed PCA process monitoring based on fault-relevant variable selection and bayesian inference. *IEEE Transactions on Industrial Electronics*, 63(1):377–386, 2015.

[110] S. Yin, X. Zhu, and O. Kaynak. Improved PLS focused on key-performance-indicator-related fault diagnosis. *IEEE Transactions on Industrial Electronics*, 62(3):1651–1658, 2014.

[111] B. C. Juricek, D. E. Seborg, and W. E. Larimore. Fault detection using canonical variate analysis. *Industrial & Engineering Chemistry Research*, 43(2):458–474, 2004.

[112] V. Krishnan and F. Pasqualetti. Data-driven attack detection for linear systems. *IEEE Control Systems Letters*, 5(2):671–676, 2020.

[113] J. Noom, O. Soloviev, C. Smith, and M. Verhaegen. Online input design for discrimination of linear models using concave minimization. *preprint available at arXiv:2401.05782*, 2024.

[114] J. Dong and M. Verhaegen. Subspace based fault detection and identification for LTI systems. *IFAC Proceedings Volumes*, 42(8):330–335, January 2009. doi: 10.3182/20090630-4-ES-2003.00055.

[115] H. J. Palanthandalam-Madapusi and D. S. Bernstein. A subspace algorithm for simultaneous identification and input reconstruction. *International Journal of Adaptive Control and Signal Processing*, 23(12):1053–1069, 2009. doi: 10.1002/acs.1057.

[116] J. Hou, T. Liu, and Q.-G. Wang. Recursive subspace identification subject to relatively slow time-varying load disturbance. *International Journal of Control*, 91(3):622–638, 2018.

[117] G. Fattore and M. E. Valcher. A data-driven approach to UIO-based fault diagnosis. In *IEEE 63rd Conference on Decision and Control*, pages 6831–6836. IEEE, 2024.

[118] T. Liu, J. Hou, S. J. Qin, and W. Wang. Subspace model identification under load disturbance with unknown transient and periodic dynamics. *Journal of Process Control*, 85:100–111, 2020.

[119] J. Noom, O. Soloviev, and M. Verhaegen. Proximal-based recursive implementation for model-free data-driven fault diagnosis. *Automatica*, 165:111656, 2024.

[120] Y. Wan, T. Keviczky, and M. Verhaegen. Fault estimation filter design with guaranteed stability using markov parameters. *IEEE Transactions on Automatic Control*, 63(4):1132–1139, 2017.

[121] E. Naderi and K. Khorasani. A data-driven approach to actuator and sensor fault detection, isolation and estimation in discrete-time linear systems. *Automatica*, 85:165–178, 2017.

[122] M. A. Sheikhi, P. M. Esfahani, and T. Keviczky. A kernel-based approach to data-driven actuator fault estimation. *IFAC-PapersOnLine*, 58(4):318–323, 2024.

[123] G. A. Gleizer. Output behavior equivalence and simultaneous subspace identification of systems and faults. *IEEE Control Systems Letters*, 9:1285–1290, 2025.

[124] Z. Chen, K. Liang, S. X. Ding, C. Yang, T. Peng, and X. Yuan. A comparative study of deep neural network-aided canonical correlation analysis-based process monitoring and fault detection methods. *IEEE Transactions on Neural Networks and Learning Systems*, 33(11):6158–6172, 2021.

[125] M. El-Koujok, M. Benammar, N. Meskin, M. Al-Naemi, and R. Langari. Multiple sensor fault diagnosis by evolving data-driven approach. *Information Sciences*, 259: 346–358, 2014.

[126] M. Kallas, G. Mourot, D. Maquin, and J. Ragot. Data-driven approach for fault detection and isolation in nonlinear system. *International Journal of Adaptive Control and Signal Processing*, 32(11):1569–1590, 2018.

[127] M. Bakhtiaridoust, F. N. Irani, M. Yadegar, and N. Meskin. Data-driven sensor fault detection and isolation of nonlinear systems: Deep neural-network koopman operator. *IET Control Theory & Applications*, 17(2):123–132, 2023.

[128] F. N. Irani, M. Yadegar, and N. Meskin. Koopman-based deep iiss bilinear parity approach for data-driven fault diagnosis: Experimental demonstration using three-tank system. *Control Engineering Practice*, 142:105744, 2024.

[129] J. Hou, T. Liu, and Q.-G. Wang. Subspace identification of hammerstein-type nonlinear systems subject to unknown periodic disturbance. *International Journal of Control*, 94(4):849–859, 2021.

[130] L. Liu, Z. Wang, and H. Zhang. Data-based adaptive fault estimation and fault-tolerant control for MIMO model-free systems using generalized fuzzy hyperbolic model. *IEEE Transactions on Fuzzy Systems*, 26(6):3191–3205, 2017.

[131] S. X. Ding. *Model-based fault diagnosis techniques: design schemes, algorithms, and tools*. Springer, 2008.

[132] A. Varga. *Solving fault diagnosis problems*. Springer, 2023.

[133] V. Venkatasubramanian, R. Rengaswamy, K. Yin, and S. N. Kavuri. A review of process fault detection and diagnosis: Part i: Quantitative model-based methods. *Computers & Chemical Engineering*, 27(3):293–311, 2003.

[134] J. W. Polderman and J. C. Willems. *Introduction to mathematical systems theory: a behavioral approach*. Springer, 1998.

[135] J. C. Willems. From time series to linear system—part i. finite dimensional linear time invariant systems. *Automatica*, 22(5):561–580, 1986.

[136] J. Chen and R. J. Patton. *Robust model-based fault diagnosis for dynamic systems*, volume 3. Springer Science & Business Media, 2012.

[137] R. J. Patton and J. Chen. A review of parity space approaches to fault diagnosis. *IFAC Proceedings Volumes*, 24(6):65–81, 1991.

[138] D. Henrion and M. Sebek. An algorithm for polynomial matrix factor extraction. *International Journal of Control*, 73(8):686–695, 2000.

[139] J. Wang, L. Ye, R. X. Gao, C. Li, and L. Zhang. Digital twin for rotating machinery fault diagnosis in smart manufacturing. *International Journal of Production Research*, 57(12):3920–3934, 2019.

[140] M. C. Campi and S. Garatti. The exact feasibility of randomized solutions of uncertain convex programs. *SIAM Journal on Optimization*, 19(3):1211–1230, 2008.

[141] P. Mohajerin Esfahani, T. Sutter, and J. Lygeros. Performance bounds for the scenario approach and an extension to a class of non-convex programs. *IEEE Transactions on Automatic Control*, 60(1):46–58, 2014.

[142] B. Svetozarevic, P. Mohajerin Esfahani, M. Kamgarpour, and J. Lygeros. A robust fault detection and isolation filter for a horizontal axis variable speed wind turbine. In *American Control Conference*, pages 4453–4458, 2013.

[143] H. Habibi, I. Howard, and S. Simani. Reliability improvement of wind turbine power generation using model-based fault detection and fault tolerant control: A review. *Renewable Energy*, 135:877–896, 2019.

[144] B. Mu, X. Yang, and J. K. Scott. Comparison of advanced set-based fault detection methods with classical data-driven and observer-based methods for uncertain nonlinear processes. *Computers & Chemical Engineering*, 166:107975, 2022.

[145] S. J. Qin. Survey on data-driven industrial process monitoring and diagnosis. *Annual Reviews in Control*, 36(2):220–234, 2012.

[146] M. Verhaegen. Identification of the deterministic part of MIMO state space models given in innovations form from input-output data. *Automatica*, 30(1):61–74, 1994. doi: 10.1016/0005-1098(94)90229-1.

[147] A. Chiuso. The role of vector autoregressive modeling in predictor-based subspace identification. *Automatica*, 43(6):1034–1048, 2007.

[148] M. Yin, A. Iannelli, and R. S. Smith. Maximum likelihood estimation in data-driven modeling and control. *IEEE Transactions on Automatic Control*, 68(1):317–328, 2021.

[149] S. X. Ding. Data-driven design of monitoring and diagnosis systems for dynamic processes: A review of subspace technique based schemes and some recent results. *Journal of Process Control*, 24(2):431–449, 2014.

[150] T. Kailath. *Linear systems*, volume 156. Prentice-Hall Englewood Cliffs, NJ, 1980.

[151] G. Disarò and M. E. Valcher. On the equivalence of model-based and data-driven approaches to the design of unknown-input observers. *IEEE Transactions on Automatic Control*, 2024.

[152] M. S. Turan and G. Ferrari-Trecate. Data-driven unknown-input observers and state estimation. *IEEE Control Systems Letters*, 6:1424–1429, 2021.

[153] A. Willsky. On the invertibility of linear systems. *IEEE Transactions on Automatic Control*, 19(3):272–274, 2003.

[154] S. D. Kadam and H. J. Palanthandalam-Madapusi. A note on invertibility and relative degree of MIMO LTI systems. *IFAC Journal of Systems and Control*, 20:100193, 2022.

[155] J. Bokor and Z. Szabó. Fault detection and isolation in nonlinear systems. *Annual Reviews in Control*, 33(2):113–123, 2009.

[156] I. Markovsky. *Low Rank Approximation*. Springer, 2018.

[157] G. Basile and G. Marro. *Controlled and conditioned invariants in linear system theory*. Prentice Hall, Englewood Cliffs, N.J, 1992. ISBN 978-0-13-172974-2.

[158] S. Sanjeevini and D. S. Bernstein. Counting zeros using observability and block toeplitz matrices. *IEEE Transactions on Automatic Control*, 66(3):1301–1305, 2020. doi: 10.1109/TAC.2020.2989269.

[159] D. Bernstein. *Scalar, vector, and matrix mathematics: theory, facts, and formulas-revised and expanded edition*. Princeton university press, 2018.

[160] M. A. Sheikhi, G. de Albuquerque Gleizer, and T. Keviczky. Data-driven characterization of multivariable LTI system zeros. Submitted to IEEE Transactions on Automatic Control (Under Review), .

[161] D. Liu, B. Besselink, S. Baldi, W. Yu, and H. L. Trentelman. An adaptive disturbance decoupling perspective to longitudinal platooning. *IEEE Control Systems Letters*, 6: 668–673, 2021.

[162] M. Sassano and A. Astolfi. Model matching and passivation of mimo linear systems via dynamic output feedback and feedforward. *IEEE Transactions on Automatic Control*, 65(10):4016–4030, 2019.

[163] B. Zhang, Y. Ren, and D.-W. Ding. Optimal tracking and regulation performance of networked control systems with time delay and input quantization. *IEEE Transactions on Automatic Control*, 2025.

[164] V. Kučera. Decoupling with stability of linear systems by static-state feedback. *IEEE Transactions on Automatic Control*, 66(10):4684–4699, 2020.

[165] G. Conte, A. M. Perdon, and E. Zattoni. Fault detection problems for switching linear systems: A structural approach. *IEEE Transactions on Automatic Control*, 68 (10):5890–5905, 2022.

[166] F. Pasqualetti, F. Dörfler, and F. Bullo. Attack detection and identification in cyber-physical systems. *IEEE Transactions on Automatic Control*, 58(11):2715–2729, 2013. doi: 10.1109/TAC.2013.2266831.

[167] C. B. Schrader and M. K. . Research on system zeros: a survey. *International Journal of Control*, 50(4):1407–1433, 1989. doi: 10.1080/00207178908953438.

[168] N. Karcanias and B. Kouvaritakis. The output zeroing problem and its relationship to the invariant zero structure: a matrix pencil approach. *International Journal of Control*, 30(3):395–415, 1979. doi: 10.1080/00207177908922783.

[169] J. Tokarzewski. Zeros in discrete-time MIMO LTI systems and the output-zeroing problem. *International Journal of Applied Mathematics and Computer Science*, 2000.

[170] A. Isidori. The zero dynamics of a nonlinear system: From the origin to the latest progresses of a long successful story. *European Journal of Control*, 19(5):369–378, 2013. doi: 10.1016/j.ejcon.2013.05.014.

[171] W. M. Wonham. *Linear multivariable control*, volume 101. Springer, 1974.

[172] B. D. Anderson. Output-nulling invariant and controllability subspaces. *IFAC Proceedings Volumes*, 8(1):337–345, 1975. doi: 10.1016/S1474-6670(17)67757-7.

[173] P. Antsaklis. Maximal order reduction and supremal (a, b)-invariant and controllability subspaces. *IEEE Transactions on Automatic Control*, 25(1):44–49, 1980. doi: 10.1109/TAC.1980.1102231.

[174] H. Aling and J. M. Schumacher. A nine-fold canonical decomposition for linear systems. *International Journal of Control*, 39(4):779–805, 1984. doi: 10.1080/00207178408933206.

[175] J. Coulson, J. Lygeros, and F. Dörfler. Data-enabled predictive control: In the shallows of the deepc. In *18th European Control Conference*, pages 307–312. IEEE, 2019. doi: 10.23919/ECC.2019.8795639.

[176] W. Favoreel, B. De Moor, and M. Gevers. SPC: Subspace predictive control. *IFAC Proceedings Volumes*, 32(2):4004–4009, 1999. doi: 10.1016/S1474-6670(17)56683-5.

[177] A. Emami-Naeini and P. Van Dooren. Computation of zeros of linear multivariable systems. *Automatica*, 18(4):415–430, 1982. doi: 10.1016/0005-1098(82)90070-X.

[178] J. M. P. Delgado and A. Goel. Computing invariant zeros of a linear system using state-space realization. In *American Control Conference*, pages 2746–2751. IEEE, 2024. doi: 10.23919/ACC60939.2024.10644992.

[179] H. L. Trentelman, A. A. Stoorvogel, M. Hautus, and L. Dewell. *Control theory for linear systems*. Springer London, 2002.

[180] B. Moore and A. Laub. Computation of supremal (A,B)-invariant and controllability subspaces. *IEEE Transactions on Automatic Control*, 23(5):783–792, 1978. doi: 10.1109/TAC.1978.1101882.

[181] F. Padula, A. Ferrante, and L. Ntogramatzidis. Eigenstructure assignment in linear geometric control. *Automatica*, 124:109363, 2021. doi: 10.1016/j.automatica.2020.109363.

[182] L. Ntogramatzidis, F. Padula, and A. Ferrante. New results on algorithms for the computation of output-nulling and input-containing subspaces. *International Journal of Control*, 97(7):1586–1593, 2024. doi: 10.1080/00207179.2023.2216316.

[183] F. Celi and F. Pasqualetti. Data-driven meets geometric control: Zero dynamics, subspace stabilization, and malicious attacks. *IEEE Control Systems Letters*, 6:2569–2574, 2022. doi: 10.1109/LCSYS.2022.3170866.

[184] J. Kreiss and J.-F. Trégouët. Input redundancy: Definitions, taxonomy, characterizations and application to over-actuated systems. *Systems & Control Letters*, 158: 105060, 2021. ISSN 01676911. doi: 10.1016/j.sysconle.2021.105060.

[185] W. M. Wonham and A. S. Morse. Decoupling and pole assignment in linear multivariable systems: a geometric approach. *SIAM Journal on Control*, 8(1):1–18, 1970. doi: 10.1137/0308001.

[186] L. Ntogramatzidis and R. Schmid. Robust eigenstructure assignment in geometric control theory. *SIAM Journal on Control and Optimization*, 52(2):960–986, 2014. doi: 10.1137/130912906.

[187] M. Sain and J. Massey. Invertibility of linear time-invariant dynamical systems. *IEEE Transactions on automatic control*, 14(2):141–149, 1969.

[188] Z. Gao, C. Cecati, and S. X. Ding. A survey of fault diagnosis and fault-tolerant techniques—part I: Fault diagnosis with model-based and signal-based approaches. *IEEE Transactions on Industrial Electronics*, 62(6):3757–3767, 2015.

[189] M. Zhong, S. X. Ding, Q.-L. Han, and Q. Ding. Parity space-based fault estimation for linear discrete time-varying systems. *IEEE Transactions on Automatic Control*, 55(7):1726–1731, 2010.

[190] E. Naderi and K. Khorasani. Unbiased inversion-based fault estimation of systems with non-minimum phase fault-to-output dynamics. *IET Control Theory & Applications*, 13(11):1629–1638, 2019.

[191] A. Ansari and D. S. Bernstein. Input estimation for nonminimum-phase systems with application to acceleration estimation for a maneuvering vehicle. *IEEE Transactions on Control Systems Technology*, 27(4):1596–1607, 2018.

[192] E. Naderi and K. Khorasani. Inversion-based output tracking and unknown input reconstruction of square discrete-time linear systems. *Automatica*, 95:44–53, 2018.

[193] K. George, M. Verhaegen, and J. M. Scherpen. Stable inversion of MIMO linear discrete time non-minimum phase systems. In *Proceedings of the 7th Mediterranean Conference on Control and Automation*, pages 267–281, 1999.

[194] J. van Zundert and T. Oomen. On inversion-based approaches for feedforward and ilc. *Mechatronics*, 50:282–291, 2018.

[195] G. Pillonetto, F. Dinuzzo, T. Chen, G. De Nicolao, and L. Ljung. Kernel methods in system identification, machine learning and function estimation: A survey. *Automatica*, 50(3):657–682, 2014.

[196] N. Aronszajn. Theory of reproducing kernels. *Transactions of the American Mathematical Society*, 68(3):337–404, 1950.

[197] L. Blanken and T. Oomen. Kernel-based identification of non-causal systems with application to inverse model control. *Automatica*, 114:108830, 2020.

[198] P. Van den Hof, B. Wahlberg, P. Heuberger, B. Ninness, J. Bokor, and T. O. e Silva. Modelling and identification with rational orthogonal basis functions. *IFAC Proceedings Volumes*, 33(15):445–455, 2000.

[199] T. Chen and L. Ljung. Regularized system identification using orthonormal basis functions. In *European Control Conference*, pages 1291–1296. IEEE, 2015.

[200] M. A. Sheikhi, P. Mohajerin Esfahani, and T. Keviczky. Input design for system order estimation. Accepted at 23rd IFAC World Congress, 2026.

[201] S. Misra and M. Nikolaou. Adaptive design of experiments for model order estimation in subspace identification. *Computers & Chemical Engineering*, 100:119–138, 2017.

[202] Y. Yu, S. Talebi, H. J. Van Waarde, U. Topcu, M. Mesbahi, and B. Açıkmeşe. On controllability and persistency of excitation in data-driven control: Extensions of willems' fundamental lemma. In *IEEE 60th Conference on Decision and Control*, pages 6485–6490. IEEE, 2021.

[203] M. Verhaegen and P. Dewilde. Subspace model identification part 2. analysis of the elementary output-error state-space model identification algorithm. *International Journal of Control*, 56(5):1211–1241, 1992.

[204] M. Aoki and R. Staley. On input signal synthesis in parameter identification. *Automatica*, 6(3):431–440, 1970.

[205] C. R. Rojas, J. S. Welsh, G. C. Goodwin, and A. Feuer. Robust optimal experiment design for system identification. *Automatica*, 43(6):993–1008, 2007.

[206] R. Mehra. Optimal inputs for linear system identification. *IEEE Transactions on Automatic Control*, 19(3):192–200, 1974.

[207] K. Lindqvist and H. Hjalmarsson. Identification for control: adaptive input design using convex optimization. In *Proceedings of the 40th IEEE Conference on Decision and Control*, volume 5, pages 4326–4331, 2001.

[208] X. Bombois, M. Gevers, R. Hildebrand, and G. Solari. Optimal experiment design for open and closed-loop system identification. *Communications in Information and Systems*, 11(3):197–224, 2011.

[209] N. Dirkx, J. van de Wijdeven, and T. Oomen. Frequency response function identification for multivariable motion control: Optimal experiment design with element-wise constraints. *Mechatronics*, 71:102440, 2020.

[210] A. Wagenmaker and K. Jamieson. Active learning for identification of linear dynamical systems. In *Proceedings of Thirty Third Conference on Learning Theory*, pages 3487–3582. PMLR, 2020.

[211] B. Ho and R. E. Kálmán. Effective construction of linear state-variable models from input/output functions. *Regelungstechnik*, 14(1-12):545–548, 1966.

[212] G. Van der Veen, J.-W. van Wingerden, M. Bergamasco, M. Lovera, and M. Verhaegen. Closed-loop subspace identification methods: an overview. *IET Control Theory & Applications*, 7(10):1339–1358, 2013.

[213] A. S. Lewis and H. S. Sendov. Nonsmooth analysis of singular values. part i: Theory. *Set-Valued Analysis*, 13(3):213–241, 2005.

[214] T. Sarkar, A. Rakhlin, and M. A. Dahleh. Finite time LTI system identification. *Journal of Machine Learning Research*, 22(26):1–61, 2021.

[215] F. Zheng, Y. Jedra, and A. Proutière. Minimal order recovery through rank-adaptive identification. In *IEEE 64th Conference on Decision and Control*, pages 69–74. IEEE, 2025.

[216] A. Tsiamis, I. Ziemann, N. Matni, and G. J. Pappas. Statistical learning theory for control: A finite-sample perspective. *IEEE Control Systems Magazine*, 43(6):67–97, 2023. doi: 10.1109/MCS.2023.3310345.

[217] Y. Abbasi-Yadkori, D. Pál, and C. Szepesvári. Improved algorithms for linear stochastic bandits. *Advances in neural information processing systems*, 24, 2011.

[218] E. Elhamifar and R. Vidal. Sparse subspace clustering: Algorithm, theory, and applications. *IEEE Transactions on Pattern Analysis and Machine Intelligence*, 35(11): 2765–2781, 2013. doi: 10.1109/TPAMI.2013.57.

[219] S. X. Ding. *Advanced methods for fault diagnosis and fault-tolerant control*, volume 184. Springer, 2021.

[220] V. K. Mishra, I. Markovsky, A. Fazzi, and P. Dreesen. Data-driven simulation for NARX systems. In *29th European Signal Processing Conference*, pages 1055–1059. IEEE, 2021. doi: 10.23919/EUSIPCO54536.2021.9616226.

[221] S. L. Brunton and J. N. Kutz. *Data-driven science and engineering: Machine learning, dynamical systems, and control*. Cambridge University Press, 2022.

[222] A. Fazzi and A. Chiuso. Simulation of nonlinear systems trajectories: between models and behaviors. In *10th International Conference on Control, Decision and Information Technologies*, pages 2049–2054. IEEE, 2024. doi: 10.1109/CoDIT62066.2024.10708264.

[223] S. Sanjeevini, S. A. U. Islam, and D. S. Bernstein. On the zero dynamics of linear input–output models. *International Journal of Control*, 95(4):924–933, 2022. doi: 10.1080/00207179.2020.1831077.

[224] S. Roman. *Advanced linear algebra*. Springer, 2005.

[225] G. Salomon, K. Zhou, and E. Wu. A new balanced realization and model reduction method for unstable systems. *IFAC Proceedings Volumes*, 32(2):1696–1701, 1999.

[226] L. Pernebo and L. Silverman. Model reduction via balanced state space representations. *IEEE Transactions on Automatic Control*, 27(2):382–387, 1982.

[227] B. Moore. Principal component analysis in linear systems: Controllability, observability, and model reduction. *IEEE Transactions on Automatic Control*, 26(1):17–32, 1981.

[228] P. S. Heuberger, P. M. Hof, and B. Wahlberg, editors. *Modelling and Identification with Rational Orthogonal Basis Functions*. Springer, 2005.

[229] R. A. Roberts and C. T. Mullis. *Digital signal processing*. Addison-Wesley Longman Publishing Co., Inc., 1987.

[230] P. Bodin. Recursive calculation of expansion coefficients for generalized orthonormal rational bases. *IFAC Proceedings Volumes*, 32(2):4141–4146, 1999.

[231] T. J. de Hoog, P. S. Heuberger, and P. M. Van den Hof. A general transform theory of rational orthonormal basis function expansions. In *Proceedings of the 39th IEEE Conference on Decision and Control*, volume 5, pages 4649–4654. IEEE, 2000.

[232] B. Ninness and F. Gustafsson. A unifying construction of orthonormal bases for system identification. *IEEE Transactions on Automatic Control*, 42(4):515–521, 1997.

[233] H. Akçay. Discrete-time system modelling in lp with orthonormal basis functions. *Systems & Control Letters*, 39(5):365–376, 2000.

[234] B. Ninness, H. Hjalmarsson, and F. Gustafsson. Generalized fourier and toeplitz results for rational orthonormal bases. *SIAM Journal on Control and Optimization*, 37(2):429–460, 1999.

[235] M. A. Sheikhi, C. R. Rojas, G. de Albuquerque Gleizer, P. Mohajerin Esfahani, and T. Keviczky. Non-asymptotic analysis of data-driven input estimation in linear systems. Submitted to IFAC Journal of Systems and Control (Under Review), .

[236] A. Amini, M. A. Sheikhi, Y. de Loore, P. Hacking, and P. Mohajerin Esfahani. Fault isolation in inkjet printers using self-sensing piezo actuators. Submitted to 13th IFAC SAFEPROCESS (Under Review).

[237] M. A. Sheikhi, G. de Albuquerque Gleizer, P. M. Esfahani, and T. Keviczky. Data-driven fault isolation in linear time-invariant systems: A geometric approach. In *44th Benelux Meeting on Systems and Control*, pages 68–68. Rijksuniversiteit Groningen, 2025.

List of Publications

M. A. Sheikhi, G. de Albuquerque Gleizer, and T. Keviczky. Data-driven characterization of multivariable LTI system zeros. Submitted to IEEE Transactions on Automatic Control (Under Review), .

M. A. Sheikhi, C. R. Rojas, G. de Albuquerque Gleizer, P. Mohajerin Esfahani, and T. Keviczky. Non-asymptotic analysis of data-driven input estimation in linear systems. Submitted to IFAC Journal of Systems and Control (Under Review), .

M. A. Sheikhi, G. d. A. Gleizer, T. Keviczky, and P. M. Esfahani. Fault diagnosis in dynamical systems: Geometric interpretation and tractable algorithms. *Annual Review of Control, Robotics, and Autonomous Systems*, 9, 2026.

M. A. Sheikhi, G. de Albuquerque Gleizer, P. M. Esfahani, and T. Keviczky. Data-driven fault isolation in linear time-invariant systems: a subspace classification approach. *IEEE Control Systems Letters*, 2025.

M. A. Sheikhi, P. Mohajerin Esfahani, and T. Keviczky. Input design for system order estimation. Accepted at 23rd IFAC World Congress, 2026.

M. A. Sheikhi, P. M. Esfahani, and T. Keviczky. A kernel-based approach to data-driven actuator fault estimation. *IFAC-PapersOnLine*, 58(4):318–323, 2024.

A. Amini, M. A. Sheikhi, Y. de Loore, P. Hacking, and P. Mohajerin Esfahani. Fault isolation in inkjet printers using self-sensing piezo actuators. Submitted to 13th IFAC SAFEPROCESS (Under Review).

M. A. Sheikhi, G. de Albuquerque Gleizer, P. M. Esfahani, and T. Keviczky. Data-driven fault isolation in linear time-invariant systems: A geometric approach. In *44th Benelux Meeting on Systems and Control*, pages 68–68. Rijksuniversiteit Groningen, 2025.

Included in this thesis.

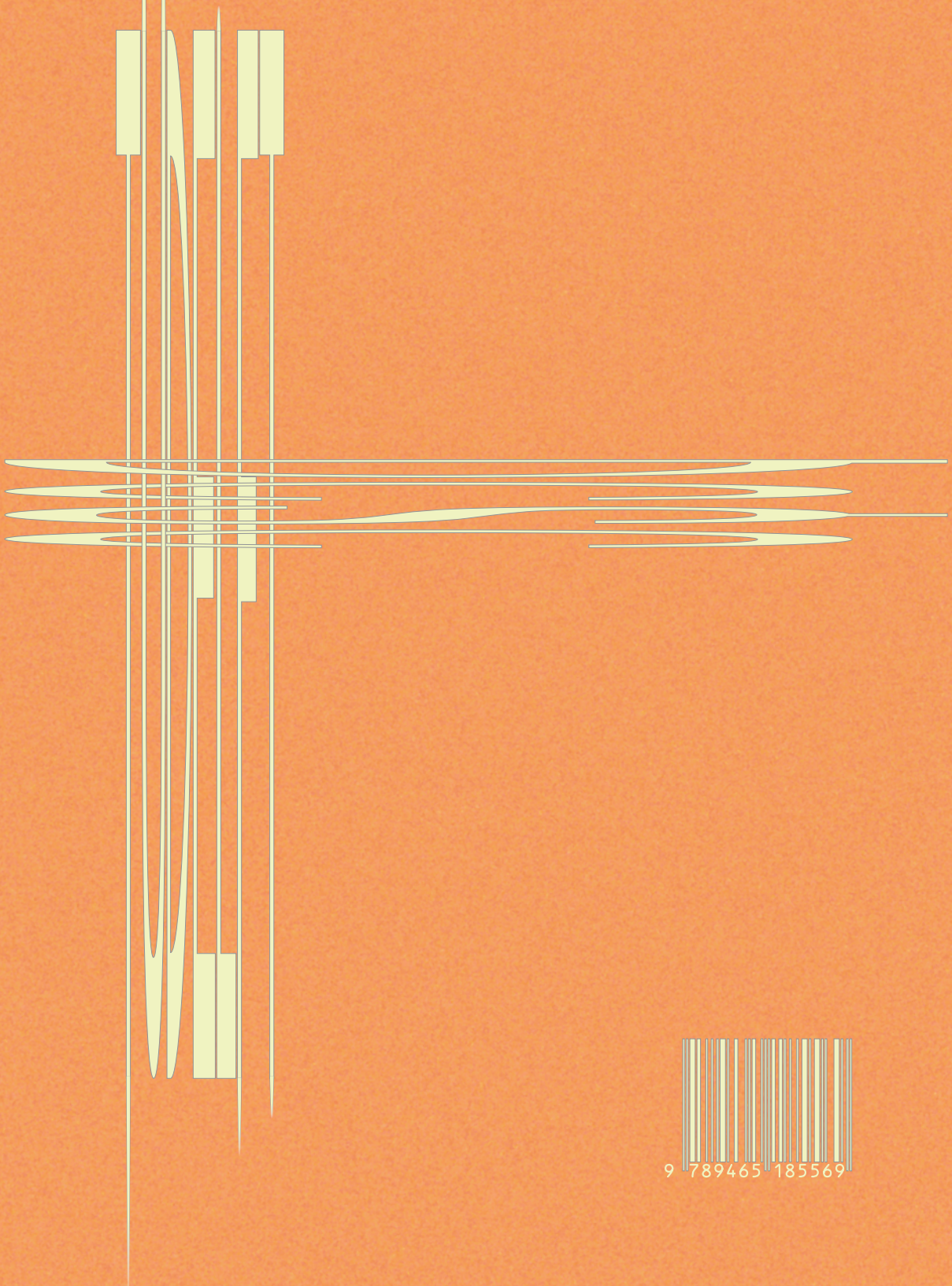
9 789465 185569